Order Number 9230509

Mid-ocean ridge magmatism: Style of mantle upwelling, partial melting, crustal level processes, and spreading rate dependence. A petrologic approach

Niu, Yaoling, Ph.D.

University of Hawaii, 1992

U·M·I
300 N. Zeeb Rd.
Ann Arbor, MI 48106

MID-OCEAN RIDGE MAGMATISM: STYLE OF MANTLE UPWELLING, PARTIAL MELTING, CRUSTAL LEVEL PROCESSES, AND SPREADING RATE DEPENDENCE ——— A PETROLOGIC APPROACH

A DISSERTATION SUBMITTED TO THE GRADUATE DIVISION OF THE UNIVERSITY OF HAWAI'I IN PARTIAL FULFILLMENT OF THE REQUIREMENTS FOR THE DEGREE OF

DOCTOR OF PHILOSOPHY

IN

GEOLOGY AND GEOPHYSICS

MAY 1992

BY

Yaoling Niu

Dissertation Committee:

Rodey Batiza, Chairperson
Michael O. Garcia
John J. Mahoney
Jill L. Karsten
David W. Muenow

ACKNOWLEDGMENTS

I have learned that to complete a Ph.D. dissertation is difficult, so I have worked very hard in fear of a failure. It is finally finished now, but it would not have been possible without the generous help of many people, only a few of whom are mentioned here.

I would like to extend my wholehearted thanks first to Dr. Rodey Batiza, my advisor, and more accurately, the best friend of mine. I first met Rodey at Northwestern University in spring 1988 when I was about to begin my Ph.D. study. He gave me a small set of seamount rock data to play with. It took me several months to just feel comfortable with the data through extensive reading and discussions with him, but it was this exercise that stimulated my great interest in ocean floor petrology and mantle melting processes. I am very grateful for his encouragement to work in this field and to come with him to Hawaii, which turned out to be the right place for my Ph.D. research. His help with my dissertation has been enormous and my scientific development owes a great deal to him! My apologies also go first to him because of my frequent impatience with him, but he never seemed to feel bad about it. Instead, he always encouraged me to keep eagerness and aggressiveness in science. I especially thank him for his charitable mind and sympathetic understanding of me and my family, which I deeply feel, have helped me greatly with my dissertation research.

This may be the only opportunity that I can take to thank my wife, Lijun, for her wholehearted support of me. She deserves recognition for the part she played in the completion of this work. With her, I was able to work all of the time without worrying about cooking meals and doing laundry. Her understanding and love gave me encouragement and comfort whenever I felt overwhelmed. Unfortunately, when she felt lonely, I was in the microprobe room, in the computer room, at the microscope in the office, or even in front of our computer at home. When she needed me on weekends, my

answer was always "I have too much to do!". I thank my daughter, Lily. She does not know anything about geology, but she did give Daddy a great deal of relief whenever I was frustrated.

My particular thanks go to my dissertation committee members for their willingness to help me and their overall support in all stages — particularly their effort in designing excellent comprehensive exams and their careful reviews of my dissertation. Mike Garcia gave my wife and me a welcome orientation about the department, HIG, and UH campus on the very first day we arrived in Hawaii, and instructed me how to use HIG microprobe. John Mahoney always gave me the right answers to my questions and open-minded suggestions. Discussions of scientific questions with John Sinton were beneficial, and his well thought-out ideas were always inspiring, stimulating, and encouraging. Dave Muenow's encouragement was particularly important. Although Jill Karsten came late to my committee, her role in my dissertation research has been very important in all stages: her critical reviews of my dissertation, constructive comments on my papers, and open discussions on many scientific questions have been extremely helpful. Several other people, while not on my committee, always provided suggestions and important input: Sieger van der Laan, Dick Hey, and Li-Chung Ming deserve particular mention.

Many thanks go to my friendly fellow graduate students over the years. Ruth Multhaup made Lijun and I feel welcome in Hawaii from the very beginning and Steve Spengler kindly provided us with two weeks of free accommodation while we were looking for housing. Beth Jorgenson, Frank Trusdell, and Suki Smaglik helped me with various kinds of machines around. Mary MacKay, a classmate of mine, helped me with learning French. Occasional chatting with many has made my graduate student life a little easier.

I thank R. Korotev at Washington University for INAA analyses, T. O'Hearn at the Smithsonian Institution for some glass analyses, and Tom Hulsebosch and Jo Ann Sinton for their readily available help that guaranted my excellent analytical data for the research.

This work was funded by grants from NSF and ONR to Dr. Rodey Batiza.

Lastly, I wish to thank Secretaries Karen Ogino, Leona Anthony, and Carol Koyanagi for their ordinary, but important work, for easing the lives of graduate students. I am especially grateful to Carol Koyanagi whose always available assistance saved a lot of my time so that I could have more time to do my research.

I must say, I like Hawaii; Hawaii is the right place for graduate study, not because the weather is excellent, not because the beach is nearby, but because people are so nice and helpful in the department.

ABSTRACT

This dissertation deals with magmatic processes of the mid-ocean ridge (MOR) system on a global scale. The style of mantle upwelling, partial melting, crustal level processes, and the dependence on plate spreading rate are evaluated based on mid-ocean ridge basalt (MORB) chemistry. The approach is an integration of observation, data compilation, petrologic and geochemical interpretation, and theoretical modeling.

Evaluation of buoyancy forces in the melting range shows that density differences between melt and solids increase toward the surface, implying an increasing melt migration rate with upwelling and melting, but the density difference is significantly less than the commonly assumed value: $\sim 0.5 g\text{-}cm^{-3}$.

An empirical model is developed to calculate the compositions of primary magmas for MORB. Its application has revealed that: 1) most MORBs are generated by 10–20% melting at initial depths of 12–21 kbar; 2) primary MORB melts have MgO = 10–12 wt %; and 3) mantle temperature can vary up to 50°–60°C over distances of 30–50 km both across and along axis with weakly conductive temperature gradient superimposing on adiabatic gradient.

Examination of closely-spaced samples at ~ 9°30'N, EPR shows that fractional crystallization is the dominated process in axial magma chambers (AMC), but mechanical differentiation due to density differences between different phases is also very important, as revealed from crystal size distribution (CSD) and density relations. Chemical correlations with axial depth suggest a chemically zoned AMC, which is maintained by a single site magma injection (at the topographic high) and intra-chamber lateral transport.

Analysis of a global MORB data base shows that the so-called local trend is unique to slow-spreading (< 50 mm/yr) ridges, whereas the so-called global trend is characteristic of fast-spreading (> 60 mm/yr) ridges. For transitional rates (50 - 60 mm/yr), both trends

appear. Passive upwelling with efficient compaction and melt segregation can well explains the global trend at fast-spreading ridges, whereas diapiric upwelling with slow melt segregation and solid-melt reequilibration can explain the local trend at slow-spreading ridges, consistent with other geophysical observations.

TABLE OF CONTENTS

LIST OF TABLES

LIST OF FIGURES

CHAPTER 1

INTRODUCTION

1.1 What we know about mid-ocean ridge processes

The mid-ocean ridge system has received extensive study in the past decades because of its tectonic importance on a global scale: 1) it represents a site of the best access to processes occurring in the earth's interior through magmatism and hydrothermalism compared with other tectonic settings; 2) it is the place where new ocean basins are initiated and oceanic crust is created through extrusion and intrusion of basaltic melt generated by partial melting of mantle material as a result of plate spreading; and 3) it is this divergent plate boundary that provides an additional opportunity to understand mantle-crust recycling over the history of the earth. In short, a great deal has been learnt about the ridge dynamic processes in petrology, geochemistry, as well as geophysics in the past decades [e.g., *Macdonald*, 1982; *Sempéré and Macdonald*, 1987; *Phipps Morgan*, 1991; *Klein*, 1991]. Some important advances may be categorized as follows.

1.1.1 Spreading-rate-dependent features at MOR

Plate spreading rate, which varies from 10 - 160 mm/yr (full rate), has been shown to control the morphology of ridges and the roughness of ridge flanks [e.g., *Macdonald*, 1982]. Slow (< 50 mm/yr full rate) spreading centers such as the mid-Atlantic ridge (MAR) have rugged topography and are characterized by a 1 - 3 km deep, 15 - 30 km wide axial rift valley; intermediate (50 - 80 mm/yr full rate) spreading centers such as Galapagos spreading center (GSC) have a 50 - 400 m deep, 7 - 20 km wide rift valley; and fast spreading centers such as the East Pacific Rise (EPR) have a 200 - 400 m tall, 5 - 15 km wide axial high with a 0 - 300 m axial summit caldera (ASC) [*Haymon et al.*, 1991*b*].

Along-axis topographic and gravity variations have been shown to depend on the spreading rate [*Lin and Phipps Morgan*, 1992]. At fast spreading centers (e.g., the EPR) the axial depth varies by as little as a few hundreds of meters over the great lengths (~ 3000 km) of the ridge and the gravity profile is very smooth. In contrast, at slow spreading centers (e.g., the MAR) the axial depth varies as much as 1.5 km over a length scale of only ~ 100 km and the mantle Bouguer anomaly, which correlates negatively with axial depth, varies by as much as 30 mgal over the same length scale.

Petrologically, differences in MORB chemistry between slow (MAR) and fast (EPR) spreading ridges have also been observed [*Natland*, 1980*b*; *Flower*, 1980; *Morel and Hekinian*, 1980; *Batiza, 1991*; *Sinton and Detrick, 1992*] with slow spreading centers characterized by more primitive (higher $Mg^{\#}$) and petrologically and petrographically more diverse lavas than fast spreading centers [e.g., *Rhodes et al.*, 1979]. Isotopic variability seems also to exhibit signatures related to the ridge spreading rate [e.g., *Batiza*, 1984; *Allègre et al.*, 1984; *Ito et al.*, 1987]; slow spreading ridges have much greater isotopic variations that fast spreading ridges [e.g., *Batiza*, 1984]. Mantle plume effects seem to be more important at slow-spreading ridges (e.g., the mid-Atlantic ridge) [e.g., *Schilling et al.*, 1983] than at fast-spreading ridges (e.g., the East Pacific Rise).

1.1.2 Ridge segmentation

Although the ridge system circles the globe, it is not a continuous, uninterrupted, feature. Instead, it is characterized by segmentation at various scales. Recent extensive geophysical observations with multibeam and side-scan sonar systems have greatly enhanced our understanding of seafloor structure and tectonic features of the ridge system. In addition to large, stable transform faults and fracture zones which offset ridge segments by 40 - 400 km, spreading centers are segmented by numerous smaller discontinuities. These include propagating rifts (PRs) [*Hey*, 1977; *Hey et al.*, 1980], overlapping

spreading centers (OSCs) [*Macdonald and Fox*, 1983; *Londsdale*, 1983], small non-overlapping offsets (SNOOs) [*Batiza and Margolis*, 1986], and deviations from axial linearly (DEVALs) [*Langmuir et al.*, 1986], which , although discovered in the Pacific, have also been recognized at the mid-Atlantic ridge [e.g., *Sempéré et al.*, 1990; *Forsyth et al.*, 1990; *Patriat et al.*, 1990; *Grindlay et al.*, 1991].

Interestingly, petrologic variations of MORB have been found to partly reflect ridge segmentation [*Langmuir et al.*, 1986; *Macdonald et al.*, 1987; *Dick*, 1989; *Sinton et al.*, 1991]. This magmatic segmentation seems to show a hierarchical arrangement that may correspond to different characteristic length scales of petrologic processes such as melting, mantle source composition, segregation systematics, and differentiation patterns. The length scale of magmatic segmentation appears to be proportional to the spreading rate [*Sinton et al.*, 1991].

1.1.3 MORB chemical systematics on a global scale

Recent work by *Dick et al.* [1984] and *Klein and Langmuir* [1987] based on data available at the time enhanced our first order knowledge about MORB mantle melting systematics in terms of along-axis mantle temperature distribution. Hotter mantle begins to melt at a greater depth and produces greater amounts of melt for crust formation. The recent data from the superfast-spreading portion of the EPR [*Sinton et al.*, 1991] and the slow-spreading Indian Ocean ridges [*Mahoney et al.*, 1989; *Klein et al*, 1991] extend the global MORB data base for more detailed investigation.

Most importantly, geochemical studies have shown that MORBs display a uniquely "depleted" nature in isotopic systematics and incompatible trace element abundances that is not observed elsewhere in oceanic or continental volcanic domains [e.g., *Allègre* , 1982; *Allègre et al.*, 1984; *Zindler and Hart*, 1986; *Hart and Zindler*, 1989]. This has provided important information about present-day mantle compositional structure and the evolution

of oceanic mantle over the history of the earth [e.g., *White and Hofmann*, 1982; *Saunders et al.*, 1984; *White*, 1985; *Zindler and Hart*, 1986; *Hart and Zindler*, 1989].

1.1.4 Near-ridge seamounts

Near-ridge seamounts are found to be ubiquitous near the EPR [*Batiza*, 1981; 1982; *Fornari et al.*, 1987; *Batiza et al.*, 1989*a*; *Allan et al.*, 1989; *Batiza et al.*, 1990] as well as at the MAR [*Batiza et al.*, 1989*b*]. Most of those from the EPR flanks are volcanically active and their lavas are chemically indistinguishable from the nearby axial MORB except that the seamount lavas are, on average, more primitive and more diverse than axial lavas [*Batiza and Vanko*, 1984; *Batiza et al*, 1990]. Interestingly, many near-ridge seamounts are members of well-defined seamount chains, which are parallel either to absolute plate motion or relative plate motion directions [*Vogt*, 1971; *Barr*, 1974; *Batiza and Vanko*, 1983; *Davis and Karsten*, 1986; *Fornari et al.*, 1984; *Batiza et al.*, 1990]. These observations provide limits on mantle thermal structure across the ridge axis, the geometry of mantle melting regime beneath ridge axis, and the width of mantle upwelling underneath the plate boundary zone.

1.1.5 Axial magma chambers (AMC)

Because of the much more fractionated chemical compositions of observed MORB than theoretically predicted for primary magmas [*O'Hara*, 1966], plus models of oceanic crust structure inferred from ophiolite studies and seismic data, magma chambers have been proposed to play an important role in MORB petrogenesis. Recent multichannel seismic (MCS) reflection studies [*Detrick et al.*, 1987; *Mutter et al.*, 1988; *Harding et al.*, 1989; *Vera et al.*, 1990; *Kent et al.*, 1990; *Detrick et al.*, 1990] reveal the existence of axial magma chambers (AMCs) at intermediate to fast ridges (such as the EPR). Interestingly, slow spreading ridges (such as the MAR) have no chambers even at magmatically robust segments [*Detrick et al.*, 1990], confirming the prediction of *Natland* [1980*b*]. In addition,

recent geophysical study by *Kent et al.* [1992] has shown that the size of an AMC is much smaller than previously thought and actual AMCs are characterized by a thin lens of melt body overlying a large volume of mush [e.g., *Sinton and Detrick, 1992*].

1.1.6 Mantle melting and melt supply to the ridge axis

Studies of mantle melting and melt supply, though controversial, have greatly enhanced our knowledge about the physical processes which could operate beneath the ridge axis. It has been generally accepted that magma generation at mid-ocean ridges is accomplished by decompression-induced melting as mantle passively upwells in response to plate separation [e.g., *Oxburgh and Turcotte*, 1968; *Hanks*, 1971; *Bottinga and Allègre*, 1978; *Houseman*, 1983]. It has also been recognized recently that melting beneath the ridge axes is polybaric [*McKenzie*, 1984; *Klein and Langmuir*, 1987; *McKenzie and Bickle*, 1988] and can be visualized as a column melting process. A parcel of mantle, following an adiabatic pressure-temperature (P-T) gradient, rises vertically, intersects the solidus at a depth determined by its temperature and melting characteristics, and begins to melt. Continued upwelling is accompanied by continuous melting, matrix compaction, and melt segregation. Application of the results of peridotite melting to MORB has been proven to be very useful in understanding mantle melting processes and the mantle temperature variation along ridge axis [e.g., *Klein and Langmuir*, 1987].

1.2 Unresolved problems and questions

Despite the achievements briefly reviewed above, many questions remain unresolved and many problems need solving. Among these, some key questions are briefly discussed below.

1.2.1 Style of mantle flow and width of mantle upwelling beneath MORs

Although passive mantle upwelling in response to plate separation has gained a general acceptance, diapiric upflow has also been proposed [*Rabinowicz et al.*, 1987; *Whitehead et al.*, 1984; *Crane*, 1985; *Schouten et al.*, 1985; *Nicolas*, 1986; 1989; *Lin and Phipps Morgan, 1992*], particularly for slow-spreading ridges where ridge segmentation patterns and drastic axial depth variations seem to warrant such an explanation. As for the width of mantle upwelling, controversies remain. Although the mid-ocean ridge system is of global scale, the axial volcanic zone at ridges is extremely narrow (< 1km). In addition, seismic evidence suggests that ocean floor achieves its full thickness (5 - 7 km) within only a few kilometers of the axis [*Detrick et al.*, 1987], indicating that off-axis additions of material to the crust are small. To explain the narrowness of the axial accretion zone, two groups of models have been proposed. (1) The mantle upwelling zone is broad, as suggested by models for passive mantle upwelling in response to plate separation, but additional processes are required to focus melt toward the axis [*Spiegelman and McKenzie*, 1987; *Phipps Morgan*, 1987; *Sleep*, 1988; *Ribe*, 1988; *Sparks and Parmentier*, 1991]. These models suggest that the flow of melt converges toward the axis, whereas mantle flow lines of the solid residue diverge away from the axis. (2) The mantle upwelling zone is narrow, an explanation that circumvents the difficulty of focusing melt flow [*Bottinga and Allègre*, 1978; *Scott and Stevenson*, 1989; *Buck and Su*, 1989; *Rabinowicz et al.*, 1987].

1.2.2 Physical details of melting, melt segregation, and melt supply

It is agreed that upwelling mantle begins to melt across the solidus, but the mechanism that segregates melt into an eruptable magma body at the crustal level is completely unknown. The amount and distribution of melt in the melting region, the mechanism of melt segregation, and the role of lateral melt migration to focus melt below

the very narrow (< 1 km) crustal accretion zone are controversial. Theoretical arguments [e.g., *McKenzie*, 1984; *Richter and McKenzie*, 1984; *Ribe*, 1987; *Riley and Kohlstedt*, 1990] suggest that the maximum melt retention in mantle is likely to be small (1 - 3 %), but exactly how small is debatable. The level and physical mechanisms of melt segregation are also controversial. The maximum depth where dikes may be efficient melt conduits [*Nicolas*, 1986; *Sleep*, 1988] is presently unknown. If the zone of upwelling is wide, then lateral melt migration toward the axis may be needed to focus eruptions in the narrow accretion zone [*Phipps Morgan*, 1987; *Scott and Stevenson*, 1989], but the importance of this process is presently very difficult to evaluate.

1.2.3 Spreading-rate-dependence of mantle upwelling and melt supply

Several studies [e.g., *Scott and Stevenson*, 1989; *Sotin and Parmentier*, 1989] have suggested that upwelling may be episodic or periodic at slow spreading rates. *Schouten et al.*[1985] suggested a spreading-rate dependence of the spacing of central supply conduits feeding ridges. In contrast, others [*Langmuir et al.*, 1986; *Macdonald et al.*, 1988; *Sinton et al.*, 1991] suggest a hierarchical supply geometry. Recently, *Lin and Phipps Morgan* [1992] suggested that fast spreading ridges may be dominated by spreading-induced passive upwelling, whereas at slow spreading ridges, buoyant "plumes" may be more important. The buoyancy could come from the presence of melt, large temperature differences, and/or compositional variation created by melting process, but the buoyancy forces have not been quantitatively evaluated.

1.2.4 Mantle thermal profile

Mantle temperature structure beneath the mid-ocean ridge system is unknown. The only reasonably direct indication of mantle thermal structure comes from the chemistry of the "zero-age" MORB as it is a function of mantle melting temperature. Because MORB chemistry varies greatly on both regional and global scales [e.g., *Klein and Langmuir*,

1987; *Brodholt and Batiza*, 1989; *Klein and Langmuir*, 1989], it is likely that mantle isotherms are not horizontal; however, a quantitative approach to map the mantle temperature is needed.

1.2.5 Nature of primary magma

The debate over the nature of primary magma parental to MORBs has been active for over two decades; our current knowledge is largely based on interpretations of isobaric batch melts produced in the laboratory plus the use of simplified phase diagrams (versus complicated, natural, multicomponent systems) invented by experimental petrologists. Two opposing schools of thoughts exist: 1) the primary magmas parental to MORB are of picritic composition and are generated at high pressures (e.g., 20 - 30 kb) [*O'Hara*, 1968; *Green et al.*, 1979; *Stolper*, 1980; *Jaques and Green*, 1980; *Elthon and Scarfe*, 1984; *Falloon and Green*, 1987]; and 2) most primitive MORBs themselves are primary magmas produced at medium pressures (~ 10 kb) [*Presnall and Hoover*, 1984; *Fujii and Scarfe*, 1985; *Fujii and Bougault*, 1983]. To reveal the nature of the primary magmas is of great importance because composition of primary magma can provide most reliable information about the mantle melting conditions (e.g., temperature and pressure), which are essential for understanding many physical details of melting and melt segregation processes.

1.2.6 Some observed perplexing features in magma chamber processes

Comparison of low pressure experimental results with natural MORBs shows that crustal level fractionation (presumably occurring in magma chambers) is an important part of MORB petrogenesis [*Walker et al.*, 1979; *Grove and Bryan*, 1983]. However, several observations are perplexing in terms of simple crystal fractionation. Magma mixing in a periodically replenished and erupted magma chamber seem to explain some features, but not others. Over-enrichment of certain incompatible trace elements in terms of perfect (Rayleigh) fractionation has been found in several areas [e.g., *Perfit et al.*, 1983; *Hekinian*

and Walker, 1987]. Open-system, frequently replenished magma chamber models [*O'Hara*, 1977; *O'Hara and Mathews*, 1981] and in-situ crystallization [*Langmuir*, 1989] have been invoked to explain this phenomenon, but in natural magma chambers fractionation may not be Rayleigh-type. Instead, equilibrium or semi-equilibrium crystallization may be more realistic if solid sorting is inefficient when crystallinity is high and chambers are small, as proposed by *Sinton and Detrick* [1992]. Another unresolved question is the so-called "clinopyroxene paradox" [e.g., *Rhodes et al.*, 1979], where clinopyroxene is apparently required in models of fractionation in lava suites without clinopyroxene phenocrysts. Models invoking picritic parental magmas [*Bryan et al.*, 1981; *Francis*, 1986], second-stage melting [*Duncan and Green*, 1987], resorption of clinopyroxene during melting [*O'Donnell and Presnall*, 1980; *Fujii and Bougault*, 1983], magma mixing [*Walker et al.*, 1979], and high-pressure fractionation [*Tormey et al*, 1987] have all been proposed. Mechanical fractionation due to density differences between solid phases and melt, and among solid mineral phases may play an important role, but has not been previously evaluated in detail.

1.2.7 "Zero-age" lavas

The lack of a reliable dating technique for MORB hampers our ultimate understanding of many questions. The assumption of zero-age is obviously not true in detail. This assumption is more reasonable for fast spreading ridges, but may be seriously erroneous for slow spreading ridges. Two promising techniques, ^{39}Ar-^{40}Ar and U-Th disequilibrium, are expected to provide ages on young MORB and will probably modify previous interpretations.

1.3 Purpose of this dissertation research and methods employed

This study is intended to deal with mid-ocean ridge magmatism in a broad sense with emphasis on the questions mentioned above such as style of mantle upwelling, partial melting, crustal level processes, and spreading rate dependence. These questions are approached from a petrological viewpoint. The methods are an integration of observation, data compilation, petrological and geochemical interpretation, and theoretical modeling.

1.4 Organization of dissertation

The dissertation is organized into four chapters in terms of the questions to be answered and the methods employed. Each chapter represents a separate and complete project, although they are related and deal with the general topic of mid-ocean ridge dynamics as a whole.

In Chapter 2, the buoyancy forces in the mantle melting environment are quantitatively evaluated through careful and critical examination of data in the literature on density, thermal expansion, and compressibility of silicate melt and relevant mineral phases. I present a computer program for calculating the densities of melt and mineral phases as a function of temperature, pressure, and composition in the mantle melting environment.

In Chapter 3, I use the experimental data set of *Jaques and Green* [1980], *Falloon and Green* [1987, 1988], and *Falloon et al.* [1988] to develop an empirical model for calculating the compositions of primary magmas produced beneath mid-ocean ridges. This model is applied to natural MORB melts in several different settings (a fast-spreading ridge, a slow-spreading ridge, and near-fast-ridge seamounts) to resolve several important questions, including 1) nature of primary magma parental to natural MORB melts; 2) range of mantle melting depth for MORB; 3) width of the mantle upwelling zone and

geometry of the melting regime beneath the MOR system; 4) mantle thermal structure beneath MORs; and 5) potential differences in melting and melt supply mechanism between fast- and slow-spreading ridges.

In Chapter 4, many details of axial magma chamber (AMC) processes are discussed using petrographic, petrologic, and geochemical data of closely-spaced lava samples at 9°30' N EPR. The petrological consequences of magma chamber processes are carefully investigated. Although crystal fractionation is known to be the most important process for the observed chemical variation, mechanical differentiation is found to be significant as revealed by crystal size distribution (CSD) analysis and density relations among melt and mineral phases. For example, the density relations are found to be responsible for the so-called clinopyroxene paradox (olivine-clinopyroxene paradox in this case). In addition, small-scale magmatic segmentation, longevity of the magma chamber, and the patterns of melt supply are also examined.

In Chapter 5, the potential differences in melting and melt supply mechanism between fast- and slow-spreading ridges are examined by analysis of a global data set of MORB chemistry. Melting and melt supply mechanisms are shown to depend on the rate of plate spreading, as do axial morphology, topography, and gravity signals. It is found that the fast-spreading ridges are dominated by passive, plate-driven, upwelling with efficient melt segregation, whereas the slow-spreading ridges are dominated by buoyant upwelling of highly centralized mantle diapirs in which slow-melt segregation and solid-melt reaction are both important processes.

CHAPTER 2

IN-SITU DENSITIES OF BASALT MELTS AND MANTLE MINERALS AS A FUNCTION OF TEMPERATURE, PRESSURE, AND COMPOSITION IN THE MELTING RANGE

2.1 Abstract

Recent theoretical studies of mid-ocean ridge (MOR) accretion have shown that the density differences between silicate melt and solid phases and between fertile and residual mantle may be important controls on the upward flow of upper mantle and separation of melt from the upwelling matrix. Both compositional and thermal buoyancy may play an important role. To quantitatively assess the magnitude of these effects, variations in density of silicate melts and solid phases as a function of temperature, pressure, and composition must be accurately known. I have compiled the available data for calculating densities as a function of composition, temperature (1000°C-1500°C), and pressure (1 atm to any pressure where the solid phases of interest remain stable). I include measured and calculated values of thermal expansion and compressibility for both solids and liquids. My calculations for mantle material undergoing decompression-induced melting show that density differences between instantaneous melt and residual solids increase toward the surface, implying an increasing melt migration rate with continuing upwelling and melting. However, the density difference is significantly less than the value of $\sim 0.5 g\text{-}cm^{-3}$, commonly assumed in theoretical models. In agreement with previous studies, I also find that residual mantle is less dense than unmelted mantle. However, using realistic pressures for MORB generation, the difference is small.

2.2 Introduction

The processes that contribute to the formation of oceanic crust are of great interest because of the geologic importance of ocean crust and its role in plate tectonic cycles. An important aspect of the genesis of ocean crust and the mid-ocean ridge basalt (MORB) of which it is made, is the mechanism which causes hot solid mantle material to upwell beneath active spreading ridges. Upwelling may occur as a passive response to the separation of plates [*Oxburgh and Turcotte*, 1968; *Hanks*, 1971; *Bottinga and Allègre*, 1978; *Houseman*, 1983; *Phipps Morgan*, 1987]. Recent analysis of topography and gravity data [*Lin and Phipps Morgan*, 1992] indicates that this may be the dominant mechanism of mantle upwelling beneath fast-spreading ridges. Even so, along-axis topographic variation [*Macdonald et al.*, 1984; *Macdonald*, 1989], petrologic evidence [*Langmuir et al.*, 1986], and my model temperature profiles beneath mid-ocean ridges (See Chapter 3) indicate that mantle upwelling is characterized by some three dimensionality. Thus, passive, two-dimensional upwelling of upper mantle alone cannot explain all the observations, even at fast-spreading ridges.

Another possible mechanism of mantle upwelling beneath active mid-ocean ridges is diapiric upflow. Gravity data at the slow-spreading mid-Atlantic ridge [*Lin and Phipps Morgan*, 1992] suggest that such a mechanism may be important at slow-spreading ridges. Geologic evidence for diapiric flow has been found in ophiolites [*Rabinowicz et al.*, 1987], and several theoretical models indicate that diapir-like instabilities may be important below mid-ocean ridges [*Whitehead, et al.*, 1984; *Crane*, 1985; *Schouten et al.*, 1985]. These buoyant instabilities may be driven by thermal buoyancy, compositional buoyancy or buoyancy provided by basalt melt [*Oxburgh and Parmentier*, 1977; *Jordan*, 1979].

Buoyancy forces may thus play an important role in the generation of ocean crust. Many models of mid-ocean dynamics [e.g., *Lachenbruch*, 1976; *Ribe*, 1988; *Nicolas*,

1986; *Scott and Stevenson*, 1989; *Buck and Su*, 1989; *Sotin and Parmentier*, 1989] discuss the importance of buoyancy forces. Density differences, along with other forces, are also important for melt migration and melt segregation below ridge crests [e.g., *Ahearn and Turcotte*, 1979; *McKenzie*, 1984, 1985; *Spiegelman and McKenzie*, 1987; *Richter and McKenzie*, 1984; *Sleep*, 1988; *Ribe*, 1985]. Because of the great importance of melt and solid densities in these dynamic processes associated with the genesis of ocean crust, I have compiled up-to-date data on the densities of minerals. In addition, I compiled data needed to compute in-situ densities at variable temperature and pressure in the melting range of peridotite for MORB. The purpose of this note is to present this compilation, to discuss briefly how these data are used to calculate densities and to present some results of these calculations. My new compilation and methodology allow rapid calculations of in-situ density for melts and solids as a function of temperature, pressure, and composition. For example, most recent models assume a density contrast of 0.5 g-cm^{-3} between MORB melt and solid mantle. My new results show that this may be too high, by up to a factor of two.

2.3 Density calculation for silicate melt

2.3.1 Temperature effect on melt density

Several methods exist to calculate the densities of silicate melts as a function of temperature and compositions [*Bottinga and Weill*, 1970; *Nelson and Carmichael*, 1979; *Bottinga et al.*, 1982, 1983; *Lange and Carmichael*, 1987]. All these methods are based on models relating the partial molar volumes of major element oxides to experimentally measured density data and volume-mixing behavior between the oxide components in a melt. Of these models, I use that of *Lange and Carmichael* [1987] because it is based on experimental density measurements by the most precise technique, the double-bob

Archimedean method. In addition, the measurements by *Lange and Carmichael* [1987] avoids the effects of inter-laboratory errors due to the differences in techniques used to measure density. They found that silicate liquid volumes in multicomponent systems have a linear dependence on liquid composition [*Lange and Carmichael*, 1987] with the exception of TiO_2 which interacts with Na_2O forming an excess volume term, the only volume-mixing nonideality recognized for silicate melts:

$$V(T,1) = \Sigma X_i (T,1) \overline{V}_i (T,1) + X_{Na_2O} X_{TiO_2} \overline{V}_{Na_2O\text{-}TiO_2} \qquad (2.1)$$

where V is the volume of melt in the experiment, X_i is the oxide (SiO_2, TiO_2, Al_2O_3, Fe_2O_3, FeO, MgO, CaO, Na_2O, K_2O) mole fraction in the melt, and $\overline{V}_i$ is the partial molar volume of oxide i at temperature T and 1 atmosphere pressure. The second term on the right hand side of (2.1) is the nonideal contribution to the volume of the melt. The partial molar volumes were determined by least squares fit to the measured density data, V(T). The effect of temperature on partial molar volume of each oxide are then separately regressed by fitting

$$\overline{V}_i (T,1) = \overline{V}_{i,T_R} + \frac{d\overline{V}_i}{dT} (T - T_R). \qquad (2.2)$$

where $\overline{V}_{i,T_R}$ is the partial molar volume of oxide i at the reference temperature T_R (1400°C), and $d\overline{V}_i/dT$ is the temperature derivative of the partial molar volume. Since no partial molar volume data for MnO is available in this model, I use the thermal expansion data of *Bottinga et al.* [1982] to obtain it, *i.e.*:

$$\overline{V}_{MnO} (T, 1) = 14.13 * \exp\{15.1 * 10^{-5} * (T - T_R)\} \qquad (2.3)$$

Thus, the molar volume of the melt at temperature T is V(T,1) = V(T, 1) (from (2.1)) + $\overline{V}_{MnO}$ (T, 1)(from (2.3)). In calculating the density of a melt of given composition at any temperature, (2.2) is substituted in (2.1), and the density of the melt is given by

$$\rho\ (T,\ 1) = \frac{\text{Molecular weight of the melt}}{V(T,\ 1)} \qquad (2.4).$$

No data for P_2O_5 is available. Model data required in equations 1 and 2 are taken from Table 8 of *Lange and Carmichael* [1987].

2.3.2 Pressure effect on melt density

Two existing models for dealing with the pressure effect on the density of natural silicate melts are presented by *Lange and Carmichael* [1987; denoted LC] and *Herzberg* [1987*a*, 1987*b*; denoted H]. LC, employing their newly obtained thermal expansion data combined with the available ultrasonic velocity data [*Rivers and Carmichael*, 1987] and heat capacity data [*Richet and Bottinga*, 1984,1985; *Stebbins et al.*, 1984; *Zeigler and Navrotsky*, 1986], obtain the isothermal compressibility (ß) by

$$ß_T = \frac{V}{c^2} + \frac{T\ V\ \alpha^2}{C_P} \qquad (2.5)$$

where V = volume, T = temperature, α = thermal expansion, C_P = isobaric heat capacity, and c = sound velocity. A quantity $ß_{i,T}$, which represents the compressibility of individual oxide components in the melt at temperature T, is thus obtained, by assuming ideal mixing, and least-squares fit to the equation

$$ß_T = \Sigma\ X_i\ ß_{i,T} \qquad (2.6),$$

Likewise , the temperature derivative of $ß_i$ is determined by least-squares fit to

$$ß_{i,T} = ß_i^o + dß_i^o/dT\ (T - T_R) \qquad (2.7).$$

Data for $ß_{i,T}$ and $dß_i^o/dT$ are from Table 12 of *Lange and Carmichael* [1987]. The compressibility of the melt is simply related to the bulk modulus by

$$K_T = 1/ß_T \qquad (2.8).$$

Herzberg [1987*a* , 1987*b*] derived a set of isothermal bulk moduli for individual oxide components ($K_{T,i}$) based on his own detailed fusion curve analysis (For SiO_2, FeO and MgO) and those ultrasonic data of *Rivers and Carmichael* [1987] for Al_2O_3, CaO, Na_2O, and K_2O. The ultrasonic data were converted to isothermal bulk modulus by

$$K_T = 1/(K_s^{-1} + T\alpha^2/\rho C_P), \qquad (2.9)$$

where $K_S = \rho c^2$, ρ is the measured density of the melts, and c is the ultrasonic velocity. The bulk moduli for each of oxide components were then obtained by fitting the Voit-Reuss-Hill mixing equation

$$K_T = (K_V + K_R)/2 \qquad (2.10)$$

where $K_V = \Sigma V_i K_{i,T}$ and $K_R = (\Sigma(V_i/K_{i,T})^2$. Comparison of the LC compressibility ($ß_{i,T}$) and H bulk modulus ($K_{i,T}$) for individual oxide components between the two models is not straightforward because $K_{i,T}$ does not necessarily equal the $1/ß_{i,T}$. However, comparison between their K_T's for a given melt composition shows that the H's values are greater than the values derived by LC mainly due to the contribution by $K_{FeO,T}$ and $K_{MgO,T}$. Herzberg's very high K_T values (high incompressibility) have been used to argue against the hypothesis of olivine-floatation at high pressures [*Stolper et al.*, 1981]. In contrast, LC's compressibility data support the notion. The fact that olivine does indeed float at high pressures in experiments by *Agee and Walker* [1988] suggests that Herzberg's K_T values for liquid FeO and MgO may be too high. Therefore, I use the model

compressibility data of *Lange and Carmichael* [1987]. The isothermal bulk modulus at reference temperature (1400°C) is denoted K_T^o.

Using these data, the pressure effect on the density of silicate melts is evaluated using the well-known third order Birch-Murnaghan equation of state:

$$P = \frac{3}{2} K_T [R^{7/3} - R^{5/3}][1 + \frac{3}{4}(4 - K')(R^{3/2} - 1)] \qquad (2.11)$$

derived from finite strain theory. Although (2.11) was originally derived to model the compressions of solids under hydrostatic pressure, its applicability to silicate melts has been proven useful [*Stolper et al.*, 1981; *Herzberg*, 1987*a*, 1987*b*; *Lange and Carmichael*, 1987; *Agee and Walker*, 1988]. In (2.11), K_T is the isothermal bulk modulus at temperature of interest and atmospheric pressure, which is usually calculated by $K_T = K_T^o + dK_T^o/dT\ (T - T_R)$, and for silicate melt here, it is directly calculated from (2.6) and (2.8). K' is the pressure derivative of K_T^o, dK_T^o/dP. For silicate melt, $K' \approx 4$ [*Lange and Carmichael*, 1987; *Herzberg*, 1987*a*, 1987*b*; *Agee and Walker*, 1988]. $R = V(T,1)/V(T,P) = r(T,P)/r(T,1)$, where r(T,1) is calculated by (2.4), and the unknown r(T,P) is evaluated by successive approximation of the pressure calculated by (2.11) to the pressure of interest.

2.4 Density calculation for solid mineral phases

Except for olivine, complete data for calculating the in-situ densities of important mantle silicates are lacking. For example, precise determination of the densities of orthopyroxene, clinopyroxene, garnet, spinel, and plagioclase as a function of temperature, pressure, and composition are unavailable. Partly this is due to insufficient thermal expansion and compressibility data for end-members of the phases and the difficulty in treating mixing among complex solid solutions. Even so, I have compiled the published data that are available and use these to derive equations needed to calculate the densities of

these minerals as a function of temperature, pressure, and composition. For simplicity, I calculate the densities of end members as a function of temperature and then evaluate the densities of the solid solutions by assuming ideal mixing. Non-ideal mixing is, of course, probably more realistic, however, we lack the information needed to consider it quantitatively. Ideal mixing should be a valid assumption for density, an intensive thermodynamic quantity. The bulk moduli of the solid solutions are calculated using the Voit-Reuss-Hill mixing model as done by *Herzberg* [1987*a*, 1987*b*] rather than ideal mixing. This model has been demonstrated to be the most satisfactory algorithm for reproducing experimentally determined elastic properties on complex mixtures of crystalline solids from their end members [*Watt et al.*, 1976]. Finally, I use the Birch-Murnaghan equation of state ((2.11)) to evaluate the pressure effect on the densities of these mineral phases.

In the following sections, I discuss the data compilation used to calculate the mineral densities.

2.4.1 End members or components of solid solutions

For olivine, orthopyroxene, and plagioclase solid solutions, only two end-members or components are required to specify the compositions appropriate to upper mantle conditions (Table 2.1), because other end-members probably comprise less than 2 wt % of mantle minerals [*Dick and Fisher*, 1983; *Maaløe and Aoki*, 1977]. However, for clinopyroxene, garnet, and spinel which are crystallographically very complex, more end-members are required (Table 2.1). I have used traditional end-member compositions for these phases, although the choice of components is somewhat arbitrary. For orthopyroxene (Opx), I do not consider an aluminum component (Ca-, Mg, and/or Fe-Tschermaks) because there are no data available on thermal expansion and compressibility. At low pressures, the Tschermak components in Opx is not significant, but at higher

Table 2.1. Parameters used to calculate mineral densities

Formula	Name	ρ (g/cc)	a	b	K_T^0	dK_T^0/dT	dK/dP
		(25°C, 1 atm)	$x10^{-5}$/°C	$x10^{-8}$/°C	Kbar	Kbar/°C	(dimensionless)
Olivine							
Mg_2SiO_4	Forsterite	3.223(28)	- 10.353	- 1.9697(3,28,34)	1271(3,28,34)	- 0.239(3,28,34)	5.39(24)
Fe_2SiO_4	Fayalite	4.400(32)	- 12.124	- 2.2511(3,32,34)	1368(3,32,34)	- 0.268(3,32,34)	5.20(15)
Orthopyroxene							
$Mg_2Si_2O_6$	Enstatite	3.204(8)	- 9.4732	- 0.0486(31)	1070(11,21,35)	- 0.270(14)	5.00(11)
$Fe_2Si_2O_6$	Ferrosilite	4.003(8)	- 11.685	- 0.0826(31)	1010(7,24)	- 0.300(14)	5.00(11)
Clinopyroxene							
$Mg_2Si_2O_6$	Clinoenstatite	3.206(8)	- 9.3865	- 0.0334(31)	1070†	- 0.270†	5.00†
$Fe_2Si_2O_6$	Clinoferrosilite	4.005(29)	- 11.722	- 0.0686(31)	1010†	- 0.300†	5.00†
$CaMgSi_2O_6$	Diopside	3.272(23)	- 2.0119	- 0.1008(12)	1130(21)	- 0.200(1)*	4.50(26,27)
$CaFeSi_2O_6$	Hedenbergite	3.632(29)	- 2.2436	- 0.1003(31)	1200(21)	- 0.200(1)*	4.50(1)*
$NaAlSi_2O_6$	Jadeite	3.347(29)	- 8.7469	- 0.1803(10)	1430(21)	- 0.200(1)*	4.50(1)*
$CaAl_2SiO_6$	Ca-Tschermak	3.432(17)	- 7.7055	- 1.3155(17)	1200(1)*	- 0.200(1)*	5.00(1)*
Garnet							
$Mg_3Al_2Si_3O_{12}$	Pyrope	3.562(18)	- 8.7253	- 0.0474(31)	1750(18,25,30)	- 0.210(9)	4.50(25)
$Fe_3Al_2Si_3O_{12}$	Almandine	4.324(29)	- 9.9226	- 0.4912(31)	1779(5,30)	- 0.201(9)	5.45(36)
$Ca_3Al_2Si_3O_{12}$	Grossular	3.594(22)	- 8.1304	- 0.2493(31)	1700(18,25)	- 0.220(33)*	4.25(36)
$Mn_3Al_2Si_3O_{12}$	Spessartine	4.190(29)	- 11.113	- 0.3450(31)	1742(5,30)	- 0.220(33)*	4.59(36)
$Ca_3Fe_2Si_3O_{12}$	Andradite	3.860(29)	- 9.4224	- 0.0773(31)	1570(6)	- 0.220(33)*	5.00(1,11)*
$Ca_3Cr_2Si_3O_{12}$	Uvarovite	3.848(29)	- 9.3377	- 0.1233(31)	1620(6)	- 0.220(33)*	5.00(1,11)*
Spinel							
$MgAl_2O_4$	Spinel	3.577(29)	- 9.4271	- 0.1251(31)	1940(13)	- 0.220(1)*	4.00(13,37)
$FeAl_2O_4$	Hercynite	4.265(29)	- 9.8861	- 0.4143(31)	2103(37)	- 0.200(1)*	4.00(1,11)*
$FeCr_2O_4$	Chromite	5.086(29)	- 8.5401	- 0.1246(31)	2103(1)*	- 0.200(1)*	4.00(1,11)*
$FeFe_2O_4$	Magnetite	5.201(29)	- 21.439	- 0.7541(31)	1860(13)	- 0.200(1)*	4.00(2,13)
$MgCr_2O_4$	Picrochromite	4.415(29)	- 7.5781	- 2.4431(31)	2100(1)*	- 0.200(1)*	4.00(1,11)*

Table 2.1. Parameters used to calculate mineral densities(continued)

Formula	Name	ρ (g/cc)	a	b	K_T^0	dK_T^0/dT	dK/dP
		(25°C, 1 atm)	$x10^{-5}$/°C	$x10^{-8}$/°C	Kbar	Kbar/°C	(dimensionless)
Plagioclase							
$NaAlSi_3O_8$	Albite	2.611(29)	- 3.2612	- 0.8190(31,39)	699.3(4)	- 0.200(1)*	4.00(1)*
$CaAl_2Si_2O_8$	Anorthite	2.762(29)	- 1.6459	- 1.3693(16,31)	943.4(4)	- 0.200(1)*	4.00(1)*

† No data for clinoenstatite and clinoferrosilite are available, but those of enstatite and ferrosilite are used instead (see text for discussion).
* No data or no consistent data available, the values are assumed (see text for discussion).

References: 1) *Anderson* [1989]; 2) *Anderson and Anderson* [1970]; 3) *Anderson and Suzuki* [1983]; 4) *Angel et al.* [1988]; 5) *Babusaka et al.* [1978]; 6) *Bass* [1986]; 7) *Bass and Weidner* [1984]; 8) *Berman* [1988]; 9) *Bonczar et al.* [1977]; 10) *Cameron et al.* [1973]; 11) *Duffy and Anderson* [1989]; 12) *Finger and Ohashi* [1976]; 13) *Finger et al.* [1986]; 14) *Frisillo and Barsch* [1972]; 15) *Graham et al.* [1988]; 16) *Grundy and Brown* [1974]; 17) *Haselton et al.* [1984]; 18) *Hazen and Finger* [1978]; 19) *Hazen and Prewitt* [1977]; 20) *Isaak and Graham* [1976]; 21) *Kandelin and Weidner* [1988]; 22) *Krupka et al.* [1979]; 23) *Krupka et al.* [1985]; 24) *Kuwazawa and Anderson* [1969]; 25) *Leitner et al.* [1980]; 26) *Levien and Prewitt* [1981]; 27) *Levien et al.* [1979]; 28) *Matsui and Manghnani* [1985]; 29) *Robie et al.* [1967]; 30) *Sato et al.* [1978]; 31) *Skinner* [1966]; 32) *Suzuki et al.* [1981]; 33) *Suzuki et al.* [1983*a*]; 34) *Suzuki et al.* [1983*b*]; 35) *Vaughan and Bass* [1983]; 36) *Wang and Simmons* [1974]; 37) *Wang and Simmons* [1972]; 38) *Weaver et al.* [1976]; 39) *Winter et al.* [1979].

pressures may comprise up to 2 wt % in mantle Opx [*Maalφe and Aoki*, 1977]. For clinopyroxene, spinel , and garnet, the components necessary in terms of their stoichiometry at mantle conditions [*Nixon*, 1987; *Lindsley*, 1983] are considered.

2.4.2 End member density data at 25°C and 1 atmosphere

I choose 25°C and 1 atmosphere pressure as the reference state. Examination of the published data for the mineral end members of interest shows that reported data of both molar volume (V_i^o) and molar density (ρ_i^o) vary slightly for almost all these end members (superscript ^{o} refers to reference state, and subscript $_i$ refers to end member i). Because the newly determined V_i^o and ρ_i^o for forsterite (Fo) and fayalite (Fa) by *Suzuki et al.* [1981, 1983] and *Matsui and Manghnani* [1985] are consistent with those of X-ray diffraction data tabulated by *Robie et al.*[1967], I believe that Robie's data are still the best and I therefore adopted their values of V_i^o and ρ_i^o in Table 2.1.

2.4.3 Thermal expansion data

Except for Fo [*Suzuki et al.*, 1983; *Anderson and Suzuki*, 1983; *Matsui and Manghnani*, 1985], Fa [*Suzuki et al.*, 1981; *Anderson and Suzuki*, 1983], Jd [*Cameron et al.*, 1973], and Ca-Ts [*Haselton et al.*, 1984], the only thermal expansion data set available for end members of orthopyroxene, clinopyroxene, garnet, spinel, and plagioclase are those tabulated by *Skinner* [1966]. Thus, these data are adopted here (Table 2.1). Some data are available for solid solutions, for example, *Frisillo and Buljan* [1972] determined thermal expansion of an orthopyroxene solid solution (En_{80}-Fs_{20}). Also, *Suzuki and Anderson* [1983] determined the thermal expansion of a natural garnet solid solutions.

Skinner [1966] reported the thermal expansion data for mineral end members in two ways, by thermal expansivity (α's) at several temperatures, and by the percentages of volume expansion (ΔV%'s) at several elevated temperatures (from 20°C to 1400°C). Because there are more data for ΔV to determine $d\alpha°/dT$, I have converted Skinner's

$\Delta V\%$'s to $\Delta\rho\%$'s and express other new thermal expansion data also in terms of $\Delta\rho\%$'s to have consistency. Plots of these $\Delta\rho\%$'s against temperature (T - 25°C) show that a second degree of polynomial is the best expression to describe the thermal expansion of end-member components of all the mineral phases of interest with $R^2 = 0.995$:

$$\rho\,(T) = \rho^{o}_{25°C} + a\ (T - 25\ (°C)) + b\ (T - 25\ (°C))^2, \qquad (12)$$

where *a* and *b* are regression coefficients.

2.4.4 Isothermal bulk modulus data

Much work has been done determining the elastic properties of the minerals and end members of interest. As will be discussed in the following, for some end members, multiple values have been reported, but for others (which are usually minor components in the mantle) no information is available at all. For the former, I choose those which have been recently recommended, and for the latter, appropriate values are assumed. These values are listed In Table 2.1 and are briefly discussed in the following paragraphs.

2.4.4.1 Olivine

The K^o_T and dK^o_T/dT (1271 Kbar and -0.236 Kbar/°C for forsterite; 1368 Kbar and -0.268 Kbar/°C for fayalite) are obtained by least-square fitting $K_T = K^o_{25} - dK^o_T/dT\ (T - 25)$ to the data of *Suzuki et al.* [1983], *Anderson and Suzuki* [1983], and *Matsui and Manghnani* [1985] with $R^2 = 1.000$ (Figure 2.2). Different values for K' (see (2.11)) have been reported in the literature, but as suggested by *Anderson and Suzuki* [1983], the values of 5.39 [*Kuwazawa and Anderson*, 1969] for Fo and 5.97 for Fa [*Chung*, 1971] may be the best. On the other hand, *Graham et al.* [1988] argue that 5.97 is too high for Fa based on their new experiments. Thus, the model value of 5.2 for Fa recommended by*Graham et al.*, [1988] and 5.39 for Fo by Kuwazawa *and Anderson*, [1969] are used here.

2.4.4.2 Orthopyroxene

Duffy and Vaughan [1988] reported a model value of 1023 Kbar for K_T^o of enstatite (En). A value of 1070 Kbar is reported by *Vaughan and Bass* [1983] and *Kandelin and Weidner* [1988]. The two model values are very close and a value of 1070 Kbar is adopted here as suggested by *Kandelin and Weidner* [1988]. Several values for ferrosilite (Fs) have been reported in the literature [*Akimoto,* 1972; *Chung*, 1974; *Weidner et al.*, 1978; *Weidner and Vaughan*; 1982; *Bass and Weidner*, 1984; *Kandelin and Weidner*, 1988], which range from 1010 to 1160 Kbar. I use the value of 1010 Kbar, as suggested by *Bass and Weidner* [1984] and *Kandelin and Weidner* [1988]. No accurate determination has yet been made for dK_T^o/dT. I use the values of - 0.22 Kbar/°C for En, and - 0.30 Kbar/°C for Fs as suggested by *Frisillo and Barsch* [1972].. No consistent K' values are available, so, as suggested by *Duffy and Anderson* [1989], I use a value of 5 for both En and Fs.

2.4.4.3 Clinopyroxene

Clinopyroxene (Cpx) is a very complex solid solution series. Although Mg and Fe^{2+} are the two most important cations of Cpx in peridotite, the two end-members, clinoenstatite (CEn) and clinoferrosilite (CFs), rarely occur as individual minerals naturally, so no elastic properties are available. Here I assume that their elastic behavior is similar to that of En and Fs. This assumption may be valid because structural difference between Opx and Cpx derives mainly from the introduction of larger cations such as Ca and Na [*Kandelin and Weidner*, 1988]. Thus, the contribution of the CEn and CFs to elasticity may be similar to the contribution of their counterparts in Opx structure. Acmite might be an important component of mantle Cpx, but since oceanic mantle is very reduced [*Bryndzia et al.*, 1989] it must be very minor. Several sets of elastic properties for natural clinopyroxenes have been reported, but few deal with their individual components. K_T^o's calculated from a new model based on available data and a new detailed crystallographic

analysis by *Kandelin and Weidner* [1988] are probably the best available and are adopted here: 1120 Kbar for diopside, 1200 Kbar for hedenbergite, 1430 Kbar for jadeite, and 1060 Kbar for acmite (Table 2.1). No dK_T^o/dT's are available at all but any value between -0.2 to -0.3 Kbar/°C is probably reasonable [*Anderson*, 1989]. Here I use a value of - 0.20 Kbar/°C. No consistent data for K' available, but a value of 4.5 for diopside (Di) [*Levien et al.*, 1979; *Levien and Prewitt*, 1981] may be appropriate. I assume a similar value for hedenbergite (Hd), Jadeite (Jd), and Ca-Tschermak (Ca-Ts) as suggested by *Anderson* [1989] and *Duffy and Anderson* [1989].

2.4.4.4 Garnet

Garnet is another complex solid solution series. The six components needed for mantle garnets are pyrope (Pyr), almandine (Alm), spessartine (Spes), grossular (Gro), andradite (And), and uvarovite (Uvr) (Table 2.1). There exist many determinations of elastic data for natural garnets and several models for calculating the elasticities of the end members are also available [*Wang and Simmons*, 1974; *Weaver et al.*, 1976; *Bonczar et al.*, 1977; *Sato et al.*, 1978; *Babusaka et al.*, 1978; *Leitner et al.*, 1980]. The reported K_T^o values for the end members vary slightly. The K_T^o values I use are 1750 Kbar for pyrope [*Leitner et al.*, 1980], 1779 Kbar for almandine [*Babusaka et al.*, 1978], 1742 Kbar for spessartine [*Babusaka et al.*, 1978], 1700 Kbar for grossular [*Leitner et al.*, 1980], 1570 Kbar for andradite [*Bass*, 1986], and 1620 Kbar for uvarovite [*Bass*, 1986]. *Bonczar et al.* [1977] reported dK_T^o/dT values, - 0.21 Kbar/°C for pyrope and - 0.201 Kbar/°C for almandine, but no values are available for the other components. With these two values as reference, plus the calculated value of - 0.22 Kbar/°C from a natural garnet studied by *Suzuki and Anderson* [1983], I use - 0.22 Kbar/°C for the other components. Values for K's are incomplete and variable in a small range. I choose 4.5 for pyrope [*Leitner et al.*, 1980], 5.45 for almandine [*Weaver et al.*, 1976], 4.59 for spessartine [*Isaak and Graham*,

1976], 4.25 for grossular [*Wang and Simmons*, 1974]. No K's are available for andradite and uvarovite, but 5 is assumed to be appropriate for both by *Anderson* [1989] and *Duffy and Anderson* [1989].

2.4.4.5 Spinel

Five end members, spinel (Spl), hercynite (Her), magnetite (Mgt), chromite (Chr), and pichromite (Pch) are considered (Table 2.1) because they describe fully the oceanic peridotite spinel minerals (estimated from various mantle xenoliths from *Nixon*, 1987 and oceanic peridotites by *Dick and Fisher*, 1983]. Relatively consistent elastic data are available for these end members [*Anderson and Anderson*, 1970; *Wang and Simmon*, 1972; *Chang and Barsch*, 1974; *Finger et al.*, 1986] except for chromite and pichromite because they play only a minor part as components for most of the fertile peridotite spinels. I choose the following K_T^o values: 1940 Kbar for spinel [*Finger et al.*, 1986], 2103 Kbar for hercynite [*Wang and Simmons*, 1972], and 1860 Kbar for magnetite [*Finger et al.*, 1986]. Since no K_T^o is available for chromite, I use the value of hercynite. This is reasonable because of the similarity in atomic radii of Cr^{3+}(1.83 Å) and Al^{3+} (1.82Å), and the fact that both occupy M^{3+} site and have Fe^{2+} on M^{2+} site. No dK_T^o/dT values are reported for spinel mineral end members, thus a value of - 0.20 Kbar/°C is assumed for these end members following *Anderson* [1989]. A value 4 of K' is reported for spinel [*Wang and Simmons*, 1972; *Finger et al.*, 1986] and magnetite [*Anderson and Anderson*, 1970; *Finger et al.*, 1986], and I use this value for hercynite and chromite also [*Anderson*, 1989].

2.4.4.6 Plagioclase

Room temperature compressibilities for albite (Ab) are given by *Birch* [1966] and *Hazen and Prewitt* [1977]. For anorthite (An), values are available in *Birch* [1966]. Recently, *Angel et al.* [1988] reported new compressibility data determined between 1 bar

and 50 kbar by single crystal diffraction techniques using a Merrill-Bassett type diamond cell: the bulk moduli, K_T^o, are 699.3 Kbar for albite, and 943.4 Kbar for anorthite (at pressures < 25 kb) respectively . The temperature effect on the bulk moduli is unknown. So, I assume a reasonable value of - 0.2 Kbar/°C for now as this value may be reasonable for common silicate minerals [*Anderson*, 1989]. More experimental data are needed to constrain dK_T^o/dT. No K data are available either, but a value of 4 is probably reasonable for both albite and anorthite [*Anderson*, 1989].

2.4.5 Summary of elastic data of solid minerals

As discussed above, elastic data compiled in Table 2.1 are the best presently available to calculate the densities of olivine, orthopyroxene, clinopyroxene, garnet, spinel, and plagioclase. A number of assumptions have been made for the elastic properties of some of the end member components, particularly the temperature derivatives of bulk modulus for spinel and plagioclase. In computing the densities, I ignore the pressure effect on thermal expansivity, *i.e.*, I assume that $d\alpha/dP = 0$ following *Lange and Carmichael* [1987] and *Herzberg* [1987*a*, 1987*b*]. This assumption should be valid for the pressure range of interest (5 kb to 30 kb) because $(\partial\alpha/\partial P)_T = 1/K_T^2(\partial K_T/\partial T)_P$ (see Table 2.1) gives values ranging from 10^{-7} to 10^{-8} $Kbar^{-1}$ $°C^{-1}$ for solids. The effects on the calculated densities would be on the order of about 10^{-6}, which can be ignored for this purpose. A highly interactive program, DENSCAL, has been written in microsoft BASIC to calculate the densities of silicate melts and solid phases as a function of temperature, pressure, and composition. Appendix I lists the code and on a 3.5" Macintosh diskette with RUNTIME is provided under Appendix III.

2.5 Application

Using the data of table 2.1 and (2.11) and (2.12), densities of mantle material may be calculated. My melting model calculation (See Chapter 3) shows that decompression-induced mantle melting for most observed MORBs begins at solidus pressures ranging from about 10 and 22 kbars. This pressure range is well within spinel and plagioclase stable fields, which is consistent with oceanic mantle peridotite studies of *Dick et al.* [1984]. I thus consider this pressure range in the following calculation.

Figure 2.1 shows the density variation of a fertile mantle (unmelted mantle peridotite: MPY-90 of *Falloon and Green* [1987] as a function of temperature and pressure by assuming no melting occurs. It is clear from this figure that thermal buoyancy is only 0.013-0.014 g-cm^{-3}/100°C. The pressure (depth) effect is on the order of 0.032 g-cm^{-3}/10kb for both spinel- and plagioclase-peridotite fields. A dramatic density change accompanies the spinel/plagioclase phase transition. Note that the spinel/plagioclase phase transition is arbitrarily set at 9 kb in my calculation. Thus, the overall pressure effect on melt-free solid mantle densities in the pressure range for MORB genesis beneath mid-ocean ridges may be up to 0.05 g-cm^{-3}/10kb.

Compositional buoyancy due to melt extraction may also be important [*Oxburgh and Parmentier*, 1977; *Jordan*, 1979; *Buck and Su*, 1989; *Sotin and Parmentier*, 1989]. I use my adiabatic upwelling melting model (See Chapter 3) to evaluate the effect. This model calculates major element compositions of MORB melts using solid-liquid partition coefficients empirically derived from peridotite melting experiments [*Jaques and Green*, 1980; *Falloon et al.*, 1988; *Falloon and Green*, 1987, 1988]. Because the very low melt retention in mantle and rapid melt extraction process [*McKenzie*, 1984, 1985*b*] suggest that melting and melt extraction occurs continuously in the mantle, I consider in this model that melting occurs as a series of infinitesimally small incremental batches in the course of

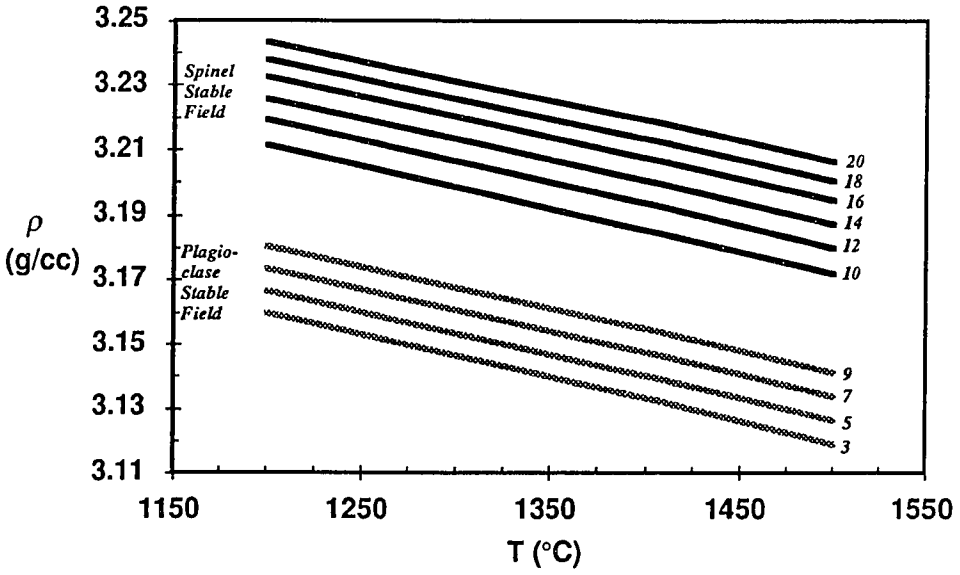

Fig. 2.1 Calculated densities of a fertile mantle, MPY-90 of Falloon and Green [1987], to show the effect of temperature and pressure alone without considering compositional effect (i.e., no melting is assumed) for pressure range of MORB genesis. Numerals to the right are pressures in kilobars. It is clear that the temperature effect on densities is only about 0.013 to 0.014 g-cm-3/100°C. The pressure (depth) effect is also small, on the order of 0.032 g-cm-3/10kb for both spinel- and plagioclase-peridotite fields. The overall pressure effect on mantle densities in peridotite melting beneath mid-ocean ridges may be as much as 0.05 g-cm-3/10kb.

continuous melting by instantaneous melt extraction as mantle adiabatically upwells. Figure 2.2 shows the adiabatic paths at 4 initial melting pressures (20, 16, 12, and 8 kbars). These incremental batches may aggregate or accumulate to form MORB melts. For simplicity and because of lack of experimental data for low degrees of melting, the first melt I produce is a 4% isobaric batch melt which is followed by incremental steps of 1%. In each step, the residue is calculated by mass balance, and it serves as the source of the next increment of melting. The partition coefficients are recalculated in response to the changes in P and F (or T) at each step along the paths shown in Figure 2.2. The mineralogy and mode of the residual mantle are calculated using a revised version of the CIPW norm algorithm in combination with a least-squares procedure that agrees well with the experimental data and the modal data of *Dick et al.* [1984].

Figure 2.3 shows the effect of melt extraction on solid (melt-free) residual mantle. With initial melting beginning at 8, 12, 16 and 20 Kbars, for various extents of melt extraction (total amount of melt extraction from unmelted fertile mantle) along the adiabatic melting paths shown in figure 2.2, the density differences between fertile mantle (solid lines) and residual mantle (stippled lines) are smaller than estimated in the literature (e.g., 0.10g-cm^{-3} with 30% melt extraction of Buck and Su 1989; ~ 0.06g-cm^{-3} with 20% melt extraction of *Sotin and Parmentier* [1989]. Figure 2.3 shows that in decompression-induced melting 0.035 - 0.040 g-cm^{-3} may be the maximum and for most conditions the effect is only 0.015-0.025 g-cm^{-3}. Considering the uncertainties of this model, primarily derived from modal estimates of solid phases discussed later, the value of 0.06g-cm^{-3} [*Sotin and Parmentier*, 1989] may be the extreme. Thus compositional buoyancy due to melt extraction, while larger than the effect of thermal expansion or compressibility alone (Figure 2.1), is rather small in the spinel or plagioclase peridotite field. Despite the small absolute value of this effect, if compositional and thermal buoyancy are dynamically

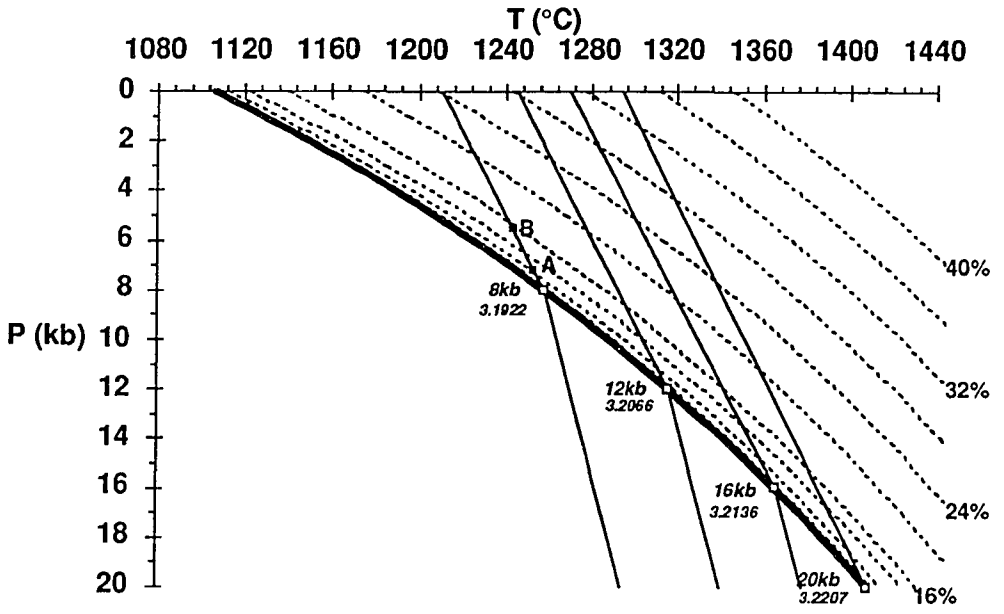

Fig. 2.2 Adiabatic melting paths of upwelling mantle in P-T space. Thick solid line and thin dashed lines are mantle (MPY-90) solidus and isopleths of extent of partial melting (See Chapter 3). Thin solid lines are adiabatic upwelling paths adopted from *McKenzie* [1984]. Pressure values (20, 16, 12, and 8 kbars) indicate the initial melting pressures along the paths across the solidus. Values in italics are the densities of unmelted mantle at indicated P-T points (open squares). A - B path at P_o = 8 kbar is referred in Figure 2.3.

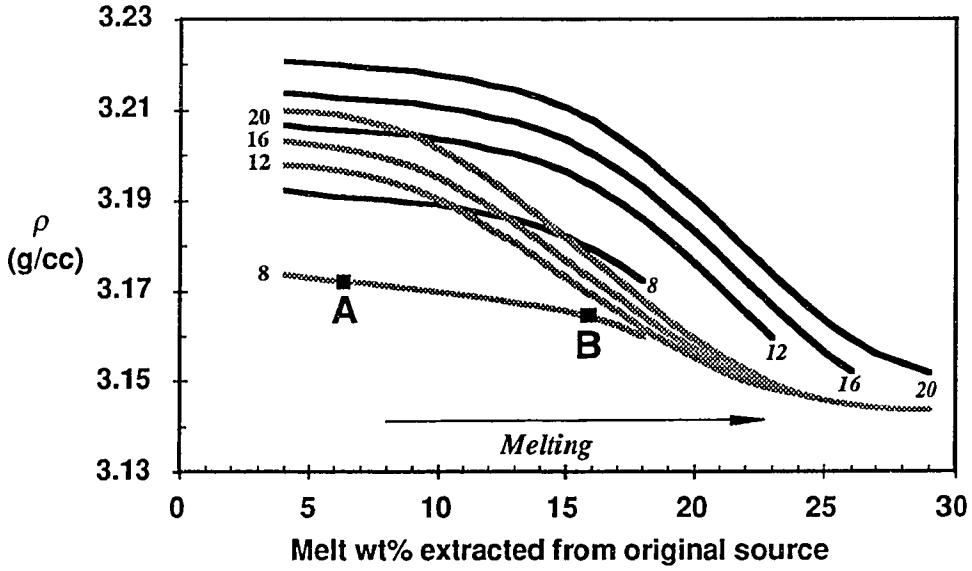

Fig. 2.3 Calculated densities of residual solids (stippled lines) as melting proceeds. Numerals to the left are the pressures (in kilobars) of initial melting along the four adiabatic paths (Figure 2.2 shows how the extents of melt extracted relate to pressure release along the paths: A - B path along $P_0 = 8$ kbar, for example). In comparison, the densities of a fertile mantle (solid lines) without melting are also plotted using the same P-T conditions. Numerals to the lower right are corresponding initial melting pressures along these paths. This comparison explicitly displays the density reduction of solid mantle due to melt extraction. The largest density reduction is only about 0.035 g-cm^{-3} and for most conditions the effect is only 0.015-0.025 g-cm^{-3}. The possible errors that stem from uncertainties in estimating modal mineralogy and the compositions may be on the order of ±0.01 - 0.04 g-cm^{-3}, but this will not expect to affect the relative density differences. See text for discussion.

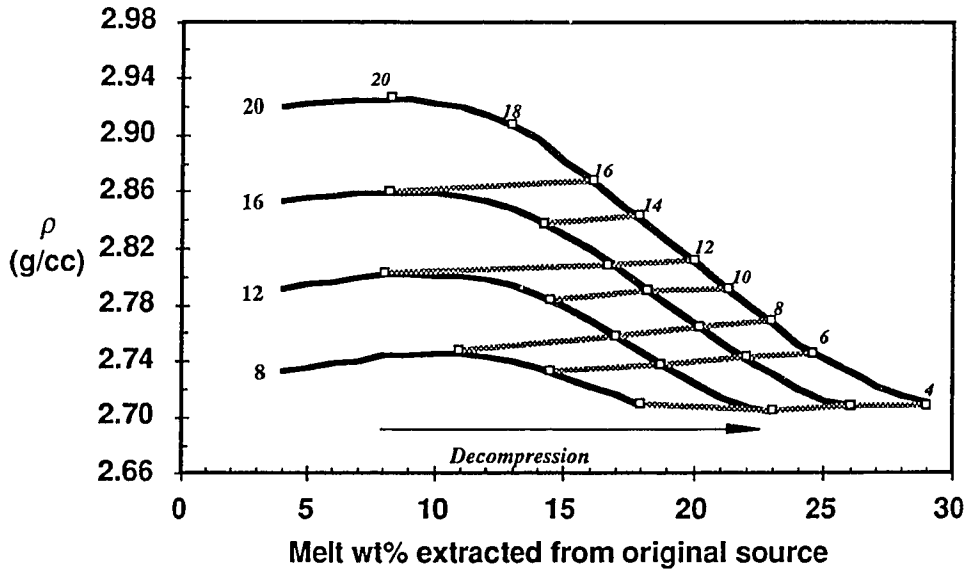

Fig. 2.4 Calculated densities (thick solid lines) of instantaneous MORB melt (1% of incremental melt except the initial 4%) as melting proceeds along the four adiabatic paths as labeled to the left (see Figure 2. 2 for input changing P and T). The compositions of the instantaneous melt as a function of P, T, and extent of melt extraction are calculated using my melting model (See Chapter 3). The stippled lines are isobars (in kilobars, labeled to the right) to show the compositional and temperature effect on instantaneous melt densities.

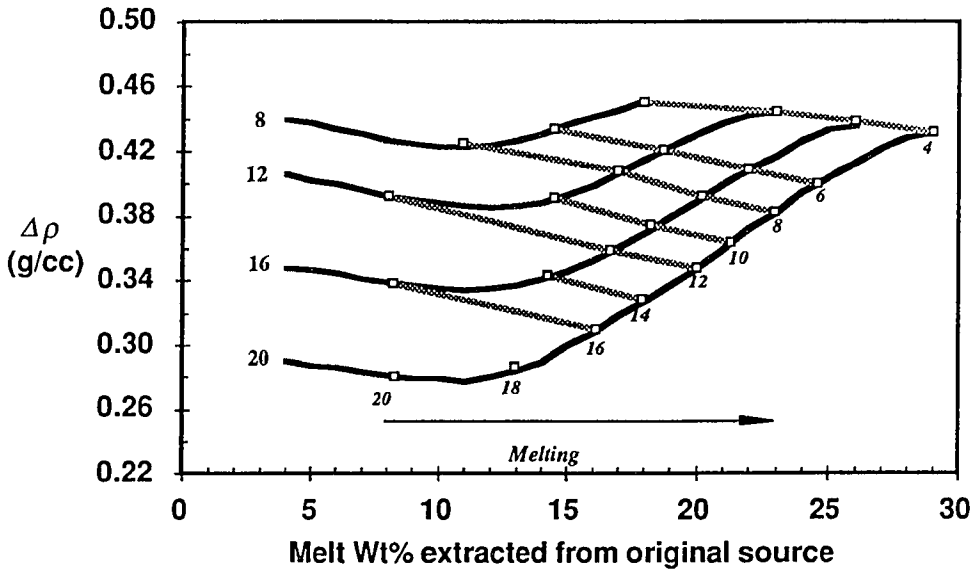

Fig. 2.5 Density differences (solid thick lines) between instantaneous MORB melt (see Figure 2. 4) and solid residues (see stippled lines in Figure 2. 3) as melting proceeds along the four adiabatic paths as labeled to the right (see Figure 2.2). The stippled lines mean the same as in Figure 2.4. This clearly shows that the differences between the melt and residue vary from 0.28 g-cm^{-3} to 0.45 g-cm^{-3}, and decrease with decreasing instantaneous melting pressures. See caption to Figure 2.3 for uncertainties for solid residues and text for discussion.

balanced [see, e.g., *Sotin and Parmentier*, 1989; *Scott and Stevenson*, 1989], time-dependent episodic behavior of mantle upwelling can result.

Figure 2.4 shows the density variations of instantaneous (or 1% incremental batch except the first 4%) melts produced by pressure-release melting as mantle adiabatically upwells (Figure 2.2) against the total melt extraction with respect to the unmelted fertile mantle. These calculated in-situ melt densities include the effects of composition (See Chapter 3), thermal expansion and compressibility. Figure 2.5 compares the density of instantaneous melt in a given increment of melting with the density of the "coexisting" solid residue. Because of the greater compressibility of melt [*Stolper et al.*, 1981; *Lange and Carmichael*, 1987; *Agee and Walker*, 1988] $\Delta\rho$ ($\rho_{residue}$ - ρ_{melt}) decreases with increasing in-situ pressure. As upwelling and melting proceed, the Δr values increase. This effect is rather large and could modify the results of *Scott and Stevenson* [1989] who assumed a greater, and pressure-independent, $\Delta\rho$ of 0.5 g-cm^{-3}.

In addition, the density of porous mantle residue containing melt can be computed. This effect can be important as shown by *Scott and Stevenson* [1989], however the amount of melt retention in upwelling mantle below ridges is presently controversial. The effect of one to two percent melt is of the order ~ 3 to ~ 9 x 10^{-3} g-cm^{-3} in reducing the densities of the bulk mantle.

2.6 Summary

The method developed in this chapter provides for rapid and accurate calculations of thermal and compositional buoyancy of melts and solid phases. The formal errors of (2.11) and (2.12) generated from compiled data are expected to be small, on the order of 5 x 10^{-4} to ~ 5 x 10^{-3} g-cm^{-3} for both silicate melt and solid minerals including the uncertainties from solid solution mixing behavior. However, the errors stem from uncertainties in estimating modes of solid phases and their compositions are difficult to

evaluate with our present knowledge. Given an uncertainty of 10% relative modal proportion for major mantle solid phases (olivine, orthopyroxene, and clinopyroxene), the calculated densities for solid mantle may be subject to errors of $\pm$ 0.01 - 0.04 g-cm^{-3}. These uncertainties will not affect the conclusions I come to in this study, particularly the relative densities between fertile mantle and residual mantle (Figure 3). In the case of density difference between residual solid and in-situ melt (Figure 5), the uncertainties may be large, but 0.5 g-cm^{-3} will in any event be the maximum at pressure range of mantle melting conditions for MORB.

One conclusion of this study is that the effect of the presence of melt on the density of mantle residue plus melt increases greatly with decreasing pressure, as expected. This has important implications for the rate of melt migration as a function of depth. The main conclusion is that the density differences between melt and solid residue, which has important implications for buoyancy below ridges, is overestimated in theoretical studies. However, the new method allow accurate density estimates to be calculated.

CHAPTER 3

AN EMPIRICAL METHOD FOR CALCULATING MELT COMPOSITIONS PRODUCED BENEATH MID-OCEAN RIDGES: APPLICATION FOR AXIS AND OFF-AXIS (SEAMOUNTS) MELTING

3.1 Abstract

In this chapter, I present a new method for calculating the major element compositions of primary melts parental to mid-ocean ridge basalt (MORB). This model is based on the experimental data of *Jaques and Green* [1980], *Falloon et al.* [1988], and *Falloon and Green* [1987, 1988] which are ideal for this purpose. My method is empirical and employs solid-liquid partition coefficients (D_i) from the experiments. I empirically determine $D_i = f(P,F)$ and use this to calculate melt compositions produced by decompression-induced melting along an adiabat (column melting). Results indicate that most MORBs can be generated by 10–20% partial melting at initial pressures (P_o) of 12–21 kbar. My primary MORB melts have MgO = 10–12 wt %. I fractionate these at low pressure to an MgO content of 8.0 wt % in order to interpret natural MORB liquids. This model allows us to calculate P_o, P_f, T_o, T_f, and F for natural MORB melts. I apply the model to interpret MORB compositions and mantle upwelling patterns beneath a fast ridge (East Pacific Rise (EPR) 8°N to 14°N), a slow ridge (mid-Atlantic Ridge (MAR) at 26°S), and seamounts near the EPR (Lamont seamount chain). I find mantle temperature differences of up to 50°–60°C over distances of 30–50 km both across axis and along axis at the EPR. I propose that these are due to upward mantle flow in a weakly conductive (versus adiabatic) temperature gradient. I suggest that the EPR is fed by a wide (~100 km) zone of upwelling due to plate separation but has a central core of faster buoyant flow. An along-axis thermal dome between the Siqueiros transform and the 11°45' Overlapping Spreading center (OSC) may represent such an upwelling; however, in general there is a

poor correlation between mantle temperature, topography, and the segmentation pattern at the EPR. For the Lamont seamounts I find regular across-axis changes in P_o and F suggesting that the melt zone pinches out off axis. This observation supports the idea that the EPR is fed by a broad upwelling which diminishes in vigor off axis. In contrast with the EPR axis, mantle temperature correlates well with topography at the MAR, and there is less melting under offsets. The data are consistent with weaker upwelling under offsets and an adiabatic temperature gradient in the subaxial mantle away from offsets. The MAR at 26°S exhibits the so-called local trend of *Klein and Langmuir* [1989]. My model indicates that the local trend cannot be due solely to intra-column melting processes. The local trend seems to be genetically associated with slow-spreading ridges, and I suggest it is due to melting of multiple individual domains that differ in initial and final melting pressure within segments fed by buoyant focused mantle flow.

3.2 Introduction

Several recent studies [*McKenzie*, 1984; *Klein and Langmuir*, 1987; *McKenzie and Bickle*, 1988] have emphasized that melting occurring in adiabatically rising mantle material is polybaric. It is now widely accepted that mid-ocean ridge basalts (MORB) are produced by such melting, commonly referred to as column melting. In this model, solid mantle material rises along an adiabatic temperature gradient, intersects the solidus at a depth determined by its temperature and melting characteristics, and begins to melt. Continued upwelling is accompanied by continuous melting, matrix compaction, and melt segregation.

While this general scenario for the genesis of MORB has gained wide acceptance, many of the details of the process and how these might vary in specific tectonic settings remain controversial. For example, some studies favor a wide (~100 km) zone of passive mantle upwelling resulting from plate separation [e.g., *Oxburgh and Turcotte*, 1968; *Hanks*, 1971; *Bottinga and Allègre*, 1978; *Houseman*, 1983; *Phipps Morgan*, 1987;

Spiegelman and McKenzie, 1987; *Sleep*, 1988; *Ribe*, 1988]. Alternatively, a narrow (10–20 km) zone of upwelling is favored by models which consider thermal, compositional, and melt buoyancy forces [e.g., *Scott and Stevenson*, 1989; *Sotin and Parmentier*, 1989; *Buck and Su*, 1989] and diapiric flow [*Rabinowicz et al.*, 1987; *Whitehead et al.*, 1984; *Crane*, 1985; *Schouten et al.*, 1985; *Nicolas*, 1986, 1989].

The amount and distribution of melt in the column, the mechanism of melt segregation, and the role of lateral melt migration to focus melt below the very narrow (~1 km) axial neovolcanic zone are also controversial. Theoretical arguments [e.g., *McKenzie*, 1984; *Richter and McKenzie*, 1984; *Ribe*, 1987; *Riley and Kohlstedt*, 1990] suggest that melt porosities in the mantle are likely to be small (1–3 %), but exactly how small is debatable. Even small (1–2%) melt porosity can provide significant buoyancy [*Scott and Stevenson*, 1989] (also see Chapter 2). Recent trace element studies of abyssal peridotites [*Johnson et al.*, 1990] also suggest small melt porosities and favor fractional melting over batch partial melting for MORBs [*Dick*, 1989]. Small melt porosities support the continuous melting model of *Langmuir et al.* [1977], also termed critical melting [*Maaløe*, 1982].

The level and physical mechanisms of melt segregation are also controversial. The maximum depth where dikes may be efficient melt conduits [*Nicolas*, 1986; *Sleep*, 1988] is unknown, but interpretation of uranium decay series isotopes [*Rubin and Macdougall*, 1985; *McKenzie*, 1985*a*; *Williams and Gill*, 1989] shows that MORB melts probably are produced, segregated, and erupted relatively rapidly. This is also favored by the observation that MORB melts do not chemically reequilibrate at shallow depths [*Bedard*, 1989; Plank and Langmuir, 1992]. If the zone of upwelling is broad, then lateral melt migration toward the axis may be needed to focus eruptions in the narrow neovolcanic zone [*Phipps Morgan*, 1987; *Scott and Stevenson*, 1989]. However, the importance of this process is presently difficult to evaluate.

Additional unresolved questions concern the manner in which mantle upwelling and magma supply vary with spreading rate of mid-ocean ridges. Several studies [e.g., *Scott and Stevenson*, 1989; *Sotin and Parmentier*, 1989] have suggested that upwelling may be episodic or periodic at slow spreading rates. *Schouten et al.* [1985] suggested a spreading rate dependence of the spacing of central supply conduits feeding ridges. In contrast, others [e.g., *Macdonald et al.*, 1988; *Sinton et al.*, 1991] suggest a hierarchic supply geometry like that proposed by *Langmuir et al.* [1986]. Recently, *Lin and Phipps Morgan* [1991] suggested that fast-spreading ridges may be dominated by spreading-induced passive upwelling, whereas at slow-spreading ridges, buoyant plumes may be more important. The buoyancy could come from melt, large temperature difference, and/or compositional buoyancy created by the melting processes. The significance of ridge offsets in perturbing mantle flow and causing edge effects on MORB chemistry also is a subject of debate [e.g., *Bender et al.*, 1984; *Phipps Morgan and Forsyth*, 1988].

The chemistry of MORB melts provides an important line of evidence for helping to answer these questions and others. The major element chemistry of MORB is particularly helpful when compared to the chemistry of melts produced in the laboratory under controlled conditions. For this reason, there have been several previous attempts to use the experiments to deduce the conditions of melting (e.g., pressure of melting, extent of partial melting, nature of the peridotite source) of natural MORB glasses. *Ito* [1973] used existing experimental data to quantify phase equilibria in the basalt-peridotite system. More recently, *Klein and Langmuir* [1987], *McKenzie and Bickle* [1988], and [*Kinzler and Grove*, 1992], using different approaches, have attempted to use experimental data to calculate the chemical compositions of MORB melts formed under a variety of melting conditions.

In this chapter, I present a method, based on experimental data, for calculating MORB melts formed by decompression-induced melting processes. My interest is not only

to understand the origin of MORB and magmatic processes at ridge axes but also to provide a self-consistent set of MORB melt compositions for use in physical models of upwelling, flow, melt migration, and other physical-chemical processes beneath mid-ocean ridges. Since the chemistry of MORB melts controls their density (see Chapter 2), viscosity, and other physical properties, chemical information will also be of use as an input to physical models of magmatic and tectonic processes at active ridges. In this paper, I first discuss the experimental data upon which my model is based. I then present the method and discuss its possible applications to interpreting the origin of natural MORB melts. Finally, I apply the method to three MORB suites from a fast ridge (the East Pacific Rise (EPR) at 8°–14°N), a slow ridge (the mid-Atlantic ridge (MAR) at 26°S), and a seamount chain formed near the EPR (the Lamont seamount chain at ~ 10°N). I discuss these results and draw some conclusions regarding magmatic processes occurring below the plate boundary zone.

3.3 The method

3.3.1 Experimental data

There exist a great deal of experimental data bearing on the origin of MORB melts. These data have been recently reviewed by *Falloon and Green* [1987, 1988], *Elthon* [1989, 1990], and *Fujii* [1989]. In this study, I have relied on the experiments of *Jaques and Green* [1980] and *Falloon et al.* [1988] and also have incorporated some results from *Falloon and Green* [1987, 1988]. These experiments are conducted with several starting compositions and cover a wide range of temperatures and pressures. *Jaques and Green* [1980] conducted isobaric batch melting runs using Hawaiian Pyrolite (HPY) and Tinaquillo Lherzolite (TQL) modified by subtracting 40% olivine ($Fo_{91.6}$ and $Fo_{91.9}$, respectively) to facilitate identification of minor phases. However, iron loss and quench

modification hamper obtaining equilibrium partial melt compositions directly. They avoided these problems by analyzing all the residual crystal phases, combined with modal analysis of the entire charge, and obtained calculated equilibrium partial melts (CEPM) by mass balance.

Recently, *Falloon and Green* [1987, 1988] and *Falloon et al.* [1988] showed that the CEPM of *Jaques and Green* [1980] are too olivine-rich. They concluded that the CEPM of *Jaques and Green* [1980] incorporated errors in the modal analysis (especially in distinguishing fine-grained olivine and orthopyroxene) and phase compositions of residual minerals when compositional zoning was present. *Falloon et al.* [1988] also point to problems in the resultant SiO_2 and Al_2O_3 contents of the CEPM. Because of these potential problems, I have carefully compared the *Jaques and Green* [1980] and *Falloon et al.* [1988] data. Plotting these data against each other shows excellent agreement for most elements for both starting compositions (HPY and TQL) as the correlations have slopes of 1.00 ± 0.05 and $R^2 > 0.94$. However, there are indeed some differences in SiO_2 and MgO for both HPY and TQL as well as in Al_2O_3 and FeO for TQL. *Falloon et al.* [1988] carried out reversal and/or sandwich experiments on CEPM of *Jaques and Green* [1980] by using Fe, Pt, and graphite capsules. The gain and loss of iron are inevitable when using Fe and Pt capsules, although the absolute amount is difficult to evaluate. However, the runs using Fe and Pt capsules should roughly bracket the unmodified melt concentrations if equilibrium is approached.

Figure 3.1 shows the comparison of these data and indicates that the discrepancies between *Jaques and Green* [1980] and *Falloon et al.* [1988] are, in general, systematic. Assuming that the data of *Falloon et al.* [1988] constrained by graphite capsule runs and bracketed by Fe and Pt capsule runs are correct, then the CEPM of *Jaques and Green* [1980] can be corrected for these discrepancies. Figure 3.1 shows that the differences in SiO_2 are ~0.5 wt % for HPY and ~1 wt % for TQL. The Al_2O_3 contents in three runs of

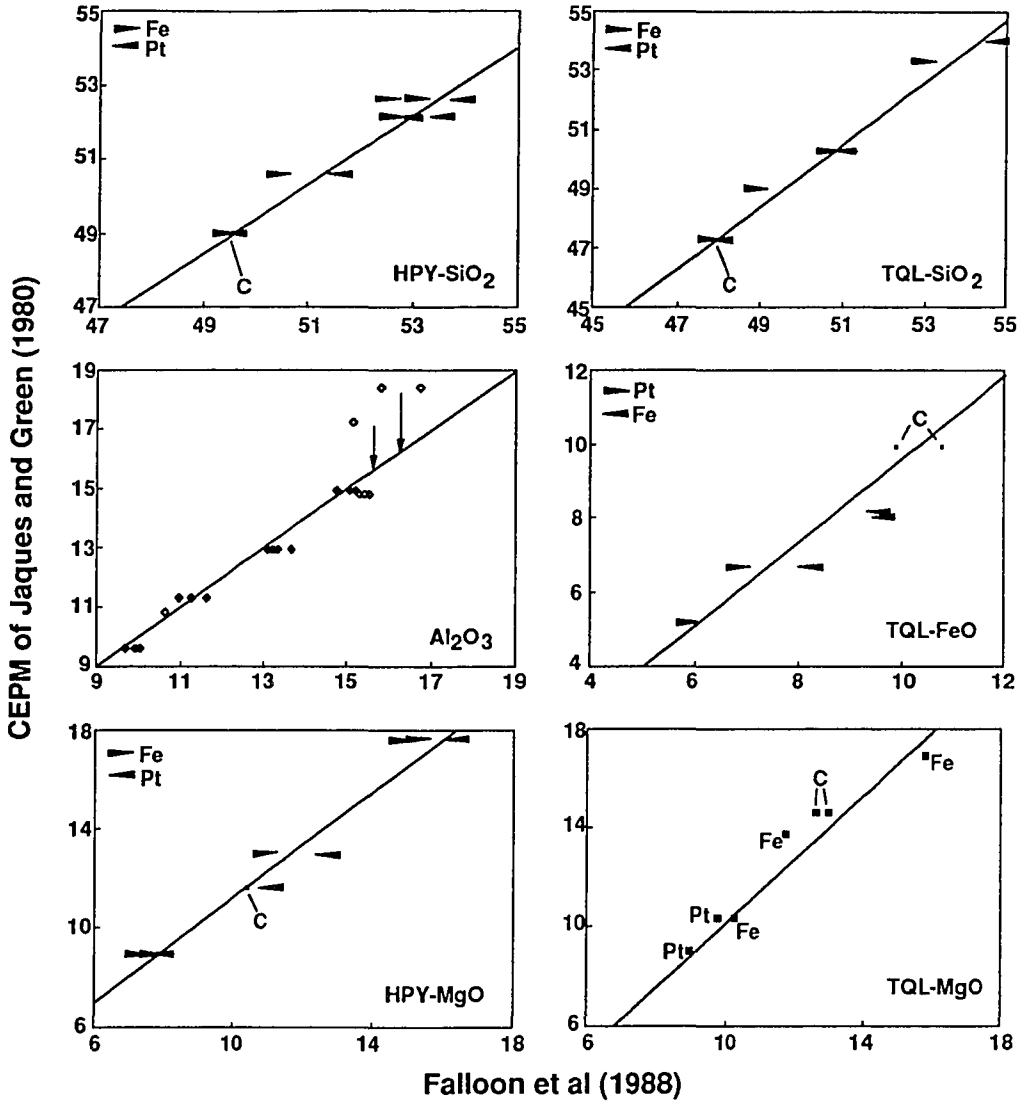

Fig. 3.1 For most elements, the calculated equilibrium partial melts (CEPM) of *Jaques and Green* [1980] are in excellent agreement with the reversal experiments of *Falloon et al.* [1988]. This figure shows that the discrepancies that do exist are systematic. The experiments of *Falloon et al.* [1988] using Pt, Fe, and graphite (C) capsules can be used to bracket the systematic differences in SiO_2 and FeO for Tinaquillo Lherzolite (TQL) and SiO_2 and MgO for Hawaiian Pyrolite (HPY). The discrepancies in MgO for TQL seem to be independent of capsule materials used. The three runs of *Jaques and Green* [1980] for TQL have obvious high values in Al_2O_3 (open diamonds). Assuming the recent experiments are more reliable, we can correct the CEPM.

TQL are clearly high, but can be corrected in a straightforward manner. The FeO difference for TQL and the MgO difference for HPY can also be corrected. For MgO of TQL the difference seems to be independent of capsule material. This comparison gives us confidence that the data set of *Jaques and Green* [1980] is in fact of high quality considering experimental difficulties. Thus, in my model I use the data of *Jaques and Green* [1980] and *Falloon et al.* [1988] for HPY and TQL plus the data of *Falloon and Green* [1987, 1988] for MORB pyrolite 90, which is a more reasonable source peridotite (see Table 3.1) for MORB than HPY (not depleted enough) or TQL (too depleted).

3.3.2 Determination of major oxide partitioning from experimental data

To compute the major element composition of peridotite melts, it would be ideal to use a thermodynamic basis taking account of mineral compositions, modal abundances, reactions occurring during melting, and changes in pressure (P) and temperature (T). For low-pressure conditions, such models have been reasonably successful [e.g., *Langmuir and Hanson*, 1980*b*; *Nielsen and Dungan*, 1983; *Ghiorso and Carmichael*, 1985; *Nielsen*, 1985, 1988; *Weaver and Langmuir*, 1990]. However, there is not yet enough information to confidently employ such models at high pressure. For this reason, my approach here is empirical.

Since the potential complexities attending melting are all reflected in melt composition, I attempt to extract from the experimental data the apparent bulk solid-liquid partition coefficients (D_i) for each oxide component (i):

$$D_i = x_i^s / x_i^l , \tag{3.1}$$

where x_i^s is the weight percent of component i in the solid and x_i^l is the weight percent of i in the liquid. Using mass balance, we have

Table 3.1. Compositions of source materials investigated

Oxide	HPY	TQL	MPY-90	
SiO_2	45.20	44.95	44.74	(44.50–45.60)
TiO_2	0.71	0.08	0.17	(0.10–0.35)
Al_2O_3	3.54	3.22	4.37	(3.85–4.44)
FeO	8.47	7.66	7.55	(7.40–8.40)
MgO	37.50	40.03	38.57	(37.50–39.5)
CaO	3.08	2.99	3.38	(3.05–4.00)
Na_2O	0.57	0.18	0.40	(0.35–0.42)
K_2O	0.13	0.02	0.03*	(0.02–0.08)
Total	99.20	99.13	99.22	

Data for HPY and TQL are from *Jaques and Green* [1980] and for MPY-90 are from *Falloon and Green* [1987]. In the parenthesis after MPY-90 are compositional ranges for which the coefficients in Tables 3.4 and 3.5 may apply.

*Assumed K_2O content for MPY-90 in our calculations.

Table 3.2. Empirical coefficients determined for extent of partial melting

Source	a	b, $Kbar^{-1}$	c, $°C^{-1}$	d, $Kbar^{-1}°C^{-1}$
HPY	- 98.620	- 6.551	0.10872	3.347×10^{-3}
TQL	- 117.149	- 6.028	0.11679	3.023×10^{-3}

$F(wt\%) = a + b\,P(kb) + \{c + d\,P(kb)\}\,T(°C)$.

HPY – Hawaiian pyrolite; TQL – Tinaquillo lherzolite.

$$x_i^o = Fx_i^l + (1 - F)x_i^s , \tag{3.2}$$

where x_i^o is the weight percent of *i* in the peridotite source and F is the fraction of melt produced. Combining (3.1) and (3.2), we thus have

$$D_i \equiv x_i^s / x_i^l = \frac{x_i^o/x_i^l - F}{1 - F}. \tag{3.3}$$

Equation (3.3) is used to derive D_i values from the experimental data of *Jaques and Green* [1980] and *Falloon et al.* [1988] of SiO_2, TiO_2, Al_2O_3, FeO, MgO, CaO, Na_2O, and K_2O for HPY and TQL source compositions. Ideally, these derived D_i values and the corresponding experimental run conditions (i.e., P and T) could be used to find an expression $D_i = f(T, P)$ for each source composition. Thermodynamically, this may be expressed in logarithmic form:

$$\ln D_i = c_1/T + c_2 + c_3 P/T + f(x) \tag{3.4}$$

where c_1, c_2, and c_3 are constants, P and T are pressure and temperature, and $f(x)$ is a function dealing with the compositions of the solid phases and liquid in the system and probably also depends on pressure and temperature. In practice, however, to find an explicit form for (3.4) is not possible with available data. Fortunately, using F, the extent of partial melting, as a single variable can substantially simplify the problem. This is because F implicitly contains temperature and compositional information about the melting process. As illustrated in Figure 3.2, I find that F is linearly related to temperature for each pressure considered by *Jaques and Green* [1980], that is,

$$F(wt\%) = a + b\,P(kb) + \{c + d\,P(kb)\}T(°C), \tag{3.5}$$

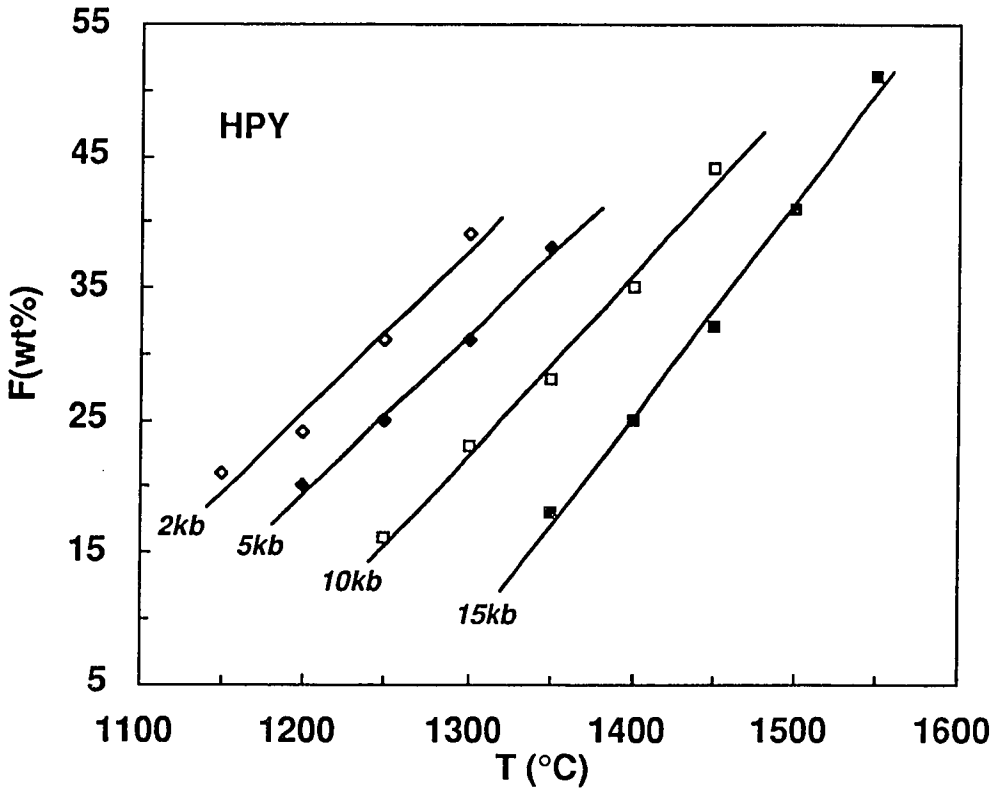

Fig. 3.2 The extent of partial melting (F, weight percent) versus temperature (T, degrees Celsius) for four pressure values from experiments on HPY of *Jaques and Green* [1980]. F is a linear function of temperature alone at constant pressure for the range of F investigated. At low F (<10%), the relationship between F and T is probably nonlinear.

where a, b, c, and d are empirical constants for each of the given source compositions (HPY and TQL). Table 3.2 gives these coefficients for HPY and TQL and shows that their dependence on bulk composition is not large, as the coefficients for these very different peridotites are within 10% of each other (except for a : 17%). Figure 3.3 compares experimental values of F with those calculated using (3.5). It is important to note that (3.5) is purely empirical and should not be extrapolated outside the range of the experimental data. For example, it cannot be used to derive the solidus because of the lack of experimental data on very low extents of partial melting, and because F increases nonlinearly in the first few tens of degrees above the solidus [*Jaques and Green*, 1980; *McKenzie and Bickle*, 1988]. Figure 3.4 shows the isopleths of F for HPY and TQL. These are calculated using (3.5) except for the solidus and dashed isopleths near the solidus, which are from *Jaques and Green* [1980, Figures 1 and 2].

The next step in my model is to empirically derive an expression for $D_i = f(P,T)$. But since at constant pressure, F only depends on T, I instead derive an expression for $D_i = f(P,F)$. My empirical technique for deriving this expression for each oxide component is illustrated in Figure 3.5 using SiO_2. This shows D_{SiO_2} as a function of F for several pressures for both HPY and TQL. For the eight oxides I consider, I find

$$D_i = e + f\,F(wt\%) + g\,/F(wt\%) + h\,P(kb) + i\,P/F, \qquad (3.6)$$

where e, f, g, h, and i are empirical coefficients which differ slightly for each bulk composition. Table 3.2 gives the coefficients for HPY and TQL, and Figure 3.6 compares calculated D_i values with those derived from the experimental data. In Figure 3.7 I directly compare the weight percent of each oxide with the CEPM for both starting compositions. This figure also shows that typical uncertainties for calculated D_i values and weight percents are about the same as analytical uncertainties.

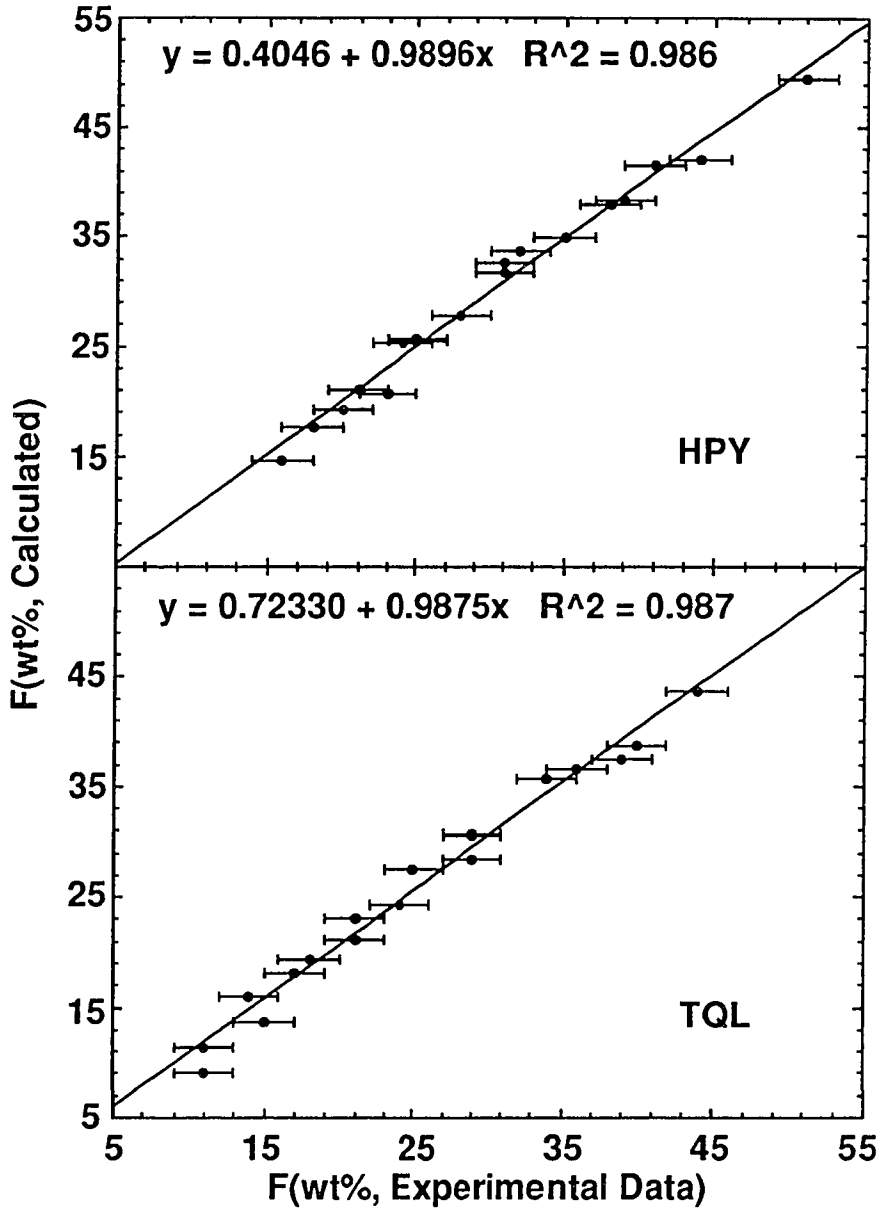

Fig. 3.3 A comparison of the extent of partial melting (F) determined by *Jaques and Green* [1980] with F calculated using my empirical expression (equation (5)) for both HPY and TQL. The equation is for the regression line.

Fig. 3.4 Calculated extent of partial melting (solid lines) using (3.5) for (*a*) HPY and (*b*) TQL as a function of temperature (degrees Celsius) and pressure (kilobars). The heavy solid line is the solidus from Figure 1 of *Jaques and Green* [1980]. The dashed isopleths are from Figure 2 of *Jaques and Green* [1980].

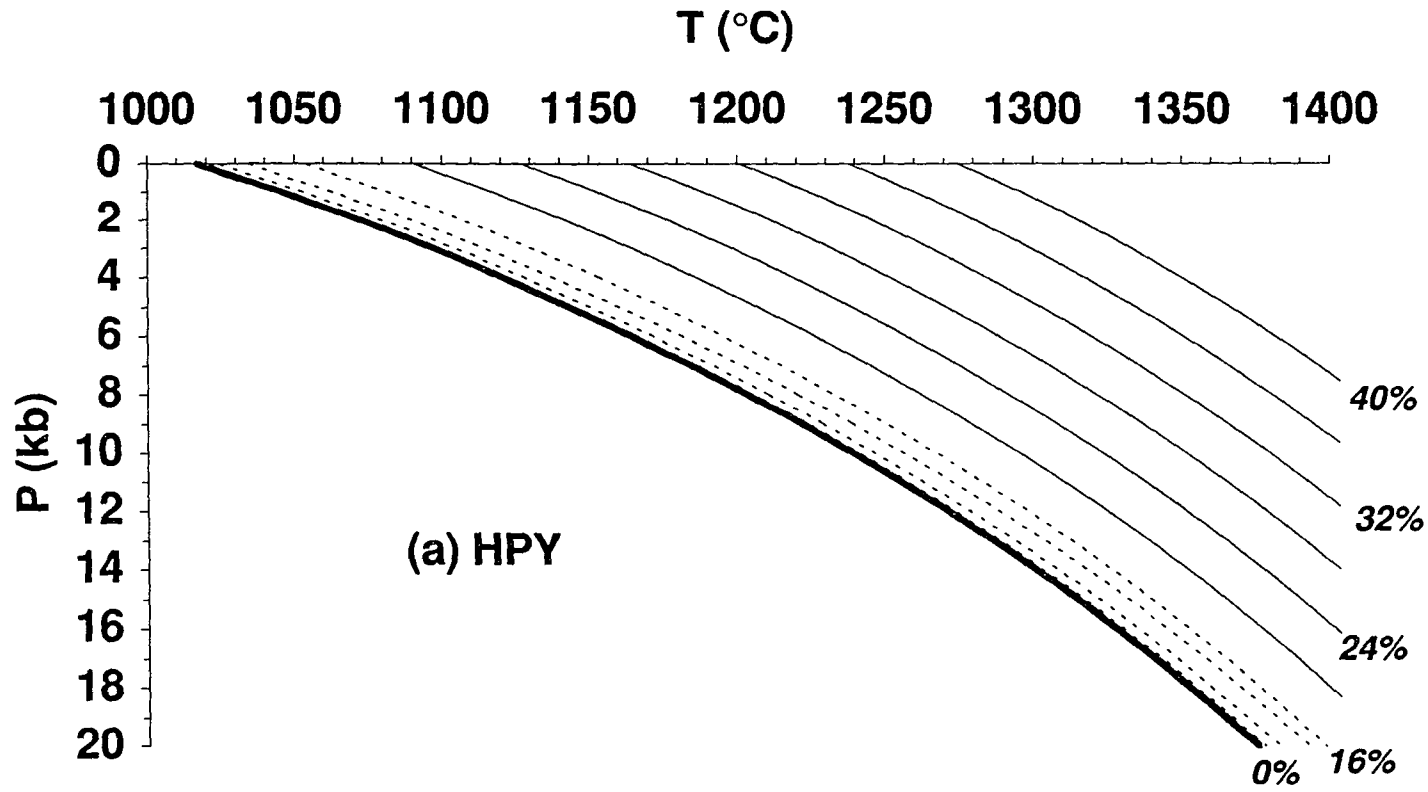
T (°C)
1000
1050
1100
1150
1200
1250
1300
1350
1400
P (kb)
0
2
4
6
8
10
12
14
16
18
20
(a) HPY
40%
32%
24%
16%
0%

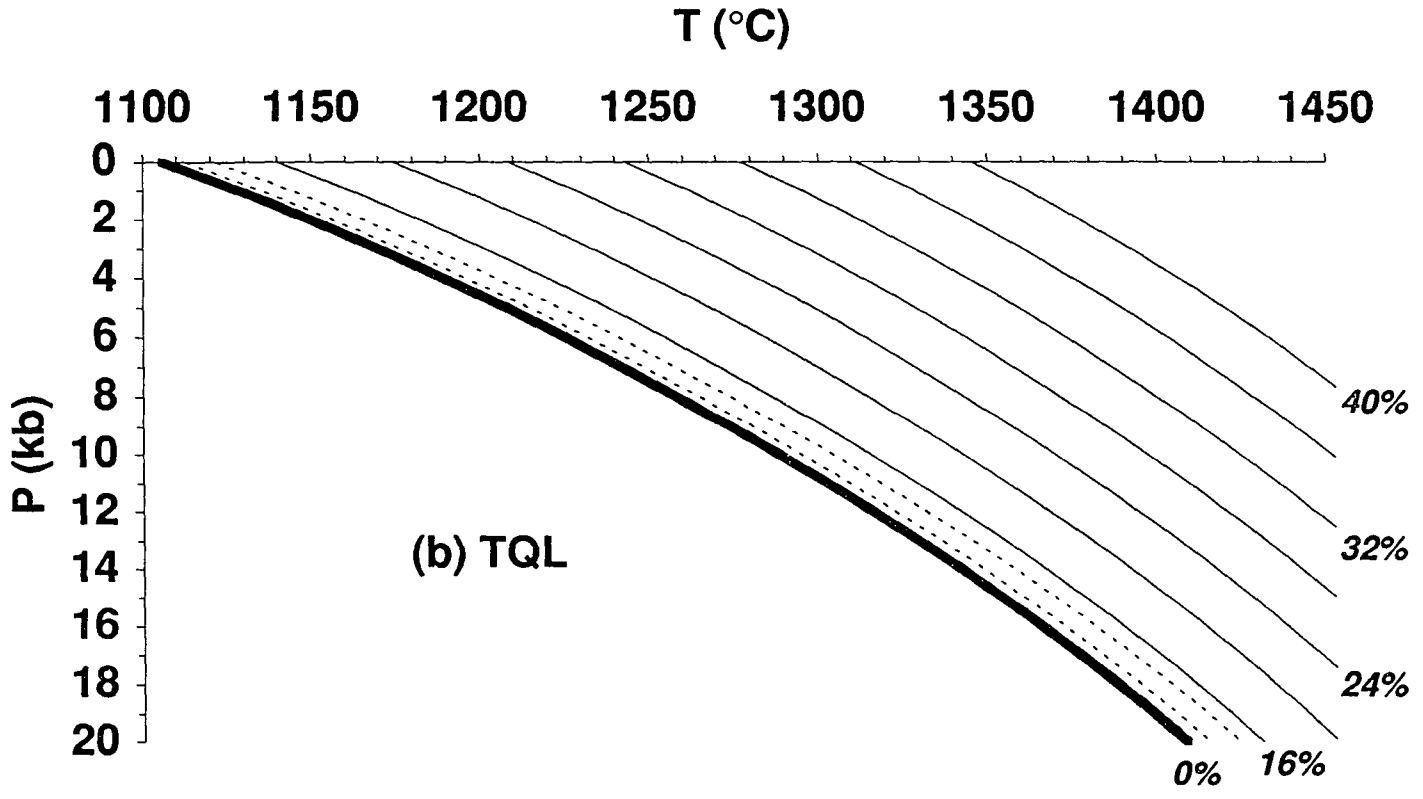
T (°C)
1100
1150
1200
1250
1300
1350
1400
1450
P (kb)
0
2
4
6
8
10
12
14
16
18
20
(b) TQL
40%
32%
24%
16%
0%

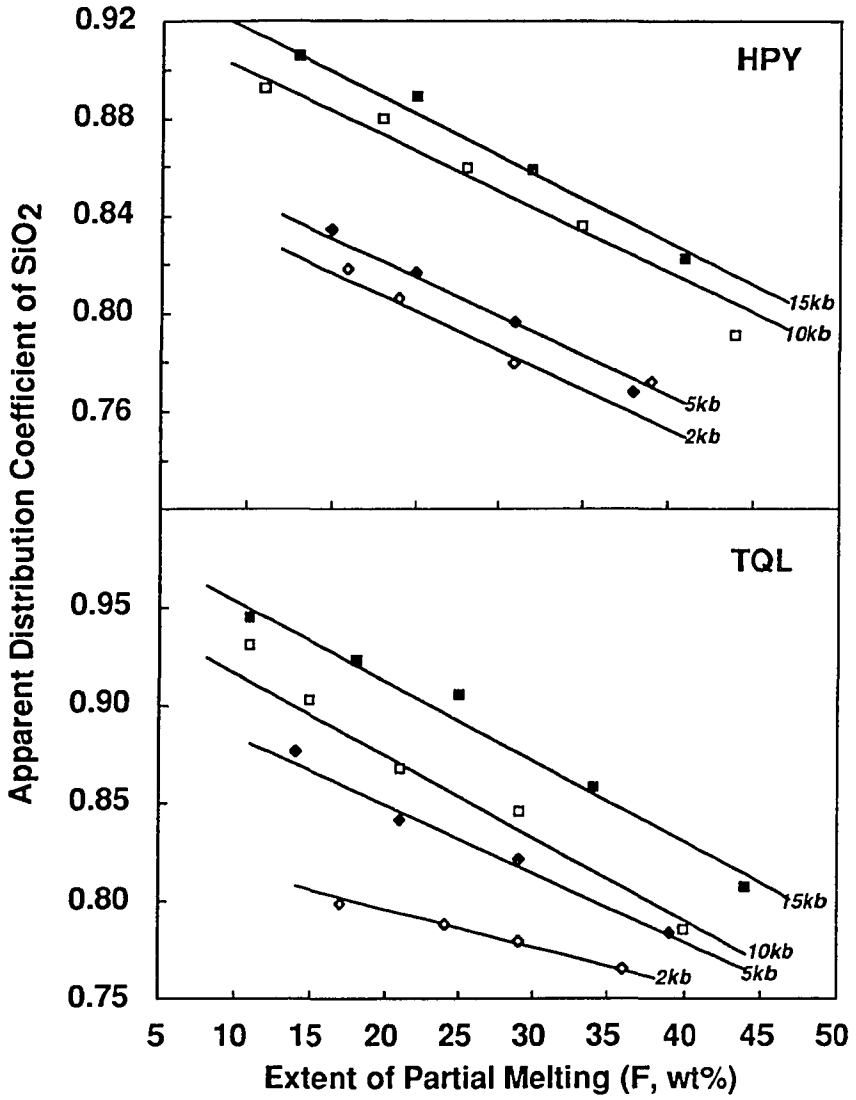

Fig. 3.5 Plots of D_{SiO_2} versus F(weight percent) for HPY and TQL. The 2-kbar and 10-kbar data for HPY show slight deviations at high F (>40%). For this reason, I place less emphasis on F > 40% and P < 5 kbar. Plots of this type were made for all elements and used to empirically determine the form of (3.6) and its coefficients.

Table 3.3. Empirical coefficients determined for apparent bulk distribution coefficients

	Hawaiian Pyrolite						Tinaquillo Lherzolite					
Oxide	*e*	*f*	*g*	*h*	*i*	R^{2*}	*e*	*f*	*g*	*h*	*i*	R^{2*}
SiO_2	0.8788 (±0.0430)	- 0.0031 (±0.0020)	0	0.0060 (±0.0020)	0	0.977	0.8840 (±0.0610)	- 0.0030 (±0.0020)	0	0.0060 (0.002)	0	0.973
TiO_2	0.0910 (±0.0020)	- 0.0020 (±0.0010)	0	0	0	0.974			0	0	0	0.974†
Al_2O_3	0.0812 (±0.0061)	- 0.0031 (±0.0001)	0.1253 (±0.0410)	0.0050 (±0.0010)	0	0.955	0.0682 (±0.0091)	- 0.0030 (±0.0080)	0.0520 (±0.0110)	0.0050 (±0.0010)	0	0.931
FeO	1.6091 (±0.2310)	-0.0181 (±0.0081)	0	0.01210 (±0.0060)	-0.8661 (±0.1380)	0.947	1.5804 (±0.2310)	-0.0192 (±0.003)	0	0.0061 (±0.003)	-0.6190 (±0.1010)	0.932
MgO	6.6463 (±0.5111)	- 0.0842 (±0.0070)	0	- 0.0760 (±0.009)	0	0.948	4.6234 (±0.4203)	- 0.0500 (±0.0060)	0	-0.0542 (±0.0040)	0	0.926
CaO	- 0.4751 (±0.0310)	0.0059 (±0.0011)	10.1521 (±1.4312)	0.0005 (±0.0002)	0	0.956	-0.1015 (±0.0210)	0.0022 (±0.0007)	3.4592 (±0.3321)	0.0005 (±0.0003)	0	0.929
Na_2O	0.0991 (±0.0080)	- 0.0042 (±0.0012)	0	0	0	0.993	0.0509 (±0.0090)	- 0.0038 (±0.0008)	0	0	0	0.993
K_2O	0.0099 (±0.001)	- 0.0002 (±2.00e-5)	0	0	0	0.994			0	0	0	0.994†
CaO‡	0.3110	- 0.0081	0.3071	0.0005	0		0.2610	- 0.0091	0.4407	0.0005	0	
FeO‡	0.9121	0	2.2670	-0.0210	-0.1213		0.8361	0	2.2870	-0.0141	-0.1922	

$D_i = e + f\,F + g/F + h\,P + i\,P/F$ is the general form to describe partitioning behavior for all the oxides. No units are necessary for the nondimensional D_i as each of the coefficients will take the reciprocal form of the corresponding variables and will be cancelled out.

*R^2 and uncertainties listed are from regression of the raw data.

† The concentration of TiO_2 and K_2O for Tinaquillo Lherzolite and experimental melts are too low to determine, so the coefficients for Hawaiian Pyrolite are used.

‡Recommended values for CaO and FeO to extrapolate the experimental data down to ~5% melting without affecting the melting ranges where data are available.

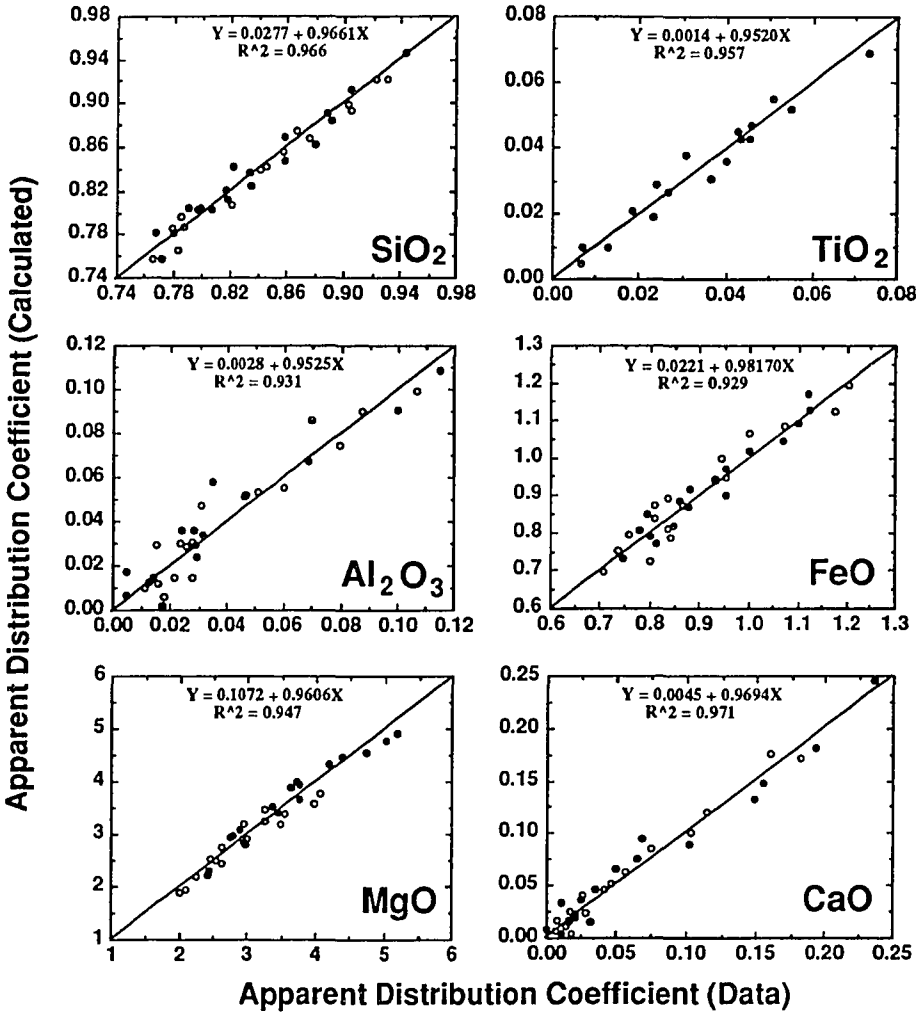

Fig. 3.6 A comparison between D_i calculated using (3.6) and D_i directly derived from experiments (equation (3)) for both HPY (solid circles) and TQL (open circles). The *Jaques and Green* [1980] data and *Falloon et al.* [1988] data are corrected using the results of Figure 3.1. For TiO_2, only HPY data are plotted, since TiO_2 values for TQL are too uncertain to be of value. D_{Na_2O} and D_{K_2O} are omitted because no mass balance could be obtained using the experimental results. Even so, (3.6) is able to reproduce available abundances in both HPY and TQL (see Figure 3.7). The equations are for the regression lines.

Equation (3.6) and Table 3.3 quantify the following features of isobaric batch melting found by *Jaques and Green* [1980] and *Falloon and Green* [1987, 1988]. (1) The D_i for all oxides are strongly dependent on F. In some cases, this dependence is linear or nearly linear, but in other cases the dependence is non-linear. (2) The D_i for SiO_2, Al_2O_3, FeO, MgO, and CaO show clear pressure dependence. (3) The behavior of FeO is complex: at low pressure, the FeO content of melts increases with F, but at high pressures the FeO content of melts decreases with F. The coefficients in Table 3.3 are optimized after multiple-regression analysis in order to place greater emphasis on the higher-pressure results of *Jaques and Green* [1980] and *Falloon et al.* [1988]. The behavior of these oxides in calculated batch melts from HPY and TQL are shown in Figures 3.8*a* and 3.8*b*.

However, neither HPY nor TQL is a good candidate for the mantle source of most MORB magmas. *Falloon and Green* [1987] showed that, in fact, these two peridotites probably represent extremes of a spectrum of peridotites likely to be found in the suboceanic mantle (Table 3.1). HPY is probably too rich in Na_2O, K_2O, and TiO_2 and too poor in CaO to be a good candidate for MORB mantle. Likewise, TQL is probably too poor in Na_2O and K_2O. From the mantle array analysis of *Falloon and Green* [1987], MORB pyrolite with Fo_{90} (MPY-90) appears to be the best candidate for the MORB source.

Unfortunately, the experiments on MPY-90 by *Falloon and Green* [1987, 1988] are sandwich experiments, so F was not determined from each run. Furthermore, the number of runs and the P-T coverage of MPY-90's behavior are insufficient to carry out the sort of analysis I performed for HPY and TQL. Instead, I used the equation (3.6) coefficients (*e* - *i*) for TQL as a starting point and by trial and error varied them to fit the available data for MPY-90. The coefficients listed in Table 3.4 are the results of this attempt. Because TQL and MPY-90 are very similar in bulk composition, I use the equation (3.5) coefficients of TQL (Table 3.2) for MPY-90. While the fit of the Table 3.4 coefficients to MPY-90

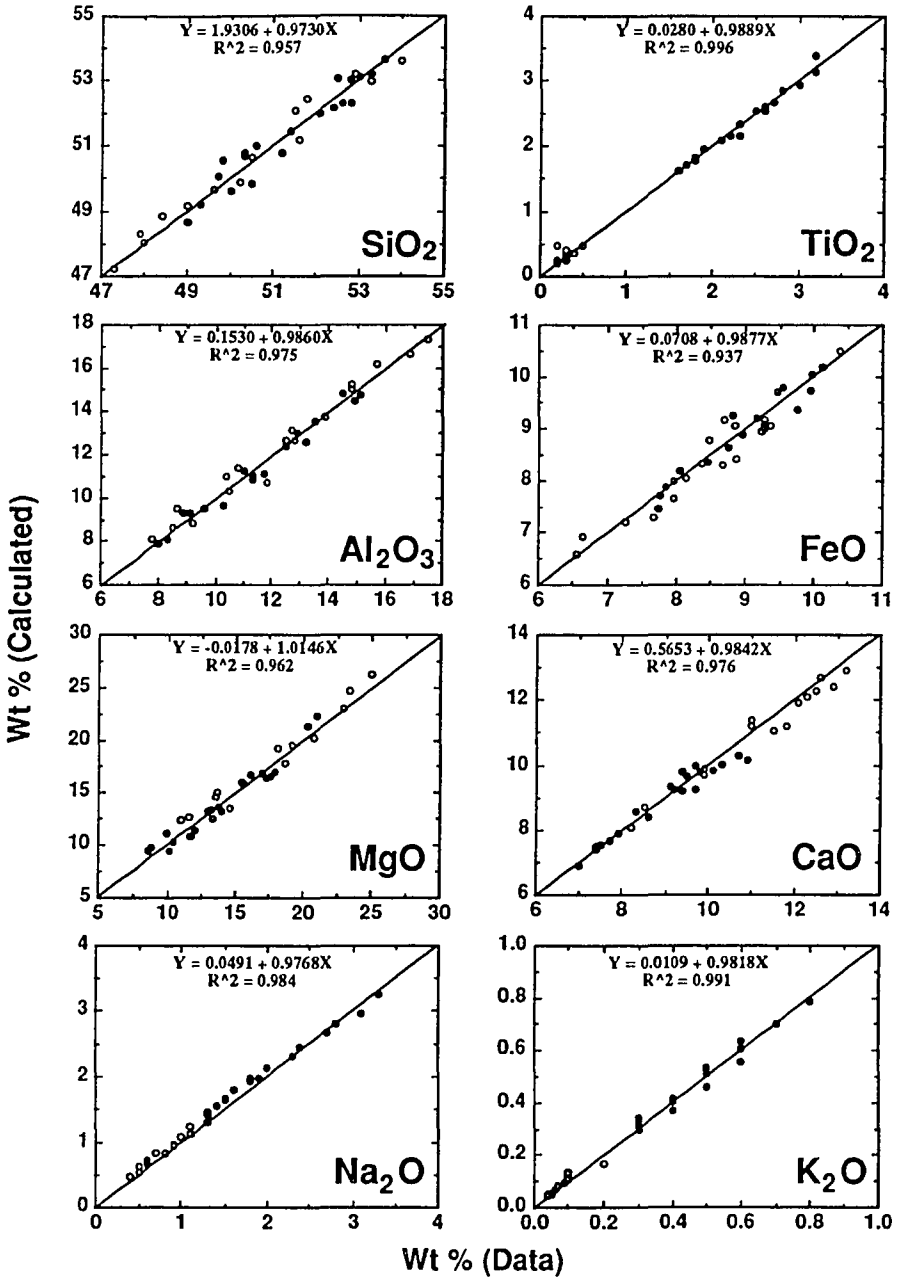

Fig. 3.7 A comparison of isobaric batch melt compositions calculated by (3.3), (3.5), and (3.6) with CEPM of *Jaques and Green* [1980] and reversal experiments of *Falloon et al.* [1988] for HPY (solid circle) and TQL (open circle). Note that with a few exceptions typical departures from the 1:1 agreement are of the order of analytical uncertainty.

behavior cannot be verified at the same level of confidence as for HPY and TQL, I am confident that these values are reasonably good. Figure 3.8*c* shows the calculated melt compositions for MPY-90 as a function of P and F.

3.2.3 Isobaric batch melting model

Figures 3.8*a*, 3.8*b*, and 3.8*c* show the calculated isobaric batch melts from HPY, TQL, and MPY-90. These are calculated using (11) of *Shaw* [1970] with F and D_i values from (3.5) and (3.6) and the data of Tables 1, 2, and 4. Each oxide is calculated independently, and the melt compositions (not shown in tabulated form) sum to 100% ± 2%. My extrapolation of the results of *Jaques and Green* [1980] from 15 kbar to 20 kbar is in excellent agreement with the results of *Falloon et al.* [1988] and *Falloon and Green* [1988] at 20 kbars and higher.

In addition to the conclusions reached by *Jaques and Green* [1980], it is worth making some additional points about the characteristics of isobaric batch melts. First, it is clear that melt concentrations of SiO_2, Al_2O_3, FeO, and MgO are affected by pressure. However, the effect can be complex, and F can exert an important control, as for FeO. CaO melt concentration reaches a maximum before clinopyroxene is consumed. Because melt composition can be strongly affected by both P and F, caution must be taken in inferring the P and F of formation of natural MORB glasses on the basis of a single oxide. In addition, of course, the bulk composition of the peridotite source can exert a significant effect, as shown by *Langmuir and Hanson* [1980*a*]. A comparison among Figures 3.8*a*, 3.8*b*, and 3.8*c* illustrates the potential effect from source heterogeneity.

3.2.4 Decompression-induced column melting model

As discussed previously, MORB melts are probably not produced by isobaric batch melting. Instead, melting is probably polybaric and occurs in response to adiabatic ascent of solid mantle material. At the same time, melt escapes the system and can accumulate by

Fig. 3.8 Calculated isobaric melt compositions for (*a*) HPY, (*b*) TQL, and (*c*) MPY-90. The results are plotted to show the behavior of each oxide component in the melts with pressure (labeled with small numbers in kilobars) and extent of partial melting (F). See text for discussion.

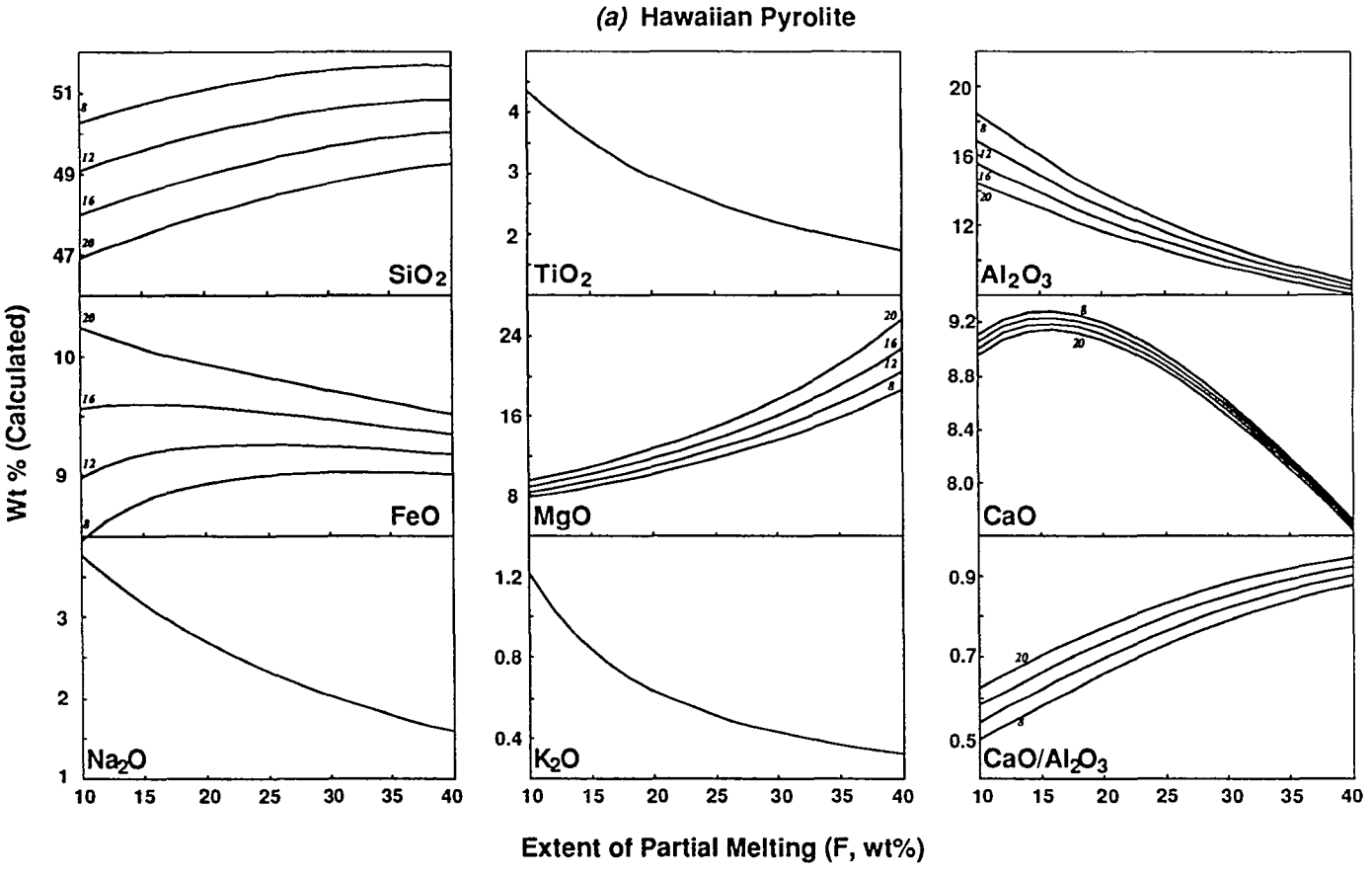
(a) Hawaiian Pyrolite
Wt % (Calculated)
SiO2
TiO2
Al2O3
FeO
MgO
CaO
Na2O
K2O
CaO/Al2O3
Extent of Partial Melting (F, wt%)

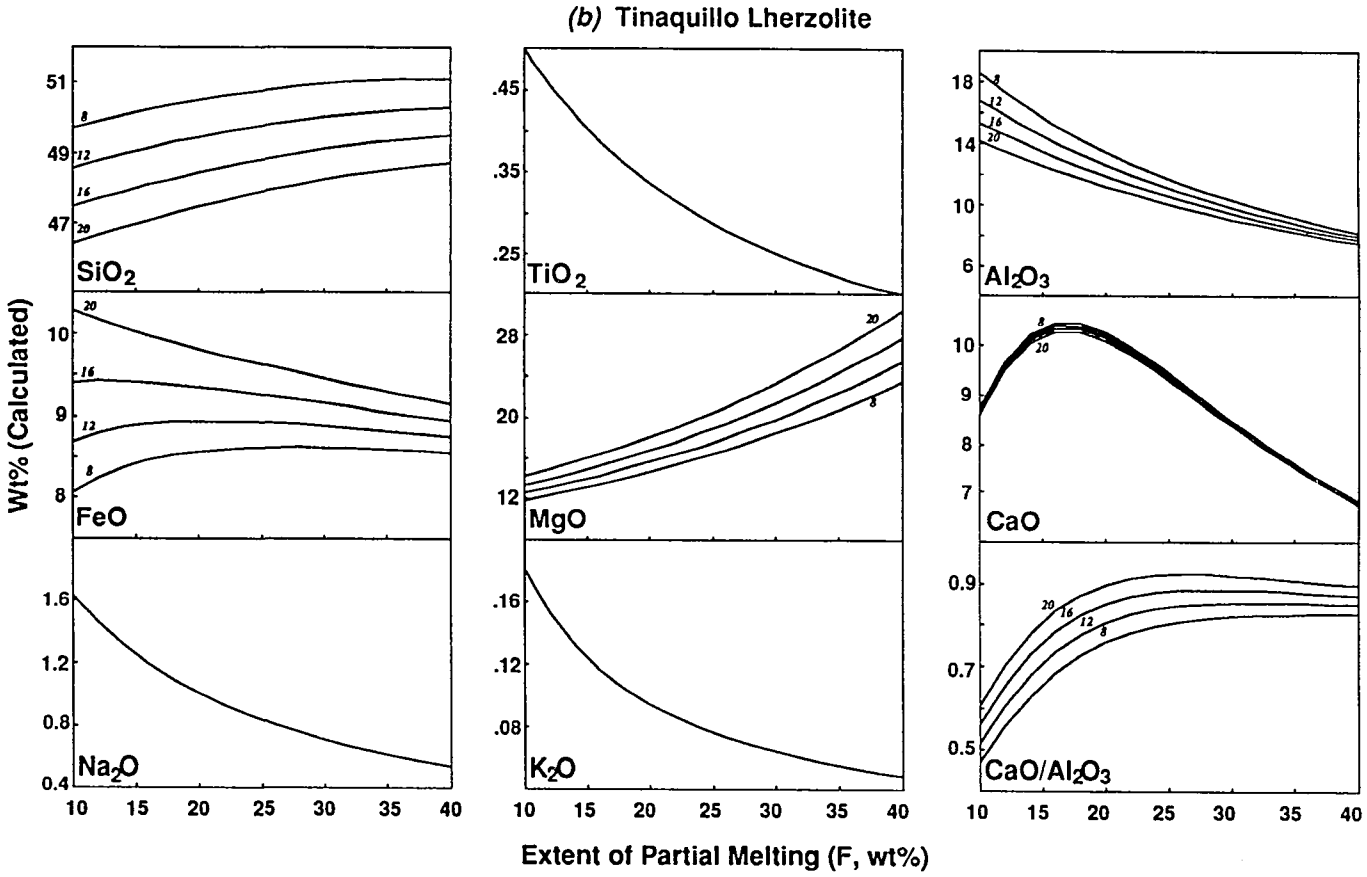
(b) Tinaquillo Lherzolite
Wt% (Calculated)
SiO2
TiO2
Al2O3
FeO
MgO
CaO
Na2O
K2O
CaO/Al2O3
8
12
16
20
Extent of Partial Melting (F, wt%)

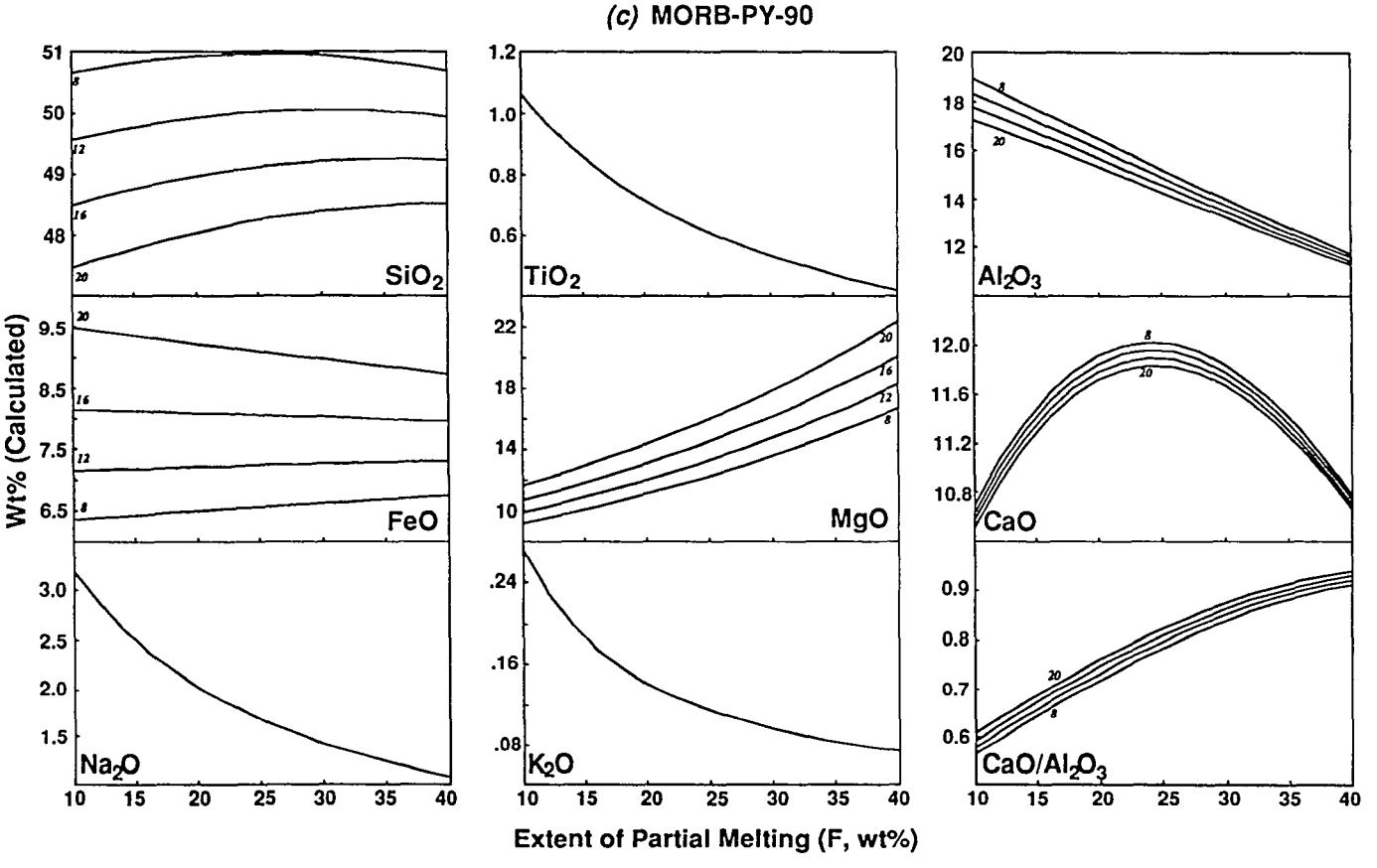
(c) MORB-PY-90
Wt% (Calculated)
SiO2
TiO2
Al2O3
FeO
MgO
CaO
Na2O
K2O
CaO/Al2O3
Extent of Partial Melting (F, wt%)

Table 3.4. Estimated coefficients for MPY-90

Oxide	*e*	*f*	*g*	*h*	*i*
SiO_2	0.8480	- 0.0022	0	0.0055	0
TiO_2	0.0910	- 0.0020	0	0	0
Al_2O_3	0.1960	- 0.0065	-0.0250	0.0021	0
FeO	1.4720	0	0.2730	- 0.0350	-0.0130
MgO	5.6230	- 0.0451	0	- 0.0810	0
CaO	0.3270	- 0.0120	0.3071	0.0005	0
Na_2O	0.0509	- 0.0038	0	0	0
K_2O*	0.0099	- 0.0002	0	0	0

*Treated the same as for Tinaquillo Lherzolite.

These coefficients are obtained by trial and error to fit the experimental data for MPY-90 [*Falloon and Green*, 1987, 1988]. The uncertainties for the coefficients are probably of the same order as the regression errors for TQL (Table 3.3).

Table 3.5. Recommended coefficients for MPY-90

Oxide	*e*	*f*	*g*	*h*	*i*
SiO_2	0.8580	- 0.0040	0	0.0050	0
TiO_2	0.0980	- 0.0050	0	0	0
Al_2O_3	0.1890	- 0.0051	-0.0250	0.0021	0
FeO	1.4420	0	0.2730	- 0.0350	-0.0130
MgO	5.2860	- 0.0640	0	- 0.0630	0
CaO	0.3180	- 0.0122	0.2720	0.0005	0
Na_2O	0.1110	- 0.0070	0	0	0
K_2O*	0.0690	- 0.0020	0	0	0

*The same as for Table 3.4. See text for discussion of how these coefficients are obtained.

Fig. 3.9 Adiabatic melting paths (light solid lines) in P-T space. The solidus (heavy solid line) and melting (F) isopleths are from Figure 3.4*b*. The adiabat gradients (3° $Kbar^{-1}$ for solid and 6° $Kbar^{-1}$ after initial melting) are from *McKenzie* [1984]. The initial melting (P_o) for each path is indicated.

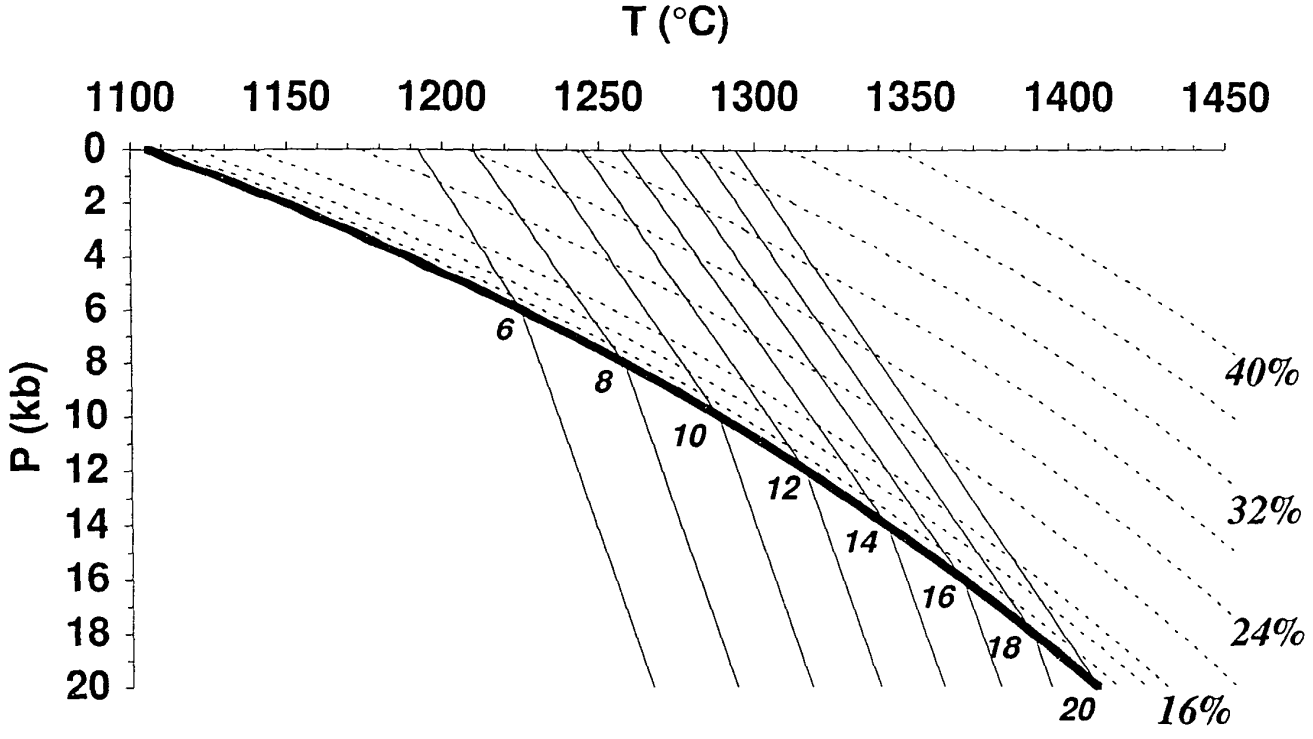
T (°C)
1100
1150
1200
1250
1300
1350
1400
1450
P (kb)
0
2
4
6
8
10
12
14
16
18
20
6
8
10
12
14
16
18
20
40%
32%
24%
16%

segregation processes. It is this process of column melting due to decompression of upwelling mantle that I wish to approximate in my model. I stress that available data allow only an approximation to this process and several uncertainties are present.

I attempt to model the melts produced by a parcel of mantle rising adiabatically and melting continuously along the idealized adiabatic paths shown in Figure 3.9. The very low melt retention in the mantle and the relatively rapid melt extraction process [*McKenzie*, 1984, 1985*b*] imply that melting and melt extraction occur continuously in the mantle. Thus, melting can be considered as a series of infinitesimally small incremental batches in the course of continuous melting accompanied by instantaneous melt extraction. These incremental batches may aggregate or accumulate to form MORB melts. The composition of each oxide in the accumulated melt can ideally be evaluated by

$$C_i^l = \frac{1}{F} \int_0^F \frac{C_i^R}{F + D_i (1 - F)} dF, \qquad (3.7)$$

where C_i^l is the concentration of i in the accumulated melt when the total amount of melting reaches F along an adiabatic ascent path, C_i^R is the concentration of oxide i in the solid residue at F, and D_i is the apparent bulk distribution coefficient of i. The integrand, the concentration of i of the incremental batch, implies that at any instance in the course of the continuous melting, only a finite amount of melt (dF) is in equilibrium with solid residue. Since $D_i = f(F,P)$ and $C_i^R = f(F,D_i)$, (3.7) cannot be solved analytically. I thus solve (3.7) numerically by finite difference. For simplicity and because of lack of data for small degree melts, the first melt I produce is a 5% isobaric batch melt which is followed by incremental steps of dF = 0.01 (1%). In each step, C_i^R, the residue, is calculated by mass balance, and it serves as the source for the next increment of melting. The D_i values are recalculated in response to the changes in P and F at each step. I calculate the accumulated melt compositions at each increment along the adiabat corresponding to eight initial

Fig. 3.10 Calculated compositions of accumulated (pooled) column melts using my empirical model. Data are from Table 3.6. Small numbers give the initial melting pressures. See text for detailed discussion.

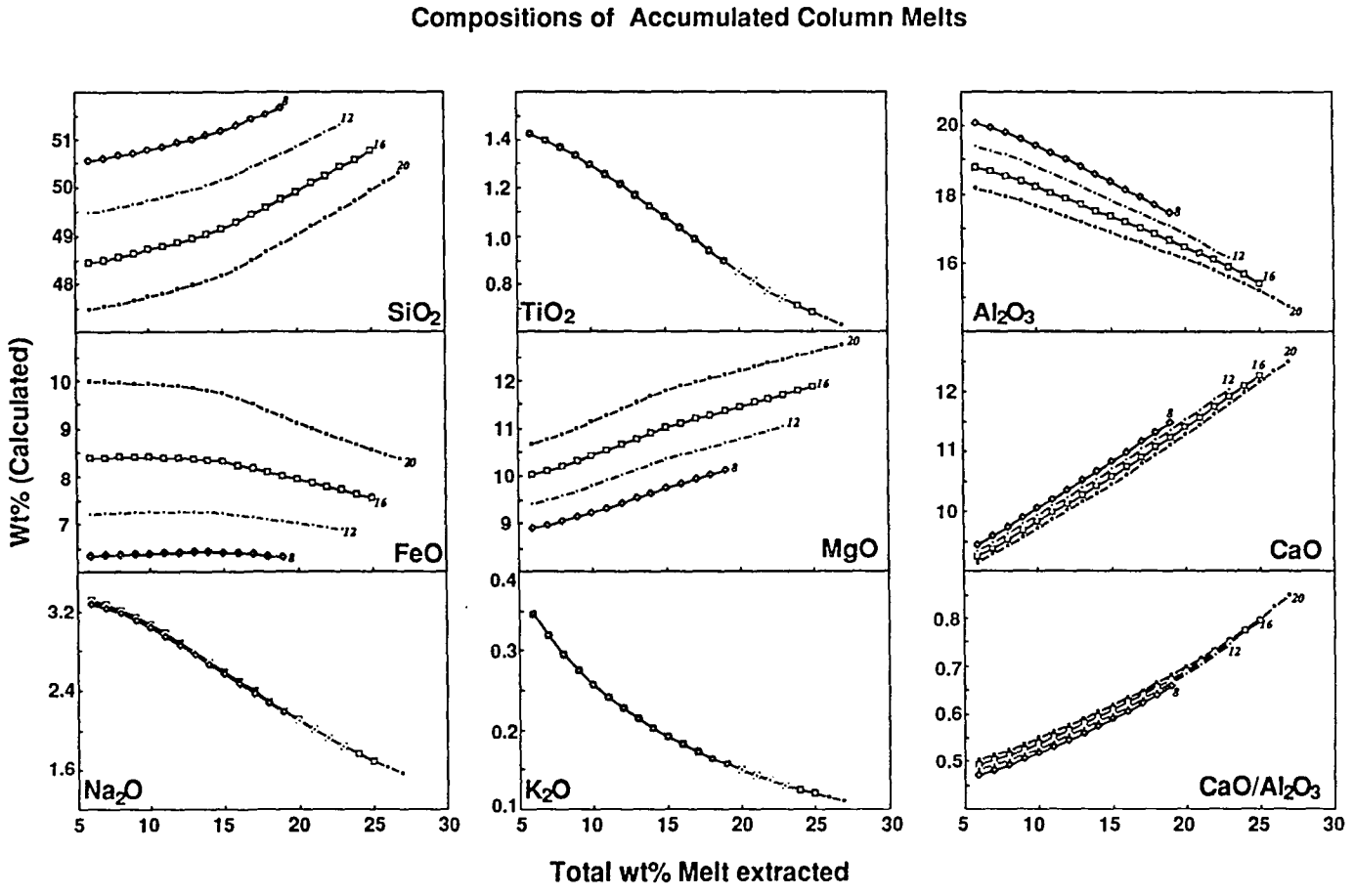
Compositions of Accumulated Column Melts
Wt% (Calculated)
SiO2
TiO2
Al2O3
FeO
MgO
CaO
Na2O
K2O
CaO/Al2O3
Total wt% Melt extracted

Table 3.6. Oxide compositions and CIPW norms of accumulated melts

F*	T†	P_f‡	SiO_2	TiO_2	Al_2O_3	FeO	MgO	CaO	Na_2O	K_2O	Sum	$\frac{CaO}{Al_2O_3}$	Mg#	Or	Ab	An	Ne	Di	Hy	Ol	Mt	Il
Initial Melting At 20 kbar																						
6	1406	19.41	47.47	1.42	18.17	9.98	10.67	9.16	3.27	0.35	100.50	0.50	67.93	2.04	22.84	33.90	2.60	9.33	0.00	25.58	1.61	2.70
8	1402	18.70	47.60	1.37	17.95	9.96	10.88	9.43	3.19	0.30	100.68	0.53	68.40	1.74	22.55	33.79	2.42	10.52	0.00	25.57	1.60	2.59
10	1397	17.85	47.74	1.29	17.68	9.93	11.13	9.72	3.08	0.26	100.83	0.55	68.95	1.52	22.23	33.63	2.09	11.81	0.00	25.60	1.60	2.46
12	1391	16.87	47.90	1.21	17.36	9.88	11.40	10.01	2.94	0.23	100.93	0.58	69.56	1.34	21.96	33.52	1.57	13.06	0.00	25.68	1.59	2.30
14	1384	15.76	48.08	1.13	17.04	9.80	11.67	10.31	2.75	0.20	100.97	0.60	70.23	1.20	21.86	33.54	0.77	14.22	0.00	25.77	1.58	2.14
16	1376	14.51	48.34	1.03	16.74	9.61	11.88	10.62	2.48	0.18	100.88	0.63	71.00	1.07	20.95	34.03	0.00	15.05	2.24	24.13	1.55	1.96
18	1368	13.12	48.67	0.94	16.46	9.36	12.04	10.95	2.20	0.16	100.79	0.67	71.81	0.97	18.62	34.54	0.00	15.95	7.10	20.42	1.51	1.79
20	1359	11.60	49.02	0.85	16.14	9.12	12.20	11.28	1.98	0.15	100.74	0.70	72.61	0.88	16.76	34.71	0.00	17.14	10.90	17.37	1.47	1.61
22	1349	9.95	49.37	0.77	15.79	8.88	12.36	11.63	1.80	0.14	100.74	0.74	73.38	0.80	15.23	34.61	0.00	18.59	13.93	14.78	1.43	1.47
24	1338	8.16	49.74	0.71	15.40	8.66	12.51	11.98	1.65	0.12	100.78	0.78	74.12	0.74	13.96	34.25	0.00	20.27	16.39	12.53	1.39	1.34
26	1327	6.23	50.11	0.65	14.97	8.44	12.67	12.34	1.52	0.12	100.83	0.82	74.83	0.68	12.89	33.67	0.00	22.14	18.41	10.53	1.36	1.24
28	1314	4.17	50.48	0.61	14.49	8.24	12.83	12.07	1.41	0.11	100.24	0.83	75.51	0.63	11.97	32.88	0.00	21.67	23.72	6.98	1.33	1.15
Initial Melting At 18 kbar																						
6	1385	17.37	47.96	1.42	18.46	9.11	10.33	9.20	3.27	0.35	100.11	0.50	69.19	2.04	24.78	34.69	1.55	8.86	0.00	24.10	1.47	2.70
8	1381	16.72	48.08	1.37	18.23	9.10	10.53	9.48	3.19	0.30	100.28	0.52	69.61	1.74	24.49	34.55	1.37	10.08	0.00	24.08	1.47	2.59
10	1376	15.94	48.22	1.29	17.94	9.09	10.76	9.78	3.08	0.26	100.43	0.54	70.10	1.52	24.17	34.37	1.04	11.41	0.00	24.11	1.46	2.46
12	1371	15.03	48.38	1.21	17.62	9.06	11.01	10.07	2.94	0.23	100.52	0.57	70.65	1.34	23.90	34.22	0.52	12.71	0.00	24.17	1.46	2.30
14	1365	13.98	48.55	1.13	17.28	9.01	11.27	10.37	2.75	0.20	100.56	0.60	71.25	1.20	23.29	34.19	0.00	13.91	0.84	23.64	1.45	2.14
16	1358	12.81	48.81	1.03	16.96	8.86	11.48	10.68	2.48	0.18	100.49	0.63	71.95	1.07	20.95	34.64	0.00	14.79	5.39	20.36	1.43	1.96
18	1350	11.51	49.13	0.94	16.65	8.67	11.64	11.01	2.20	0.16	100.41	0.66	72.69	0.97	18.62	35.08	0.00	15.74	10.12	16.80	1.40	1.79
20	1341	10.07	49.47	0.85	16.31	8.47	11.81	11.35	1.98	0.15	100.39	0.70	73.41	0.88	16.76	35.19	0.00	16.99	13.81	13.88	1.37	1.61
22	1332	8.50	49.81	0.77	15.94	8.28	11.97	11.69	1.80	0.14	100.41	0.73	74.11	0.80	15.23	35.01	0.00	18.49	16.74	11.42	1.33	1.47
24	1322	6.81	50.16	0.71	15.53	8.10	12.13	12.04	1.65	0.12	100.45	0.78	74.79	0.74	13.96	34.59	0.00	20.21	19.11	9.28	1.31	1.34
26	1311	4.98	50.52	0.65	15.07	7.93	12.30	12.39	1.52	0.12	100.50	0.82	75.45	0.68	12.89	33.94	0.00	22.12	21.05	7.38	1.28	1.24
28	1299	3.02	50.87	0.61	14.57	7.76	12.46	12.11	1.41	0.11	99.91	0.83	76.08	0.63	11.97	33.08	0.00	21.69	26.30	3.92	1.25	1.15
Initial Melting At 16 kbar																						
6	1362	15.36	48.45	1.42	18.76	8.38	10.01	9.25	3.27	0.35	99.90	0.49	70.29	2.04	26.59	35.51	0.57	8.38	0.00	22.84	1.35	2.70
8	1359	14.78	48.58	1.37	18.52	8.39	10.19	9.53	3.19	0.30	100.07	0.51	70.66	1.74	26.30	35.34	0.39	9.63	0.00	22.80	1.35	2.59
10	1355	14.07	48.71	1.29	18.22	8.38	10.42	9.83	3.08	0.26	100.20	0.54	71.11	1.52	25.98	35.12	0.05	11.00	0.00	22.81	1.35	2.46
12	1350	13.23	48.87	1.21	17.88	8.37	10.66	10.13	2.94	0.23	100.28	0.57	71.60	1.34	24.86	34.93	0.00	12.34	1.42	21.83	1.35	2.30
14	1344	12.26	49.04	1.13	17.52	8.34	10.90	10.43	2.75	0.20	100.31	0.60	72.15	1.20	23.29	34.86	0.00	13.59	3.82	20.17	1.34	2.14
16	1337	11.16	49.29	1.03	17.19	8.23	11.11	10.74	2.48	0.18	100.24	0.63	72.78	1.07	20.95	35.25	0.00	14.53	8.30	16.95	1.33	1.96
18	1330	9.93	49.60	0.94	16.85	8.08	11.28	11.07	2.20	0.16	100.18	0.66	73.45	0.97	18.62	35.62	0.00	15.53	12.93	13.50	1.30	1.79
20	1322	8.57	49.92	0.85	16.49	7.92	11.44	11.41	1.98	0.15	100.16	0.69	74.11	0.88	16.76	35.66	0.00	16.83	16.53	10.69	1.28	1.61
22	1313	7.08	50.25	0.77	16.09	7.77	11.61	11.75	1.80	0.14	100.18	0.73	74.75	0.80	15.23	35.42	0.00	18.38	19.38	8.33	1.25	1.47
24	1303	5.46	50.59	0.71	15.65	7.62	11.78	12.10	1.65	0.12	100.22	0.77	75.38	0.74	13.96	34.93	0.00	20.15	21.66	6.28	1.23	1.34
26	1292	3.71	50.93	0.65	15.17	7.48	11.95	12.45	1.52	0.12	100.26	0.82	75.99	0.68	12.89	34.21	0.00	22.11	23.55	4.46	1.21	1.24

Table 3.6. Oxide compositions and CIPW norms of accumulated melts (continued)

F*	T†	P_f‡	SiO_2	TiO_2	Al_2O_3	FeO	MgO	CaO	Na_2O	K_2O	Sum	$\frac{CaO}{Al_2O_3}$	Mg#	Or	Ab	An	Ne	Di	Hy	Ol	Mt	Il
Initial Melting At 14 kbar																						
6	1338	13.39	48.96	1.42	19.07	7.76	9.70	9.30	3.27	0.35	99.83	0.49	71.25	2.04	27.65	36.35	0.00	7.89	1.07	20.96	1.25	2.70
8	1335	12.88	49.08	1.37	18.82	7.77	9.88	9.58	3.19	0.30	100.00	0.51	71.59	1.74	27.01	36.16	0.00	9.17	1.64	20.51	1.25	2.59
10	1331	12.24	49.22	1.29	18.50	7.78	10.09	9.89	3.08	0.26	100.11	0.53	71.99	1.52	26.08	35.90	0.00	10.58	2.66	19.76	1.25	2.46
12	1327	11.48	49.37	1.21	18.15	7.78	10.32	10.19	2.94	0.23	100.18	0.56	72.44	1.34	24.86	35.66	0.00	11.97	4.24	18.64	1.25	2.30
14	1321	10.58	49.54	1.13	17.77	7.76	10.56	10.49	2.75	0.20	100.19	0.59	72.94	1.20	23.29	35.54	0.00	13.27	6.62	16.97	1.25	2.14
16	1315	9.54	49.77	1.03	17.41	7.68	10.76	10.80	2.48	0.18	100.12	0.62	73.51	1.07	20.95	35.86	0.00	14.26	11.04	13.83	1.24	1.96
18	1308	8.38	50.07	0.94	17.05	7.56	10.93	11.13	2.20	0.16	100.06	0.65	74.12	0.97	18.62	36.17	0.00	15.32	15.59	10.47	1.22	1.79
20	1300	7.09	50.38	0.85	16.67	7.44	11.10	11.47	1.98	0.15	100.03	0.69	74.72	0.88	16.76	36.14	0.00	16.68	19.11	7.74	1.20	1.61
22	1292	5.67	50.69	0.77	16.24	7.32	11.27	11.81	1.80	0.14	100.05	0.73	75.32	0.80	15.23	35.83	0.00	18.28	21.88	5.45	1.18	1.47
24	1283	4.11	51.01	0.71	15.78	7.20	11.45	12.16	1.65	0.12	100.08	0.77	75.90	0.74	13.96	35.27	0.00	20.10	24.10	3.48	1.16	1.34
Initial Melting At 12 kbar																						
6	1312	11.45	49.48	1.42	19.39	7.22	9.42	9.35	3.27	0.35	99.90	0.48	72.10	2.04	27.65	37.22	0.00	7.37	3.74	18.08	1.16	2.70
8	1310	11.03	49.60	1.37	19.13	7.24	9.59	9.64	3.19	0.30	100.05	0.50	72.40	1.74	27.01	37.00	0.00	8.69	4.31	17.61	1.17	2.59
10	1306	10.46	49.73	1.29	18.80	7.26	9.79	9.94	3.08	0.26	100.15	0.53	72.77	1.52	26.08	36.70	0.00	10.14	5.33	16.84	1.17	2.46
12	1302	9.77	49.88	1.21	18.42	7.26	10.01	10.25	2.94	0.23	100.20	0.56	73.19	1.34	24.86	36.41	0.00	11.58	6.92	15.69	1.17	2.30
14	1297	8.94	50.04	1.13	18.03	7.26	10.23	10.55	2.75	0.20	100.19	0.59	73.64	1.20	23.29	36.24	0.00	12.93	9.30	14.01	1.17	2.14
16	1292	7.97	50.28	1.03	17.65	7.20	10.43	10.87	2.48	0.18	100.11	0.62	74.17	1.07	20.95	36.51	0.00	13.98	13.68	10.88	1.16	1.96
18	1285	6.87	50.55	0.94	17.26	7.11	10.60	11.20	2.20	0.16	100.03	0.65	74.72	0.97	18.62	36.74	0.00	15.11	18.15	7.60	1.15	1.79
20	1278	5.64	50.85	0.85	16.85	7.01	10.78	11.53	1.98	0.15	100.00	0.68	75.28	0.88	16.76	36.64	0.00	16.52	21.60	4.94	1.13	1.61
22	1269	4.27	51.15	0.77	16.39	6.92	10.95	11.88	1.80	0.14	100.00	0.72	75.83	0.80	15.23	36.25	0.00	18.18	24.31	2.71	1.11	1.47
Initial Melting At 10 kbar																						
6	1285	9.55	50.01	1.42	19.72	6.75	9.15	9.40	3.27	0.35	100.07	0.48	72.86	2.04	27.65	38.12	0.00	6.84	6.29	15.41	1.09	2.70
8	1283	9.21	50.12	1.37	19.45	6.78	9.31	9.69	3.19	0.30	100.21	0.50	73.13	1.74	27.01	37.87	0.00	8.19	6.86	14.92	1.09	2.59
10	1280	8.73	50.25	1.29	19.10	6.80	9.50	10.00	3.08	0.26	100.29	0.52	73.47	1.52	26.08	37.52	0.00	9.69	7.88	14.12	1.10	2.46
12	1276	8.11	50.40	1.21	18.71	6.81	9.71	10.30	2.94	0.23	100.31	0.55	73.85	1.34	24.86	37.19	0.00	11.18	9.47	12.95	1.10	2.30
14	1272	7.34	50.56	1.13	18.29	6.82	9.93	10.61	2.75	0.20	100.29	0.58	74.27	1.20	23.29	36.95	0.00	12.59	11.84	11.25	1.10	2.14
16	1266	6.44	50.77	1.03	17.88	6.78	10.13	10.93	2.48	0.18	100.18	0.61	74.75	1.07	20.95	37.14	0.00	13.70	16.16	8.17	1.09	1.96
18	1260	5.40	51.04	0.94	17.47	6.71	10.30	11.26	2.20	0.16	100.09	0.64	75.26	0.97	18.62	37.31	0.00	14.89	20.58	4.94	1.08	1.79
20	1253	4.22	51.32	0.85	17.03	6.64	10.48	11.60	1.98	0.15	100.04	0.68	75.77	0.88	16.76	37.13	0.00	16.36	23.97	2.33	1.07	1.61
Initial Melting At 8 kbar																						
6	1256	7.68	50.55	1.42	20.06	6.34	8.90	9.45	3.27	0.35	100.34	0.47	73.53	2.04	27.65	39.05	0.00	6.29	8.74	12.91	1.02	2.70
8	1254	7.43	50.66	1.37	19.78	6.37	9.05	9.74	3.19	0.30	100.46	0.49	73.79	1.74	27.01	38.77	0.00	7.68	9.31	12.40	1.03	2.59
10	1252	7.03	50.79	1.29	19.41	6.40	9.23	10.05	3.08	0.26	100.52	0.52	74.10	1.52	26.08	38.38	0.00	9.22	10.34	11.57	1.03	2.46
12	1249	6.49	50.93	1.21	19.00	6.42	9.44	10.36	2.94	0.23	100.52	0.55	74.45	1.34	24.86	37.99	0.00	10.77	11.94	10.36	1.03	2.30
14	1244	5.79	51.08	1.13	18.56	6.42	9.64	10.67	2.75	0.20	100.47	0.58	74.84	1.20	23.29	37.69	0.00	12.24	14.31	8.64	1.04	2.14
16	1239	4.95	51.29	1.03	18.13	6.40	9.84	11.00	2.48	0.18	100.34	0.61	75.28	1.07	20.95	37.81	0.00	13.41	18.60	5.58	1.03	1.96
18	1233	3.96	51.54	0.94	17.68	6.35	10.01	11.33	2.20	0.16	100.22	0.64	75.75	0.97	18.62	37.89	0.00	14.66	22.95	2.39	1.02	1.79

Table 3.6. Oxide compositions and CIPW norms of accumulated melts (continued)

F*	T†	P_f‡	SiO_2	TiO_2	Al_2O_3	FeO	MgO	CaO	Na_2O	K_2O	Sum	$\frac{CaO}{Al_2O_3}$	$Mg^{\#}$	Or	Ab	An	Ne	Di	Hy	Ol	Mt	Il
Initial Melting At 6 kbar																						
6	1225	5.84	51.10	1.42	20.42	5.98	8.66	9.50	3.27	0.35	100.69	0.47	74.15	2.04	27.65	40.02	0.00	5.71	11.11	10.56	0.96	2.70
8	1224	5.69	51.21	1.37	20.12	6.01	8.80	9.80	3.19	0.30	100.79	0.49	74.38	1.74	27.01	39.69	0.00	7.14	11.68	10.02	0.97	2.59
10	1222	5.39	51.34	1.29	19.74	6.04	8.98	10.11	3.08	0.26	100.83	0.51	74.66	1.52	26.08	39.25	0.00	8.73	12.72	9.16	0.97	2.46
12	1219	4.92	51.47	1.21	19.30	6.06	9.17	10.43	2.94	0.23	100.81	0.54	74.99	1.34	24.86	38.81	0.00	10.34	14.32	7.92	0.98	2.30
14	1216	4.29	51.62	1.13	18.84	6.07	9.37	10.74	2.75	0.20	100.73	0.57	75.35	1.20	23.29	38.45	0.00	11.87	16.69	6.17	0.98	2.14
16	1211	3.50	51.82	1.03	18.38	6.06	9.56	11.06	2.48	0.18	100.57	0.60	75.76	1.07	20.95	38.50	0.00	13.11	20.96	3.11	0.98	1.96

Norms assume 10% of total Fe as Fe_2O_3.

*Extent of partial melting (F) is in weight percent; †Temperature (T) is in degrees Celsius; and ‡Pressure of final melting is in kilobars. All oxides and normative components are in weight percent.

pressures (P_0 = 20, 18, 16, 14, 12, 10, 8, and 6 kbar) at which upwelling mantle may cross the solidus as shown in Figure 3.9. Since we have no constraints at this stage on the depth where melting stops (P_f), I continue melting to a depth of ~2–3 kbar.

One major assumption in this model is the use of bulk D_i values derived from isobaric batch melting. This may not be directly applicable to column melting because of the progressive depletion that the source undergoes and because the compositional effects on instantaneous D_i values may differ from those in isobaric batch melting. To partly ameliorate this effect, I obtained a new set of empirical coefficients for (3.6), given in Table 3.5. They were derived from Table 3.4 by a very laborious iterative process of optimization of the "analytical" sums of oxides for each incremental melt along each of the eight adiabatic melting paths (a total of 155 incremental melts were considered) without affecting the compositions of the initial 5% isobaric batch melts.

Another potential problem is that I assume that each melt parcel follows the adiabatic melting paths shown in Figure 3.9. The slope of this adiabat and its temperature are not precisely known, but can have an important effect on the amount of melt produced. Also, because of the compositional changes that occur in the solid during melting, it is unlikely that the model adiabat (which should be curved) will be followed strictly. Whether polybaric column melting takes place in equilibrium with a small amount of interstitial liquid (continuous melting as defined by *Langmuir et al.* [1977]) or not (i.e., fractional melting), the continual depletion of the solid will affect its melting path. It is possible, for example, that melting to produce MORB occurs very close to the solidus throughout the melting interval. This effect is probably very important in determining the pressure at which melting ceases (discussed later) and underscores the importance of obtaining more experimental data, especially at small degrees of melting for a variety of depleted peridotite compositions. Note that my physical model for column melting is highly generalized and does not explicitly consider the geometry of the melting region, melt migration path, and a

variety of other issues. This is deliberate, as geometric parameters and melt distribution are poorly known, however, more specific physical models are available (e.g. Plank and Langmuir, 1992).

With these uncertainties in mind, and with (3.5)–(3.7), and the coefficients from Tables 1 and 5, I calculate the pooled or accumulated column melts. These are shown in Table 3.6 and presented graphically in Figure 3.10. These simulated melts are derived from MPY-90, and, as before, each oxide component is calculated independently.

Accumulated polybaric column melts are different in several important ways from isobaric batch melts as can be seen by comparing Figures 3.8 and 3.10. The pressure effects on SiO_2, Al_2O_3, FeO, and MgO are larger for the accumulated melts than for batch melts. SiO_2 also increases faster with increasing F than in the batch melts. No picritic melts are produced in the range of P and F that I have investigated. FeO in the accumulated melts does not increase with F at any initial pressure (in contrast to the batch melts, in which FeO increases with F at lower pressures). CaO does not have a maximum for accumulated melts, as aggregation tends to buffer drastic change in melt composition. As expected, TiO_2, Na_2O, and K_2O in accumulated melts are higher at lower F and decrease faster than in batch melts. This is also true for Al_2O_3, but the decrease is balanced by increasing Al_2O_3 in the melts as pressure decreases along the melting paths.

The normative compositions of accumulated melts also differ greatly from the batch melts. None are quartz normative even at the lowest initial melting pressures (P_o). Very few are highly depleted in Hy or have normative Ne. Overall most accumulated melts produced at F = 10–20% and P_o = 6–20 kbar are Ol-Hy normative.

3.3.5 Application

In order to apply my calculated polybaric column melts to natural MORB melts for interpretation, I follow *Klein and Langmuir* [1987] in choosing a reference level of MgO =

8.0 wt %. I fractionated my primary melts to 8.0 wt % MgO using the low-pressure liquid lines of descent algorithm of *Weaver and Langmuir* [1990]. For natural MORBs with MgO < 8.0 wt %, I correct for fractionation as described by *Klein and Langmuir* [1987] along individual liquid lines of descent appropriate to each locality. A reference level of MgO = 8.0 wt % is reasonable, since the MgO range of my computed primary column melts is small (9–12 wt %). In most cases, fractionation involves only a small amount of olivine and plagioclase subtraction. I also assume that the mantle source of MORB is homogeneous with respect to major elements.

Implicitly, I also assume high-pressure fractionation in the mantle is a minor process for MORB genesis. Many lines of evidence suggest that MORB melts rise quickly and do not reequilibrate extensively during ascent. Several arguments can also be made for the importance of high pressure fractionation at a variety of pressures [e.g., *Elthon* et al. 1982; Kinzler and Grove, 1992], however in this study I do not find it necessary to invoke this process.

Figure 3.11 shows the accumulated melts (Table 3.6, Figure 3.10) fractionated to an MgO value of 8.0 wt %. I use the subscript 8 to denote the value of other oxides at 8.0 wt % MgO. Many of the patterns seen in Figure 3.10 are still evident for the fractionated accumulated melts, but there are also some important differences. For example, the pressure dependence of Al_2O_3 and CaO for the fractionated melts is opposite to that for unfractionated melts. This is to be expected, as in this model, higher-pressure primary melts are more MgO-rich and thus fractionate more olivine to achieve higher enrichments of CaO and Al_2O_3 than lower-pressure melts that crystallize a higher proportion of plagioclase at low pressure. For fractionated melts, the decrease of FeO with increasing F is more pronounced, and the overall concentrations of SiO_2 are higher as expected from olivine and plagioclase fractionation.

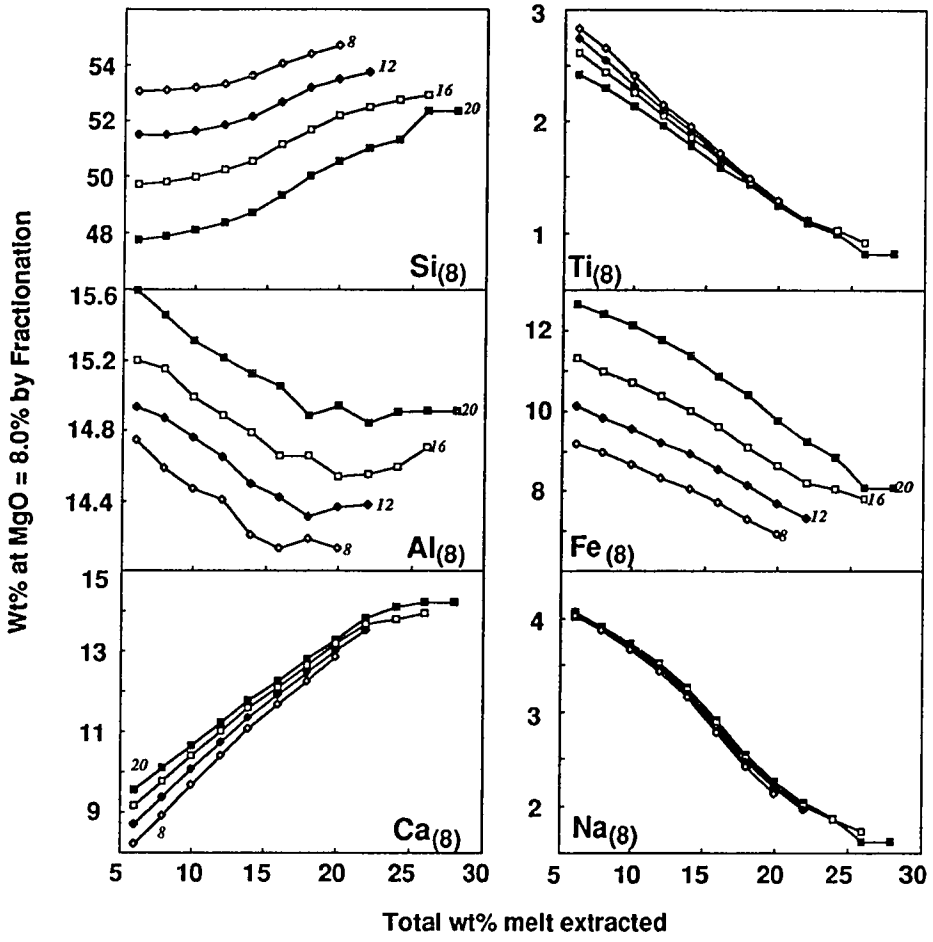

Fig. 3.11 Compositions in Table 3.6 fractionated to MgO = 8.0 wt % using low pressure liquid lines of descent program of *Weaver and Langmuir* [1990]. The abundance of each of the oxides at MgO = 8.0 wt % is shown as $Si_{(8)}$, $Ti_{(8)}$, $Al_{(8)}$, and so on. The numbers by the curves represent the initial pressures of melting (P_o = 20, 16, 12, and 8 kbar). See text for discussion.

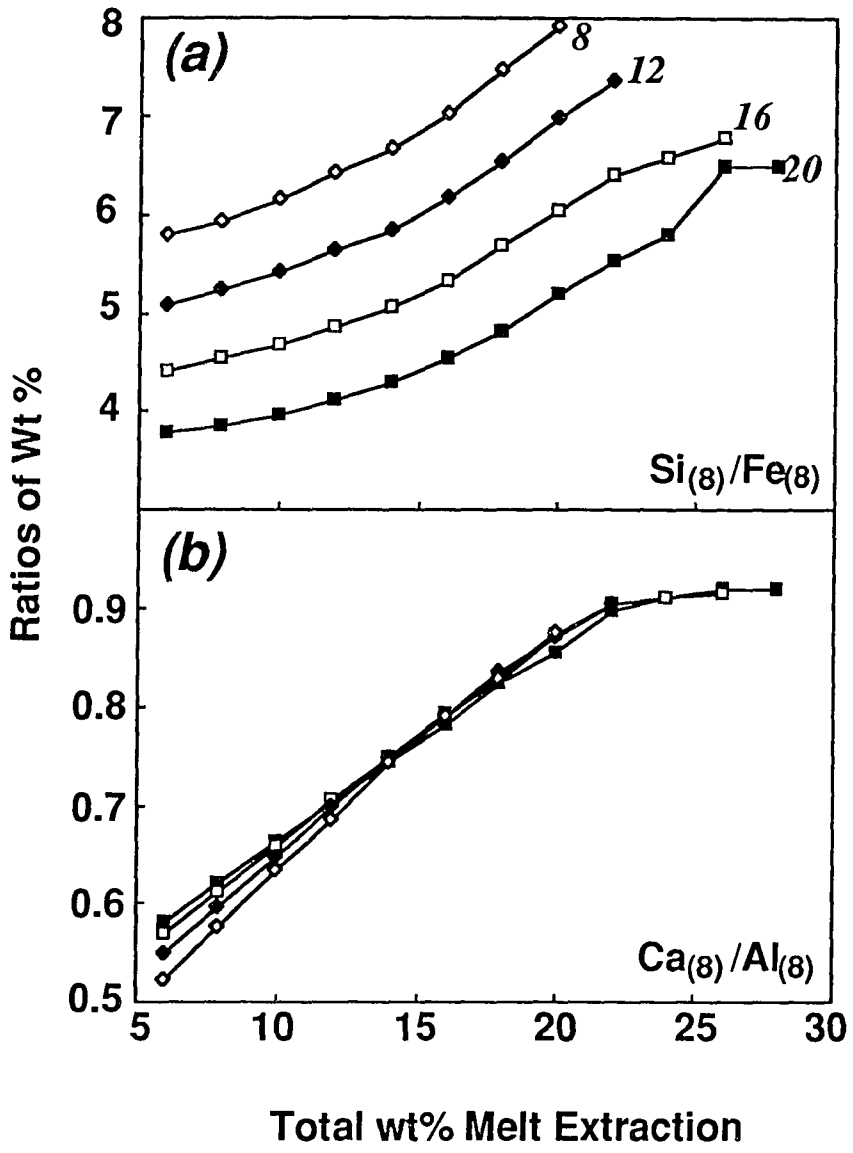

Fig. 3.12 The (*a*) $Si_{(8)}/Fe_{(8)}$ and (*b*) $Ca_{(8)}/Al_{(8)}$ ratios versus extent of partial melting. These are calculated from the results of Figure 3.11 for each P_0 (20, 16, 12, and 8 kbar as labeled). Note that $Si_{(8)}/Fe_{(8)}$ is very sensitive to pressure, and $Ca_{(8)}/Al_{(8)}$ is almost independent of pressure but strongly dependent on F. See text for discussion.

The next step toward applying my model results to natural MORBs is to find a good chemical discriminant for initial melting pressure (P_O). Figure 3.11 shows that both $Si_{(8)}$ and $Fe_{(8)}$ are sensitive to pressure, but in an opposite sense. Thus, to optimize the sensitivity, I use the ratio $Si_{(8)}/Fe_{(8)}$ as a pressure indicator. Figure 3.12*a* shows that this ratio varies rather smoothly with F and P. This allows us to quantify, for each melting path, the relationship between P_o and F. I find the expression

$$P_o(kb) = 25.98 + 0.967\ F + 45.277\ \frac{1}{F}\ - 5.186\ \frac{Si_{(8)}}{Fe_{(8)}} \qquad (3.8)$$

fits the data very well. To use (3.8), I need to determine F independently. For this I use $Na_{(8)}$ and $Ca_{(8)}/Al_{(8)}$, which, as shown in Figures 3.11 and 3.12***b***, are insensitive to pressure, but highly dependent on F [see also *Natland*, 1989]. $Ti_{(8)}$ and $K_{(8)}$ also would be good choices, but their abundances in MPY-90 are not as well constrained as Na_2O, Al_2O_3, and CaO. From the observed variation of $Na_{(8)}$ and $Ca_{(8)}/Al_{(8)}$ in fractionated accumulated column melts, I derive the expression:

$$F\ (wt\%) = 19.202 - 5.175\ Na_{(8)} + 15.537\ \frac{Ca_{(8)}}{Al_{(8)}} \qquad (3.9)$$

Figure 3.13 shows the linear inverse correlation of $Na_{(8)}$ and $Ca_{(8)}/Al_{(8)}$ for different F with superimposed natural MORB glasses with MgO = 7.8–8.2 wt % from the EPR, MAR, and Indian Ocean (W. G. Melson and T. O'Hearn, personal communication, 1989). My model indicates that these MORB melts were probably produced by 10–20 % melting, which is consistent with studies of mantle peridotite indicating that the residual mantle contains clinopyroxene [*Dick et al.*, 1984]. Finally, using (3.5) (and Figure 3.9), I can derive an expression for the final melting pressure (P_f) at which melting may cease. For this, I merely compute the amount of pressure release required to produce an amount of melt F:

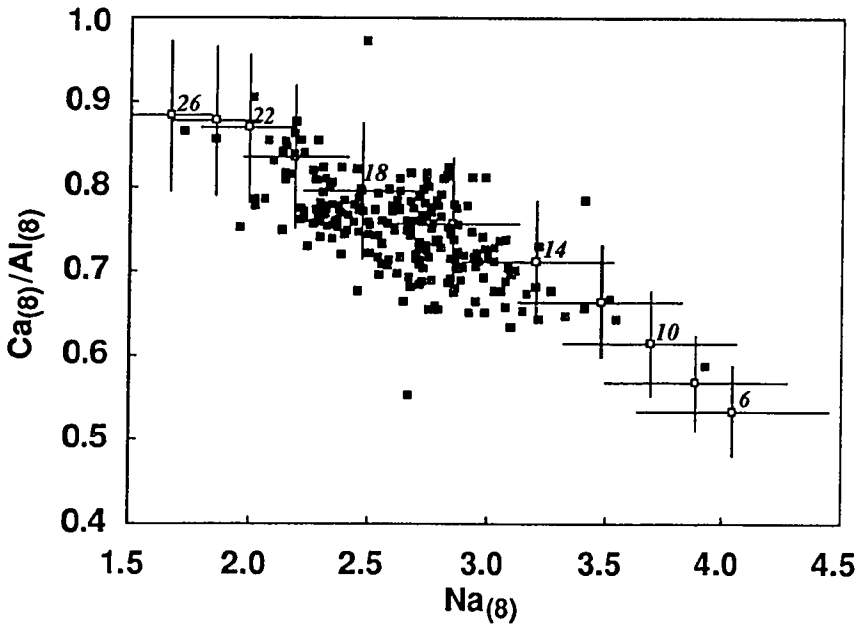

Fig. 3.13 The correlation of $Ca_{(8)}/Al_{(8)}$ with $Na_{(8)}$ for different extents of partial melting (numbered points). The error bars are derived from the main region of the mantle array analysis of *Falloon and Green* [1987] and show that mantle heterogeneity would not be expected to disturb the observed correlation. I use this correlation to determine the extent of partial melting. I also superimpose 231 natural MORB glasses with MgO = 7.8–8.2 wt % for all oceans from the Smithsonian data base [W. G. Melson and T. O'Hearn, personal communication, 1989] and the JOI Synthesis of the EPR [*Tighe*, 1988]. This indicates that most MORBs result from 10–20% partial melting.

$$P_f \text{ (kb)} = (1.3613\ P_o + 3.9103) + (-1.3458\ P_o - 13.592)/F$$
$$+ (-0.03015\ P_o - 0.2929)F \qquad (3.10)$$

Note that the (3.10) assumes adiabatic melting paths. It may not apply if melting occurs in a regime of nonadiabatic thermal gradients. In addition, given the uncertainties in the actual melting path discussed previously, the P_f values are less certain than P_o values. For the simple case of adiabatic column melting considered here, however, (3.10) is appropriate. The expressions I present for computing P_o, P_f, and F are clearly model dependent. The formal errors in these derived expressions are small (±2% for F, ±1 kbar for P_o and P_f; however, their application to natural MORBs involves several other assumptions (discussed earlier). For this reason, actual uncertainties in application of these expressions are unknown. Nevertheless, because most of the assumptions I have made are probably reasonable, in the next section I apply the model results to natural MORB compositions from three localities: a fast-spreading ridge, a slow-spreading ridge and a chain of near-EPR-axis seamounts.

3.4 Case studies

3.4.1 East Pacific Rise: 8°N to 14°N

The East Pacific Rise at 8°N to 14°N has been well studied by *Langmuir et al.* [1986] and *Batiza and Niu* [1989]. Most of the major and trace element data for this portion of the EPR are available in the Joint Oceanographic Institutes (JOI) synthesis of the EPR [*Tighe*, 1988]. I use these data (average sample spacing is < 8 km) and my model to examine patterns of P_o and F. In this analysis, I exclude a small number of samples with MgO < 5.0%, primarily from the 9°03' Overlapping Spreading Center (OSC). First I divide the EPR into seven segments [*Macdonald et al.*, 1988], even though many more chemical segments [*Langmuir et al.*, 1986] could be chosen. For each segment, I derive individual

Fig. 3.14 The East Pacific Rise (EPR) between 8° and 14°N. The bottom panel shows topography [*Macdonald et al.*, 1988] and the other panels show $Si_{(8)}/Fe_{(8)}$, $Ca_{(8)}/Al_{(8)}$, $Na_{(8)}$, and calculated (equations (3.8), (3.9), and (3.10)) initial and final melting pressures (P_o and P_f), the initial and final temperature (T_o and T_f), and the extent of partial melting (F). Note that broad along-axis dome in P_o, T_o, and F between 8°N (Siqueiros transform) and the 11°45'N OSC. Also note the edge effects at OSCs. See text for a full description of the filtering used to produce this figure and interpretations of the results.

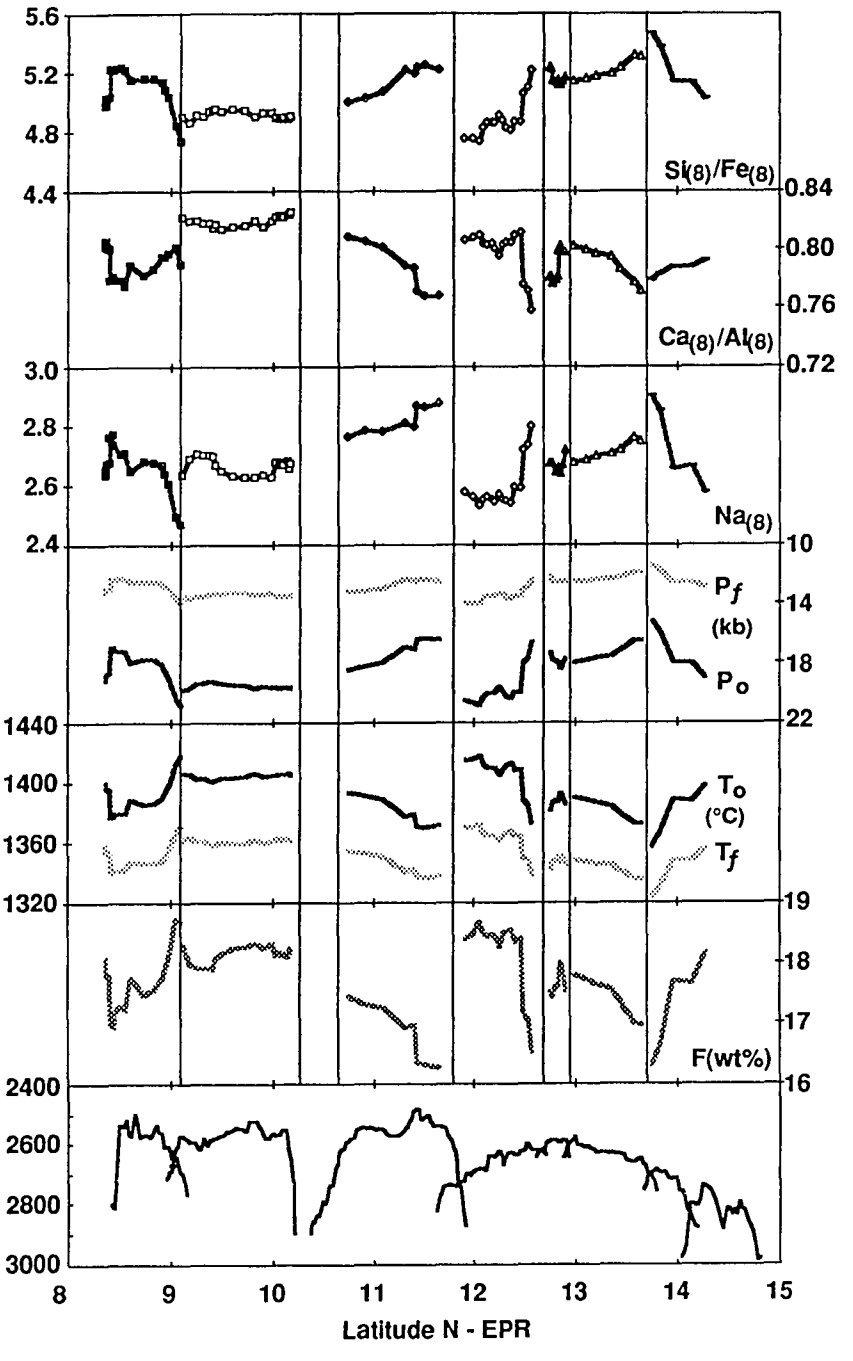
5.6
5.2
4.8
4.4
Si(8)/Fe(8)
0.84
0.80
0.76
0.72
Ca(8)/Al(8)
3.0
2.8
2.6
2.4
Na(8)
10
14
18
22
Pf
(kb)
Po
1440
1400
1360
1320
To
(°C)
Tf
19
18
17
16
F(wt%)
2400
2600
2800
3000
8
9
10
11
12
13
14
15
Latitude N - EPR

liquid lines of descent and use these to correct for low pressure fractionation (to MgO = 8.0 wt %) within each segment. For smoothing and to remove the effects of very localized chemical changes, I apply a moving boxcar filter to the data. The boxcar has a fixed width of five continuous dredge locations, except near segment boundaries where it is three dredges wide. The boxcar advances one dredge at a time to produce a moving average. Computed values of $Si_{(8)}/Fe_{(8)}$, $Ca_{(8)}/A_{(8)}$, and $Na_{(8)}$ and calculated P_o, P_f , T_o, T_f, and F are shown in Figure 3.14 against latitude.

On the basis of my model, MORB melts in this region of the EPR were produced at various initial pressures (P_o) from 15–21 kbar (45–63 km), and extent of melting (F) varying from ~16% to 19%. Edge effects can be seen at several tectonic features, but not all. The Clipperton transform is a notable exception, in agreement with *Klein et al.* [1987]. The edge effects are not consistent; for example, at the 9°03'N OSC, P_o increases toward the OSC, but at the 12°37'N and 13°43'N OSCs and the southern limb of the 11°45'N OSC, P_o decreases toward the OSC. In terms of mantle temperature [*Klein and Langmuir*, 1987; *McKenzie*, 1984], OSCs appear to be mostly underlain by relatively cool mantle, but the 9°30'N OSC is an exception. Some OSCs, such as the one at 12°54'N, show little edge effect in any melting parameter. Overall, there is only a poor correlation between large offsets (transforms and OSCs) and the melting parameters; though some edge effects are present, their magnitude and nature are inconsistent from place to place. This agrees with the findings of *Langmuir et al.* [1986].

Between the Siqueiros and the 11°45'N OSC, there seems to be a broad domal pattern in mantle temperature (T_o) with a broad high-temperature region between 9° and 10°N. This broad thermal dome extends across the Clipperton transform without apparent disruption. In contrast, the region from 11°45' to the Orozco transform, which comprises a broad along-axis topographic dome, shows a complex pattern of mantle temperature. If anything, this pattern indicates a low-temperature region at the apex of the dome, rather

than a high-temperature region as might be expected. This perplexing pattern of mantle temperature and the general question of how it might be related to mantle flow are discussed later.

3.4.2 The Mid-Atlantic Ridge at 26°S

The petrology and chemistry of the mid-Atlantic ridge (MAR) at 26°S have been discussed by *Batiza et al.* [1988] and *Castillo and Batiza* [1989]. The morphology and geophysical characteristics of the MAR segment are discussed by *Blackman and Forsyth* [1991] and *Grindlay et al.* [1991]. Figure 3.15 shows the raw data, corrected for fractionation to a MgO value of 8.0 wt %, plotted against latitude. Though scattered, there are some general patterns of correlation between topography and major element chemistry. After filtering, as with the EPR data, and plotted against depth, these patterns are evident (Figure 3.16). Using my melting model, I can interpret these patterns in terms of the melting parameters as in Figure 3.17.

In contrast with the EPR (Figure 3.14), there is a good correlation between axial depth and melting parameters such as P_0, T_0, and F. My model suggests that these MORB melts have a relatively narrow range of P_0 (14–16 kbar or 42–48 km) and F (16–18% melting). Approaching the offsets that bound the segment, the extent of melting decreases, and the depth of melting increases. I discuss the possible implications of this pattern later.

Figures 3.18 and 3.19 show that MORB from the MAR at 26°S show a positive correlation of $Na_{(8)}$ and $Fe_{(8)}$, but an inverse correlation of $Na_{(8)}$ and $Si_{(8)}$. Using the terminology of *Klein and Langmuir* [1989], the MAR at 26°S exhibits the local trend. In contrast, the EPR (8°N – 14°N) displays the global trend even within each segment. This is clearly shown in Figure 3.20, where I use $Ca_{(8)}/Al_{(8)}$ and $Si_{(8)}/Fe_{(8)}$ as proxies for F and P_0, respectively. In this diagram, as in the work of *Klein and Langmuir* [1987, 1989], the global trend is characterized by an association of increasing depth of melting with more

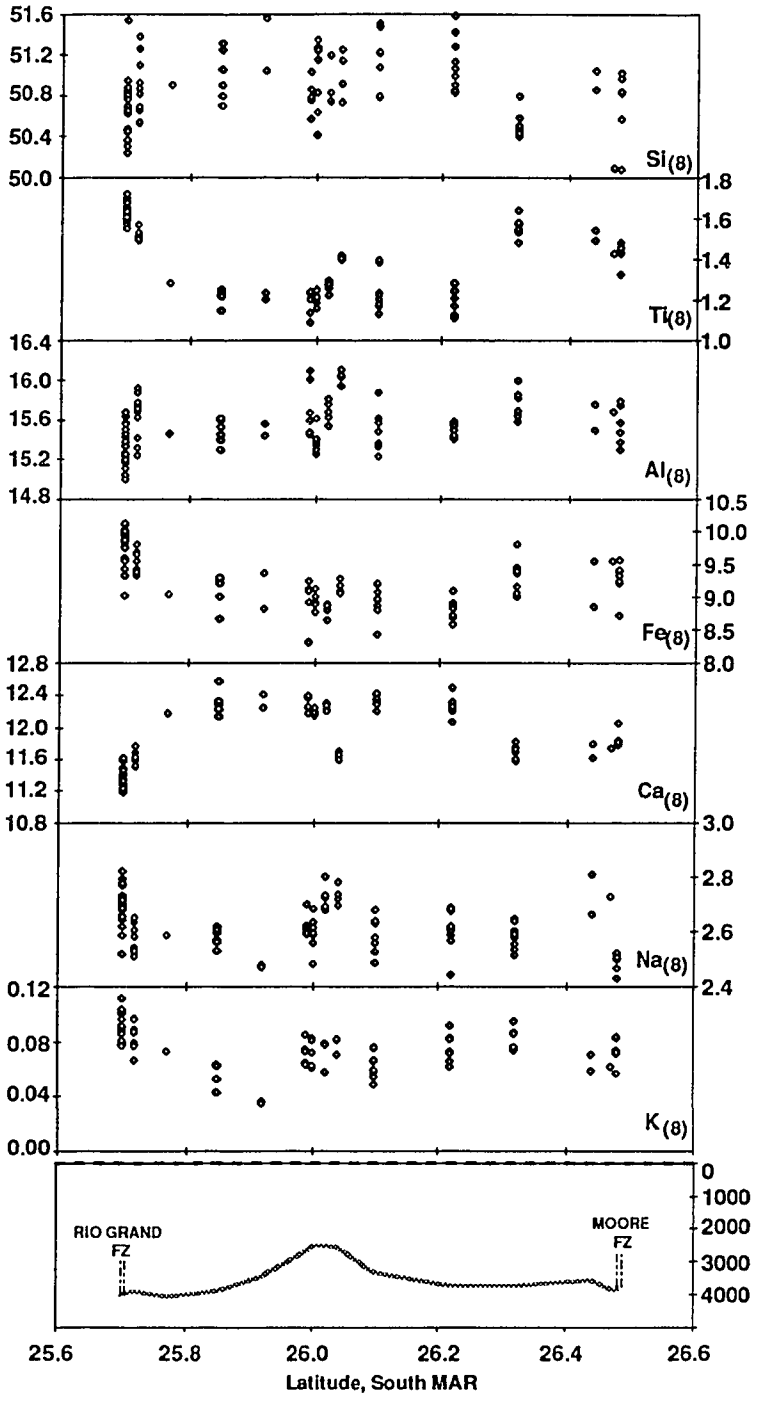

Fig. 3.15 The mid-Atlantic ridge (MAR) at 26°S from *Batiza et al.* [1988]. The raw data have been corrected for shallow fractionation to MgO = 8.0 wt %. Topography (based on dredging depths) is shown at the bottom.

Fig. 3.16 Filtered data for the MAR at 26°S plotted against axial depth (horizontal axis). Solid circles are points north of the along-axis high, and open circles are points south of the high. Note that most corrected oxide abundances vary with axial depth, particularly for the deep portions of the segment. These results show that extent of partial melting inferred from $Ca_{(8)}/Al_{(8)}$, $K_{(8)}$ and $Ti_{(8)}$ is progressively lower near the offsets (deep portions of the segment). $Na_{(8)}$ does not show a simple pattern, implying that mantle heterogeneity may play some role in this case. $Si_{(8)}$ and $Si_{(8)}/Fe_{(8)}$ indicate that melts near the offsets are produced at greater depths. See text for full discussion.

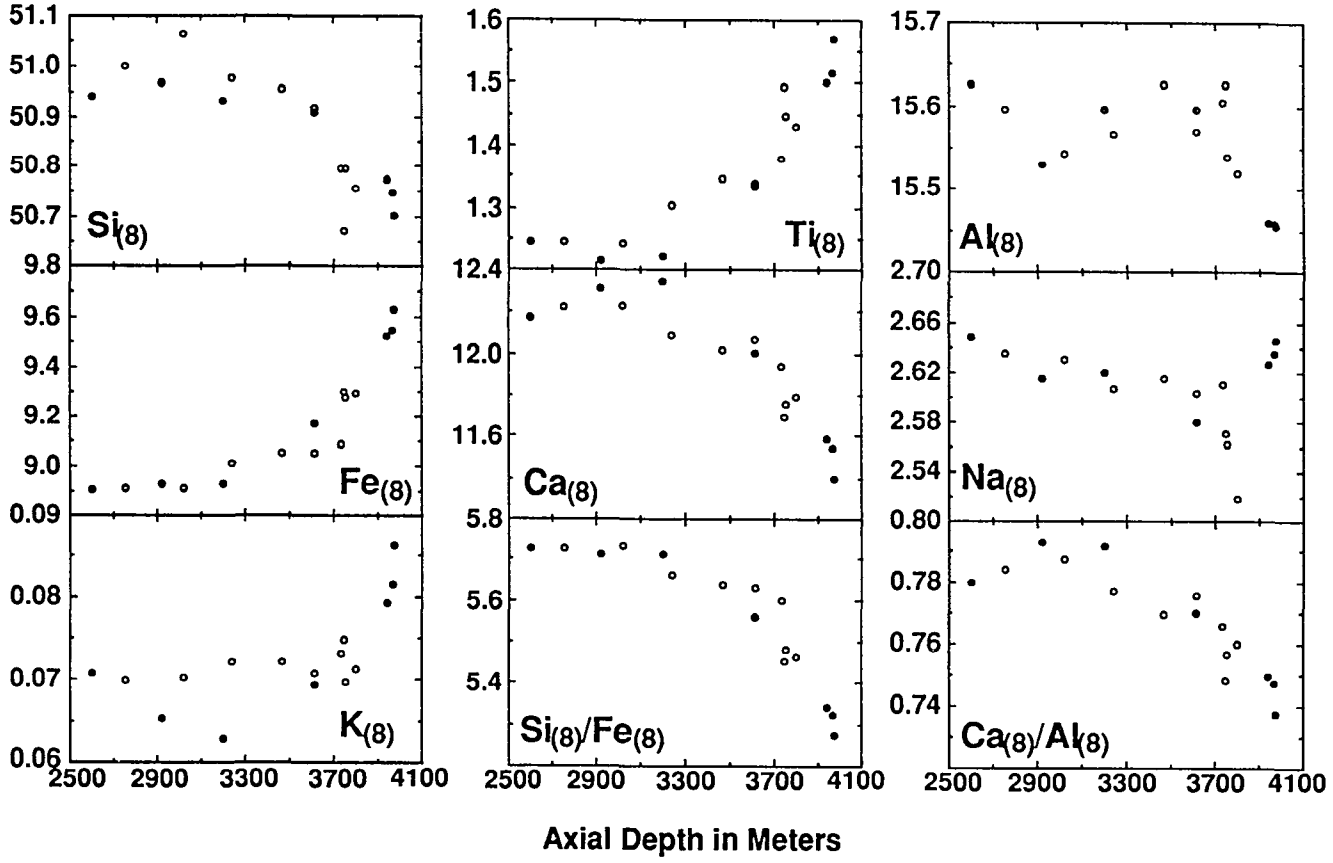
51.1
51.0
50.9
50.8
50.7
Si(8)
9.8
9.6
9.4
9.2
9.0
Fe(8)
0.09
0.08
0.07
K(8)
0.06
2500 2900 3300 3700 4100
1.6
1.5
1.4
1.3
Ti(8)
12.4
12.0
11.6
Ca(8)
5.8
5.6
5.4
Si(8)/Fe(8)
2500 2900 3300 3700 4100
15.7
15.6
15.5
Al(8)
2.70
2.66
2.62
2.58
2.54
Na(8)
0.80
0.78
0.76
0.74
Ca(8)/Al(8)
2500 2900 3300 3700 4100
Axial Depth in Meters

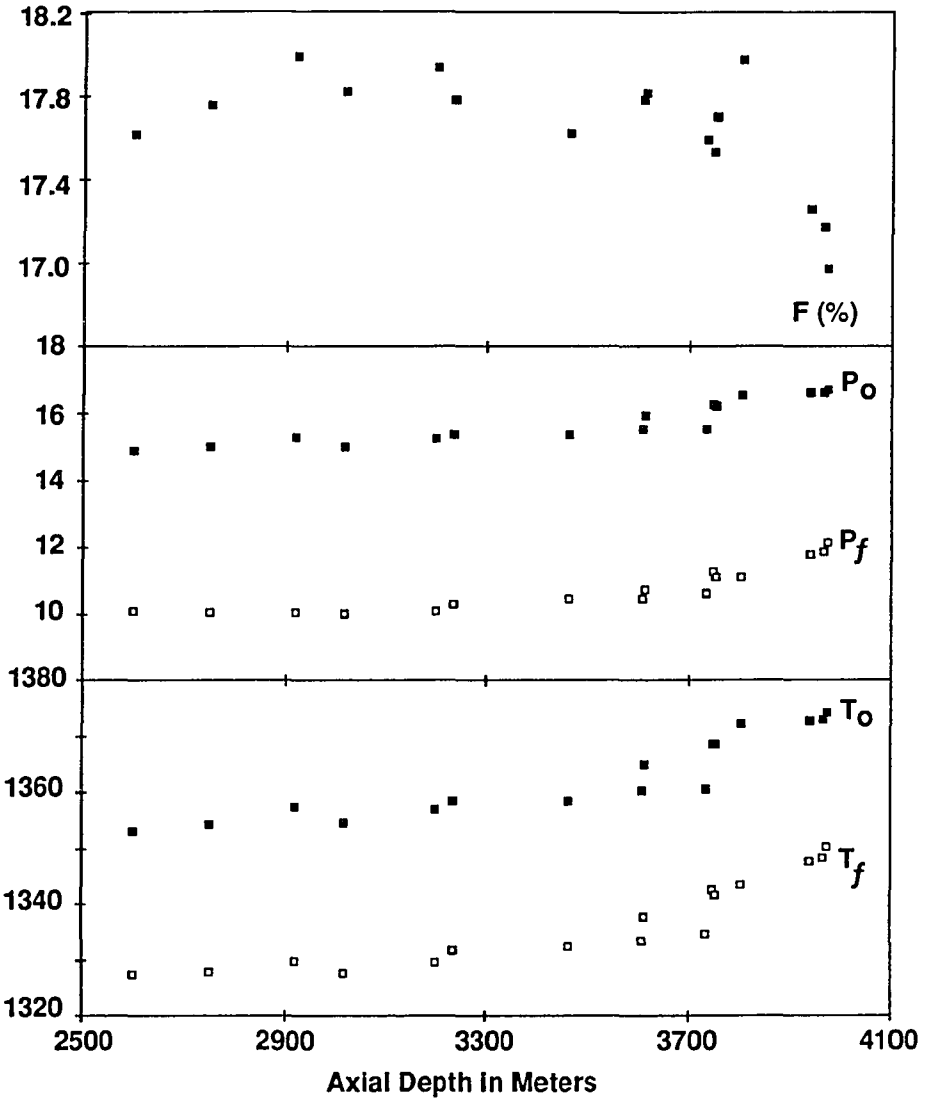

Fig. 3.17 Calculated extent of partial melting (F) and other physical parameters for the MAR at 26°S plotted against the axial depth. See text for discussion.

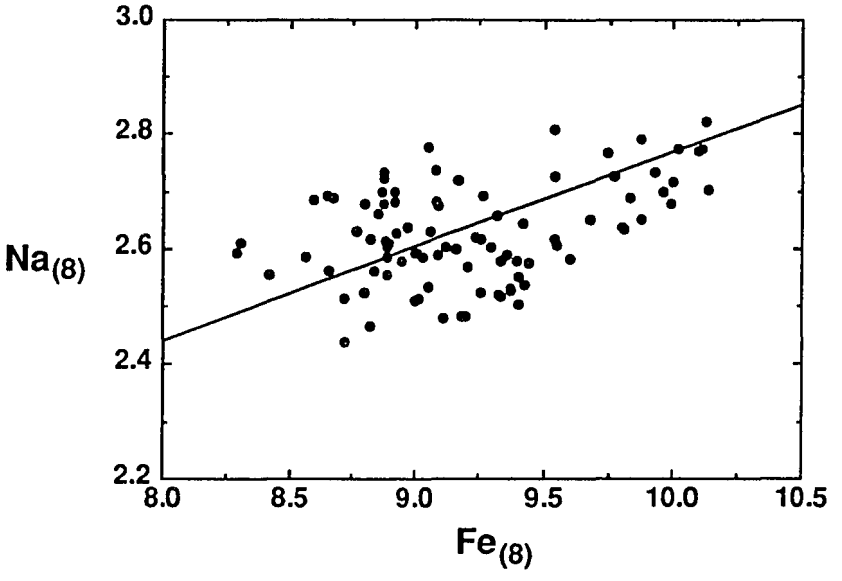

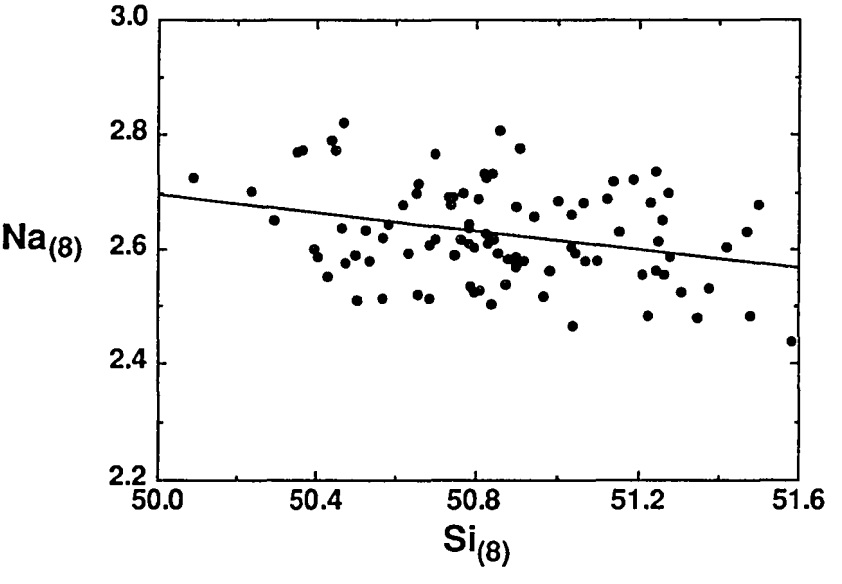

Fig. 3.18 $Na_{(8)}$ versus. $Fe_{(8)}$ and $Na_{(8)}$ versus $Si_{(8)}$ for MORB from the MAR at 26°S. These correlations represent the local trend of *Klein and Langmuir* [1989].

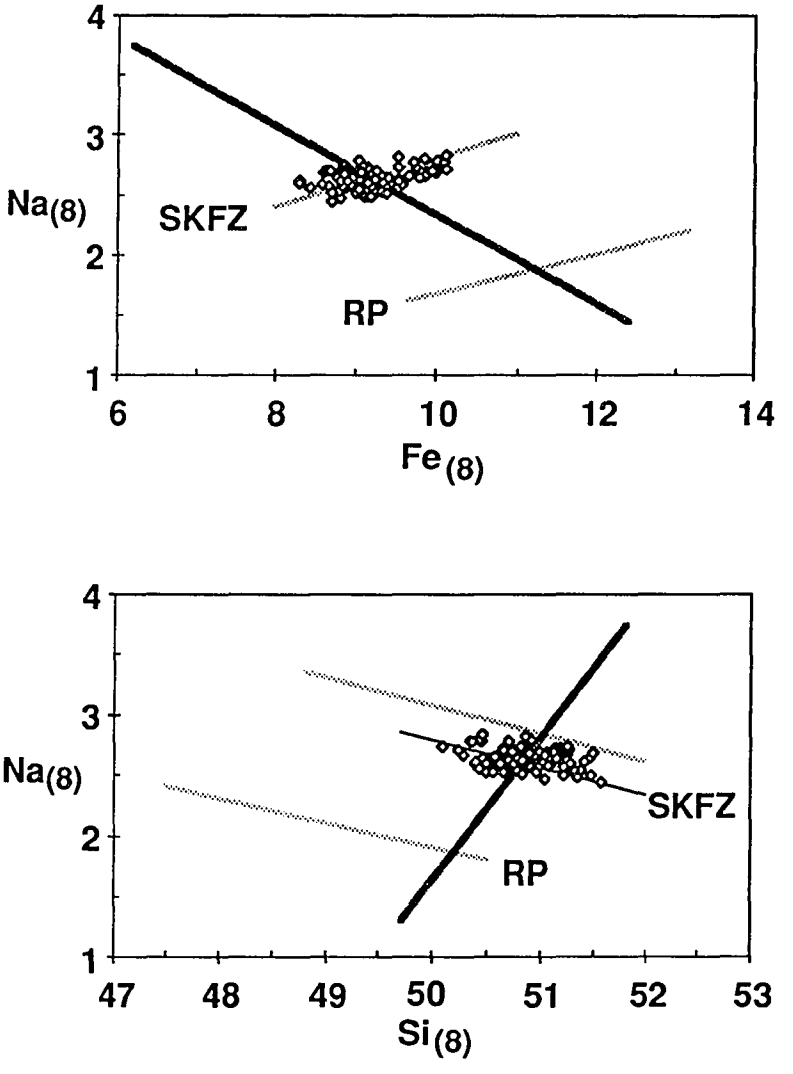

Fig. 3.19 Same as Figure 3.18 with the global trend shown as a bold line. The local trend (Reykjanes Peninsula, RP; MAR at South of Kane fracture zone, SKFZ; and MAR at 26°S, open diamonds) crosses the global trend at a high angle.

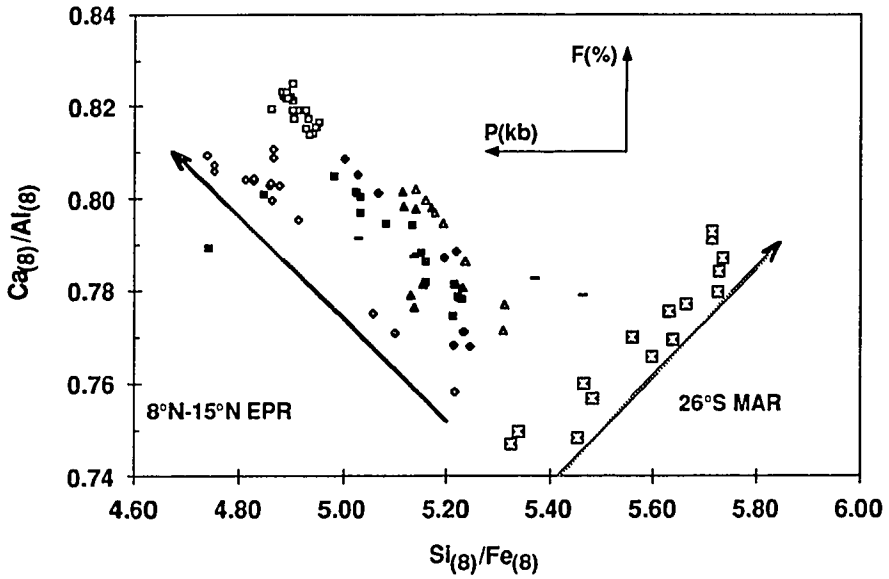

Fig. 3.20 A more sensitive plot distinguishing the global trend and local trend: $Ca_{(8)}/Al_{(8)}$ versus. $Si_{(8)}/Fe_{(8)}$ diagram, using my data for the MAR at 26°S (local trend) and the seven EPR segments (8°–14°N) (global trend). Note the opposite correlations of the extent of partial melting with the melting pressure for the two trends. Also note that the global trend applies to the entire length of EPR I studied as well as to individual segments (denoted by different symbols), and that no local trend is seen at the EPR.

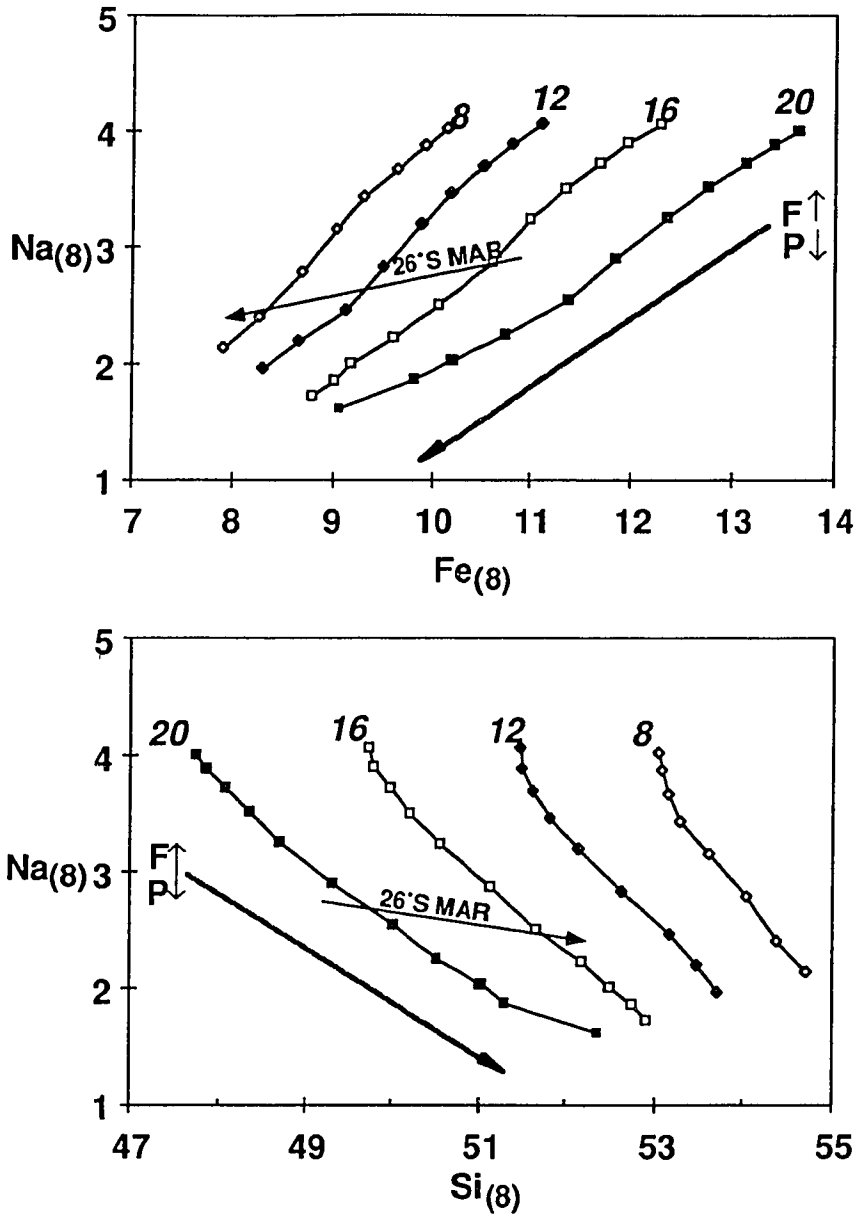

Fig. 3.21 As in Figure 3.18, calculated intra-column (at specified P_0 values) melts generated by initial melting at four pressures (20, 16, 12, and 8 kbar). Also shown is the local trend for the MAR at 26°S. Note that the local trend and the intra-column melt variations are not parallel; thus intra-column melting alone cannot explain the local trend.

extensive melting. The local trend, in contrast, is characterized by decreasing depth of melting associated with more extensive melting. Using my decompression-induced column-melting model, I can explicitly calculate the slope of the intra-column trend because this trend simply corresponds to the progressive melting of a mantle parcel undergoing column melting initiated at a single depth (P_o). In Figure 3.21, I show the calculated column melting variations for the melting paths of P_o = 8, 12, 16, and 20 kbar on $Na_{(8)}$ and $Fe_{(8)}$ and on $Na_{(8)}$ and $Si_{(8)}$ diagrams. While the slopes of the intra-column melting paths are similar in sign to the data from the MAR at 26°S (shown superimposed on Figure 3.21), the actual slopes differ significantly from each other. I discuss possible interpretations of this difference later.

3.4.3 Near-EPR-axis seamounts: Lamont seamount chain

Batiza et al.[1990] and *Niu and Batiza* [1989] recently showed that young (<1 Ma) seamount chains near the EPR, like the nearby EPR axis, are comprised mostly of zero-age MORB melts. However, near-axis seamounts MORB show systematic chemical differences with EPR axial MORB. As a group, lavas from near-axis seamount chains parallel to absolute plate motion have lower $Fe_{(8)}$ and higher $Na_{(8)}$ than axial basalts. In order to determine whether these changes occur progressively away from the EPR axis along a single seamount chain, I examine a well-studied absolute motion parallel seamount chain. The best studied of these is the Lamont seamount chain [*Fornari et al.*, 1988*a*, *b*; *Allan et al.*, 1989; *Smith and Batiza*, 1989; *Barone and Ryan*, 1990].

Figure 3.22 shows the chemical variation patterns observed away from the EPR axis along the Lamont seamount chain. Despite some obvious scatter, the patterns are regular and systematic. With my column-melting model, I calculate the melting parameters shown in Figure 3.23. These patterns suggest a gradual pinching out of the melt zone at 35–55 km off axis. P_o, P_f, and F are relatively constant off axis out to about 30 km, but at

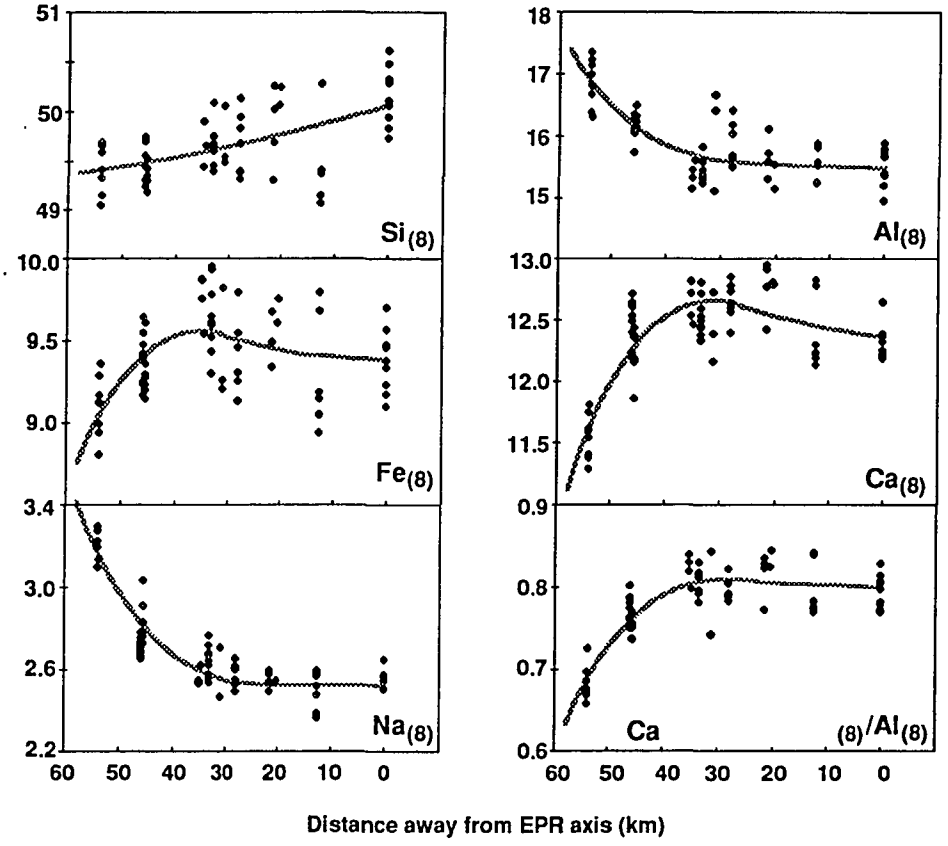

Fig. 3.22 Chemistry of the Lamont seamount and EPR plotted against distance (kilometers) from EPR axis. Shown are samples with MgO > 8.0 wt % from *Allan et al.* [1989] plus some of my RAITT 02 data. Heavy lines are calculated model compositions discussed in the text.

greater distances, P_0 shallows, and F decreases. This pattern of shallow, less extensive melting is similar to that observed at many OSCs along axis (see Figure 3.14) and is opposite to the edge effect at 26°S MAR where decreases in F are accompanied by deeper melting. The axial and off-axis melting region under the Lamont seamount chain is shown diagrammatically in Figure 3.24.

The Lamont seamount chain is highly depleted in very incompatible elements. For example, $(La/Sm)_N$ in the seamount lavas is systematically lower than at the EPR axis [*Allan et al.*, 1989]. This systematic depletion is interesting because it is opposite to what would be expected for an enriched plume or hot spot that might explain the absolute plate motion orientation of the chain. One possible explanation of the systematic depletion in incompatible elements is that it represents progressive depletion of a source due to continuous melting as upwelling mantle turns to move laterally away from the EPR axis. However, the signature of progressive melting should also appear in the major element melt compositions, but it does not. Another possibility is that the trace element signatures are affected by lateral melt migration toward the EPR axis, as envisioned by *Phipps Morgan* [1987]. In this scenario, the Lamont seamount melts would not strictly represent pooled or accumulated column melts. Instead, they would be pooled melts without the first few percent of melt which might be removed by lateral melt migration.

To test the hypothesis, I calculate the trace element abundances for melts generated by continuous melting. I used equations rederived from *Maaløe* [1982] for critical melting and varied the fraction of interstitial melt (w_0) present during continuous melting. I found that accumulated melt compositions produced in this manner do not correspond to those observed at the Lamont seamounts. However, I can produce very depleted melts as instantaneous melts (versus accumulated melts) produced by continuous column melting. Figure 3.25*a* shows the results of several calculations. The EPR axial melts are produced by high degrees of partial melting and melt pooling. The more depleted seamount melts are

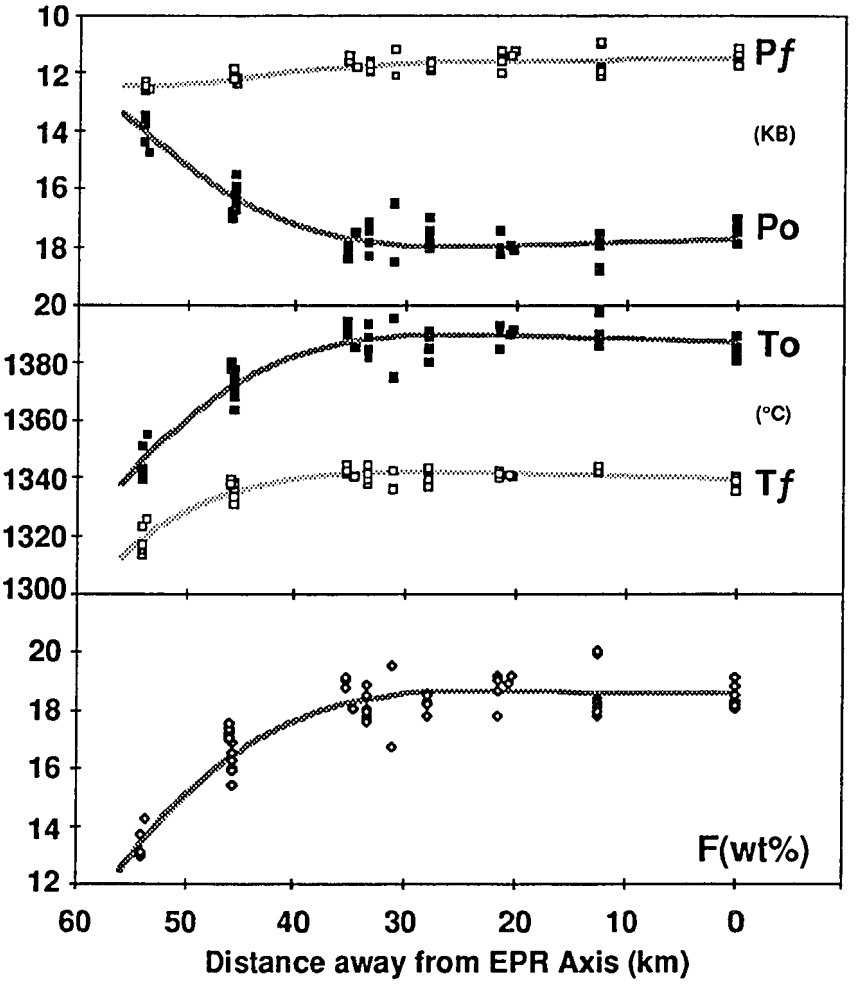

Fig. 3.23 Calculated column-melting parameters for the Lamont seamounts. Shown are extent of partial melting (F) and initial and final melting pressures and temperatures (P_o, P_f, T_o, T_f). Note that the melt zone pinches out away from the axis.

Fig. 3.24 Diagrammatic presentation of the results in Figure 3.23 showing the inferred region of melting in the vicinity of the EPR. RT60 is a lava field west of the NEW/DTD seamounts.

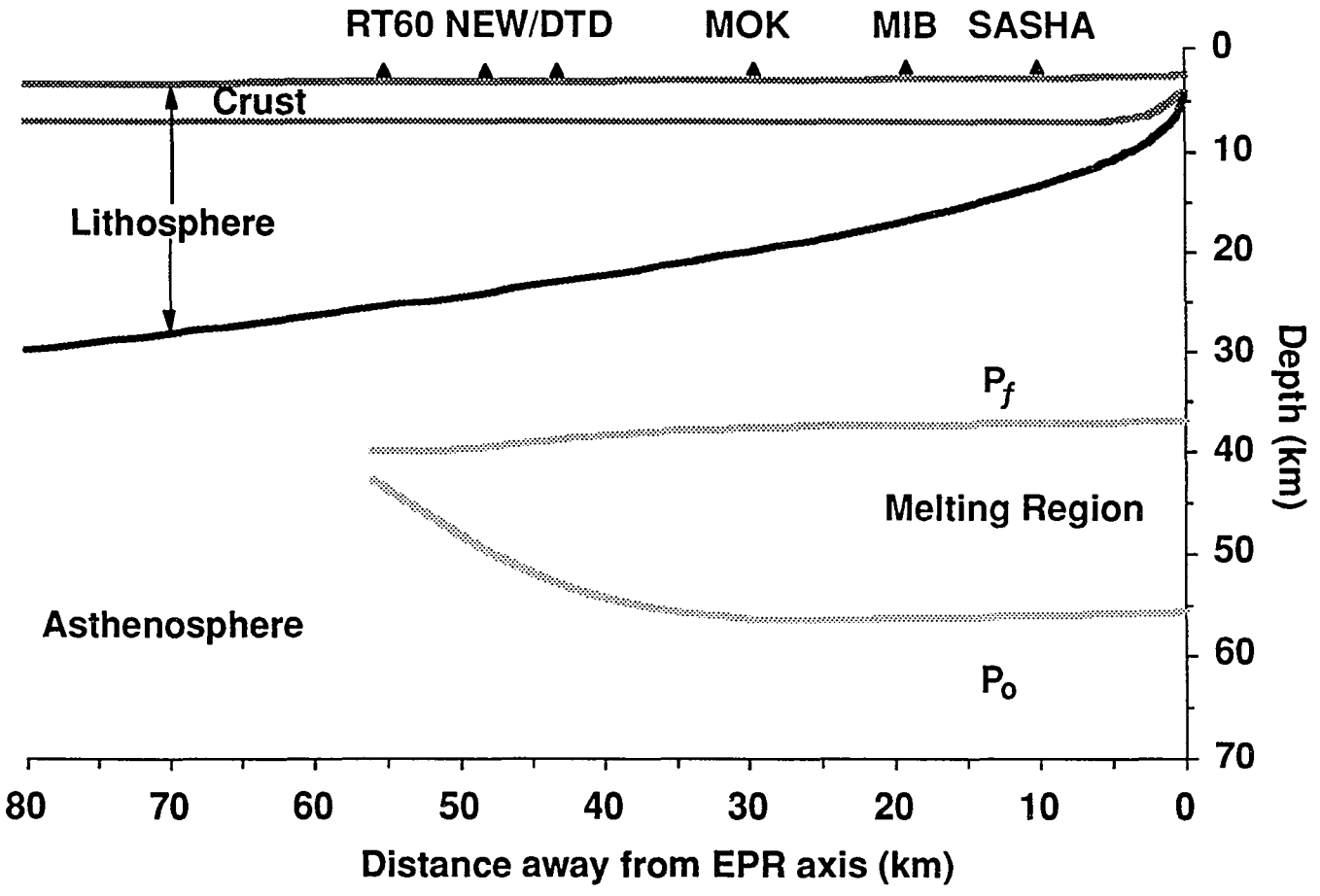
RT60 NEW/DTD
MOK
MIB
SASHA
Crust
Lithosphere
P_f
Melting Region
Asthenosphere
P_o
0
10
20
30
40
50
60
70
Depth (km)
80
70
60
50
40
30
20
10
0
Distance away from EPR axis (km)

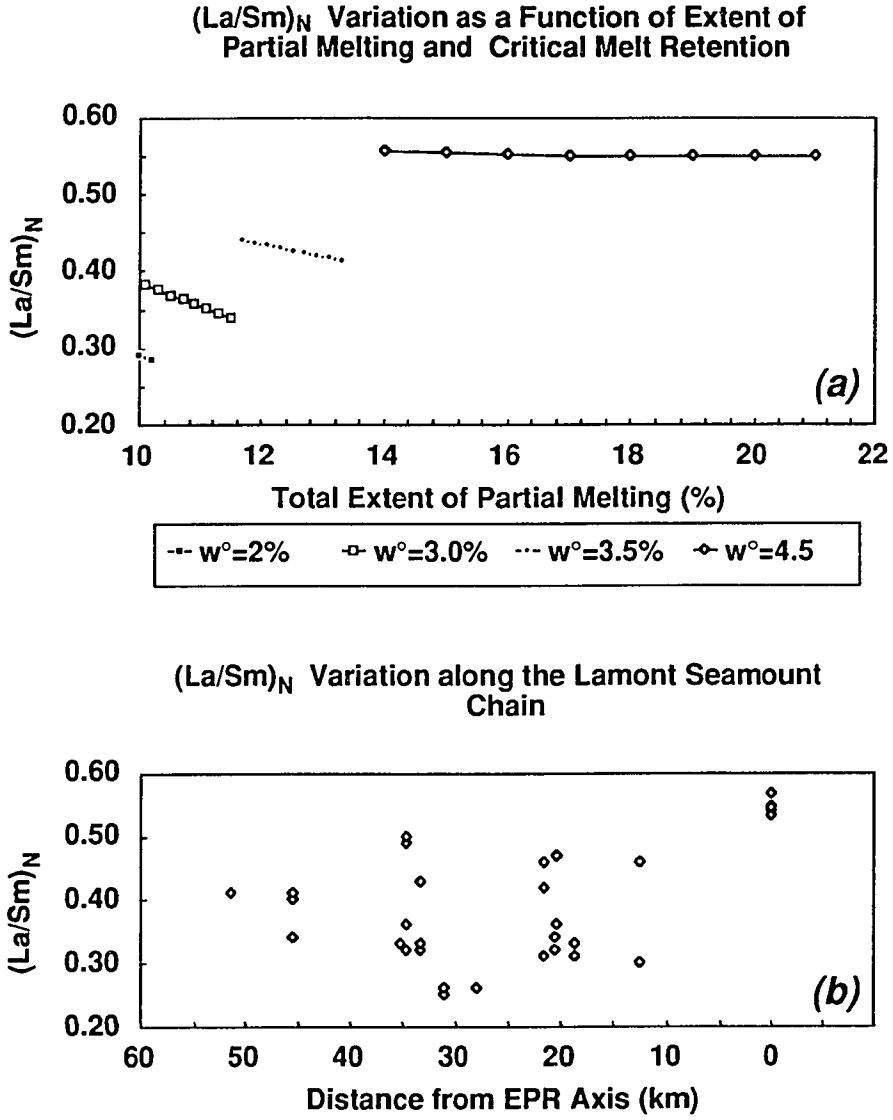

Fig. 3.25 (*a*) Continuous melting model calculations for very depleted melts of the Lamont seamount chain and the EPR. Melts with $(La/Sm)_N = 0.55$ are pooled melts (axis), whereas more depleted melts are instantaneous melts produced by column melting with various melt porosities (w_o). (*b*) The $(La/Sm)_N$ for the Lamont seamounts do not show a simple off-axis trend. See text for discussion.

produced as instantaneous melts from a source similar to that of the EPR ($(La/Sm)_N$ = 0.55) at smaller extent of melting and smaller w_0 with the first few percent of melts lacking (melt migration ?).

The good fit of the Lamont trace element data to instantaneous melts may indicate that the Lamont seamounts tap instantaneous melts rather than pooled melts. This is consistent with the hypothesis that the seamount melts are primarily supplied by dikes which tap small amounts of melt. This is also consistent with lateral melt migration which would hinder efficient pooling of melts produced in a rising vertical column. On the other hand, the major elements can be successfully modeled as pooled melts and less well modeled as instantaneous melts. Thus I infer that lateral melt migration toward the axis may play some role, but the magnitude is probably small. Furthermore, if lateral melt migration is the explanation, the pattern of this migration is not simple. A simple pattern of melt migration and tapping of instantaneous melts would result in a regular pattern of $(La/Sm)_N$ decrease away from the axis. Figure 3.25*b* shows that such a pattern is not observed. The geographic scatter of $(La/Sm)_N$ could result either from a complex pattern of lateral melt migration and tapping or from that fact that all seamount lavas are not of truly zero age [*Barone and Ryan*, 1990]. On the basis of the calculations illustrated in Figure 3.25*a*, I speculate that lateral melt migration toward the EPR has played a role in producing the trace element depletion of the Lamont lavas. I note, however, that other explanations such as small-scale mantle heterogeneity [*Fornari et al.*, 1988*b*] or complex segregation/mixing scenarios [*Langmuir et al.*, 1977] cannot presently be ruled out.

3.5 Discussion

In this section, I discuss the results of my model and some of the possible implications for subaxial magmatic processes that arise from applying the model to fast ridges (EPR), slow ridges (MAR), and near-EPR seamount chains.

3.5.1 Nature of primary magma

The debate over the nature of primary magma parental to MORBs has been active for over 20 years [*O'Hara*, 1968; *Green et al.*, 1979; *Stolper*, 1980; *Jaques and Green*, 1980; *Elthon and Scarfe*, 1984; *Falloon and Green*, 1987, 1988; *Presnall and Hoover*, 1984; *Fujii and Scarfe*, 1985; *Fujii and Bougault*, 1983] and is largely based on the interpretations of isobaric batch melts produced in the laboratory and on the use of simplified phase diagrams. As discussed by *Klein and Langmuir* [1987], if MORB is produced by polybaric column melting, not by isobaric batch melting, then the conflicting views may be reconciled. In Figure 3.26, I plot out model melts (both isobaric batch melts and polybaric column melts for comparison) on the Ol-Cpx-Qtz normative projection of *Walker et al.* [1979]. Also shown are pseudoinvariant points from *Stolper* [1980]. Figure 3.26*b* shows that for polybaric column melts, the initial melting pressure (P_o) as well as the extent of melting (F) controls the position of a melt composition in this projection.

In Figure 3.27, I plot natural MORB melts with MgO > 8.5 wt % and also my polybaric column melt compositions fractionated to 8.0 wt % MgO. The good agreement between high-MgO natural MORB and my calculated melts provides additional support for the notion that most MORBs are not primary melts. However, my primary melts have only 10–12 wt % MgO and are not picritic. My model suggests that most MORBs are generated by initial melting at 12–21 kbar and 10–20 % melting. The melts with 8.0 wt % MgO can be derived from these primary melts by variable amounts of olivine and plagioclase fractionation at lower-pressure. I thus concur with the view that many MORB melts with 10–12 wt % MgO are primary [*Bryan et al.*, 1981]. The global correlation by *Klein and Langmuir* [1987] strongly supports the idea that mantle temperature and column-melting processes control the composition of MORB melts. As shown by many previous studies, shallow fractionation is also an important process for most observed MORB compositions. Clinopyroxene-dominated fractionation at high pressure apparently plays a minor role,

Fig. 3.26 Normative projections (Cpx-Ol-Qtz from Plagioclase) of calculated partial melts produced by (***a***) isobaric batch melting, and by (***b***) polybaric column melting. The projection algorithms are taken from *Walker et al.* [1979]. High-pressure phase boundaries are from *Stolper* [1980]. In Figure 3.26***b***, the isobaric melting pressures are 20, 16, 12, and 8 kbar as labeled with extent of partial melting from 10% to 40% in the directions shown by the arrow. Except for high F (Qtz-rich) melts, all the melts should be in equilibrium with three phases (Ol-Opx-Cpx). ***b***). the compositions of accumulated polybaric column melts at the initial melting pressures P_0 = 20, 16, 12, and 8 kbars (as labeled) are shown with the arrow indicating decompression and the increasing melt extraction (1% step). Projected melt compositions are from 10% to 26%, 24%, 22%, and 20% for the initial pressures respectively. Data are from Table 3.6 and Figure 3.10.

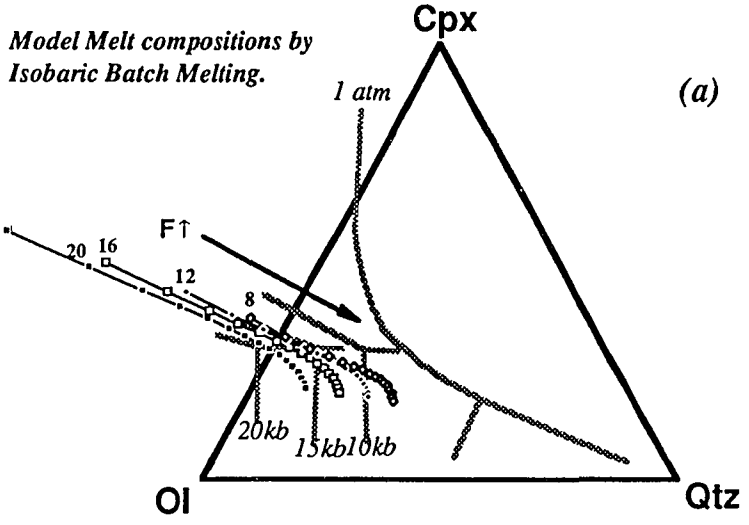
Model Melt compositions by
Isobaric Batch Melting.
Cpx
1 atm
(a)
F↑
20
16
12
8
20kb
15kb
10kb
Ol
Qtz

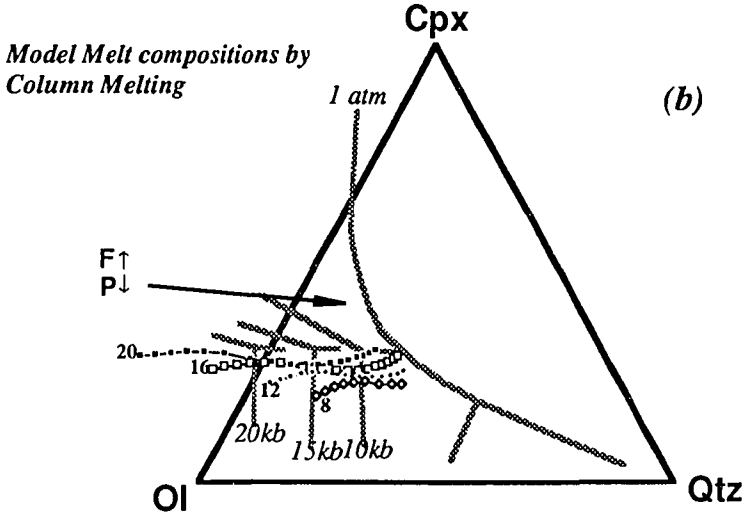
Model Melt compositions by
Column Melting
Cpx
1 atm
(b)
F↑
P↓
20
16
12
8
20kb
15kb
10kb
Ol
Qtz

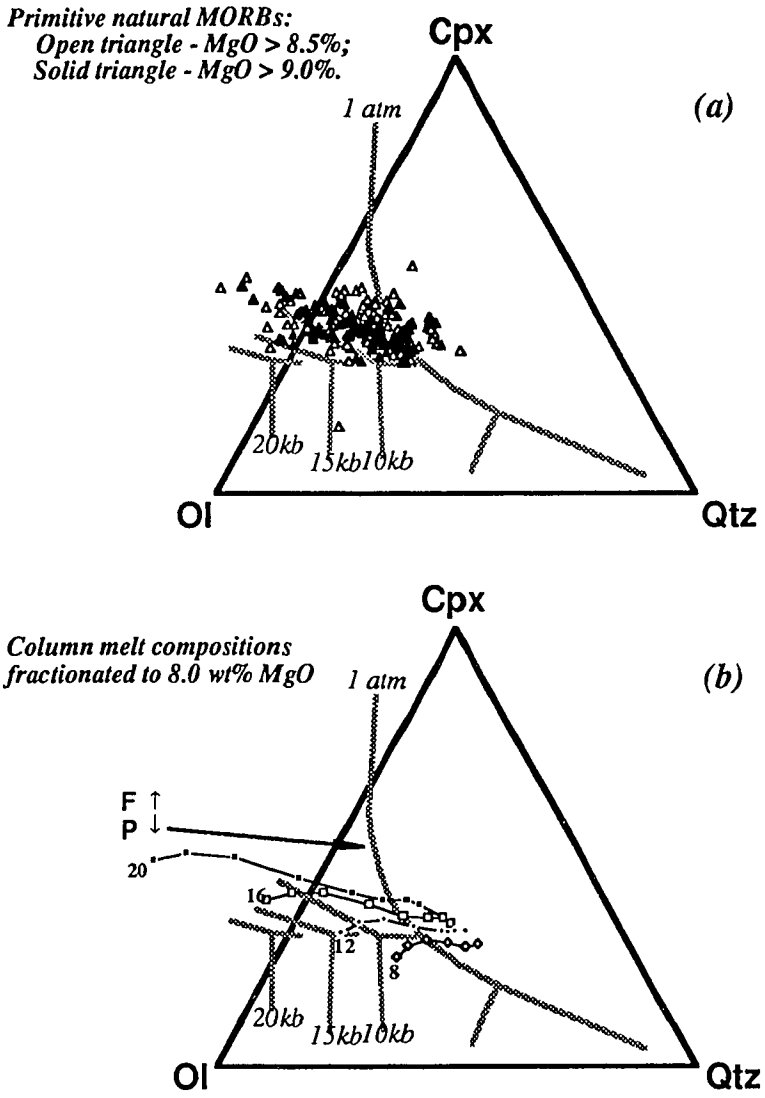

Fig. 3.27 As in Figure 3.26: (*a*) primitive MORBs with MgO > 8.5% (open triangles) and MgO >9.0% (solid triangles) from the EPR, MAR and mid-Indian ridges from the Smithsonian data base [W. G. Melson and T. O'Hearn, personal communication, 1989]; and (*b*) the fractionated compositions in Figure 3.26*b* with 2% steps for each of melting paths (P_O = 20, 16, 12, and 8 kbar as labeled). This comparison shows that the majority of observed MORBs are fractionated at low pressure from the melts accumulated during column-melting process with initial melting pressures ranging from 12 to 21 kbar and with the total melt production ranging from 10 to 20 wt %.

since this would tend to deplete SiO_2 in liquids and would lead to different fractionation patterns than those shown in Figure 3.27*b*.

3.5.2 Mantle temperature distribution and upwelling

The major element chemistry of MORB melts provides a very strong (via experimental studies) constraint on the temperature of the mantle. Though somewhat model dependent, this is probably the strongest direct constraint on mantle temperature available. I thus discuss the mantle temperature variation I infer from the application of my melting model to natural MORBs. While most physical models of mantle upwelling assume that the subaxial mantle has constant potential temperature (i.e., adiabatic temperature profile) and horizontal isotherms (Figure 3.28), I find strong evidence for significant lateral temperature differences (up to 60°C) occurring on a scale of 50–100 km. If these differences are real, their cause is important, because mantle temperature and upwelling in some cases are related. I discuss lateral temperature gradients observed both along axis and across axis.

3.5.2.1 Across-axis temperature variation

The across-axis temperature pattern shown by comparing axial chemistry and young (< 1 ma) near-axis seamounts indicates that the mantle is cooler away from the axis than directly below the axis. There can be little doubt that this pattern is real, as it is revealed by large groups of seamount samples [*Batiza et al.*, 1990] as well as individual seamount chains such as the Lamont seamount chain (Figure 3.23). This pattern of P_o and T_o (the solidus temperature and pressure), though perhaps not surprising, contradicts the assumption of horizontal isotherms in the mantle commonly assumed in simple physical models of sub-axial flow. One possibility is that this temperature difference is fortuitous and simply reflects thermal heterogeneity in the upper mantle. Such patterns could perhaps result from compositional heterogeneity and differences in thermal conductivity or stress

[*Yoder*, 1976]. However, because of the widespread occurrence of this phenomenon along the EPR [*Batiza et al.*, 1990], this seems highly unlikely.

Another possibility is that small scale convection [e.g., *Buck and Parmentier*, 1986; *Scott and Stevenson*, 1989; D. Scott, personal communication, 1991] might cool the mantle below the lithosphere adjacent to the axis. This cooling would allow upwelling patterns of hot mantle to cause a lateral thermal gradient as shown in Figure 3.28. A problem with this hypothesis is that for such a condition to be initiated, the residual mantle emplaced across axis by flow must cool a great deal to become denser than hot, fertile mantle near the axis [e.g., *Sotin and Parmentier*, 1989; L. Fleitout, personal communication, 1991] (also see Chapter 2). This cooling would be expected to take tens of millions of years, so small-scale convection very near (30–50 km) the axis may be difficult. Even so, it may not be possible to completely rule out this possibility. At any rate, any conductive or convective process operating below young lithosphere could produce the observed pattern.

Another possibility that can be considered is that the actual temperature gradient in the mantle below the ridges is slightly greater (cooler) than adiabatic for young lithosphere. An adiabatic profile is assumed below the cooling plate, which is the upper conductive boundary layer [*McKenzie and Bickle*, 1988]. However, even a small amount of conductive cooling in the asthenosphere directly underlying the lithospheric plate would make the geothermal gradient greater than adiabatic, as in the thermal boundary layer for old lithosphere proposed by *McKenzie and Bickle* [1988]. Such cooling near the boundary might be explained by long-term (10^7 years) physical proximity between the plate and the underlying asthenosphere. Since ridges are not fixed relative to the underlying mantle, this asthenosphere, with a weak conductive geotherm could be tapped by a ridge axis. If upward flow beneath the axis is partly driven by buoyant forces (not merely plate separation), and if this mantle upwells adiabatically, then upward mantle flow would result

in hot rising mantle material being emplaced next to cooler mantle at the edge of upwelling (Figure 3.28). The most vigorous buoyant upwelling in the core of the upwelling zone would be hottest because this material rises adiabatically from a deeper level within the zone characterized by a weak conductive (versus convective or adiabatic) thermal gradient. This effect would be expected to grade outward from the core of the upwelling toward the edges and would establish a lateral thermal gradient of the type observed. This effect probably need not be dramatic to produce a lateral temperature gradient of 50°–70°C over a distance of 30–50 km away from the axis.

Because of the potential difficulties with small-scale off-axis convection rolls, I favor this explanation for the observed lateral temperature gradient near the EPR. If correct, this implies that some component of buoyant upwelling may occur beneath the EPR, even if in general, the upwelling pattern is mainly controlled by plate separation (*Lin and Phipps Morgan, 1992*).

3.5.2.2 Along-axis temperature variation

Figure 3.14 shows small-scale, along-axis temperature differences of 40–50°C below the EPR. Whatever the cause of these variations, one might expect these differences to be related to upwelling flow patterns because if the composition is constant, hotter mantle would be less dense and less viscous than cooler mantle. One might even expect mantle temperature patterns and upwelling to correlate with topography along the EPR [e.g., *Macdonald et al.*, 1988]. Of course this would not necessarily be the case for flow driven exclusively by plate separation if the mantle geotherm is adiabatic.

The broad dome in T_o between Siqueiros transform and 11°45'N OSC (Figure 3.14) may indeed be a broad, along-axis upwelling. If so, a component of buoyancy-driven flow and/or a weakly conductive thermal gradient like that discussed earlier would be expected to play a role. The edge effects at OSCs, most prominent north of the 11°45'N OSC (see

Figure 3.14), are difficult to explain. One possibility is that southward propagation of the OSCs [*Macdonald et al.*, 1987] places the new limb of the OSC slightly off center from the main upwelling zone. In this case, as for the off-axis cooling documented by seamounts, the mantle material which finds itself below the newly extended ridge could be cooler than normal. In contrast, a portion of ridge that is stable (not propagating) would be expected to establish a robust passive upwelling supply centered directly underneath the axis. This stability could also be perturbed by lateral migration of the ridge away from established upwelling.

Although filtered to suppress local chemical variations, the patterns of Figure 3.14 provide no evidence for the existence of upwelling patterns linked to small-scale tectonic segmentation. Such patterns would not necessarily be reflected as temperature anomalies. However, since the EPR data are consistent with the global trend in pressure-melting relationship, the upwelling pattern should be reflected in the patterns of T_o. On the basis of gravity and morphology (*Lin and Phipps Morgan, 1992*), it seems most likely that upwelling is curtain like and mainly driven by plate separation. Thermal perturbation in this curtain flow, however, could add a component of buoyancy-driven upwelling such as may exist between Siqueiros transform and 11°45'N OSC. Superimposed on this, a hierarchical series of small perturbations could also be present [*Langmuir et al.*, 1986; *Macdonald et al.*, 1988] though the mantle temperature signal of the small features could be small to nonexistent.

In contrast with the EPR, the MAR at 26°S displays a much different pattern of lateral temperature variations and melting. The slightly smaller extent of melting seen at the offsets of the 26°S segment (Figure 3.17) may be consistent with the model of *Phipps Morgan and Forsyth* [1988] for subdued upwelling under transforms. However, the higher temperatures are not consistent with this model, though the temperature differences along the segment are small (30°–40°C). It is possible that the calculated temperature

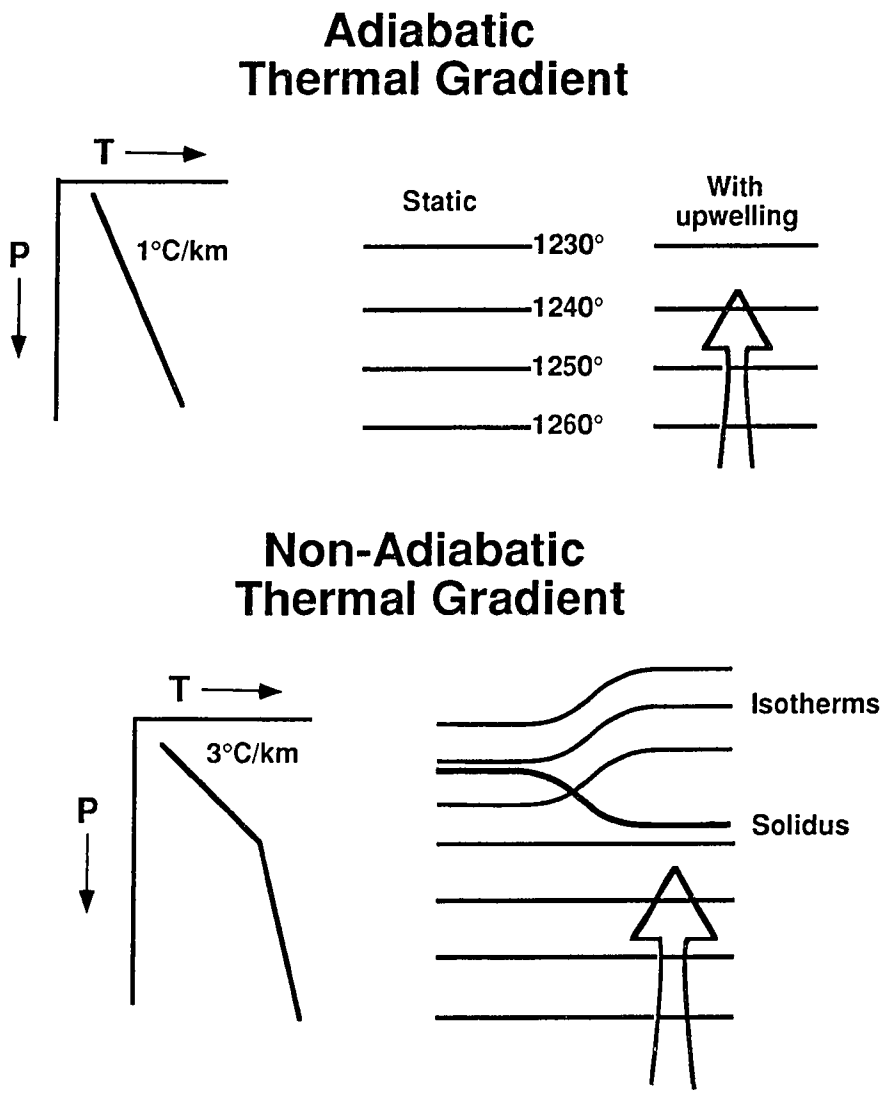

Fig. 3.28 Schematic diagram of how upwelling (arrow) in a nonadiabatic thermal gradient can affect the patterns of isotherms and the depth of initial melting. For the adiabatic case, upwelling does not perturb the pattern of isotherms because all the material has the same potential temperature [*McKenzie*, 1984; *McKenzie and Bickle*, 1988]. However, if cooling occurs (by any process) and the gradient is larger than adiabatic, upwelling material (arrow) adds heat to this region. This raises the pattern of isotherms and causes lateral temperature gradients. In addition, the hot upwelling material will have a higher temperature than the static material at depth. It will thus melt at a higher temperature and pressure if it continues to rise adiabatically. Steepness of the lateral thermal gradients is controlled by the vigor of upwelling and the size of the nonadiabatic geotherm.

pattern of Figure 3.17 is an artifact resulting from the failure of assumptions in my model. For example, the major element compositions of the mantle may be heterogeneous beneath this ridge segment. The scatter of Na_2O and Al_2O_3 (Figure 3.16) may favor this notion, but the systematics and correlations of most of oxides and ratios, particularly K_2O and TiO_2, indicate that mantle heterogeneity alone is probably inadequate to explain the results. If K_2O and TiO_2 are used to evaluate the extent of melting, then the F pattern in Figure 3.17 would be even more pronounced, i.e., the melting column approaching offsets would be even shorter than indicated in Figure 3.17. If mantle heterogeneity were the cause, then it would be fortuitous for such heterogeneity to be distributed symmetrically about the central topographic high.

My model implicitly assumes that melts rise vertically to the surface. Thus if significant lateral along-axis melt migration of the type proposed by *Phipps Morgan and Forsyth* [1988] occurs, my model would be invalid. Given the regular chemical variation patterns with depth along axis and the fact that intra-column melting cannot completely explain the chemical patterns, significant melt migration seems unlikely; however it cannot be ruled out. I also cannot rule out age differences among the axial lavas. If significant age differences occur, then the inferred patterns of T_o need not represent a steady state or snapshot of thermal conditions. Instead, the pattern would be a mixture of conditions existing at different time.

This segment shows a bull's-eye pattern of gravity (*Blackman and Forsyth*, 1992), thus the focused buoyant upwelling mantle of *Lin et al.* [1990] and *Lin and Phipps Morgan* [1991] might be expected to apply. However, there is no evidence in the melting patterns or inferred thermal structure for such a pattern. One possibility is that the geotherm under the segment is adiabatic, in which case the upwelling pattern would not disturb isotherms, and the solidus depth (P_o) and temperature (T_o) would be unaffected. This may be the case, but it does not explain the higher T_o under the offsets, which my prior arguments

would say is indicative of more vigorous, not less vigorous, upwelling. Perhaps frictional heating occurs within the transform; however, it is difficult to imagine how such heat could be transported to deeper levels of the asthenosphere.

3.5.3 Width of the upwelling zone beneath the EPR

Volcanically active seamounts exist up to 50–60 km from the EPR axis, providing clear evidence that the zone of upwelling is ~100 km wide as proposed by *Phipps Morgan* [1987]. However, because of the across-axis temperature differences discussed earlier, I also suggest that even though the passive, plate driven upwelling zone is wide, much or most of the mantle flux may actually be confined to a narrow central zone of high-velocity upwelling partly controlled by compositional, melt, and thermal buoyancy. This would explain both the across-axis and the along-axis temperature variation patterns discussed earlier, but it requires a weakly conductive versus adiabatic temperature profile.

3.5.4 Global trend versus local trend

Klein and Langmuir [1987] discovered the global correlation of MORB chemistry with ridge axial depth based on segment-averaged data and successfully explained the origin of this correlation with a simple column-melting model. *Brodholt and Batiza* [1989] independently compiled unaveraged data and confirmed this correlation, but they show great scatter about the global correlation. *Klein and Langmuir* [1989] found that the scatter partly results from regional scale chemical variations of the type found by *Batiza et al.* [1988] which show opposite correlations to the global trend. They called the global correlation the global trend and the regional scale correlation the local trend in diagrams such as Figures 3.18 and 3.19. They explained the global trend by inter-column melting by assuming a single column represents a segment or locality within which chemistry is averaged. In contrast, they interpreted the local trend as produced by melts tapped from different depths within a single column (intra-column melting). This study quantitatively

confirms their interpretation of the global trend, characterized by a positive correlation of melting pressure with extent of partial melting as represented by 8°N–14°N EPR (Figure 3.20). In the case of the EPR, however, there does not exist an obvious correlation with axial depth that may be related to the crustal thickness [*Klein and Langmuir*, 1987]. Partly, this may be because the overall topographic relief is relatively small (<400 m) at the EPR and the melting parameters vary in a narrow range. Nevertheless, the global scale correlations of MORB chemistry with ridge axial depth discovered by *Klein and Langmuir* [1987] are clearly evident.

As shown previously, however, the local trend is more problematic. Intra-column-melting processes produce similar, but not identical, data arrays as the local trend. As noted by *Klein and Langmuir* [1989], the local trend appears to be confined to slow spreading ridges like the MAR. Kinzler and Grove (1991) propose that the local trend is the result of high-pressure fractionation. If so, why does such fractionation only occur at slow-spreading ridges? Perhaps the depth and mechanism of eruption/intrusion vary systematically with spreading rate [*Klein and Langmuir* 1989].

Since the MAR at 26°S displays the local trend, it may shed light on the cause of the local trend. Earlier I concluded that mantle heterogeneity, lateral melt migration, or temporal variability in axial lavas could help explain the perplexing P_O and T_O patterns below this segment. If so, then each or any of these must vary as a function of spreading rate. I speculate that the local trend is in fact due to the dynamics of melt supply, as did *Klein and Langmuir* [1989]. *Lin and Phipps Morgan* [1992] provide strong evidence that the dynamics of upwelling change as a function of spreading rate. I suggest that at the MAR 26°S, melting columns are shorter and deeper at offsets, perhaps owing to a cold-edge effect at shallow levels. By contrast, in the center of the segment, melting columns are longer. If P_o varies and if the multiple melting columns within a segment overlap significantly in their melting range (ΔP), then groups of aggregate column melts might be

expected to yield data arrays that are intermediate in slope between inter-column and intra-column melting, as observed for the MAR at 26°S.

3.5.5 Geometry of the melting region

Application of my model to both axis and seamount melting processes shows that mantle melting actually occurs in a thin layer that pinches out laterally away from ridge axis at distances of 50–60 km in the case of EPR. The thickness of the layer, defined by ΔP (P_o - P_f), varies from 15–30 km. Equation (3.10) assumes a perfect adiabatic column melting process, and the calculated values of P_f are likely the maximum in practice if the case is nonadiabatic. If, as I suggest, the compositional effect on melting behavior is such that column melting is buffered at the solidus of a progressively depleted source, the melting could stop at a greater depth than calculated P_f. An important constraint on the final depth of melting is provided by crustal thickness, if little melt is retained in the mantle residue.

3.5.6 Crustal thickness and melt migration

My decompression-induced column-melting model allows us to crudely calculate crustal thickness as the product of the melting interval (P_o - P_f) and the melt fraction with pressure-related density corrections (see Chapter 2). Rough crustal thicknesses for the EPR and the MAR derived in this manner are slightly low, but still quite reasonable considering the model uncertainties. I obtain crustal thicknesses which vary from 2.70 to 5.01 km (with a mean thickness of 4.02 km). My crustal thicknesses are lower than those of *Klein and Langmuir* [1987] partly because my melting interval (P_o - P_f) is shorter than theirs (P_o to the base of the crust). Given the uncertainties in the exact shape of the melting region, upwelling rate of melting mantle, melt migration, and melt retention processes, it is difficult to construct a good mass balance for melt in the crust and mantle. Hopefully, future additional constraints will provide better estimates of actual crustal thickness and the melt budget. The difficulty of making a melt budget hampers direct tests of the importance

of steady state lateral melt migration. While interpretation of the trace element data for the Lamont seamounts provides weak evidence for such possible migration, this suggestion is somewhat speculative.

3.6 Summary and conclusions

From this chapter, I draw the following conclusions:

1) The experimental data of *Jaques and Green* [1980], *Falloon et al.* [1988], and *Falloon and Green* [1987, 1988] provide a good basis for a distribution coefficient based melting model. The data are self-consistent, and my model for isobaric batch melting yields very reasonable quantitative results.

2) My decompression-induced column-melting model can be used to calculate melt compositions produced by column melting of peridotite MPY-90. Since this is a reasonable parental composition for MORB, I am confident in applying the model to natural MORB compositions. A possible shortcoming of my model is the assumption that the oceanic mantle beneath mid-ocean ridges is homogeneous with respect to major elements. Thus, I suggest that the coefficients in Tables 4 and 5 should be adjusted if the mantle source composition can be determined independently for any desired specific case study.

3) Application of my model suggests that most MORBs are derived by decompression-induced column melting initiated at depths of 12–21 kbar (40–65 km) and 10–20% melting. Primary column melts for most MORBs have MgO = 10–12 wt %, so most MORBs have undergone some fractionation. I suggest that this fractionation occurs mostly at shallow level.

4) I find that $Si_{(8)}/Fe_{(8)}$ is a sensitive chemical indicator for melting pressure and that $Ca_{(8)}/Al_{(8)}$ and $Na_{(8)}$ are good indicators of degrees of melting.

5) My melting model, using primary melts modified by fractionation to MgO = 8.0 wt %, can be applied to natural MORB melts and allows quantitative estimates of parameters of column melting: P_o, P_f, T_o, T_f, and F.

6) Decompression-induced column melting occurs in a thin zone (15–30 km thick) and pinches out away from the EPR axis at 50–60 km.

7) I find lateral temperature differences in the mantle, both along axis and across axis, of 50–60°C over distances of 30–50 km. I ascribe these differences to a weakly conductive thermal profile (versus adiabatic) in the mantle immediately below the lithosphere. If so, these temperature differences can be related to patterns of mantle upwelling.

8) Across-axis melting patterns at the EPR inferred from zero-age seamount MORB melts provide evidence for a wide zone of mantle upwelling due to plate separation. However, the flow may have a central core of higher velocity due to thermal, compositional, and/or melt buoyancy.

9) Along-axis temperature patterns at the EPR suggest a broad region of hot upwelling mantle between Siqueiros and the 11°45'N OSC. Mantle temperature does not correlate with along-axis topography, but it does show a variety of edge effects. These edge effects are not consistent, implying a variety of causes. The EPR is probably supplied principally by a curtain like flow, as suggested by *Lin and Phipps Morgan* [1992]; however, a superimposed hierarchy of local upwelling is probably also present.

10) The MAR at 26°S displays good correlation between topography and melting parameters, including mantle temperature. Deep portions of the MAR, near offsets, have deeper and less extensive melting. This may be partly caused by a focused buoyant upwelling with weaker upwelling below offsets due to a cold edge effect. A variety of other factors may also play a role.

11) The MAR at 26°S exhibits the so-called local trend, which cannot be explained by intra-column melting alone. I propose that it is due to melting processes resulting from

focused buoyant upwelling at slow spreading rates, namely longer melting columns in the center and shorter, deeper columns near offsets.

CHAPTER 4

PETROLOGY AND MAGMA CHAMBER PROCESSES AT THE EAST PACIFIC RISE ~ 9°30'N

4.1 Abstract

I present new major and trace element data for a set of closely spaced (< 1.8 km) dredges along a well-studied portion of the East Pacific Rise (EPR) axis near 9°30'N (9°17'N to 9°51'N). With the exception of enriched MORB (E-MORB) at 9°35'N, the lavas are all normal mid-ocean ridge basalt (N-MORB) with a limited range of MgO (8.40 - 6.22 wt%). Major element and trace element data favor derivation of the melts from a single parental composition by low pressure crystallization of olivine, plagioclase and clinopyroxene in the ratio of 16:62:22. This model is consistent with liquid line of descent models but inconsistent with petrographic observations in that most of the N-MORB lavas have only plagioclase phenocrysts. I ascribe this to gravitational crystal settling of mafic phases and flotation of plagioclase, supported by crystal size distribution data and density relations. Most likely this occurred in the axial magma chamber (AMC) that underlies the EPR in this area. The chemistry of axial lavas varies along axis and correlates roughly with elevation of the axis and depth to the AMC. I interpret these correlations as favoring an AMC that is chemically zoned along-axis, with Fe-rich melts at its distal ends. This favors a central injection of MgO-rich melt with lateral along-axis shallow transport. The height of eruptions along axis is apparently controlled by magma density such that least dense MgO-rich melts build local volcanic constructs of the highest elevation. The E-MORB lavas are older than the N-MORB and probably erupted at a time when the AMC was absent or was much smaller in size than presently. E-MORB could have originated by deep melting processes or very shallow contamination of N-MORB. Its presence in the 9°30'N area supports the notion that magma chambers are not truly steady-state. Instead they probably

come and go on a time scale of 3000 - 6000 years. A single parental magma seems to supply melts to the AMC along the entire 60 km segment of the EPR, suggesting that central supply injection sites are widely spaced. Based on my data, there is no evidence for petrologic segmentation corresponding to 4th-order tectonic segmentation in this area, however it may be present below the resolution of the sampling.

4.2 Introduction

Magmatic processes that occur below active mid-ocean ridges are instrumental in building the oceanic crust. Melting is thought to occur as a result of decompression of hot mantle material which rises passively in response to plate separation, with or without additional buoyancy. Recent comparisons of gravity data from fast and slow spreading ridges indicate that fast ridges may be fed mostly by a quasi two-dimensional passive upwelling whereas more complex, three-dimensional buoyant mantle upwelling may be characteristic of slow ridges [*Lin and Phipps Morgan*, 1992]. Another difference between fast and slow ridges appears to be the size and longevity of crustal level magma bodies. *Detrick et al.* [1990] report the absence of magma reflectors beneath a magmatically robust section of the mid-Atlantic ridge, whereas at the East Pacific Rise (EPR), there is abundant evidence for present-day magma chamber [e.g., *Sinton and Detrick*, 1992]

The purpose of this chapter is to present new petrologic data for a well-studied portion of the EPR at ~ 9°30'N. The samples I studied are from axial dredges spaced ~ 1.8 km apart between 9°17'N and 9°40'N. These new data, together with previous data on samples from 9°40' to 9°51'N, bear on the questions of magma chamber processes and shallow magma supply dynamics at fast ridges. After discussing previous studies of this segment of the EPR, I present and interpret the new petrologic results and discuss their implications.

4.3 Previous work at the ~ 9°30'N

The EPR in the vicinity of 9°30'N is one of the best-studied segments of the EPR. The rise axis and its flanks have been well-mapped using Seabeam and Seamarc II [*Macdonald et al.*, 1984; *Lonsdale*, 1985]. These data, together with other geophysical data and observations provide constraints on the tectonic history and processes of the EPR axis and its offsets [*Macdonald et al.*, 1987, 1988; *Carbotte and Macdonald*, 1992]. The importance of crustal magma bodies and segmentation has been highlighted by a number of seismic studies [e.g., *Detrick et al.*, 1987; *Harding et al.*, 1990; *Kent et al.*, 1991; *Toomey et al.*, 1990; *Mutter et al.*, 1988]. *Haymon et al.* [1991*a*] conducted detailed geologic studies of the axis and mapped the distribution of hydrothermal activity. Follow-up submersible studies [*Haymon et al.*, 1991b; *Perfit et al.*, 1991] have provided information on volcanic processes at the axis, and new analyses of samples from the EPR axis and off-axis flanks. Additional basalt samples from the area were collected by *Langmuir et al.* [1986] as part of a larger study of the EPR axis. Nearby seamounts also have been studied in detail [*Fornari et al.*, 1984, 1988; *Allan et al.*, 1989: *Batiza et al.*, 1990].

This segment of the EPR spreads nearly symmetrically at 111 mm-yr⁻ [*Carbotte and Macdonald*, 1992] and is broadly similar to other portions of the EPR nearby, such as the EPR between 10°N - 13°N [e.g., *Macdonald and Fox*, 1988; *Hekinian et al.*, 1989; *Gente et al.*, 1986; *Thompson et al.*, 1989; *Detrick et al.*, 1987; *Perram and Macdonald*, 1991] and the faster spreading southern EPR [*Lonsdale*, 1989; *Sinton et al.*, 1991]. The 9°30'N area contrasts with the 13°N area in that morphologically (broader, higher axis) it appears to have a more robust magma supply and has a narrower and less deep linear submit collapse [*Haymon et al.*, 1991]. The axial magma chamber (AMC) in the 9°30'N area is continuously present along axis (or nearly so), but varies slightly in depth along axis (Figure 4.1). South of 9°17'N, the AMC reflector is displaced to the west. Interestingly, in the seismic tomography area (9°27'N to 9°36'N), the region of the lowest velocity about

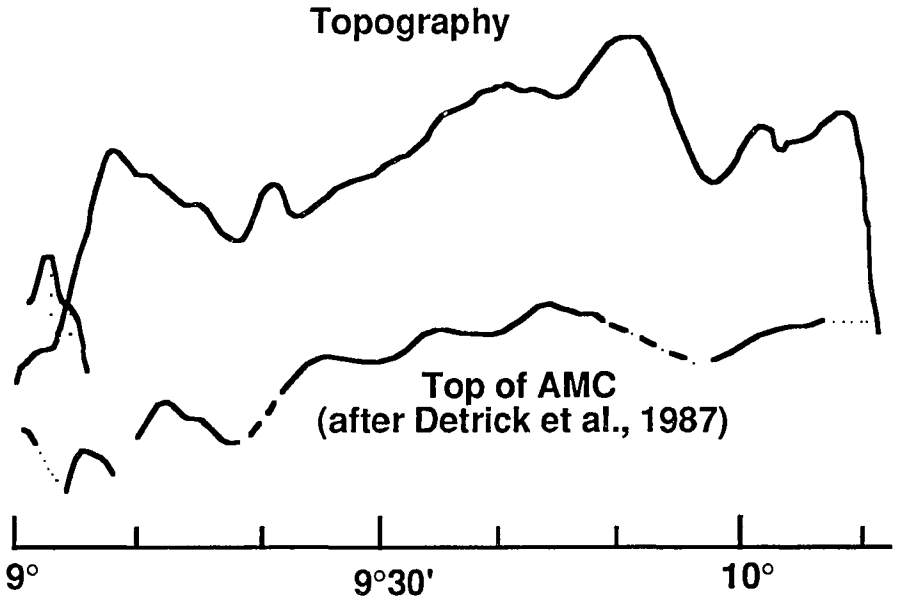

Fig. 4.1 Along-axis changes in axial topography and depth to the axial magma chamber (AMC) from *Detrick et al.* [1987[and *Macdonald and Fox* [1988]. Both profiles are greatly exaggerated vertically to show the rough correlation that exists between topography and depth to the AMC. As shown later, lava chemistry also correlates with these curves. The ranges of depth variation are different for each curve. Axial depth varies from ~ 2700 m to ~ 2540 m (~ 160 m) whereas the top of the AMC varies from ~ 2100 m to ~ 1500 m (sub-bottom). I note that *Kent et al.* [1991] suggest that depth variations in the AMC may be partly artifactual.

1 - 3 km beneath the seafloor is also offset about 1 km to the west of the axis [*Toomey et al.*, 1990] even though the AMC reflector is centered at the axis. In this area, morphologic segmentation (devals at 9°28'N and 9°35'N) corresponds to segmentation in crustal velocity structure, leading *Toomey et al.* [1990] to suggest that small scale segmentation of the EPR is magmatically controlled. *Toomey et al.* [1990] identify morphologic segmentation of linear EPR volcanoes [*Lonsdale*, 1985] on a scale of 5-10 km along axis. This corresponds to the so-called 4th-order segmentation of *Macdonald et al.* [1988]. Between 9°17'N and 9°55'N, twelve 4th-order segment boundaries have been identified (9°17N, 20', 25', 26.1', 28', 32.7' 35', 37.1', 45', 49', 51.5', and 54'N [*Langmuir et al.*, 1986; *Brodholt and Batiza*, 1988; *Toomey et al.*, 1990; *Haymon et al.*, 1991] for an average segment length of 5 - 6 km.

In contrast with the 4th-order volcano-tectonic segmentation, petrologic segmentation of the EPR [*Langmuir et al,* 1986; *Thompson et al.*, 1989; *Sinton et al.*, 1991] has usually been thought of as occurring on a slightly longer length scale. Indeed, in this chapter I show that petrologically, the EPR between 9°20'N and 9°54'N (~ 63 km) is petrologically rather uniform. With the exception of an enriched mid-ocean ridge basalt (E-MORB) at 9°35.7'N, all the axial lavas are N-MORB and appear to be related to a single parental composition. Further, magma temperature or MgO content varies regularly along axis and is crudely correlated with topographic variation. These observations provide clues about shallow processes of magma transport, storage and eruption discussed later.

4.4 Results

4.4.1 Dredges

Table 4.1 lists the sample locations, also shown on Figure 4.2. In most cases, the samples are located near or within the axial summit caldera (ASC) mapped by *Haymon et*

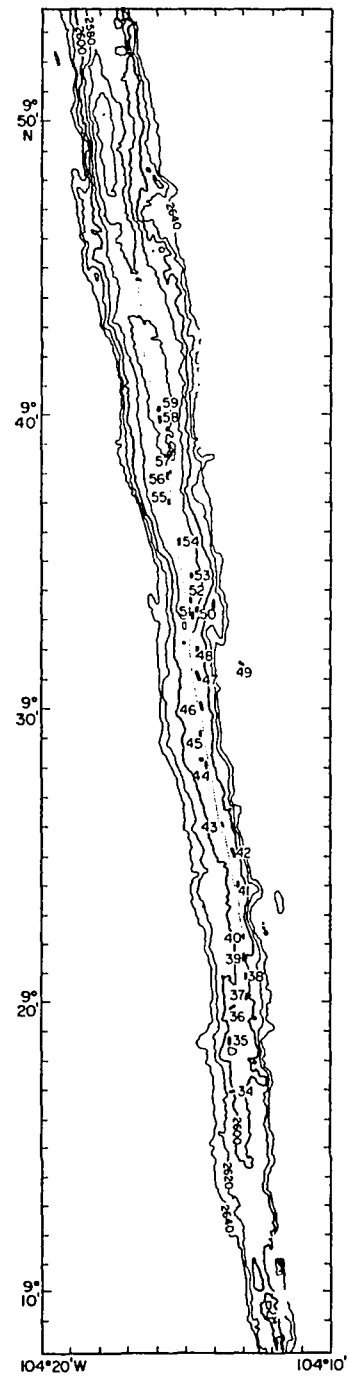

Fig. 4.2 Map of dredge locations. The Sea Beam base map is from *Toomey et al.* [1990] and the dredge locations are from Table 4.1. The dotted line shows the approximate position of the axial summit caldera (ASC) from *Haymon et al.* [1991]. Note that most of the new dredges are near the ASC.

Table 4.1. Dredge locations

Dredge	Start		End		Fix Type*	Depth	Rock
R-34†	9°16.90'N	104°13.70'W	9°16.75'N	104°13.33'W	1	2611-2615	50Kg
R-35	9°18.71'N	104°13.15'W	9°19.23'N	104°13.34'W	1	2581-2593	15Kg
R-36	9°19.76'N	104°13.09'W	9°19.77'N	104°13.42'W	1	2594-2595	0.5Kg
R-37	9°19.97'N	104°12.88'W	9°20.18'N	104°12.73'W	1	2600-2590	150Kg
R-38	9°20.54'N	104°12.95'W	9°20.81'N	104°12.82'W	2	2597-2609	1Kg
R-39	9°21.19'N	104°12.87'W	9°21.40'N	104°12.76'W	2	2586-2589	250Kg
R-40	9°21.97'N	104°12.83'W	9°22.17'N	104°12.73'W	2	2590-2596	1Kg
R-41	9°24.24'N	104°13.02'W	9°24.08'N	104°13.10'W	2	2598	5Kg
R-42	9°25.05'N	104°13.47'W	9°25.43'N	104°13.46'W	2	2588-2584	20Kg
R-43	9°26.00'N	104°13.68'W	9°26.14'N	104°13.62'W	2	2590	10g
R-44	9°27.96'N	104°14.21'W	9°28.16'N	104°14.15'W	1	2580-2583	20Kg
R-45	9°28.96'N	104°14.31'W	9°29.23'N	104°14.40'W	1	2580-2582	1g
R-46	9°29.99'N	104°14.34'W	9°30.30'N	104°14.30'W	1	2580-2581	20Kg
R-47	9°30.88'N	104°14.46'W	9°31.10'N	104°14.39'W	2	2586-2579	10Kg
R-48	9°32.00'N	104°14.61'W	9°32.15'N	104°14.58'W	2	2579-2573	20Kg
R-49†	9°31.42'N	104°12.37'W	9°31.70'N	104°12.96'W	2	2571-2699	60Kg
R-50†	9°33.23'N	104°14.49'W	9°33.42'N	104°14.42'W	2	2600-2570	10Kg
R-51	9°32.97'N	104°14.69'W	9°33.19'N	104°14.69'W	2	2575-2576	100Kg
R-52	9°33.60'N	104°14.82'W	9°33.81'N	104°14.80'W	1	2590	15Kg
R-53	9°34.38'N	104°14.70'W	9°34.57'N	104°14.68'W	1	2563-2577	10Kg
R-54	9°35.66'N	104°15.05'W	9°35.85'N	104°15.04'W	1	2559-2562	20Kg
R-55	9°36.84'N	104°15.26'W	9°37.05'N	104°15.33'W	1	2565-2565	20Kg
R-56	9°37.84'N	104°15.13'W	9°38.06'N	104°15.05'W	1	2561-2558	0.5Kg
R-57	9°38.89'N	104°15.37'W	9°38.71'N	104°15.40'W	2	2555-2554	10Kg
R-58	9°39.55'N	104°15.51'W	9°39.77'N	104°15.50'W	2	2552-2550	20Kg
R-59	9°40.30'N	104°16.00'W	9°40.50'N	104°16.00'W	2	2552	1Kg

† = off axis; * Fix Types: 1 = Global positioning system (GPS) plus Seabeam topography, and 2 = Transit Satellite and Dead-reckoning (DR) plus Seabeam topography.

al. [1991] and are thus less than a few thousand years old. More recent sampling of the area by submersible and transponder-navigated rock cores [*Perfit et al.*, 1991] greatly extends sampling of this part of the EPR. The dredges, collected on the R/V T. Washington in February, 1988 (RAITT 02), were primarily navigated using Seabeam and the new Seabeam map of *Toomey et al.* [1990]. The beam profile of Seabeam was used to track the ASC along axis. The dredges consistently were done with zero wire angle, 5 - 10 minutes on the bottom and took an average of 2.5 hours each.

All of the samples recovered are extremely fresh and glassy, with the exception of those in dredges 34, 49, and 50 located off-axis (Figure 4.2). Fresh glass was also obtained in the off-axis dredges, however the rocks are generally duller and appear older than the freshest samples. Average dredge spacing of the new dredges between 9°17'N and 9°40'N is ~ 1.8 km. In this study I also use results obtained by *Langmuir et al.* [1986] from the CHEPR expedition. Dredge locations and chemical analyses for dredges CH-84, -91 between 9°19'N and 9°49.2'N are given in the JOI synthesis of EPR data [*Tighe*, 1988]. In addition, I use data from samples collected by ALVIN dive 1567 at the EPR ~ 9°51'N [*Fornari et al.*, 1988; *Allan et al.*, 1989]. Most of the samples collected and analyzed are fragments of lobate pillows and associated ponded/collapse deposits and more rarely true sheet flows and pillow buds.

4.4.2 Petrography

All the samples between 9°17'N and 9°51'N are sparsely phyric with at most a few percent phenocrysts and microphenocrysts. A major petrographic break occurs at about 9°20'N to 9°21'N, roughly coincident with the shift in location of the AMC relative to the axis [*Mutter et al.*, 1988]. South of 9°21'N, where the AMC is centered off-axis to the west, the lavas have more abundant phenocrysts and corroded megacrysts of olivine, plagioclase, and clinopyroxene (up to 7% total). In contrast, north of this boundary up to

Table 4.2. Representative probe microanalyses of olivine

Sample	R39-8	R49-3	R49-4	R50-1	R50-4	R50-7	R52-1	R56-6	R57-5	R57-6	R52-6	CH90-2
N	12	11	10	7	10	9	9	9	10	5	17	10
SiO_2	39.72	39.30	39.42	40.03	39.94	40.06	39.82	39.74	39.84	40.26	39.64	41.73
FeO	14.71	14.39	14.35	10.91	11.27	11.92	14.68	12.49	13.51	12.90	14.94	15.63
MnO	0.23	0.22	0.24	0.17	0.11	0.21	0.24	0.22	0.23	0.19	0.00	0.26
MgO	45.40	44.18	44.65	47.07	47.55	46.51	44.60	46.43	46.03	45.68	43.32	42.76
CaO	0.39	0.37	0.34	0.37	0.39	0.35	0.34	0.35	0.37	0.52	0.38	0.34
NiO	0.11	0.08	0.20	0.30	0.17	0.23	0.12	0.18	0.16	0.22	0.12	0.11
Total	100.56	98.54	99.20	98.85	99.43	99.28	99.80	99.41	100.14	99.77	98.40	100.83
Si	0.993	1.001	0.998	1.000	0.994	1.001	1.002	0.995	0.995	1.005	1.011	1.038
Fe^{2+}	0.307	0.306	0.303	0.228	0.234	0.249	0.308	0.261	0.282	0.269	0.318	0.324
Mn	0.005	0.005	0.005	0.004	0.002	0.004	0.005	0.005	0.005	0.004	0.000	0.005
Mg	1.690	1.676	1.683	1.752	1.762	1.731	1.671	1.732	1.712	1.699	1.646	1.584
Ca	0.010	0.010	0.009	0.010	0.010	0.009	0.009	0.009	0.010	0.014	0.010	0.009
Ni	0.002	0.002	0.004	0.006	0.003	0.005	0.002	0.004	0.003	0.004	0.002	0.002
Sum	3.007	2.999	3.002	3.000	3.006	2.999	2.998	3.005	3.005	2.995	2.989	2.962
Fo	0.839	0.839	0.840	0.876	0.876	0.866	0.837	0.861	0.851	0.854	0.833	0.823
Fa	0.152	0.153	0.151	0.114	0.116	0.124	0.154	0.130	0.140	0.135	0.161	0.169
Ca-Ol	0.005	0.005	0.005	0.005	0.005	0.005	0.005	0.005	0.005	0.007	0.005	0.005
Ni-Ol	0.001	0.001	0.002	0.003	0.002	0.002	0.001	0.002	0.002	0.002	0.001	0.001
Mn-Ol	0.002	0.002	0.003	0.002	0.001	0.002	0.003	0.002	0.002	0.002	0.000	0.003

N = number of analyses. All the analyses were done at University of Hawaii.

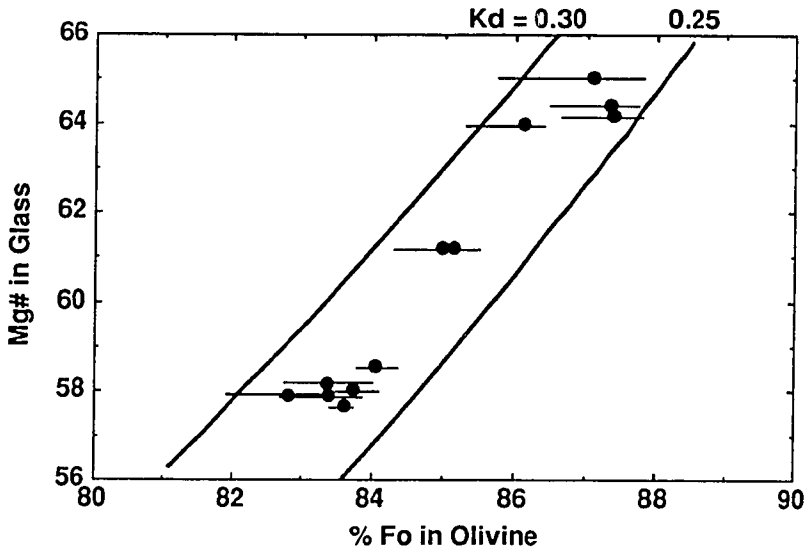

Fig. 4.3 Olivine analyses plotted against the Mg/(Mg+Fe^{2+}) of host glass. For reference, I show Kd (Fe-Mg^{Ol-Liq}) values of 0.25 and 0.30 calculated using *Roeder and Emslie* [1970]. The dots are mean compositions and the lines show observed range of variation. Note that most olivines are in equilibrium with their host melt.

Table 4.3. Probe microanalyses of plagioclase

Sample	R39-1	R39-1	R40-5	R40-5	R41-1	R42-1	R42-1	R46-2	R46-9	R46-9	R47-1	R47-1	R48-1
N	15	9	6	4	10	28	17	5	16	8	17	8	1
Grain	c	r	c	r	g	c	r	g	c	r	c	r	g
SiO_2	49.25	48.86	50.26	50.27	52.65	49.48	49.43	52.34	49.21	49.45	48.14	48.51	52.06
Al_2O_3	32.19	32.54	31.54	31.58	29.57	32.16	32.37	29.04	32.20	31.94	32.89	32.77	29.27
FeOt	0.45	0.45	0.54	0.60	0.93	0.42	0.45	1.07	0.50	0.51	0.37	0.41	0.84
MgO	0.21	0.19	0.21	0.21	0.28	0.22	0.23	0.39	0.21	0.21	0.22	0.20	0.35
CaO	15.41	15.74	14.39	14.58	12.84	15.41	15.51	12.67	15.28	15.10	15.90	15.62	12.14
Na_2O	2.65	2.49	3.09	3.10	4.29	2.73	2.66	3.95	2.75	2.92	2.24	2.36	4.14
K_2O	0.02	0.02	0.02	0.02	0.04	0.02	0.02	0.05	0.02	0.03	0.02	0.02	0.06
Total	100.17	100.29	100.03	100.34	100.60	100.46	100.67	99.51	100.17	100.15	99.78	99.89	98.86
Si	2.249	2.232	2.292	2.288	2.384	2.253	2.247	2.394	2.248	2.259	2.210	2.223	2.392
Al	1.733	1.750	1.694	1.693	1.577	1.726	1.734	1.565	1.734	1.720	1.779	1.769	1.584
Fe^{3+}	0.018	0.018	0.014	0.019	0.039	0.021	0.019	0.041	0.018	0.021	0.011	0.008	0.024
Ca	0.754	0.770	0.703	0.711	0.623	0.752	0.755	0.621	0.748	0.739	0.782	0.766	0.597
Fe^{2+}	0.002	0.002	0.007	0.005	0.002	0.001	0.002	0.004	0.003	0.001	0.004	0.007	0.009
Mg	0.014	0.013	0.014	0.014	0.019	0.015	0.015	0.026	0.015	0.015	0.015	0.014	0.024
Na	0.234	0.221	0.273	0.273	0.376	0.241	0.234	0.350	0.244	0.258	0.200	0.209	0.369
K	0.001	0.001	0.001	0.001	0.002	0.001	0.001	0.003	0.001	0.002	0.001	0.001	0.004
Cations	5.005	5.007	4.998	5.003	5.022	5.011	5.007	5.004	5.010	5.014	5.002	4.998	5.002
An%	76.20	77.62	71.98	72.19	62.16	75.61	76.24	63.75	75.35	73.98	79.58	78.46	61.62
Or%	0.11	0.11	0.09	0.09	0.25	0.12	0.13	0.28	0.10	0.15	0.11	0.13	0.36

Sample	R49-4	R49-4	R49-4	R50-7	R52-1	R54-2	R54-2	R54-2	R56-6	R56-6	R56-7	R56-7	R58-1
N	15	10	4	15	4	15	10	5	9	7	14	8	5
Grain	c	r	g	c	g	c	r	g	c	r	c	r	g
SiO_2	48.68	48.65	50.71	47.94	49.87	48.52	48.64	50.69	48.64	48.62	48.47	48.24	51.17
Al_2O_3	32.39	32.51	30.62	32.89	31.08	32.49	32.59	30.55	32.40	32.45	32.73	32.86	29.92
FeOt	0.55	0.61	0.72	0.41	0.8	0.52	0.54	0.93	0.39	0.40	0.41	0.44	0.75
MgO	0.20	0.19	0.27	0.22	0.29	0.21	0.19	0.35	0.25	0.25	0.21	0.24	0.43
CaO	15.53	15.56	13.80	16.06	13.99	15.37	15.47	13.65	15.63	15.71	15.79	15.92	13.83
Na_2O	2.52	2.49	3.45	2.24	3.35	2.63	2.61	3.51	2.55	2.46	2.44	2.35	3.56
K_2O	0.02	0.03	0.04	0.02	0.04	0.06	0.05	0.09	0.02	0.01	0.02	0.02	0.03
Total	99.90	100.04	99.61	99.77	99.41	99.79	100.09	99.78	99.88	99.91	100.07	100.06	99.69
Si	2.232	2.229	2.322	2.204	2.293	2.227	2.227	2.320	2.230	2.229	2.219	2.210	2.342
Al	1.751	1.754	1.653	1.781	1.683	1.758	1.758	1.649	1.751	1.753	1.766	1.774	1.614
Fe^{3+}	0.017	0.017	0.025	0.015	0.024	0.015	0.015	0.031	0.019	0.018	0.015	0.016	0.044
Ca	0.763	0.764	0.677	0.790	0.688	0.756	0.756	0.669	0.767	0.771	0.774	0.781	0.678
Fe^{2+}	0.004	0.007	0.005	0.002	0.007	0.005	0.006	0.004	0.001	0.001	0.003	0.004	0.004
Mg	0.014	0.013	0.018	0.015	0.020	0.014	0.013	0.024	0.017	0.017	0.015	0.016	0.029
Na	0.224	0.221	0.306	0.199	0.298	0.234	0.231	0.311	0.226	0.219	0.216	0.209	0.316
K	0.001	0.002	0.002	0.001	0.002	0.003	0.003	0.005	0.001	0.001	0.001	0.001	0.002
Cations	5.006	5.005	5.008	5.007	5.016	5.013	5.012	5.014	5.013	5.009	5.010	5.010	5.026
An%	77.19	77.44	68.72	79.80	69.63	76.09	76.36	67.88	77.15	77.85	78.10	78.84	68.08
Or%	0.15	0.17	0.24	0.10	0.21	0.34	0.31	0.54	0.09	0.07	0.09	0.09	0.20

N = number of analyses; c = core; r = rim; g = groundmass. Fe^{3+} is obtained by stoichiometry and charge balance. Note the absence of systematic zoning. All the analyses were done at University of Hawaii.

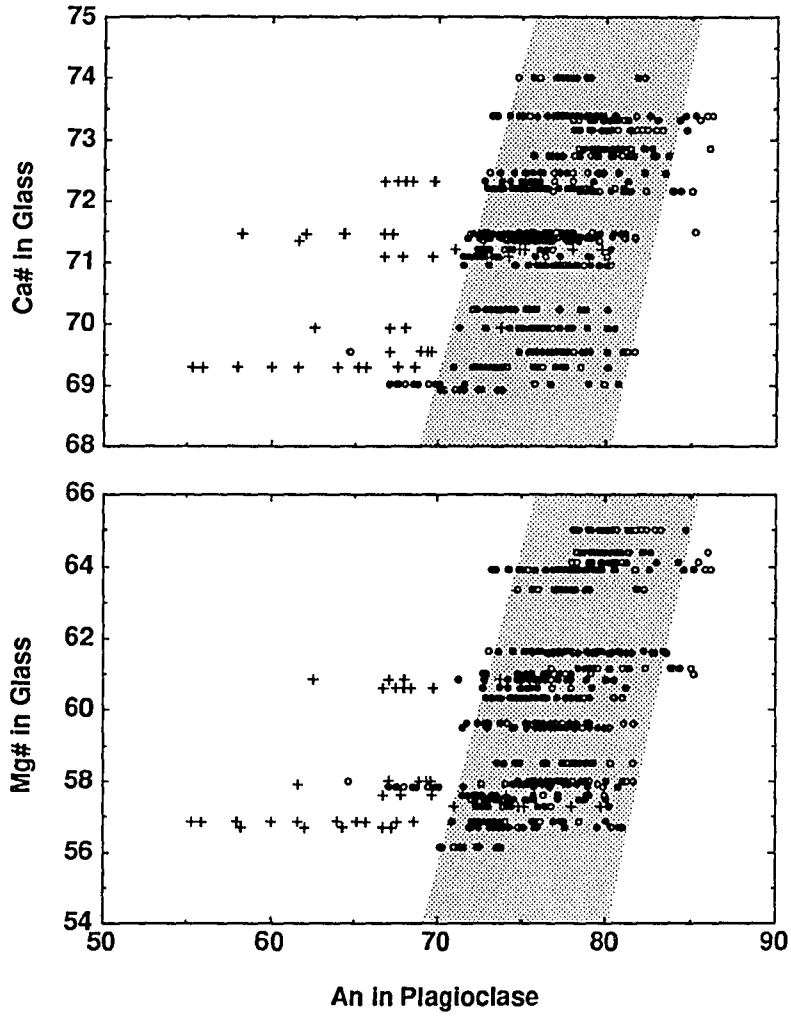

Fig. 4.4 Plagioclase analyses plotted against Ca/(Ca+Na) and Mg/(Mg+Fe^{2+}) of their host glass. Dots are cores (solid) and rims (hollow) of phenocrysts and microphenocrysts; crosses are microlites. The shaded area is a field for analyses of crystals which appear textually to be in equilibrium with their host melt.

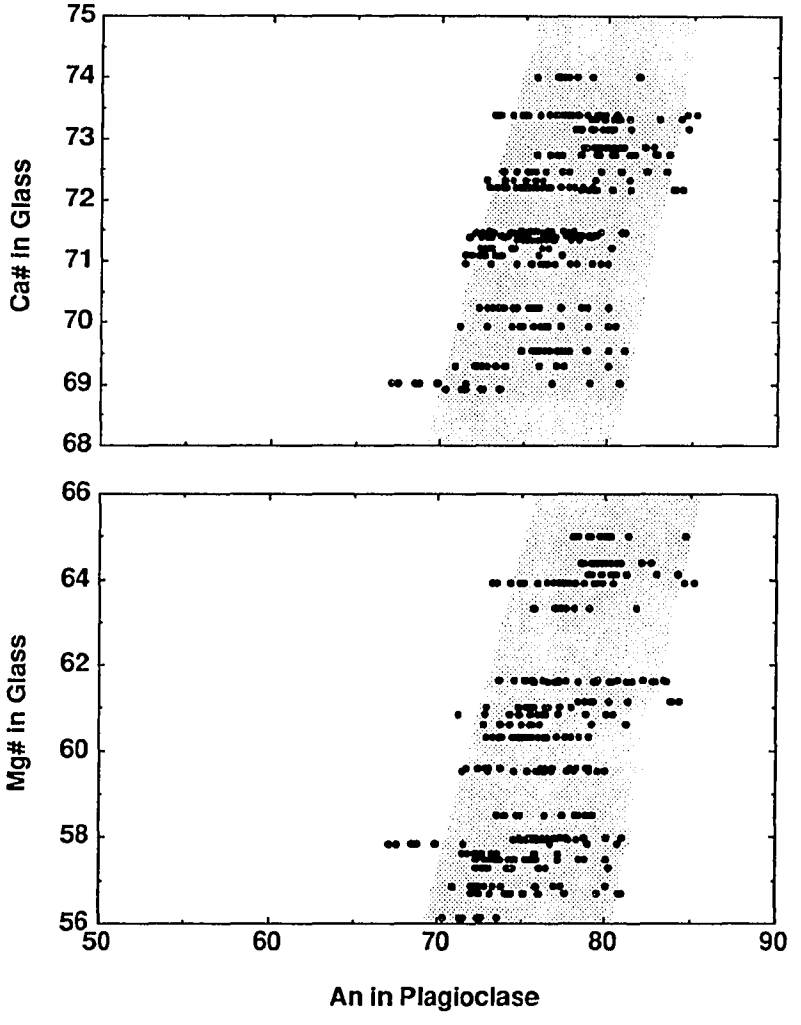

Fig. 4.5 Same as Figure 4 except that only the cores of plagioclase phenocrysts are plotted.

the Clipperton transform, the EPR axis lavas are more sparsely phyric (< 3%) and contain almost exclusively plagioclase phenocrysts and micro phenocrysts. Many also contain microlites and tiny (up to 60μ, most < 30μ) skeletal microphenocrysts of olivine. Between 9°21N and 9°25'N the lavas contain both sparse plagioclase and olivine phenocrysts. The olivine phenocrysts are up to 200μ long but are greatly subordinate to plagioclase up to 3 mm in length. A single sample (R41-2) contains cpx crystals in glass. These are anhedral to subhedral, exhibit sector zoning and do not resemble typical phenocrysts. Instead, they resemble cpx grains which commonly occur in the more crystalline portions of the lavas as glomerophyric clusters with plagioclase.

Overall, the samples exhibit mineralogic and textural features typical of EPR N-MORB elsewhere along the axis [e.g., *Batiza et al.*, 1977; *Natland*, 1980*a*]. One exception is the absence of spinel commonly found in high-MgO EPR lavas [*Natland*, 1989]. Another is the paucity of vesicles decorated with sulfide blebs. Sulfide minerals are present, but occur only as subspherical blebs up to 100μ in diameter; the walls of tiny vesicles are free of sulfides.

Olivine microphenocrysts and microlites are virtually unzoned (Table 4.2) and exhibit a narrow range of chemical variations (Fo_{88} to Fo_{82}). Figure 4.3 shows that the olivine is apparently in equilibrium with its host melt [e.g., *Roeder and Emslie*, 1970; *Ulmer*, 1989] confirming inferences based on olivine morphology. Plagioclase crystals vary more widely in chemistry (Figure 4.4 and Table 4.3) from An_{85} to An_{55}. Groundmass plagioclase microlites are systematically more sodic than phenocrysts and microphenocrysts which show a narrower range of variation (most are An_{70} to An_{82}: Figure 4.4). Zoning patterns in plagioclase phenocrysts are, as usual, very complex, with both normal and reverse zoning observed within a single rock. Despite complex zoning and compositional variation of phenocryst cores (Figure 4.5) within single rocks, the plagioclase phenocrysts are euhedral and appear to be in equilibrium. This cannot be confirmed, as plagioclase-melt

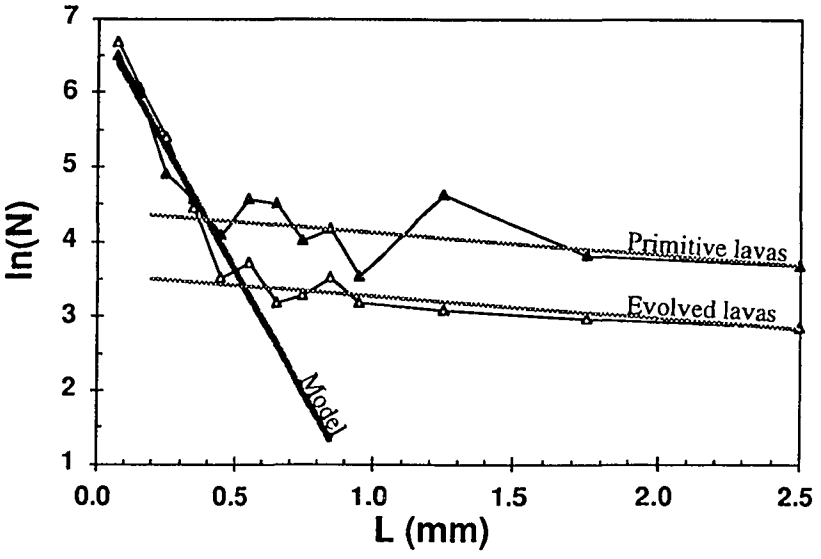

Fig. 4.6 Crystal size distribution (CSD) data for relatively primitive and relatively evolved lavas from the 9°30'N area. *ln*(N) is the natural logarithm of the number of crystals per cm^3 and L is the length (in mm) of plagioclase crystals. See text for discussion and details. These CSD patterns, which deviate from log-normal at large crystal sizes, provide evidence that plagioclase crystals were added to the magma.

equilibria is not yet fully worked out and is strongly dependent on the bulk composition of melt and other variables [e.g., *Glazner*, 1984; *Housh and Luhr*, 1991].

The size distribution of plagioclase phenocrysts and microphenocrysts in the samples is interesting (Figure 4.6). I employ the crystal size distribution (CSD) technique of *Marsh* [1988] and *Cashman and Marsh* [1988], but to get adequate statistics, multiple thin sections had to be counted. A typical EPR basalt from the 9°30'N area contains only 4 to 60 plagioclase crystals over 50μ in size per thin section. I counted five thin sections each for two relatively primitive (CH-91, ALVIN 1567) and two relatively evolved (R-40 and CH-85) lavas and combined the data. Even so, statistics are still rather poor with totals of only 117, 41, 68 and 160 crystals for each of the four rocks. Despite the low counts, the patterns of Figure 4.6 are reasonably consistent, with values of $ln(N)$ (where N is crystals per cm^3) showing a log normal distribution with crystal size up to crystal sizes of ~ 0.5 mm. Such a log-normal distribution is expected for simple cases of closed system crystallization. In contrast, the almost flat distribution of large crystals in the EPR lavas is unusual. One explanation is that the original log-normal CSD patterns have been altered by a gain of large-sized plagioclase crystals (see *Marsh* [1988] for additional discussion).

4.4.3 Basalt glass chemistry

With one exception (E-MORB glasses in dredge R-54), all the samples between 9°17'N and 9°51'N are normal MORB (N-MORB) with a limited range of MgO (8.4 to 6.22 wt%; Table 4.4). I analyzed basaltic glasses using electron microprobes at the University of Hawaii and the Smithsonian Institution (T. O'Hearn, analyst). In order to compare all these data, plus data from the Lamont-Doherty probe for CHEPR samples, I conducted a limited inter-laboratory comparison in which each laboratory analyzed glasses from 16 different MORB samples. Small systematic differences exist among all probe laboratories, but these can be corrected. The data of Table 4.4 have been adjusted using the

Table 4.4. Major element chemistry of EPR basaltic glasses

Sample	R37-1	R37-2	R37-3	R37-4	R37-5	R37-6	R37-7	R37-8	R37-12	R38-1	R39-1	R39-2	R39-3	R39-4
SiO_2	50.91	50.80	50.77	50.91	50.48	50.13	50.62	51.14	51.44	51.13	49.98	50.43	50.61	50.32
TiO_2	1.66	1.66	1.64	1.66	1.61	1.65	1.70	1.67	1.68	1.75	1.65	1.59	1.62	1.62
Al_2O_3	14.46	14.50	14.46	14.58	14.44	14.49	14.39	14.64	14.57	14.34	14.75	15.17	15.20	15.15
FeO	10.77	10.64	10.47	10.65	10.73	10.58	10.52	10.71	10.71	10.99	10.01	10.18	10.16	10.06
MnO	0.17	0.21	0.21	0.24	0.21	0.20	0.23	0.19	0.19	na	0.21	0.16	0.18	0.17
MgO	7.14	7.15	7.23	7.14	7.14	7.16	7.16	7.16	7.09	7.05	7.43	7.51	7.33	7.44
CaO	11.64	11.42	11.36	11.48	11.46	11.36	11.14	11.37	11.54	11.50	11.70	11.94	11.99	11.86
Na_2O	2.68	2.71	2.74	2.71	2.74	2.75	2.77	2.75	2.58	2.68	2.64	2.66	2.70	2.68
K_2O	0.10	0.11	0.11	0.12	0.09	0.11	0.10	0.11	0.12	0.14	0.13	0.16	0.14	0.16
P_2O_5	0.15	0.18	0.20	0.14	0.19	0.20	0.14	0.22	0.23	0.20	0.15	0.17	0.17	0.18
Total	99.69	99.39	99.18	99.63	99.08	98.62	98.77	99.97	100.20	99.78	98.65	99.97	100.10	99.63
Mg#	56.77	57.10	57.77	57.04	56.85	57.27	57.41	57.00	56.72	55.96	59.50	59.36	58.84	59.43

Sample	R39-5	R39-6	R39-7	R39-8	R39-9	R39-10	R39-11	R39-12	R39-16	R39-17	R39-18	R39-19	R40-1	R40-2
SiO_2	50.44	49.84	50.21	49.95	50.27	50.56	50.05	50.31	50.31	50.06	50.07	49.46	50.84	50.90
TiO_2	1.62	1.69	1.64	1.58	1.63	1.68	1.66	1.68	1.63	1.67	1.64	1.63	1.86	1.84
Al_2O_3	14.70	15.03	14.98	14.83	15.15	14.76	14.87	14.84	14.96	14.81	14.67	14.92	14.36	14.32
FeO	10.35	10.23	10.04	10.34	10.14	10.42	10.41	10.47	10.42	10.38	10.27	10.09	11.29	10.67
MnO	na	0.17	0.19	na	0.19	0.19	0.16	0.19	na	0.18	0.18	0.17	0.17	0.21
MgO	7.51	7.44	7.33	7.36	7.51	7.33	7.38	7.36	7.40	7.51	7.31	7.47	6.80	6.82
CaO	11.80	11.78	11.77	11.97	11.89	12.01	12.05	11.99	11.82	11.67	11.95	12.04	11.45	11.34
Na_2O	2.67	2.72	2.71	2.64	2.70	2.66	2.63	2.67	2.61	2.65	2.60	2.65	2.79	2.82
K_2O	0.11	0.16	0.14	0.11	0.14	0.12	0.12	0.13	0.12	0.13	0.13	0.12	0.14	0.16
P_2O_5	0.19	0.19	0.20	0.18	0.17	0.17	0.17	0.17	0.18	0.18	0.18	0.17	0.21	0.23
Total	99.39	99.25	99.21	98.96	99.80	99.91	99.50	99.81	99.45	99.26	99.01	98.73	99.91	99.31
Mg#	58.97	59.02	59.12	58.50	59.47	58.22	58.41	58.21	58.45	58.90	58.50	59.46	54.41	55.85

Sample	R40-3	R40-4	R40-5	R41-1	R41-2	R41-3	R41-4	R42-1	R42-2	R42-3	R42-4	R42-5	R42-6	R42-7
SiO_2	50.10	49.95	50.54	50.79	50.59	49.95	50.07	51.04	50.27	50.96	51.14	50.92	51.13	50.88
TiO_2	1.90	1.90	1.88	1.70	1.65	1.77	1.70	1.54	1.49	1.50	1.54	1.52	1.51	1.47
Al_2O_3	14.15	14.28	14.33	14.72	14.61	14.45	14.40	14.75	14.93	14.94	14.95	14.83	14.97	15.06
FeO	11.22	11.27	10.48	10.63	10.40	10.63	10.51	9.98	9.97	9.89	10.00	9.84	9.85	9.87
MnO	0.19	0.20	0.22	0.20	0.21	0.20	0.19	na	0.20	0.18	0.17	0.17	0.18	0.18
MgO	7.01	6.75	6.76	7.07	7.06	7.11	7.22	7.66	7.76	7.75	7.76	7.60	7.78	7.80
CaO	11.76	11.26	11.27	11.75	11.79	11.64	11.60	12.03	11.93	12.12	12.07	11.93	12.06	12.26
Na_2O	2.77	2.76	2.80	2.87	2.80	2.85	2.70	2.55	2.58	2.51	2.57	2.56	2.55	2.63
K_2O	0.13	0.17	0.14	0.13	0.14	0.15	0.13	0.11	0.13	0.12	0.10	0.13	0.11	0.13
P_2O_5	0.25	0.23	0.13	0.21	0.19	0.20	0.23	0.17	0.24	0.16	0.17	0.18	0.15	0.14
Total	99.48	98.76	98.56	100.10	99.43	98.95	98.75	99.83	99.50	100.10	100.50	99.68	100.30	100.40
Mg#	55.31	54.27	56.10	56.84	57.35	56.97	57.65	60.32	60.65	60.81	60.59	60.47	61.00	61.01

Sample	R44-1	R44-2	R44-3	R44-4	R44-5	R44-6	R44-7	R44-12	R44-13	R44-14	R45SG	R46-1	R46-2	R46-3
SiO_2	50.82	50.97	51.35	51.15	51.10	50.88	50.46	51.34	50.95	50.63	50.59	50.40	50.71	50.61
TiO_2	1.71	1.71	1.72	1.70	1.71	1.69	1.66	1.72	1.73	1.74	1.71	1.63	1.71	1.63
Al_2O_3	14.67	14.61	14.55	14.57	14.59	14.47	14.49	14.51	14.59	14.60	14.50	14.47	14.82	14.59
FeO	9.95	10.54	10.58	10.57	10.63	10.61	10.58	10.58	10.66	10.77	10.55	10.31	10.36	10.10
MnO	0.21	0.19	0.19	0.18	0.18	na	na	0.18	0.19	0.19	na	0.21	na	0.18
MgO	7.09	7.30	7.28	7.27	7.26	7.18	7.18	7.31	7.32	7.33	7.35	7.45	6.84	6.87
CaO	11.57	11.85	11.79	11.80	11.91	11.77	11.77	11.80	11.79	11.82	11.76	11.53	12.10	11.57
Na_2O	2.88	2.63	2.63	2.61	2.68	2.62	2.66	2.64	2.69	2.68	2.65	2.65	2.66	2.73
K_2O	0.16	0.11	0.12	0.11	0.12	0.12	0.12	0.11	0.11	0.11	0.14	0.14	0.13	0.16
P_2O_5	0.19	0.20	0.17	0.18	0.19	0.20	0.15	0.19	0.19	0.18	0.16	0.18	0.17	0.19
Total	99.24	100.10	100.40	100.20	100.40	99.54	99.07	100.40	100.20	100.10	99.41	98.98	99.50	98.63
Mg#	58.53	57.85	57.67	57.66	57.49	57.27	57.34	57.77	57.62	57.40	57.98	58.87	56.67	57.40

Table 4.4. Major element chemistry of EPR basaltic glasses (continued)

Sample	R46-4	R46-5	R46-6	R46-7	R46-8	R46-9	R46-10	R47-1	R47-2	R47-3	R47-4	R47-5	R47-6	R48-1
SiO_2	50.59	51.25	50.41	50.64	50.76	50.82	50.70	50.33	50.50	50.65	50.41	50.32	50.67	50.83
TiO_2	1.64	1.68	1.65	1.61	1.68	1.64	1.69	1.43	1.40	1.41	1.40	1.39	1.61	1.70
Al_2O_3	14.64	14.60	14.60	14.62	14.64	14.60	14.53	15.22	15.16	15.30	15.17	15.18	14.60	14.65
FeO	10.24	10.00	10.29	10.26	10.50	10.53	10.51	9.74	9.50	9.71	9.58	9.59	10.40	10.36
MnO	0.19	0.22	0.18	0.22	0.20	0.20	0.18	0.21	0.20	na	0.16	0.18	0.19	0.16
MgO	6.92	7.43	7.40	7.36	7.23	7.18	7.17	7.89	7.88	7.87	7.88	7.82	7.29	7.20
CaO	11.90	11.59	11.57	11.53	11.53	11.61	11.70	12.06	11.83	12.28	11.91	11.88	11.58	11.75
Na_2O	2.60	2.66	2.66	2.71	2.68	2.71	2.65	2.49	2.61	2.57	2.57	2.58	2.67	2.60
K_2O	0.11	0.13	0.13	0.13	0.13	0.13	0.11	0.13	0.13	0.12	0.15	0.14	0.11	0.11
P_2O_5	0.19	0.13	0.17	0.19	0.19	0.19	0.20	0.21	0.17	0.16	0.17	0.15	0.18	0.21
Total	99.02	99.68	99.07	99.27	99.54	99.62	99.44	99.71	99.39	100.10	99.40	99.23	99.29	99.58
Mg#	57.23	59.53	58.75	58.69	57.70	57.47	57.48	61.60	62.16	61.62	61.98	61.76	58.12	57.92

Sample	R48-2	R48-3	R48-4	R48-5	R48-6	R49-1	R49-2	R49-3	R49-4	R50-1	R50-2	R50-3	R50-4	R50-5
SiO_2	50.67	50.50	50.44	50.55	50.49	50.14	51.02	50.62	50.07	50.24	50.38	50.27	50.29	49.93
TiO_2	1.66	1.62	1.62	1.66	1.66	1.90	1.87	1.69	1.67	1.29	1.26	1.26	1.23	1.25
Al_2O_3	14.50	14.70	14.67	14.59	14.58	14.21	14.17	14.69	15.09	15.69	15.64	15.51	15.61	15.70
FeO	10.47	10.43	10.46	10.42	10.41	11.20	11.31	10.04	10.17	9.22	9.02	9.25	9.16	9.00
MnO	0.18	0.18	na	0.18	0.20	0.22	0.21	0.22	na	0.18	0.16	0.17	0.15	na
MgO	7.23	7.08	7.08	6.95	7.27	6.58	6.22	6.95	7.08	8.31	8.26	8.29	8.35	8.40
CaO	11.53	11.71	11.87	11.66	11.75	11.04	11.25	11.44	11.90	12.21	12.17	12.10	12.13	12.27
Na_2O	2.67	2.70	2.65	2.70	2.69	2.90	2.86	2.83	2.87	2.45	2.47	2.46	2.49	2.43
K_2O	0.13	0.11	0.14	0.12	0.14	0.14	0.14	0.23	0.26	0.10	0.10	0.12	0.11	0.12
P_2O_5	0.19	0.18	0.17	0.22	0.17	0.23	0.19	0.24	0.18	0.16	0.13	0.14	0.14	0.12
Total	99.24	99.23	99.10	99.06	99.36	98.56	99.25	98.94	99.29	99.86	99.59	99.59	99.67	99.22
Mg#	57.75	57.36	57.28	56.91	58.04	53.79	52.13	57.83	57.96	64.09	64.47	63.97	64.35	64.90

Sample	R50-6	R50-7	R51-1	R51-2	R51-3	R51-4	R51-5	R51-6	R51-7	R51-8	R51-9	R51-10	R51-11	R51-12
SiO_2	50.45	50.46	50.32	50.43	50.96	50.96	50.81	51.06	50.91	50.78	50.73	50.74	50.88	50.82
TiO_2	1.28	1.28	1.20	1.27	1.49	1.49	1.49	1.47	1.52	1.46	1.50	1.47	1.52	1.53
Al_2O_3	15.58	15.55	15.73	15.44	14.69	14.68	14.61	14.75	14.67	14.54	14.73	14.72	14.50	14.85
FeO	9.03	8.93	9.17	9.13	9.90	10.12	9.97	10.08	10.14	9.81	10.00	10.07	10.06	10.10
MnO	0.19	0.19	na	0.18	0.20	0.18	0.19	0.21	0.18	0.18	0.21	0.20	0.19	0.18
MgO	8.31	8.37	7.98	7.99	7.37	7.34	7.42	7.33	7.39	7.43	7.48	7.39	7.43	7.22
CaO	12.17	12.21	12.52	12.25	11.89	12.01	11.96	11.79	12.07	11.67	12.01	12.01	12.07	12.19
Na_2O	2.40	2.47	2.52	2.48	2.66	2.65	2.64	2.69	2.70	2.63	2.71	2.66	2.68	2.73
K_2O	0.10	0.11	0.09	0.09	0.11	0.09	0.09	0.09	0.08	0.09	0.10	0.09	0.08	0.07
P_2O_5	0.13	0.11	0.12	0.12	0.14	0.16	0.14	0.16	0.16	0.13	0.15	0.15	0.14	0.15
Total	99.64	99.69	99.65	99.38	99.40	99.70	99.32	99.63	99.83	98.72	99.62	99.49	99.57	99.83
Mg#	64.57	64.98	63.28	63.42	59.59	58.95	59.59	59.03	59.08	60.01	59.71	59.22	59.41	58.59

Sample	R51-13	R51-14	R51-15	R51-16	R52-1	R52-2	R52-3	R52-4	R52-5	R52-6	R53SG	R54-1	R54-2	R54-3
SiO_2	50.86	51.02	50.66	51.04	50.40	50.69	50.48	50.39	50.43	50.55	50.09	50.38	49.83	50.25
TiO_2	1.48	1.55	1.53	1.48	1.69	1.62	1.63	1.67	1.60	1.65	1.23	1.62	1.58	1.64
Al_2O_3	14.63	14.70	14.65	14.68	14.88	14.84	14.97	14.71	14.79	14.54	16.08	15.65	15.93	15.68
FeO	9.84	10.92	10.25	10.07	10.54	10.53	10.53	10.34	10.42	10.29	8.86	9.01	9.19	8.98
MnO	0.21	0.22	na	0.21	na	0.19	0.20	0.19	0.19	0.21	na	0.18	na	0.19
MgO	7.33	6.96	7.49	7.29	7.23	7.34	7.19	7.28	7.22	7.21	8.37	7.37	7.21	7.33
CaO	11.80	11.81	12.03	12.01	11.74	11.75	11.82	11.71	11.54	11.52	12.36	11.66	11.87	11.65
Na_2O	2.67	2.70	2.69	2.67	2.63	2.62	2.67	2.65	2.60	2.69	2.44	2.77	2.81	2.76
K_2O	0.12	0.12	0.10	0.10	0.11	0.12	0.10	0.11	0.08	0.10	0.08	0.43	0.36	0.42
P_2O_5	0.15	0.15	0.17	0.17	0.18	0.18	0.18	0.19	0.17	0.20	0.15	0.26	0.21	0.28
Total	99.09	100.10	99.57	99.72	99.40	99.87	99.77	99.24	99.04	98.98	99.66	99.34	98.99	99.20
Mg#	59.61	55.80	59.14	58.94	57.60	57.99	57.49	58.22	57.87	58.11	65.17	61.83	60.84	61.77

Table 4.4. Major element chemistry of EPR basaltic glasses (continued)

Sample	R54-4	R54-5	R54-6	R54-7	R54-8	R54-9	R54-10	R54-11	R54-12	R55SG	R56-1	R56-2	R56-3	R56-4
SiO_2	50.42	50.16	50.50	50.54	50.28	49.86	50.57	50.57	50.68	50.09	50.18	49.82	50.35	50.10
TiO_2	1.60	1.61	1.61	1.62	1.64	1.56	1.65	1.62	1.62	1.72	1.41	1.31	1.28	1.28
Al_2O_3	15.56	15.59	15.60	15.69	15.56	15.62	15.70	15.67	15.81	14.58	15.11	15.34	15.44	15.33
FeO	9.03	8.92	8.89	9.03	9.15	8.96	9.04	9.04	9.11	10.66	9.75	9.10	9.21	9.07
MnO	0.17	0.18	0.16	0.18	0.17	0.17	0.18	0.17	0.17	na	0.19	0.17	na	0.15
MgO	7.42	7.35	7.43	7.40	7.26	7.48	7.45	7.49	7.10	7.35	7.71	8.23	8.23	8.10
CaO	11.66	11.63	11.62	11.67	11.70	11.51	11.67	11.68	11.84	11.67	11.78	12.06	12.21	12.00
Na_2O	2.77	2.72	2.76	2.81	2.80	2.80	2.74	2.77	2.77	2.68	2.49	2.31	2.40	2.40
K_2O	0.43	0.45	0.45	0.44	0.44	0.42	0.41	0.42	0.45	0.10	0.09	0.08	0.09	0.09
P_2O_5	0.25	0.26	0.23	0.27	0.23	0.29	0.29	0.26	0.24	0.18	0.16	0.12	0.14	0.13
Total	99.29	98.87	99.27	99.65	99.25	98.67	99.71	99.69	99.81	99.03	98.87	98.55	99.35	98.66
Mg#	61.95	62.03	62.36	61.89	61.12	62.32	62.01	62.14	60.71	57.73	61.04	64.16	63.90	63.90

Sample	R56-5	R56-6	R57-1	R57-2	R57-4	R57-6	R58-1	R58-2	R58-3	R58-4	R59-1	R59-3	R59-4
SiO_2	49.99	50.20	50.29	50.50	50.31	50.65	50.05	50.18	49.70	50.18	50.16	50.86	50.57
TiO_2	1.29	1.28	1.25	1.51	1.49	1.53	1.63	1.51	1.52	1.53	1.75	1.75	1.76
Al_2O_3	15.28	15.33	15.48	14.96	15.02	15.15	15.28	15.35	15.36	15.09	14.58	14.69	14.66
FeO	9.41	9.07	9.08	9.69	9.58	9.88	9.94	9.63	9.64	9.75	10.77	10.34	10.81
MnO	na	0.18	0.20	0.18	0.16	na	na	0.19	0.24	0.19	na	0.20	0.20
MgO	8.20	8.10	8.06	7.65	7.64	7.85	7.72	7.79	7.70	7.70	7.10	7.10	7.02
CaO	12.36	12.00	12.02	11.65	11.96	11.95	11.77	11.61	11.56	11.42	11.59	11.68	11.72
Na_2O	2.39	2.40	2.42	2.51	2.51	2.54	2.48	2.54	2.56	2.51	2.63	2.62	2.69
K_2O	0.09	0.09	0.08	0.10	0.10	0.08	0.09	0.10	0.10	0.10	0.12	0.11	0.12
P_2O_5	0.15	0.14	0.16	0.16	0.16	0.18	0.17	0.17	0.17	0.19	0.19	0.19	0.17
Total	99.16	98.79	99.05	98.92	98.93	99.81	99.13	99.09	98.57	98.66	98.89	99.54	99.72
Mg#	63.32	63.90	63.73	61.00	61.23	61.15	60.60	61.57	61.27	61.01	56.63	57.63	56.26

Samples without MnO were analyzed at the Smithsonian Institution: T. O'Hearn analyst. Others were analyzed at University of Hawaii.

Group means (not listed) are computed by averaging together analyses of individual glass samples from the same dredge, provided they are similar within analytical uncertainty for all elements. For most dredges, the group means are simple averages of the individual glass analyses, however some dredges have two groups of samples as follows: R47a: R47-1,2,3,4,5; R47b: R47-6; R49a: R49-1,2; R49b: R49-3,4; R51a: R51-3,4,5,6,7,8,9,10,11,12,13,14,15,16; R51b: R51-1,2; R56a: R56-2,3,4,5,6; R56b: R56-1; R57a: R57-2,4,6; R57b: R57-1.

In this study, I have corrected U. Hawaii and Lamont probe glass data to conform with Smithsonian analyses. To do this, we multiply each oxide by the factors given below:

	SiO_2	TiO_2	Al_2O_3	FeO	MnO	MgO	CaO	Na_2O	K_2O	P_2O_5
U. Hawaii	0.9994	1.0005	1.0040	0.9737	-	1.0000	0.9792	0.9996	1.0355	1.2597
LDGO	1.0064	1.0006	1.0057	1.0062	-	0.9323	0.9876	1.0037	1.0870	1.0377

Complete results of the interlaboratory comparison are available from the authors and from C. Langmuir (LDGO) or J. Bender (UNCC). The probe mount of 16 glasses is kept at LDGO.

$Mg^{\#}$ is 100 x Mg/(Mg + Fe^{2+}) with $Fe^{2+}/(Fe^{2+} + Fe^{3+}) = 0.9$.

Table 4.5. Trace element chemistry of representative glasses

Sample	R37-1	R38-1	R39-1	R41-1	R42-1	R44-6	R46-2	R47-3	R48-1	R49-4	R51-1	R50-1	R52-1	R54-2	R56-5	R57-6	R58-1	R59-1
La	3.54	3.86	3.83	4.29	3.61	3.92	4.08	3.52	3.76	3.83	2.50	2.94	3.68	8.40	2.75	3.38	3.37	3.95
Ce	10.70	11.90	11.50	13.70	10.40	11.90	11.60	10.00	11.40	11.60	7.70	8.50	11.70	18.90	8.50	10.60	10.50	11.80
Sm	3.71	4.04	3.67	3.91	3.33	3.70	3.69	3.27	3.70	3.75	2.84	2.84	3.73	3.80	2.93	3.36	3.61	3.96
Eu	1.33	1.41	1.32	1.39	1.21	1.33	1.35	1.20	1.33	1.31	1.07	1.07	1.37	1.36	1.07	1.20	1.26	1.41
Tb	0.91	0.95	0.92	0.92	0.84	0.89	0.94	0.77	0.94	0.90	0.71	0.66	0.96	0.82	0.69	0.78	0.88	0.94
Yb	3.41	3.74	3.42	3.50	3.07	3.48	3.55	3.10	3.56	3.51	2.71	2.64	3.58	2.96	2.76	3.18	3.35	3.75
Lu	0.501	0.565	0.488	0.506	0.445	0.514	0.507	0.429	0.500	0.513	0.385	0.394	0.504	0.412	0.405	0.458	0.487	0.540
FeO	10.72	10.87	10.28	10.53	9.91	10.44	10.66	9.88	10.35	10.47	9.12	9.04	10.56	9.05	9.17	9.81	9.95	10.86
Na_2O	2.78	2.75	2.68	2.92	2.64	2.70	2.79	2.66	2.68	2.75	2.60	2.57	2.72	2.86	2.45	2.60	2.66	2.75
Sc	43.8	43.7	42.8	44.5	42.9	43.1	44.2	43.0	42.9	43.5	40.9	39.5	42.7	41.3	39.8	41.3	39.6	43.4
Cr	177	160	313	210	293	226	251	325	233	234	345	353	264	311	344	304	301	235
Co	44.7	43.8	43.4	43.4	43.9	43.1	44.6	44.3	42.9	43.5	43.3	43.7	44.3	40.8	43.3	43.4	43.7	44.0
Ni			70	100	80	80		80	70	70	100	140	110		120	80	140	
Cs							0.21							0.15				
Sr	100	160	130	160	170	100	160	160	170	130	70	160	140	210	180	120	120	120
Ba														61				
Zr	90		150	130	150	120	120		90	150	80	110	130	130		100	110	130
Ta	0.17	0.20	0.19	0.20	0.20	0.14	0.16	0.16	0.16	0.19	0.14	0.13	0.16	0.74	0.11	0.15	0.15	0.11
Hf	2.84	3.01	2.84	2.94	2.49	2.98	2.95	2.47	2.84	2.97	2.11	2.13	2.86	2.91	2.16	2.58	2.68	3.11
Th	0.09	0.19	0.14	0.14	0.14	0.22	0.13	0.08	0.19	0.13	0.13	0.09	0.11	0.67	0.11	0.16	0.16	0.10
U														0.26				
(La/Sm)n	0.668	0.669	0.731	0.768	0.759	0.742	0.774	0.754	0.711	0.715	0.616	0.725	0.691	1.547	0.657	0.704	0.653	0.698
(La/Lu)n	0.730	0.706	0.811	0.876	0.838	0.788	0.832	0.848	0.777	0.771	0.671	0.771	0.754	2.107	0.702	0.763	0.715	0.756
(Ce/Yb)n	0.635	0.644	0.681	0.792	0.686	0.692	0.661	0.653	0.648	0.669	0.575	0.652	0.661	1.292	0.623	0.675	0.634	0.637
Mg#	56.77	55.96	59.50	56.84	60.32	57.27	56.67	61.62	57.92	57.96	63.28	64.09	57.60	60.84	63.32	61.15	60.60	56.63

Trace element were obtained by Instrumental Neutron Activation Analysis at Washington University, St. Louis [*Lindstrom and Korotev*, 1982]. Analytical precision is computed for each sample and these vary slightly. Typical uncertainties (2σ) are : La and Sm - 4%, Yb - 5%, Eu and Lu - 6%, Ce - 7%, Hf - 9%, Tb - 10%, and Na_2O - 0.08 wt%, FeO - 0.3 wt%, Sc - 1.2 ppm, Cr - 10 ppm, Co - 1.2 ppm, Ni - 30ppm, Sr - 40ppm, Zr - 50ppm, Ba - 18ppm, Cs - 0.07ppm, Ta - 0.04ppm, Th - 0.04ppm and U - 0.09ppm.

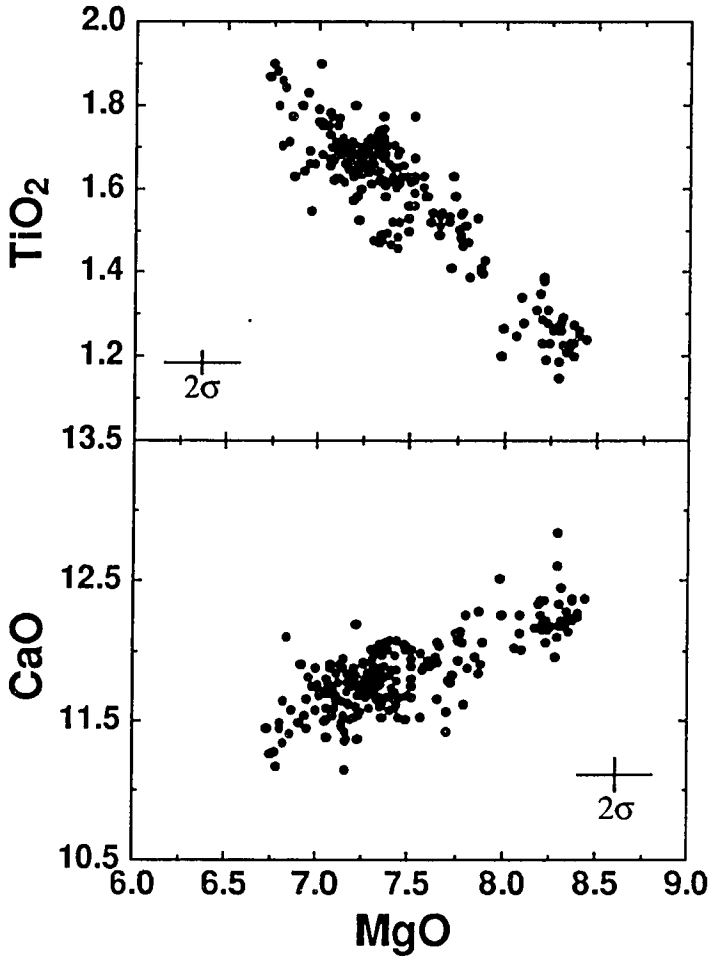

Fig. 4.7 Plots of TiO_2 and CaO vs. MgO for all the individual glass analyses in the 9°30'N area. This plot includes data from the new axial RAITT 02 dredges, the CHEPR dredges and the ALVIN samples.

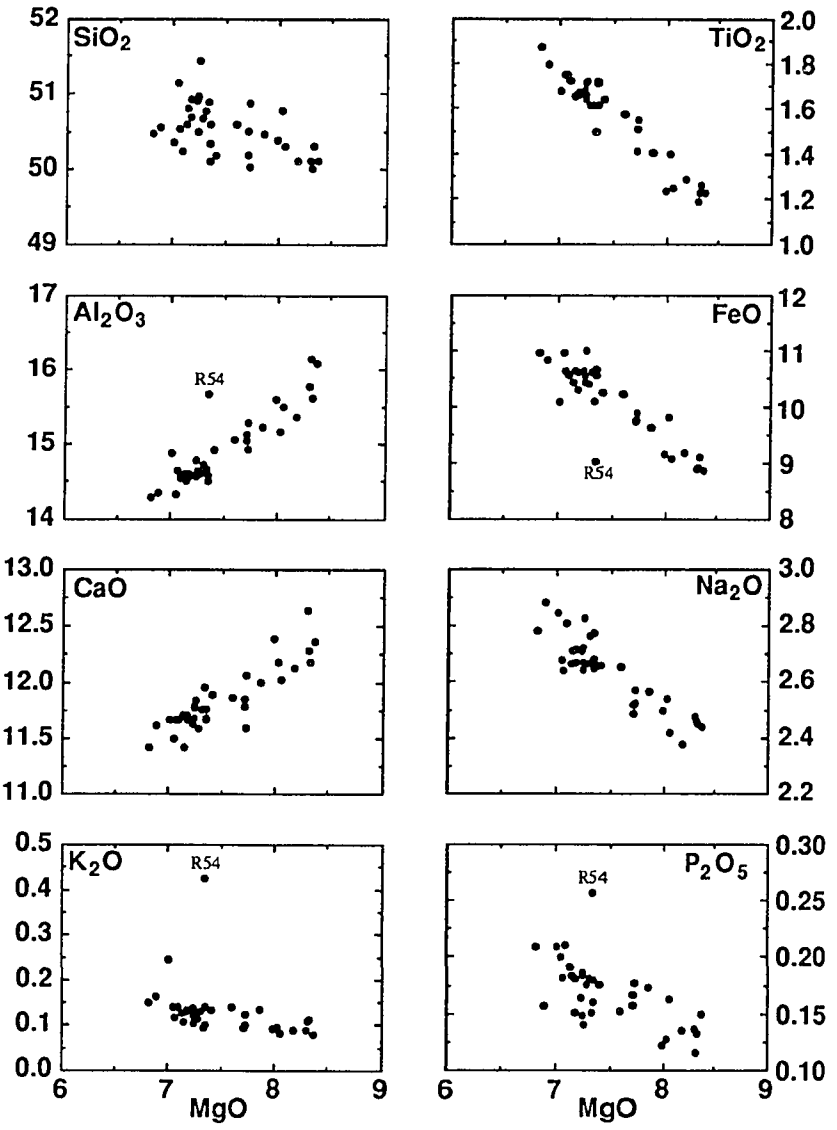

Fig. 4.8 MgO variation diagrams for the group means (see Table 4.4 notes). The E-MORB (R54) is labeled on some of the plots.

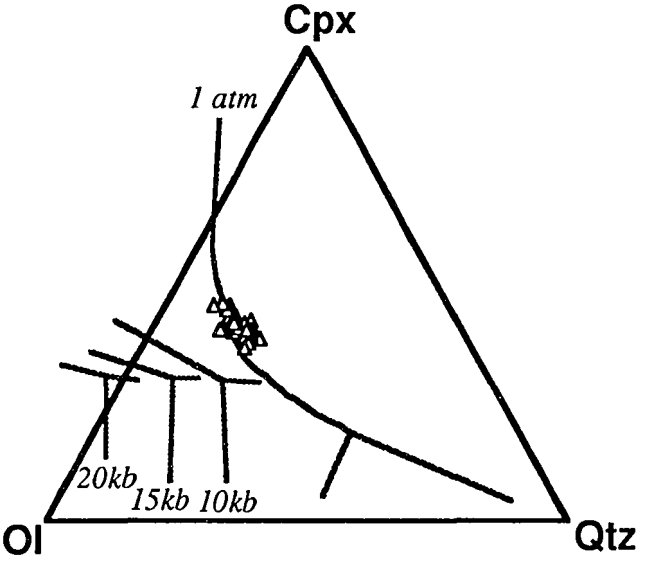

Fig. 4.9 Phase diagram (Di-Ol-Qtz) projected from plagioclase with 1 atmosphere phase boundaries from *Walker et al.* [1979] and high pressure phase boundaries from [*Stolper*, 1980]. Note that the 9°30'N samples exhibit a very small range and plot close to the 1 atm three phase cotectic.

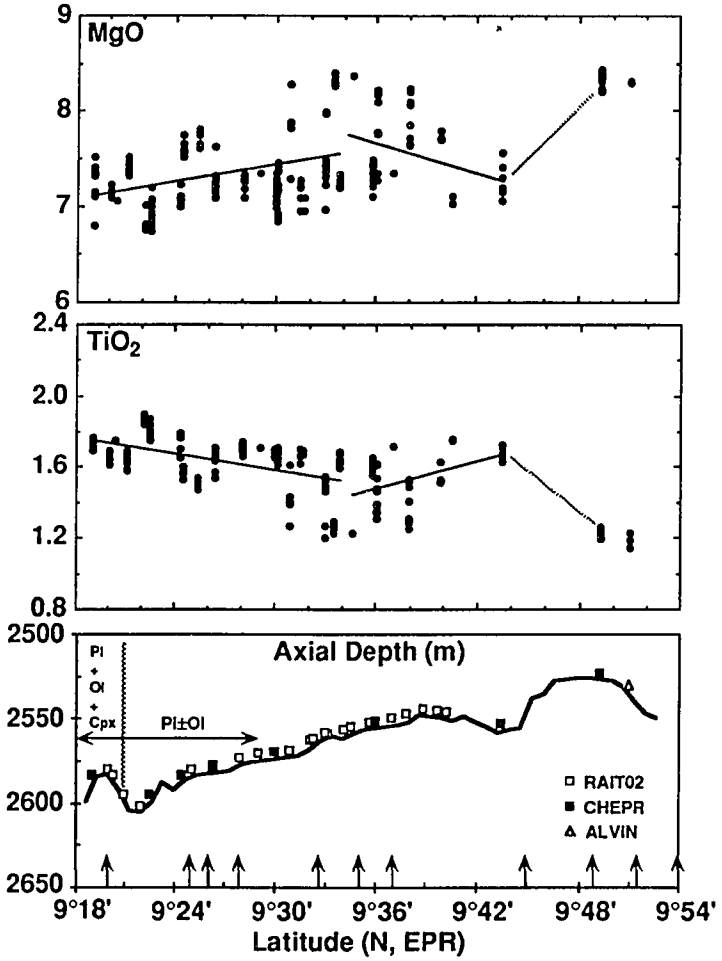

Fig. 4.10 Plots of MgO and TiO_2 against latitude. Dots are individual analyses. Note that local variability (scatter) is superimposed on a regular along axis trend of variation (regression lines). Regression lines are shown solid in areas of close-spaced samples and stippled when sampling is less dense. Also shown are dredge locations, devals (arrows), topography and petrographic observations from the 9°30'N lava suite. Note the rough correlation between average lava chemistry and topography. Comparison with Figure 1 shows that depth to the AMC also correlates with chemistry and topography. For interpretations of this correlation see text discussions.

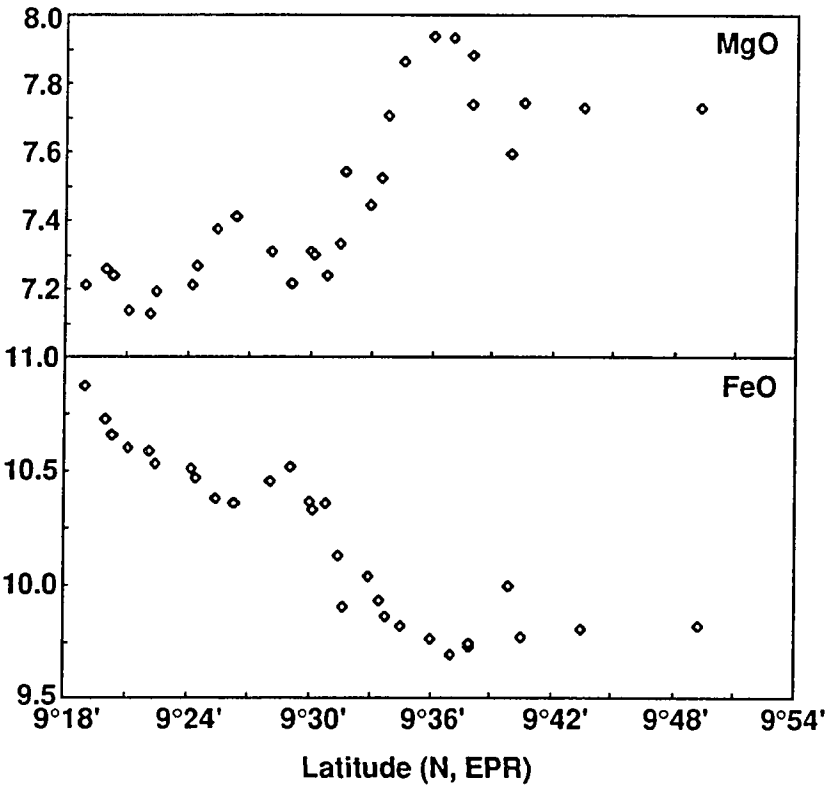

Fig. 4.11 The data of Figure 10 after smoothing with a moving boxcar 5 dredges in width like that used in Chapter 3. The regression lines in Figure 10 and the smoothed data shown here both indicate that local scatter is superimposed on a trend of regular along-axis variation.

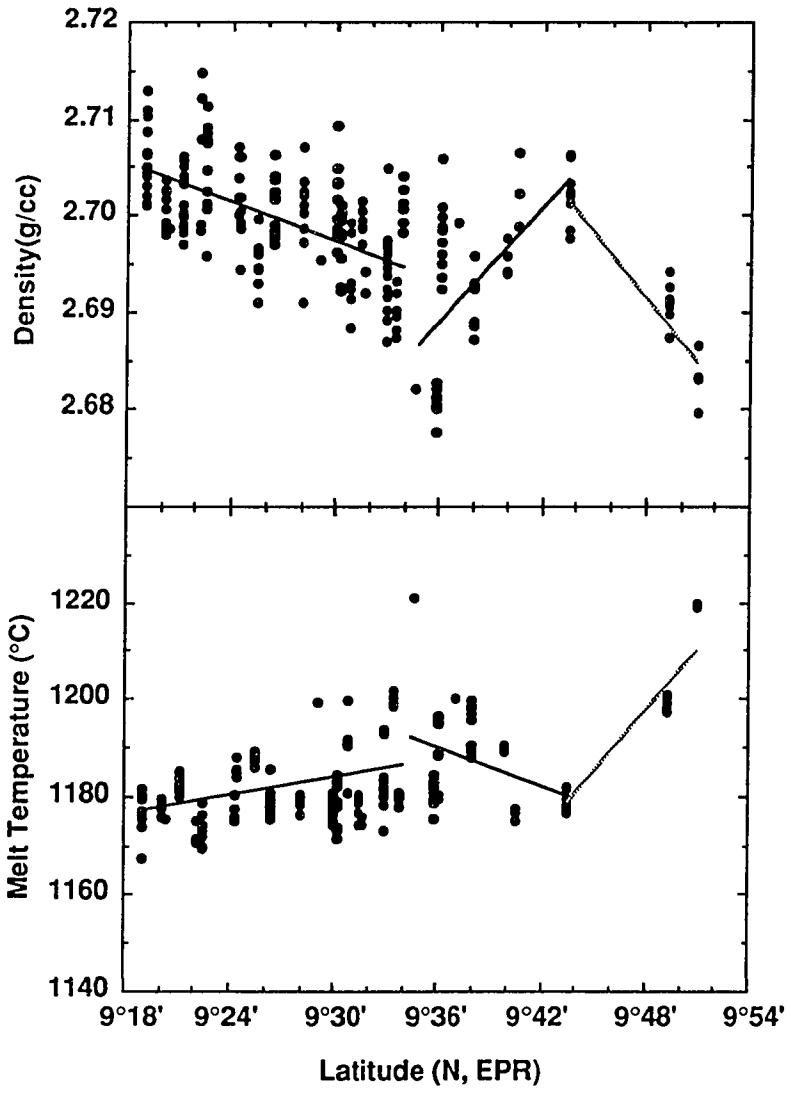

Fig. 4.12 Calculated density (see Chapter 2 for the method) and eruption temperature calculated using *Bender et al.* [1984] for the 9°30'N lavas. Note that both correlate with topography (Figure 10). The least dense, highest temperature melts are erupted at local topographic highs whereas the denser, Fe-rich melts are erupted at topographic lows where the AMC is also deepest (Figure 1).

factors given in the note to Table 4.4. Accuracy and precision of the U. Hawaii electron microprobe for basalt glasses and minerals are given in *Garcia and Wolfe* [1988] and *Garcia et al.* [1986].

Except for the E-MORB samples, the samples display chemical variations of the type typical of N-MORB suites from elsewhere along the mid-ocean ridge system [e.g., *Perfit et al.*, 1983; *Thompson et al.*, 1989; *Walker et al.*, 1979] often interpreted as the result of shallow fractionation processes. The 9°30'N suite is quite coherent (with scatter) and comprises a linear, continuous series on MgO variation diagrams (Figure 4.7). For convenience in data handling, I have computed group means (see Table 4.4 notes) and plot these group means in Figure 4.8 (MgO variation diagrams) and Figure 4.9 (Normative mineralogy).

Trace element data by Instrumentation Neutron Activation Analysis (INAA) for selected glasses are given in Table 4.5. These also show limited variation which can be explained almost entirely by fractional crystallization as discussed later.

4.4.4 Along-axis chemical variation

The chemical variation of lavas along axis in the 9°30'N area is not random. While there is significant chemical variation at each place along the axis, the mean values exhibit a fairly regular pattern of along-axis variation. Figure 4.10 shows that MgO and TiO_2 (other element as well) show local scatter, but also a crude variation along axis that correlates with topography. The along-axis pattern is clearly evident after smoothing with a moving boxcar filter (Figure 4.11). Local topographic highs at 9°48'N, and the 9°32'N to 9°38'N area correspond to the highest MgO and lowest TiO_2 values. The mean and maximum MgO values decrease away from the local topographic highs. Local topographic lows (e.g., at 9°43'N) and topographic gradients in slope (e.g., the deepening between 9°38'N and 9°20'N) can also be seen in the pattern of along-axis chemical variation. At the same

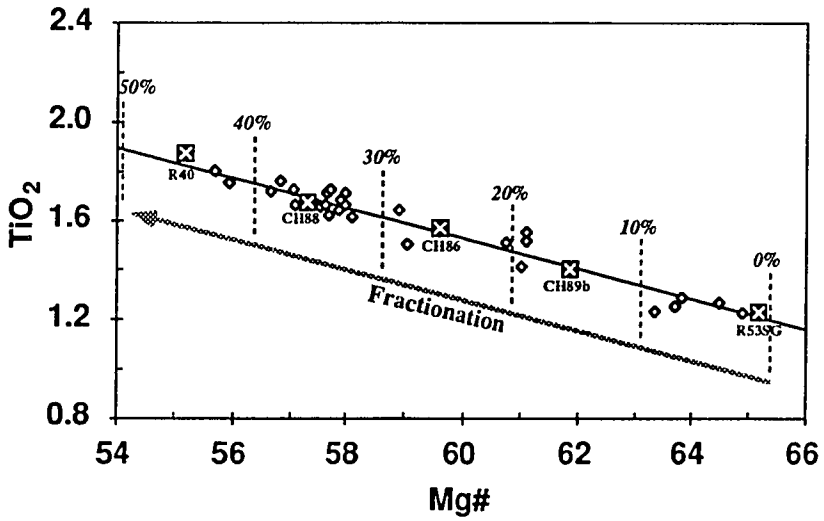

Fig. 4.13 Plot of TiO_2 vs. $Mg/(Mg+Fe^{2+})$ for the chemical group means of the 9°30'N area to illustrate my fractional crystallization model (Table 4.6). Additional models tested connect all the group means and consistently yield good fits for reasonable solid assemblages.

Table 4.6. Representative fractionation model results

Parent	+	Olivine	+	Plagioclase	+	Clinopyroxene†	= Daughters	Σxtl	Residuals
(R53SG)									
1.1679		-0.0258(Fo85.0)		-0.1076(An78.0)		-0.0291(Wo45.6En42.5Fs11.9)	CH89b	-0.1625	0.0124
1.2617		-0.0369(Fo85.0)		-0.1536(An77.0)		-0.0709(Wo43.1En42.9Fs12.4)	CH86	-0.2614	0.0372
1.3379		-0.0543(Fo84.4)		-0.2027(An76.0)		-0.0846(Wo42.3En34.6Fs23.1)	CH88	-0.3416	0.0213
1.4415		-0.0661(Fo84.0)		-0.2607(An75.0)		-0.1243(Wo42.3En34.6Fs23.1)	R40	-0.4511	0.0976

† Compositions taken from *Allan et al.* [1989] with similar host melt compositions. Olivine and plagioclase compositions are from Tables 4.2 and 4.3 respectively.

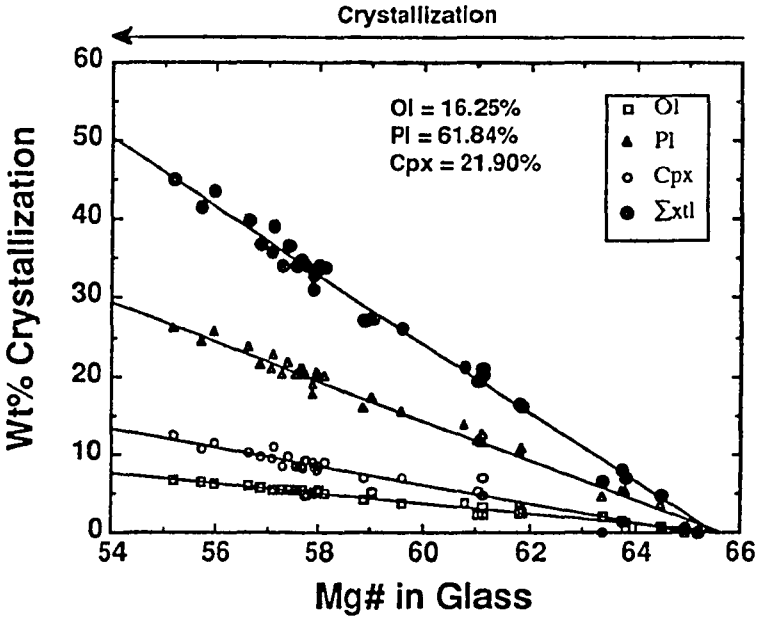

Fig. 4.14 Summary of the fractionation models I calculated. Note that in this range of temperature, the calculated phase proportions of the solid removed are essentially constant.

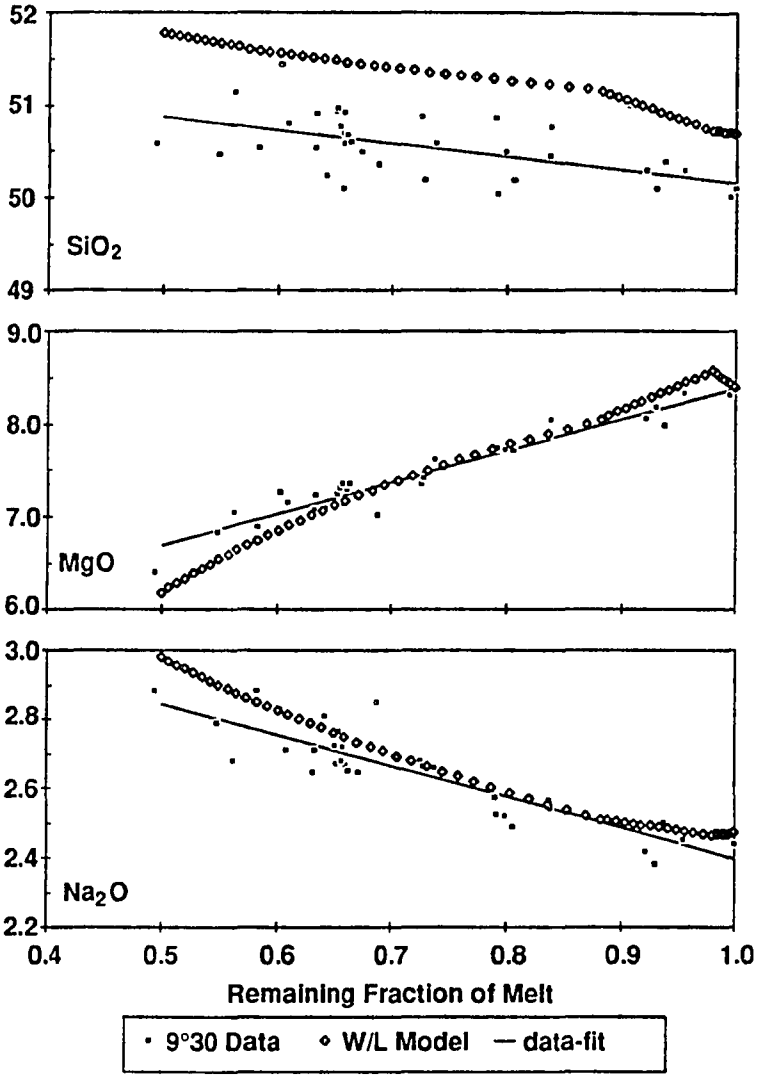

Fig. 4.15 Plots of SiO_2, MgO, and Na_2O versus calculated fraction of liquid remaining. These plots compare data (solid squares), my fractional crystallization model (thin solid line) and liquids predicted by the liquid-line-of-descent model (open diamonds) of *Weaver and Langmuir* [1990]. The offset in SiO_2 is due to a normalization procedure in the Weaver and Langmuir model. Note that data, my fractional crystallization model and the liquid-line-of-descent model all agree reasonably well. This agreement is reasonable for all elements, not just the ones shown here.

time, there is a range of variation at any latitude, for example MgO shows a variation of 1 wt % or more throughout the 9°30'N area. However, smoothing of this scatter shows that axial topography and depth to the top of the AMC (Figure 4.1) are correlated with axial MORB chemistry. As expected, computed melt density (see Chapter 2) and melt eruption temperature [*Bender et al.*, 1984] shown on Figure 4.12 also exhibit a crude correlation with depth to the AMC and axial topography, with the least dense, hottest magmas erupting at the local topographic highs near 9°36'N and 9°48'N to 9°50'N.

4.4.5 Radiogenic isotopes and eruption ages

Harpp et al. [1990] presented Sr and Nd isotope data for samples from the 9°30'N area. These results will be fully presented elsewhere, however I note here that the N-MORB samples exhibit only a small range of $^{87}Sr/^{86}Sr$ (0.70248 to 0.70252) which is within analytical error. In contrast, the E-MORB from dredge R-54 is significantly higher (0.70264). Results of U-Th disequilibrium dating and ^{226}Ra-^{230}Th-Ba dating will likewise be presented elsewhere. *Volpe and Goldstein* [1990] presented preliminary results indicating that N-MORB from 9°30'N area are significantly younger (~ 2700-3000 years) than the E-MORB samples (~ 6500 years). These data, though preliminary, indicate that the E-MORB samples from 9°35'N are not related temporally to the vast majority of N-MORB erupted along this portion of the EPR.

4.5 Interpretation and discussions

4.5.1 Petrogenesis of N-MORB

Data presented earlier suggest that the 9°30'N N-MORB suite may be related by fractional crystallization, so I have quantitatively modeled this process. Several hundred models were tested [*Bryan*, 1986], which essentially tested the derivation of each lower-MgO liquid from each higher-MgO liquid (group means). All models considered yield very

good fits (residual < 0.1) using reasonable phenocryst assemblages. A series of representative fractionation models is illustrated in Figure 4.13 (and Table 4.6) showing that the most fractionated liquids can be derived successively by fractional crystallization of the more MgO-rich melts. I emphasize that all the N-MORB melts in the 9°30'N area can be related in this manner, not only those shown in Figure 4.13.

A summary of the calculated models is shown in Figure 4.14. The phase proportions of olivine, plagioclase and cpx do not vary in this temperature interval and even the most primitive, highest temperature liquids ($Mg^{\#} \approx 65$) are multiply saturated in all three phases, in agreement with the liquid-line-of-descent model of *Weaver and Langmuir* [1990] (Figure 4.15) and normative mineralogy of the glasses (Figure 4.9). In a later section, I consider the question of why, if the fractionation model fits so well, are large cpx and olivine phenocrysts virtually absent from the suite of lavas.

Figure 4.16 shows that trace element abundances in the lavas are consistent with the fractionation model. Only a few elements, mostly in fractionated samples, fail to match the model within analytical uncertainty. Overall, the fit of major and trace element data to the model calculations is good and is consistent with isotopic data. But could some other processes also be involved which could lead to sporadic poor fits to the trace elements?

In order to test this notion further, I have carefully evaluated mixing models using both major and trace element data. In general, the fits of mixing models to the data are no better, and in many cases are much worse, than the fractionation models. I thus cannot preclude limited mixing, however fractional crystallization is apparently the dominant process at work in the 9°30'N area, as in the area north of the Clipperton transform [*Thompson et al., 1989*]. Trace element ratios, like trace element abundances, are in general, explained within analytical uncertainties by the fractionation models. A few exceptions, involving only La and Ce are shown in Figure 4.17. Inconsistently, one or more samples exhibit trace element ratios outside the range predicted by my simple

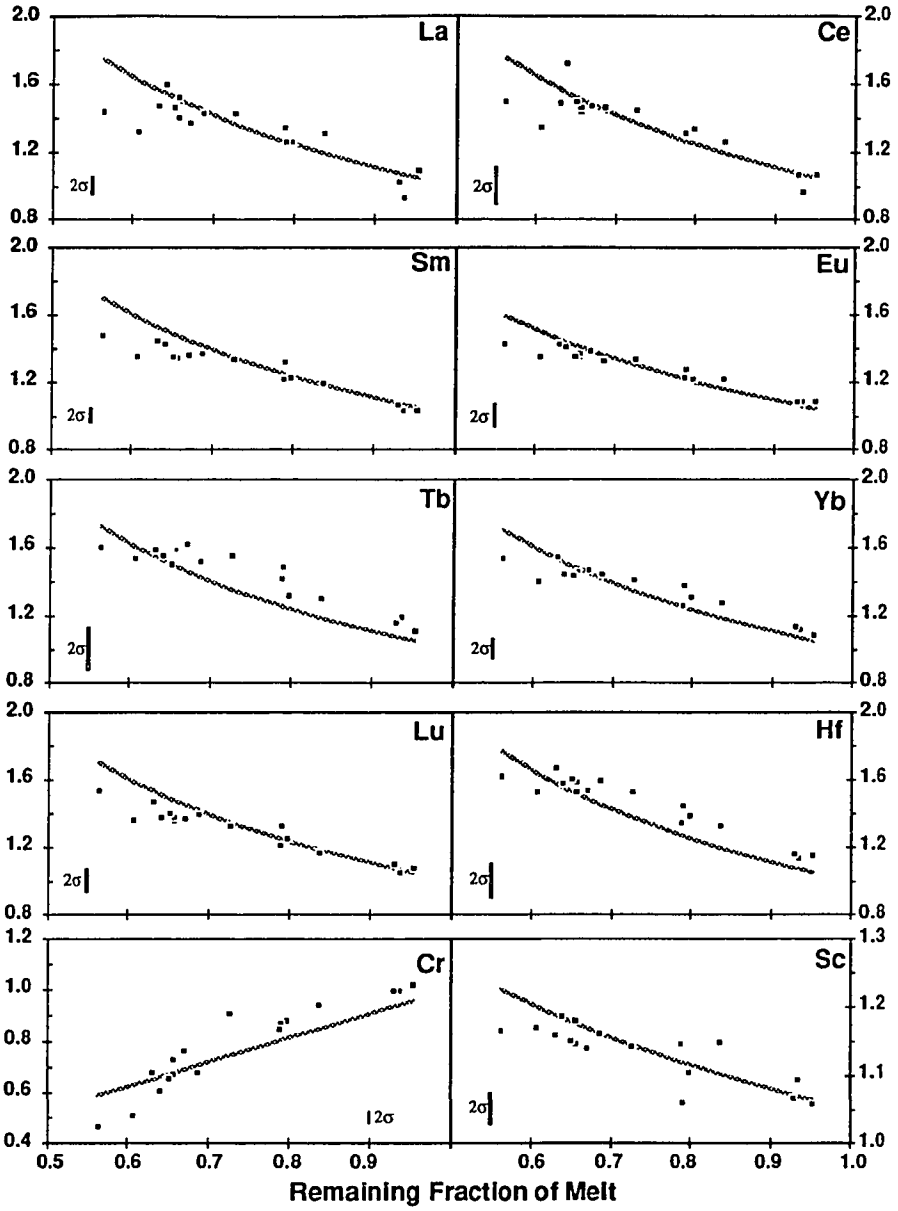

Fig. 4.16 Selected trace elements (Table 4.5) plotted to test the fractional crystallization model. The plots are all of enrichment factor ($^{Cl}/_{Co}$) versus remaining melt fraction predicted by the major element model (Figures 4.13 & 4.14). Partition coefficients used are from *McKay* [1989] for REE and *Henderson* [1982] for Hf, Sc and Cr. The lines are the model predictions for Rayleigh fractionation (perfect fractional crystallization). Analytical error bars are plotted on each panel. Note that with very few exceptions, the data and model are in good agreement.

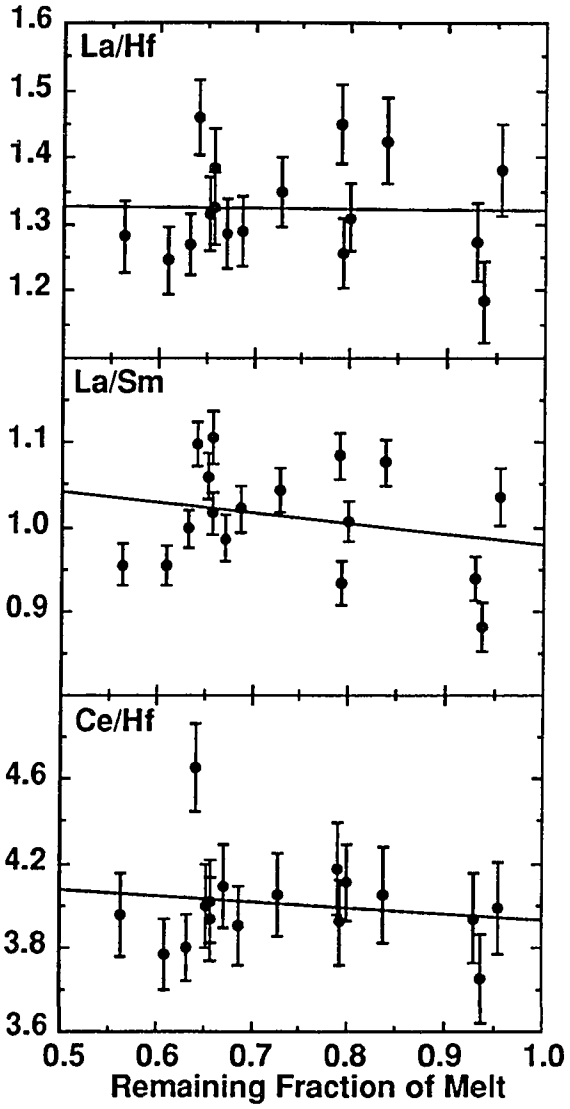

Fig. 4.17 Most trace element ratios agree within error (propagated as per *Le Maitre* [1982]) with the fractional crystallization model. Some rare examples of disagreement between the model (solid line) and the data are shown here. Note the lack of consistency in the mismatches. See text for discussion of possible interpretations.

fractionation model. This is interesting, and suggests that some additional process(es) may be involved in the petrogenesis of lavas. This process clearly does not have a large effect, as most trace element ratios even for La and Ce are predicted within error by the model. Further, this process does not affect the same samples in a consistent manner, nor are individual samples affected for all geochemically coherent elements. In addition this process does not lead to systematic enrichment or depletion relative to the fractionation model. Thus, I am at a loss to convincingly explain the origin of these minor inconsistencies. Many processes such as mantle heterogeneity, selective contamination, vapor transport and others could be involved, however there is no independent evidence nor convincing consistency with other data for any of these processes. Indeed, the major and trace element data plus isotope ratios are, with the few exceptions noted, well explained by a simple model of cooling and fractional crystallization from a single parent magma.

Using the chemical data presented earlier, I have tried to determine whether a single parental magma could give rise, by fractionation, to the entire 9°30'N suite of N-MORB or whether, alternatively, more than one parent is required. Within analytical uncertainties, and given the non-uniqueness of fractionation models, only one parental composition is required. In any case, if multiple parental liquids exist along the EPR axis between 9°20'N and 9°51'N, they are chemically very similar. The simplest hypothesis is that only a single parental liquid was injected to feed this entire ~ 60 km segment of the EPR.

As for the origin of this parental liquid, it could be derived from the type of aggregate primary melt proposed by *Klein and Langmuir* [1987], *McKenzie and Bickle* [1988], and this study, see Chapter 3). If so, using the method in Chapter 3 indicates that it could be derived by column melting initiated at ~ 19 kb (~60 km) and 1395°C and ending at ~ 12 kb (~ 40 km) and 1360°C. This aggregate melt represents about 18.5 percent melting of a mantle source such as MPY-90 [*Falloon and Green*, 1987].

4.5.2 Petrogenesis of E-MORB

The E-MORB at ~ 9°35'N appears to be temporally unrelated to the N-MORB suite. Because of isotopic and chemical differences, it cannot be related to the N-MORB by a simple process. Clearly, if the E-MORB is derived by simple melting of the same mantle that yielded the N-MORB, it must be a very tiny fraction of melt. However, the isotopic ratios preclude this simple scenario. Like E-MORB on seamounts near the axis of the EPR [*Batiza and Vanko*, 1984; *Zindler et al.*, 1984; *Graham et al.*, 1988], the E-MORB could be a mix of an enriched mantle plume [*Hanson*, 1977] with more depleted mantle matrix.

Alternatively, a volatile-rich, tiny melt fraction of the type suggested by *Hunter and McKenzie* [1989] might be involved. The E-MORB lavas are highly vesicular (up to ~ 10% in patches) and richer in plagioclase phenocrysts than the N-MORB, perhaps consistent with this notion. On the other hand, I cannot preclude a shallow origin of the E-MORB, as assimilation or in-situ crystallization [*Langmuir*, 1989; *Hekinian and Walker*, 1987] can also explain some features of the chemistry of the E-MORBs. Interestingly, the E-MORBs are the least dense melts within the 9°30'N area (Figure 4.18), even ignoring volatiles.

E-MORB is relatively rare in the 9°30'N area [*Perfit et al.*, 1991] and the 10°-11°N area of the EPR [*Thompson et al.*, 1989]. In contrast, it is much more abundant in the 12° - 13°N of the EPR [*Hekinian et al.*, 1989]. Following the hypothesis of *Hekinian et al.* [1989], it is possible that the 9°30'N E-MORB are relict from a prior E-MORB-dominated stage of activity, now complete at 9°30'N. Their model involves episodic melting, but time variation in the processes of deep magma transport and lateral melt focusing might also produce the same results.

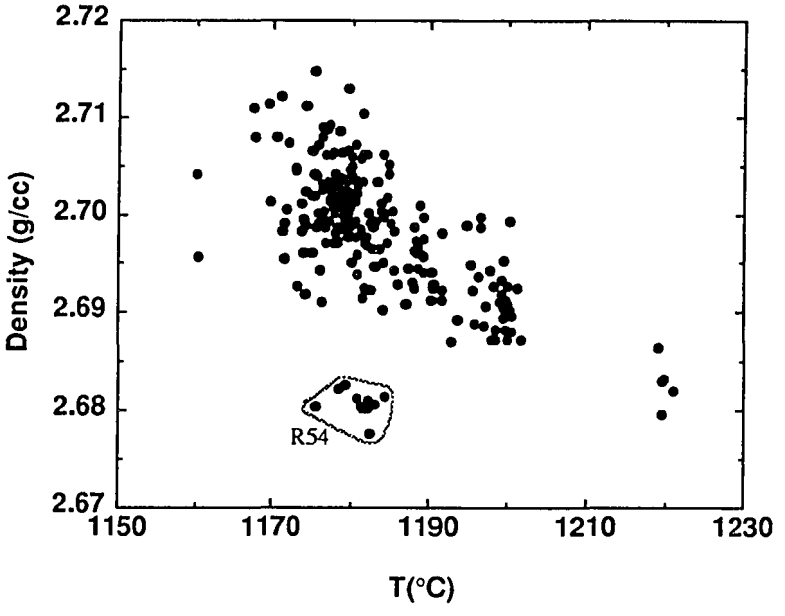

Fig. 4.18 Calculated volatile-free density and temperature for the 9°30'N magmas (see caption to Figure 11 for methods used). This plot illustrates the fact that the E-MORB magmas are the least dense of the low temperature liquids and thus are highly eruptable.

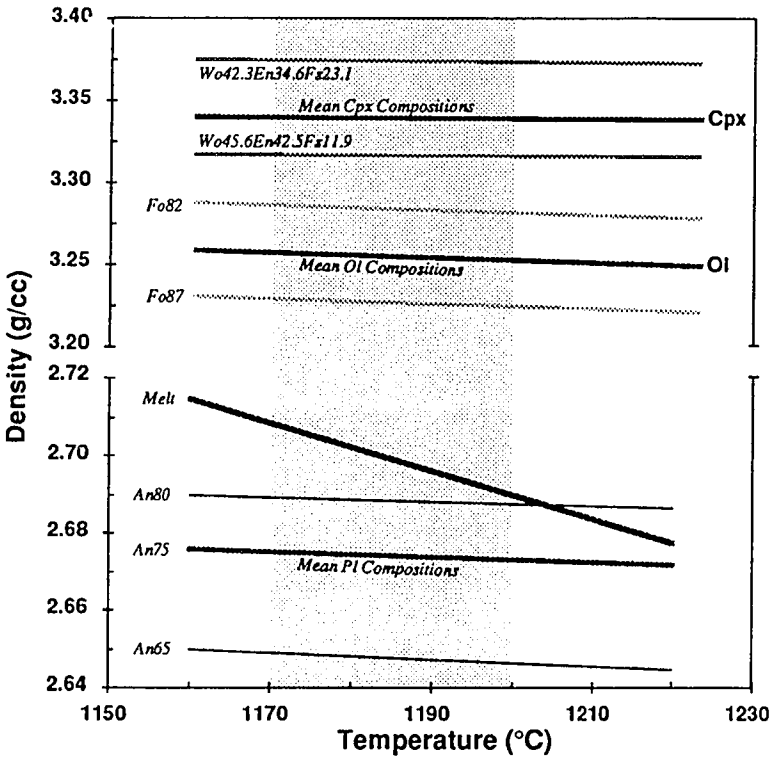

Fig. 4.19 Calculated densities of 9°30'N melts and solid phases (see Chapter 2 for the method) showing that plagioclase should float in most melts (shaded area) and olivine and cpx should sink. Note the broken density scale.

4.5.3 Where is the missing olivine and clinopyroxene?

Although fractional crystallization models, normative mineralogy, and liquid-line-of-descent models all predict that the N-MORBs should be multiply saturated with olivine, plagioclase and cpx, most of the lavas carry phenocrysts of only plagioclase. I propose that most of the lavas have suffered solid-liquid fractionation and two lines of evidence support this idea. First, the crystal size distribution data for plagioclase suggests a pattern that has been disturbed by the addition of plagioclase crystals (> 0.5 mm in size). Second, the calculated densities of N-MORB liquids and phenocrysts (Figure 4.19) indicate that plagioclase should float and mafic crystals should sink in the N-MORB melts. The consistent indication is that the 9°30'N lavas represent fractionated melts with some plagioclase added and mafic phenocrysts removed by some process. Most likely this process is gravitational, though flow differentiation cannot be ruled out.

It is of interest to attempt to determine where in the magma pluming system this solid-liquid fractionation took place, since this would provide clues on residence times and possibly rates of flux through the various reservoirs in the system. Clearly, solid-liquid separation could occur below the AMC or in the AMC [e.g., *Sinton and Detrick*, 1992], however it is also possible that cooling, crystallization and solid-liquid fractionation could occur in dikes and/or after eruption.

The latter possibility seems unlikely because if crystal settling occurred within cooling lava flows, then at least a few samples of the plagioclase-poor, olivine - cpx rich complement to the 9°30'N lavas should have been sampled. Collapse fractures, faulting, fissuring, and other processes at the axis prevent selective sampling of only the tops of lava flows.

In order to test whether it is plausible that the fractionation processes occurred in dikes, I consider possible cooling times of basalt liquid rising in dikes. For cooling, crystallization and solid-liquid fractionation to have occurred in dikes, the most primitive

melts would have to cool up to 60°C (see Figure 4.12). For a dike 1 meter wide, rising in crust buffered by a hydrothermal convective geotherm (~ 400°C), this amount of cooling would require on the order of 12 hours [*Jaeger*, 1968, p.508]. However, crystal settling in a dike 1 km long or more would require several orders of magnitude longer [e.g., *Kerr and Lister*, 1991] by which time the dike would be fully solidified. This simple calculation indicate that dikes are unlikely loci for extensive cooling, fractionation and crystal settling.

These arguments tend to favor the AMC as the most likely place for solid-liquid fractionation to occur. If melt zones (or liquid-rich mush zones) are small, as seems likely [*Kent et al.*, 1990; *Sinton and Detrick*, 1992], settling distances would be relatively short (< 100 m?) and the process could occur relatively rapidly. A complication is that the large plagioclase crystals I infer to be of cumulate origin represent only a small fraction of the total plagioclase which I infer from the modeling must have crystallized from the fractionated melts. This indicates that conditions of crystallization and solid-liquid fractionation in the AMC melt-mush are probably quite complex. Crystallization in the melt lens versus surrounding mush zones may be quite different, both physically and chemically. The higher crystal content, plus the presence of cpx megacrysts in lavas south of 9°17'N where the AMC reflector is off-axis, provide evidence that a crystal-rich mush zone surrounds the small AMC melt lens, as proposed by *Sinton and Detrick* [1992].

4.5.4 Along-axis chemical variation

I now return to consider the possible causes for along-axis chemical variation within the 9°30'N area. I wish to explain not only the along-axis variation (Figure 4.11) but also the observed scatter that is superimposed (Figure 4.10). Evidently both effects are the result of shallow-level fractional crystallization which occurred principally in the AMC melt zone, not the surrounding zone of mush. This assumes, of course, that the lavas I sampled were erupted from an AMC of roughly the same depth, extent and geometry as presently

observed. I first consider the along axis chemical variation which correlates roughly with variations in AMC depth and topography (Figures 4.1, 4.10 and 4.11).

If the AMC occupies a level of neutral buoyancy along axis, which seems very likely [*Ryan*, 1987], then simple extreme possibilities are 1) that the crustal lid has along-axis differences in density structure (and the melt has constant density) or 2) that the melt varies in density and composition (and the lid has a constant density gradient with depth) as shown in Figure 4.20. For these cases, if the axial basalts were erupted from a chamber of the present depth configuration, the along-axis chemical differences arise either because the AMC is chemically zoned along axis, or because the extent of fractionation is proportional to the lid thickness. The latter is reasonable since the amount of cooling that the melt will undergo in dikes is proportional to the distance between the top of the AMC and the surface for constant ascent rate. However, crystallization accompanies cooling, and I already have argued that it is unlikely for melt-crystal fractionation to occur in dikes.

The evidence thus seems to favor a laterally zoned magma chamber. Other more complex scenarios are also possible, of course. However if the assumption that the axial basalts erupted from an AMC of the present extent and depth is correct, a laterally zoned chamber is the simplest interpretation. If so, then the age of the N-MORBs [~ 2700 - 3000 years, *Volpe and Goldstein*, 1990] implies an AMC which is in steady-state on the time scale of ~ 3000 years. Figure 4.21 shows the scenario I favor based on the data and arguments presented above. Eruptions from a zoned chamber could also explain small scale topographic changes, as the least dense melts (Figure 4.12) are located at the highest portion of the axis, as predicted by simple magma-static head arguments.

While an AMC that is chemically zoned along-axis seems to adequately explain the along-axis variation, it does not provide a simple explanation for the observed local scatter (Figure 4.10). If the chamber were chemically stratified, then individual eruptions from the AMC could vary chemically, but if the AMC is very small [*Kent et al.*, 1990; *Sinton and*

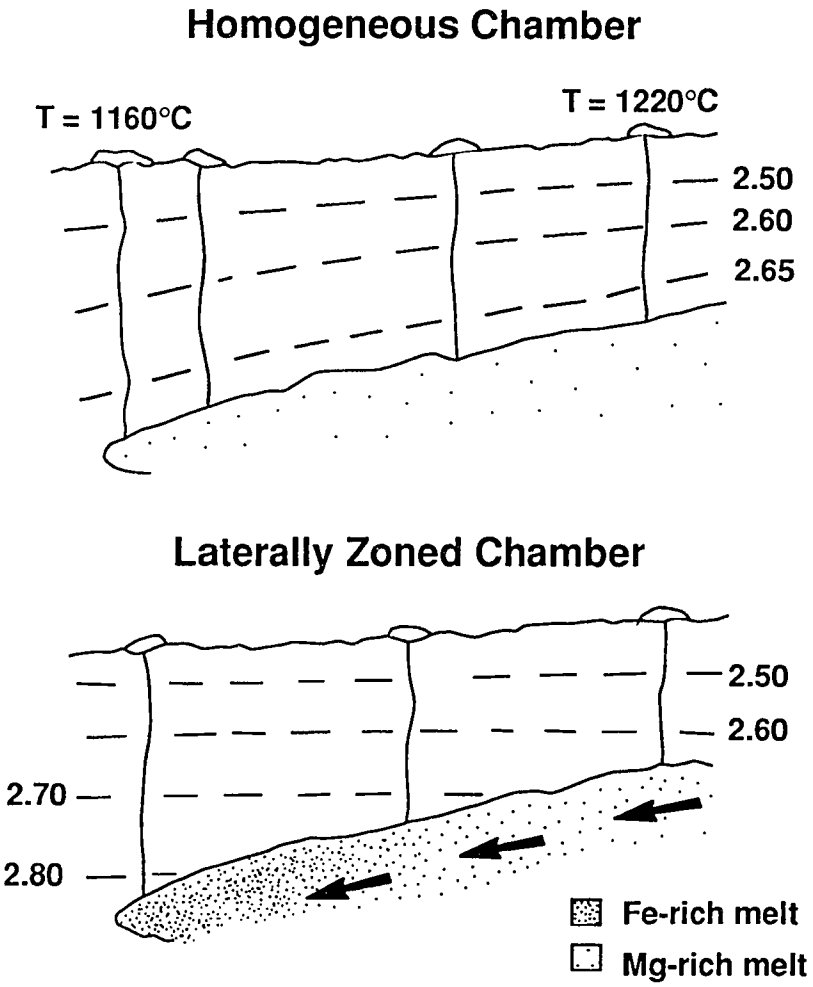

Fig. 4.20 Cartoon view of two extreme scenarios that result from the assumption that the AMC occupies a level of neutral buoyancy. I favor the interpretation in the lower panel because of the observed along-axis variation in chemistry and because it is unlikely that chemical differentiation could arise from processes occurring in dikes or in flows after eruption.

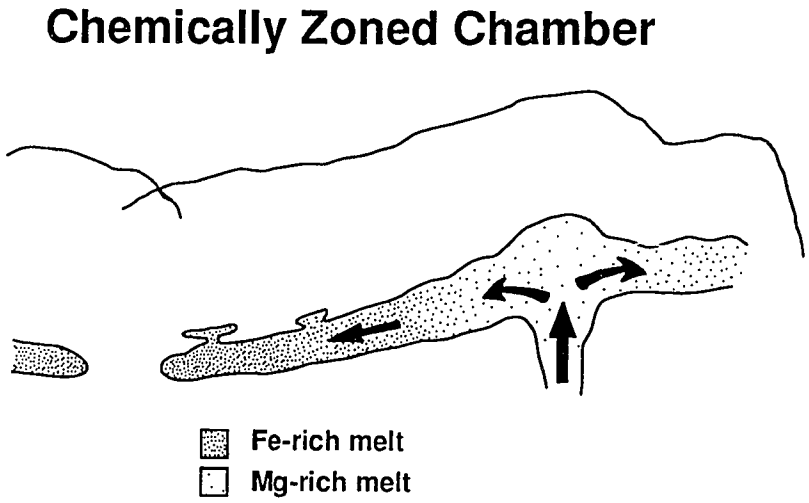

Fig. 4.21 Cartoon view of the scenario I favor to explain the along-axis chemical variation in the 9°30'N area. This shows a chemically zoned magma lens with small, semi-isolated pockets of melt to explain the local chemical variation observed at any place along the axis (scatter).

Detrick, 1992] chemical stratification seems unlikely. However, small scale along-axis segmentation of the AMC, with small semi-isolated pockets of melt which cool at slightly different rate, could explain the observed scatter. Small scale temporal variation caused by the dynamic processes of AMC recharge could enhance local variation at any spot along the EPR axis.

4.5.5 AMC resupply dynamics

If a laterally zoned magma chamber is present below the 9°30'N area of the EPR, it is of interest to ask how it achieved its chemically zoned state. One possibility is that when it was first emplaced it was homogeneous, and that simple cooling has resulted in chemical zonation. However, this seems unlikely, as the deepest portions of the chamber (most Fe-rich) would have to cool the most. This would require large lateral gradients in thermal structure for which there is no evidence. Another possibility is that the chamber was emplaced in a zoned configuration by vertical ascent of magma from below. This also is possible but requires that the observed fractionation occur during this deeper ascent prior to emplacement. Petrological evidence presented earlier makes this unlikely.

Another possibility is that the chamber acquired its zonation during emplacement or resupply. If I consider a central injection model of the type suggested by *Sempéré and Macdonald* [1986] and *Macdonald et al.* [1988], which is similar to models of magmatic pluming below Icelandic and Hawaiian rift zones, then very slow along-axis emplacement of an AMC could cause chemical zonation. In this model of very slow emplacement, the earliest magma emplaced would travel along axis the farthest from the initial site of vertical injection and consequently would cool the most. However, for a small AMC, the emplacement time in this model would have to be a significant fraction of the life of the AMC itself. This fraction is essentially the time needed for the magma to cool ~ 60°C

balanced against the time needed for complete solidification (cooling of 100°C - 200°C, *Yoder*, 1976]. For this reason, a very slow along-axis injection model seems unlikely.

An alternative to slow injection is episodic central recharge of the AMC. This model also could produce a zoned chamber if new melt batches have a higher probability of being injected only a short distance along axis [*Macdonald et al.*, 1987]. Lateral mixing by convection in a long chamber with a small cross section is thought to be negligible [*Oldenberg et al.*, 1989; *Sinton and Detrick*, 1992], so, if new melt batches are injected only limited distances along axis and do not reach the distal ends, older fractionated magma could be preserved even with frequent episodes of lateral resupply. If this occurred in the 9°30'N area, all the melt batches supplied episodically would have to be identical or nearly identical chemically and isotopically.

4.5.6 Implications for magma supply at the EPR

My interpretations of the data presented above favor a chemically zoned AMC beneath 9°30'N. I favor a melt zone or lens of the type suggested by *Kent et al.* [1990] and *Sinton and Detrick* [1992]. A long, narrow and laterally restricted melt lens can explain most of the features we observe. If the melt lens is segmented [*Toomey et al.*, 1990], and/or has a complex geometry and/or the thermal structure is heterogeneous, such a lens may simultaneously host melts of variable chemistry. This could explain the range of chemistry we see at any given site along axis. Alternatively, this variation may be the result of small age differences among the N-MORB lavas at any given site. Recent dense sampling of the 9°30N area [*Perfit et al.*, 1991] will probably be extremely helpful in distinguishing among the possibilities.

In order to create a zoned magma chamber, I favor a dynamic along-axis emplacement model like that of *Macdonald et al.* [1987, 1988], with episodic resupply of magma. Thermal models [e.g., *Wilson et al.*, 1988] suggest that chambers may come and go at any

locality along the EPR. The presence of older E-MORB in the 9°30'N area is consistent with the episodic presence of the AMC because the E-MORB most likely erupted at a time when the AMC was absent or much smaller in size. Otherwise, it would have mixed with N-MORB in the AMC prior to eruption. If so, the present AMC at 9°30'N is probably younger than ~ 6500 years (the age of the E-MORB).

My data favor an important role for the AMC in volcanic-tectonic segmentation of the EPR [*Toomey et al*, 1990]. But since I find the same parental magma along ~ 60 km of the EPR, central injection sites must be spaced at greater intervals than the smallest scale segmentation. Deval-bounded, 4th-order segmentation may be correlated with systematic along-axis fractionation differences, but these are below the resolution of the sampling so far. Overall, the new data favor a hierarchical supply system like that proposed by *Langmuir et al.* [1986], *Macdonald et al.* [1987, 1988] and *Sinton et al.* [1991].

4.6 Summary and conclusions

The major conclusions of this chapter are as follows:

1) The axis of the EPR in the 9°30'N area (9·17'N to 9°51;N) has mostly N-MORB with a narrow range of MgO and usually plagioclase phenocrysts only. The chemistry of the lavas varies along axis, correlating roughly with elevation of the axis and depth to the axial magma chamber (AMC).

2) Major and trace element data are best explained by derivation of all the 9°30'N N-MORB from a single parental melt by fractional crystallization of olivine, plagioclase, and clinopyroxene.

3) The virtual absence of olivine and cpx phenocrysts plus crystal size distribution analysis for plagioclase are best explained by crystal settling (olivine and cpx) and flotation (plagioclase) occurring in the AMC. However in detail, this process is probably complex, involving melt migration from the mush zone into the melt lens.

4) Enriched E-MORB at 9°35'N is older and not directly related to the N-MORB. It probably erupted at a time when the AMC was absent or much smaller in size, perhaps at the initiation of a new magmatic cycle.

5) Along-axis chemical variation and correlation of chemistry with depth to the AMC is best explained as the results of eruptions from an AMC that is chemically zoned along its length, with Fe-rich dense melts at the distal, deep ends of the AMC. Correlation with topography may be explained by melt density with least dense melts creating higher volcanic constructions.

6) Local chemical variations at any site along the EPR at ~ 9°30'N may be due to segmentation of the AMC, small pockets of melt, heterogeneity in thermal structure and/or small scale temporal variation resulting from AMC resupply dynamics.

7) Chemical zonation of the AMC could result from numerous processes, but I favor a dynamic cause related to central episodic injection of MgO-rich magma at sites along the axis with lateral along-axis transport. Injection sites are apparently spaced on the order of 50 km or more and thus do not correspond to the 4th-order deval-bounded segmentation.

CHAPTER 5

CHEMICAL VARIATION TRENDS AT FAST AND SLOW-SPREADING MID-OCEAN RIDGES

5.1 Abstract

I examine an expanded global data set of MORB major element analyses. In agreement with previous results, I show that slow-spreading ridges tend to have more primitive (high Mg/Fe) lavas than fast-spreading ridges. Fractionation-corrected values of $Na_{(8)}$ and $Ca_{(8)}/Al_{(8)}$ (indices of the extent of melting) and $Si_{(8)}/Fe_{(8)}$ (an index of the pressure of melting) do not vary systematically with spreading rate. Assuming a mantle that is generally homogeneous in major elements, I conclude that mantle temperature below mid-ocean ridges is independent of spreading rate. Using data for thirty-two best-sampled ridge segments of variable length scales, I show that the so-called global and local trends of chemical variation [*Klein and Langmuir*, 1989] are systematically distributed with spreading rate. The global trend occurs at fast-spreading ridges (> 60 mm/yr), whereas the local trend occurs at slow-spreading ridges (< 50 mm/yr). Because this distribution is independent of geographic length scale, I refer to the two trends of chemical variation as the fast and slow trends. Among the thirty-two ridge systems I examine, the slopes of the two trends on chemical diagrams show some variability, but no regular pattern, such as fanning.

The global or fast trend is well-explained by mantle temperature differences occurring at several length scales within mantle rising passively in response to plate separation. I propose that the slow trend arises from processes occurring in buoyant diapirs undergoing melting and melt-solid reequilibration. Several lines of geophysical and geological evidence point to the importance of buoyant, 3-D mantle upwelling beneath slow-spreading ridges. Petrologic modeling presented here is consistent with this hypothesis, as is the

existence of the slow trend in the chemical variation of seamounts on the flanks of the East Pacific Rise.

5.2 Introduction

Mid-ocean ridges are tectonically and magmatically active sites of generation of oceanic crust. It is well-established that spreading rate is an important variable associated with many significant differences along the global mid-ocean ridge system. For example, morphologic differences are largely controlled by spreading rate [e.g., *Macdonald*, 1982; *Franchteau and Ballard*, 1983], with slow-spreading ridges typically having deep axial rift valleys that are much less pronounced or absent at fast spreading rates. Related topographic roughness on the flanks of mid-ocean ridges also depends on spreading rate [*Pockalny and Detrick*, 1983; *Malinverno and Pocklany*, 1990; *Malinverno*, 1991; *Hayes and Kane*, 1991; *Small and Sandwell*, 1989]. Along-axis gravity [*Lin et al.*, 1990; *Lin and Phipps Morgan*, 1992] shows important changes with spreading rate, interpreted to reflect fundamental differences in the style of mantle upwelling, with dominantly 2-D, plate-driven upwelling below fast ridges and more 3-D, buoyantly driven, diapiric upwelling beneath slow-spreading ridges.

In addition to topographic and geophysical differences, petrologic differences exist between fast and slow-spreading ridges [e.g., *Morel and Hekinian*, 1980; *Natland*, 1980; *Flower*, 1980; *Batiza*, 1991; *Sinton and Detrick*, 1992] with slow ridges typically having more primitive (higher Mg/Fe) lavas and fast ridges more fractionated ones. Though isotopic variability may also be a function of spreading rate [e.g., *Cohen and O'Nions*, 1982; *Allègre et at.*, 1984; *Batiza*, 1984], this is controversial [e.g., *Macdougall and Lugmair*, 1986; *Ito et al.*, 1987; *Holness and Richter*, 1989], as any simple relationship between spreading rate and isotopic diversity is greatly complicated by plate recycling, mantle convection and mixing [e.g., *Hart and Zindler*, 1989; *Hart*, 1988].

In this study, made possible by the recent availability of several large data sets of mid-ocean ridge basalt (MORB), I examine an expanded global data set of MORB major element analyses. I first confirm previous results regarding spreading-rate dependence of the extent of fractionation of MORB. In agreement with previous studies, I find that fast-spreading ridges have, on average, more fractionated, lower Mg/Fe MORB lavas than slow-spreading ridges.

I then use data for thirty-two well-sampled portions of the global ridge system to evaluate chemical variation trends as a function of plate spreading rate. *Klein and Langmuir* [1987] showed that globally, MORBs show an inverse correlation between $Fe_{(8)}$ and $Na_{(8)}$, where the subscript denotes values corrected for shallow fractionation to an MgO content of 8.0 wt%. They interpreted this result in terms of a polybaric decompression melting model and showed that deep (high $Fe_{(8)}$), extensive (low $Na_{(8)}$) melting would be expected from the pooling of polybaric melts produced from a long mantle column with high initial melting temperature. In contrast, a short mantle melting column with low initial melting temperature would be expected to produce pooled melts reflecting shallower (low $Fe_{(8)}$) and less extensive (higher $Na_{(8)}$) melting. Regionally averaged MORB analyses exhibit a trend of negative correlation between $Fe_{(8)}$ and $Na_{(8)}$, called the global trend by *Klein and Langmuir* [1989].

However, some mid-ocean ridge segments, such as the mid-Atlantic ridge at 26°S [*Batiza et al.*, 1988], exhibit an opposite trend: $Fe_{(8)}$ and $Na_{(8)}$ show a positive, not inverse correlation. That is, shallow (low $Fe_{(8)}$), extensive (low $Na_{(8)}$) melting is on a trend with deep (high $Fe_{(8)}$), less extensive (high $Na_{(8)}$) melting. This trend of chemical variation was termed the local trend by *Klein and Langmuir* [1989]. The global and local trends are shown in Figure 5.1.

In this study, I find that the so-called global trend is found at fast (> 60 mm/yr full rate) spreading ridges and that the so-called local trend is found at slow (< 50 mm/yr)

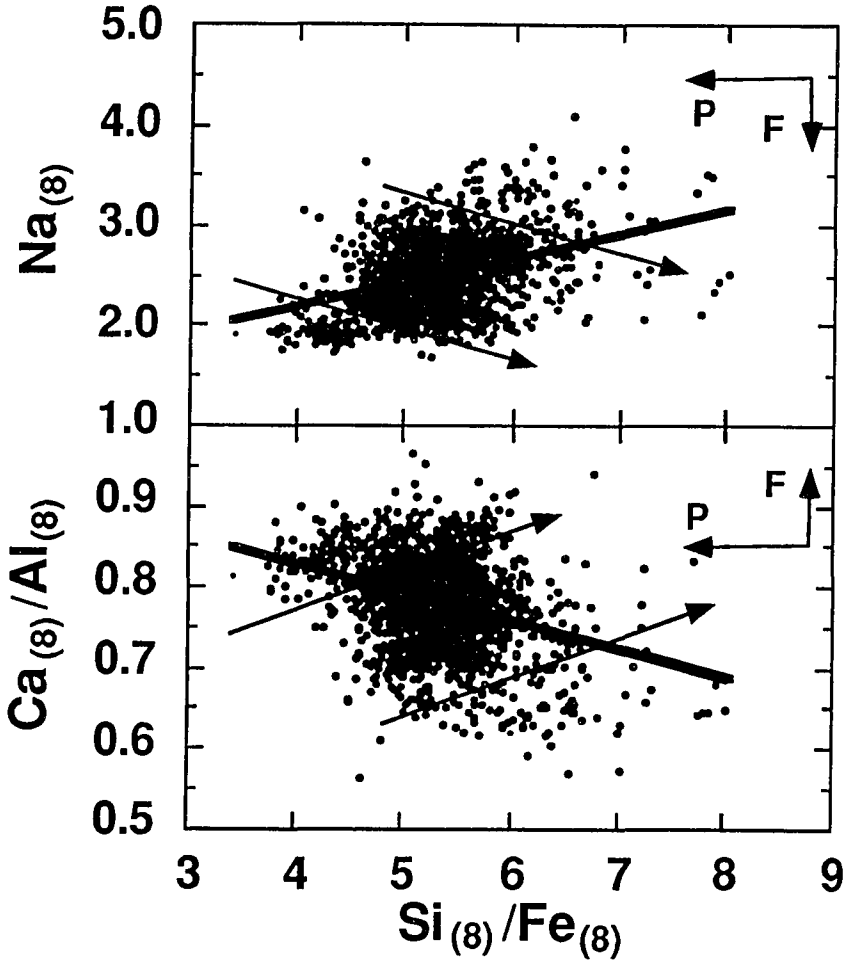

Fig. 5.1 The global and local trends of chemical variation [*Klein and Langmuir*, 1989] are shown here on $Na_{(8)}$ and $Ca_{(8)}/Al_{(8)}$ vs. $Si_{(8)}/Fe_{(8)}$. The subscript denotes values of the oxide corrected for shallow fractionation to a MgO content of 8.0 wt % [*Klein and Langmuir*, 1987]. Following my technique in Chapter 3, I use both $Na_{(8)}$ and $Ca_{(8)}/Al_{(8)}$ as indices of the extent of melting and $Si_{(8)}/Fe_{(8)}$ as an index of the pressure of melting. Arrows on each diagram point to high pressure and higher extent of melting. The data points are from the new global data set of MORB. The heavy line shows the so-called global trend and the thin solid lines with arrows (pointing to increasing extent of melting) show (schematically) examples of local trends.

spreading ridges. Transitional ridges (50 - 60 mm/yr) may exhibit either trend of chemical variation. This finding is independent of the ridge length and thus, for simplicity, in this chapter I refer to these two trends of chemical variation as the fast and slow trends rather than global and local trends. I consider several possible origins for the slow trend and conclude that it is due to fundamental differences in the dynamics of mantle upwelling beneath slow-spreading ridges.

5.3 The data set

To the global MORB glass data set of *Brodholt and Batiza* [1989], I have added the data of *Sinton et al.* [1991] for the southern East Pacific Rise (EPR), *Thompson et al.* [1989] and *Hekinian et al.* [1989] for the northern EPR, *Klein et al.* [1991] and *Dosso et al.* [1988] for the South-East Indian ridge, *Humler and Whitechurh* [1988] for the Central Indian ridge, *Michael et al.* [1989] for the Explorer ridge, and *Bougault et al.* [1990] for the northern mid-Atlantic ridge (MAR). I also use the updated 1991 version of Melson and O'Hearn's Smithsonian Institution Volcanic Glass Project (SIVGP) data set. I use sample group means for the analysis and include both glass and whole rock data (< 5%). Using correction factors in Chapter 4, I adjust Lamont-Doherty Geological Observatory and University of Hawaii probe glass analyses to conform with the Smithsonian analyses. Data sources of MORB analyses are given in Table 5.1.

Spreading rates are from NUVEL 1 [*DeMets et al.*, 1990], except for the Explorer ridge [*Botros and Johnson*, 1988], Juan de Fuca [*Wilson*, 1988] and Gorda ridge [*Davis and Clague*, 1987].

Table 5.1. Data set

Ridge	# Group Means	MgO>5wt%	Data Sources
N. EPR	553	531	1,4,6,11,23,24,25,26,30,35,42,43,54,55,56
S. EPR	263	243	1,12,45,51,55
Gorda	28	28	1,16
Juan de Fuca	184	181	1,19,31,32
Explorer	87	83	1,15,41
Galapagos	172	130	1,2,13,14,21,22,46,47
Easter, East Ridge	15	15	1,49
Easter, West Ridge	40	40	1,49
N. MAR	712	704	1,7,8,9,29,34,40,43,44,48,50,52
S. MAR	97	89	1,5,17,28,39,56
Cayman Rise	26	26	1,53
Carlsberg	10	10	1
Red Sea	19	18	1
America-Antarctic	46	46	1,38
S. W. Indian	39	39	1,20,36,37
S. E. Indian	63	63	1,3,18,33
Central Indian	33	33	1,27
Total	2387	2279	

1, Smithsonian; 2, *Anderson et al.* [1975]; 3, *Anderson et al.* [1980]; 4, Chapter 4; 5, *Batiza et al.* [1988]; 6, *Bender et al.* [1984]; 7, *Bougault & Hekinian* [1974]; 8, *Bougault et al.* [1988]; 9, *Bryan & Moore* [1977]; 10, *Bryan* [1979]; 11, *Byers et al.* [1986]; 12, *Campsie et al.* [1984]; 13, *Christie & Sinton* [1986]; 14, *Clague et al.* [1981]; 15, *Cousens et al.* [1984]; 16, *Davis & Clague* [1987]; 17, *Dickey et al.* [1977]; 18, *Dosso et al.* [1988]; 19, *Eaby et al.* [1984]; 20, *Engel & Fisher* [1975]; 21, *Fisk et al.* [1982]; 22, *Perfit et al.* [1983]; 23, *Hawkins & Melchior* [1980]; 24, *Hekinian & Walker* [1987]; 25, *Hekinian et al.* [1985]; 26, *Hekinian et al.* [1989]; 27, *Humler & Whitechurch* [1988]; 28, *Humphris et al.* [1985]; 29, *Jakobsson et al.* [1978]; 30, *Juteau et al.* [1980]; 31, *Karsten* [1988]; 32, *Karsten et al.* [1990]; 33, *Klein et al.* [1990]; 34, *Langmuir et al.* [1977]; 35, *Langmuir et al.* [1986]; 36, *Le Roex et al.* [1982]; 37, *Le Roex et al.* [1983]; 38, *Le Roex et al.* [1985]; 39, *Le Roex et al.* [1987]; 40, *Melson & O'Hearn* [1986]; 41, *Michael et al.* [1989]; 42, *Moore et al.* [1977]; 43, *Morel* [1979]; 44, *Neumanm & Schilling* [1984]; 45, *Renard et al.* [1985]; 46, *Schilling et al.* [1976]; 47, *Schilling et al.* [1982]; 48, *Schilling et al.* [1983]; 49, *Schilling et al.* [1985]; 50, *Sigurdsson* [1981]; 51, *Sinton et al.* [1991]; 52, *Stakes et al.* [1984]; 53, *Thompson et al.* [1980]; 54, *Thompson et al.* [1989]; 55, *Tighe* [1988, EPR synthesis]; 56, data from Chapter 4 and some unpublished data from 26°S MAR.

5.4 Results

5.4.1 Oxide trends with spreading rate

Plots of the global MORB data against spreading rate show much scatter but statistically significant trends for all the major and minor elements except SiO_2, which is known to have little variation during fractionation. Table 5.2 gives the slope, intercept, and correlation coefficients of these linear trends and Figure 5.2 shows representative examples. With increasing spreading rate, TiO_2, FeO, Na_2O and P_2O_5 increase, while Al_2O_3, MgO and CaO decrease. These trends confirm previous findings that lavas from fast ridges are typically more fractionated than those erupted at slow ridges. Note that although K_2O shows a statistically significant correlation with spreading-rate, it is inconsistent with a fractionation process (negative slope). This is not suprising because K_2O is a very incompatible trace element oxide and is not controlled by stoichiometry of mantle mineral phases, so its variation to a large extent reflects source heterogeneity; higher K_2O contents in lavas from slow spreading ridges may indeed result from hot-shot effect such as at the North mid-Atlantic ridge. When the analyses are corrected for shallow fractionation by backtracking along liquid lines of descent (LLD) using a procedure similar (see Appendices C and D for details) to that of *Klein and Langmuir* [1987], these correlations virtually disappear. As shown in Table 5.2 and Figure 5.2, after correction, the slopes are reduced by as much as an order of magnitude; plots of chemical variations against spreading rate are essentially flat (with much scatter).

Assuming mantle source is homogeneous with respect to major elements, which is reasonable because major elements are controlled by mineral stoichiometry, and a column melting model similar to that of *Klein and Langmuir* [1987], I next plot indices of the extent of melting and depth of melting against spreading rate (Figure 5.3). $Si_{(8)}/Fe_{(8)}$ is a very

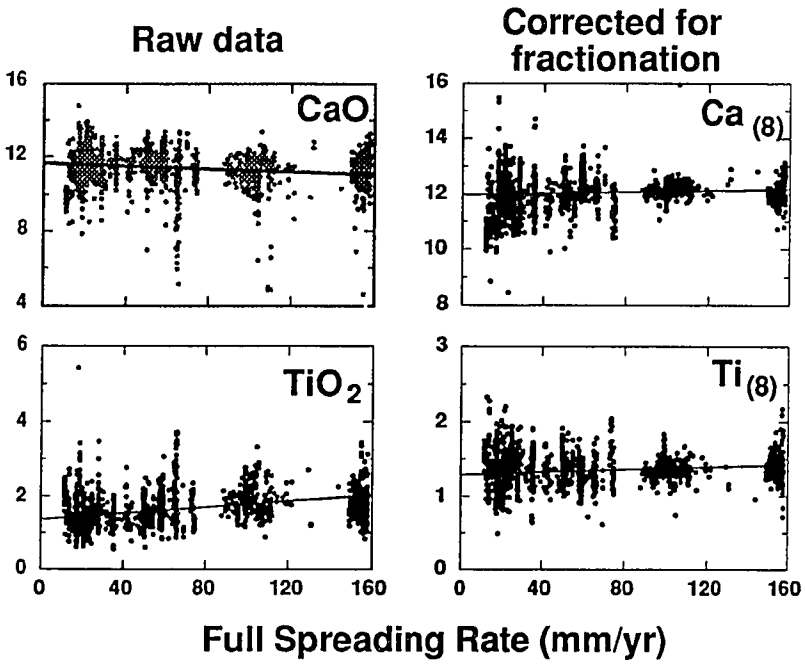

Fig. 5.2 Examples of the correlation between major element variation and full spreading rate. The lines are simple regression lines of oxides against the spreading rate because the uncertainty for the spreading rate is much less than that for the oxides considering the large range in the spreading rate. These correlations are consistent with increasing degrees of low pressure fractionation with increasing spreading rate, as shown by the absence of trends in plots of fractionation-corrected data. See Table 5.2 for data on other major elements.

Table 5.2. Global correlations

	Raw data			Corrected for fractionation*		
	Slope	Intercept	R	Slope	Intercept	R
SiO_2	7.45×10^{-4}	50.65	2.63×10^{-2}	-2.18×10^{-3}	50.52	1.45×10^{-1}
TiO_2	3.84×10^{-3}	1.39	3.73×10^{-1}	6.96×10^{-4}	1.31	1.42×10^{-1}
Al_2O_3	-7.14×10^{-3}	15.30	3.12×10^{-1}	-2.60×10^{-3}	15.63	1.87×10^{-1}
FeO	8.87×10^{-3}	9.98	2.51×10^{-1}	-2.04×10^{-3}	9.70	1.04×10^{-1}
MgO	-6.43×10^{-3}	7.65	2.55×10^{-1}	-	-	-
CaO	-4.17×10^{-3}	11.70	1.79×10^{-1}	1.04×10^{-3}	11.99	7.09×10^{-2}
Na_2O	2.40×10^{-3}	2.51	2.61×10^{-1}	8.81×10^{-4}	2.45	1.19×10^{-1}
K_2O	-4.74×10^{-4}	0.21	1.33×10^{-1}	-8.89×10^{-4}	0.20	3.11×10^{-1}
P_2O_5	5.22×10^{-4}	0.14	2.84×10^{-1}	2.11×10^{-4}	0.13	1.64×10^{-1}

* Corrections for fractionation follow *Klein and Langmuir* [1987] except that I apply a regional correction to data from each major geographic area as listed in Table 5.1. Furthermore, we use all samples with MgO ≥ 5wt % and a second-order polynomial fit in order to account for the curvature of variation trends in the region of MgO = 9 - 7 wt %. We corrected all oxides to MgO = 8.0 wt%. Corrected oxide values sum to 100±1% and plots of corrected oxide values against original (uncorrected) MgO show essentially zero slope, suggesting that this correction procedure does not introduce any artifacts. Values of $R > 0.081$ are significant at 99% confidence level (F-test for N = 2387: 99% confidence at F = 6.63).

sensitive indicator of the pressure of melting (see Chapter 3) and $Na_{(8)}$ and $Ca_{(8)}/Al_{(8)}$ are good indices of the extent of partial melting of pooled column melts [*Klein and Langmuir*, 1987; also see Chapter 3]. As shown in Figure 5.3, plots of these quantities against spreading rate exhibit much scatter. There is a suggestion that the scatter is more pronounced at slow spreading rates. The cause for the greater variation at slow-spreading rates may be several fold: sampling artifacts, mantle source heterogeneity, or less melt homogenization both in mantle melting regimes or magma chambers at slow-spreading ridges. In any case, there is no evidence for systematic trends in either depth of melting or extent of melting with differences in spreading rate. This is an interesting finding because it confirms that mantle temperature, an important control on melting below ridges [*McKenzie*, 1984; *Klein and Langmuir*, 1987; *McKenzie and Bickle*, 1988], is variable, but essentially independent of spreading rate.

5.4.2 Chemical variation trends versus spreading rate

Next, I search the global data set for spreading-rate dependence in MORB chemical variation trends. As shown by *Klein and Langmuir* [1989], regionally averaged MORB data exhibit correlations among axial depth, inferred extent of melting and inferred depth of melting. Unaveraged raw data exhibit similar trends [*Brodholt and Batiza*, 1989], such that deeper melts (high $Fe_{(8)}$, low $Si_{(8)}/Fe_{(8)}$) are formed by higher extents of melting (low $Na_{(8)}$ and high $Ca_{(8)}/Al_{(8)}$). Similarly, shallower melts (low $Fe_{(8)}$, high $Si_{(8)}/Fe_{(8)}$) are formed by lower extents of melting (higher $Na_{(8)}$). This behavior, observed globally, was called the global trend by *Klein and Langmuir* [1989]. The opposite trend, with a positive correlation between $Fe_{(8)}$ and $Na_{(8)}$ [e.g., *Batiza et al., 1988*], was called the local trend by *Klein and Langmuir* [1989]. I wish to determine whether the distribution of the so-called global and local trends is systematic with spreading rate.

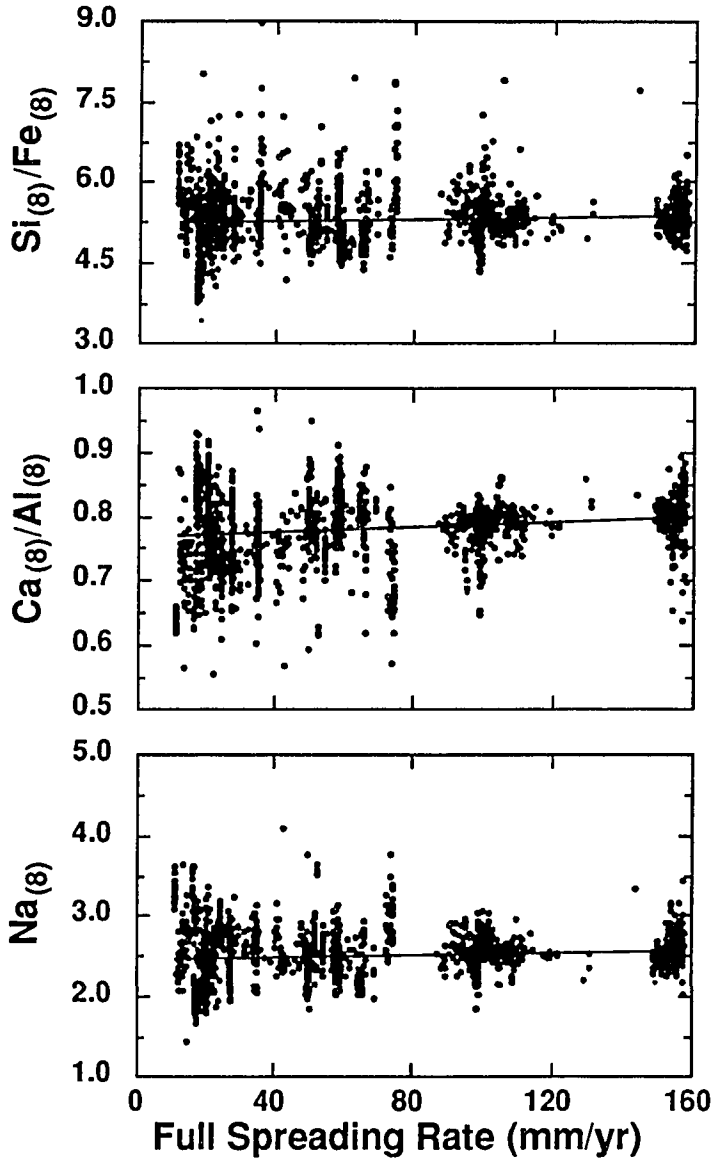

Fig. 5.3 Variations of $Si_{(8)}/Fe_{(8)}$, $Na_{(8)}$ and $Ca_{(8)}/Al_{(8)}$ as a function of spreading rate. The lines are simple regression lines against the spreading rate as in Figure 5.2. Note that these appear to have greater dispersion at slow spreading rates, but that values are essentially constant (and scattered) with spreading rate.

Table 5.3. Summary of data for the 32 best- sampled ridges and ridge portions

Plot ID	Ridge	Lat. A	Long. A	Lat. B	Long. B	Length (km)	SR (mm/yr)	Range (mm/yr)	#CG	SD (sample/10km)	R $Ca_{(8)}/Al_{(8)}$	95%	R $Na_{(8)}$	95%	GLBL/LOCL	Quality of match	Score
1	Mid-Cayman Rise	18.13	-81.69	18.11	-81.87	19.14	11.80	±0.00	26	13.58	0.48	+	-0.59	+	LOCL	GOOD	-1.13
2	Reykjanes Peninsula	63.86	-22.60	63.88	-21.50	53.88	17.58	±0.02	22	4.08	0.90	+	-0.97	+	LOCL	GOOD	-1.38
3	American-Antarctic Ridge	-57.71	-7.66	-56.90	-6.04	132.49	17.67	±0.21	22	1.66	0.53	+	0.14	-	LOCL	MED	-0.24
4	North MAR (FAMOUS)	36.79	-33.27	36.92	-33.13	19.07	20.94	±0.02	113	59.26	0.39	+	-0.26	+	LOCL	GOOD	-1.08
5	North MAR (Narrowgate)	36.54	-33.52	36.78	-33.28	34.19	20.99	±0.04	73	21.35	0.73	+	-0.52	+	LOCL	GOOD	-1.56
6	North MAR (AMAR)	35.84	-34.18	36.49	-33.65	86.47	21.14	±0.10	79	9.14	0.75	+	-0.29	+	LOCL	GOOD	-1.30
7	North MAR (South of Kane FZ)	15.88	-46.58	23.67	-44.78	885.81	26.20	±1.21	141	1.59	0.17	+	-0.48	+	LOCL	GOOD	-0.54
8	Explorer Ridge (Southern segment)	48.97	-130.90	49.90	-129.50	144.61	28.00	±0.03	59	4.08	0.74	+	-0.57	+	LOCL	GOOD	-1.06
9	South MAR (near Triple junction)	-55.33	-1.72	-54.67	-0.02	130.83	30.70	±0.08	15	1.15	0.35	-	-0.36	-	LOCL	POOR	-0.22
10	South MAR (~26°S area)	-25.70	-13.91	-26.49	-13.76	89.05	35.67	±0.01	92	10.33	0.71	+	-0.40	+	LOCL	GOOD	-1.27
11	North EPR (~ 22°N area)	22.35	-108.33	23.15	-109.13	120.93	50.14	±0.42	61	5.04	0.19	-	0.07	-	LOCL	POOR	-0.06
12	North EPR (~ 20°N area)	20.82	-109.10	20.93	-109.50	43.29	52.34	±0.06	29	6.70	-0.43	+	0.67	+	GLBL	GOOD	1.07
13	Galapagos (90.95°-95.62°W)	2.44	-95.62	1.90	-90.95	522.02	53.98	±3.58	37	0.71	0.33	-	-0.32	-	LOCL	POOR	-0.18
14	Gorda Ridge (Northern)	42.47	-126.90	42.94	-126.60	57.69	55.00	±0.01	15	2.60	0.57	+	0.13	-	LOCL	MED	-0.29
15	Juan de Fuca (End)	47.33	-129.00	48.20	-129.00	96.67	58.29	±0.23	46	4.76	-0.66	+	0.36	+	GLBL	GOOD	0.98
16	Juan de Fuca (NSR)	46.27	-129.60	47.27	-129.10	117.45	58.68	±0.15	26	2.21	0.52	+	-0.20	-	LOCL	MED	-0.51
17	Juan de Fuca (Axial)	45.56	-130.10	46.22	-129.80	76.92	59.08	±0.25	50	6.50	-0.47	+	0.32	+	GLBL	GOOD	0.75
18	Juan de Fuca (B)	45.13	-130.20	45.47	-130.00	40.89	59.40	±0.07	14	3.42	-0.03	-	0.13	-	GLBL	POOR	0.11
19	Juan de Fuca (SSR)	44.53	-130.50	45.00	-130.20	57.34	59.74	±0.25	45	7.85	0.26	-	0.02	-	LOCL	POOR	-0.09
20	Galapagos (85.84°-90.81°W)	1.06	-90.81	0.76	-85.84	553.20	61.58	±3.81	42	0.76	-0.43	+	0.46	+	GLBL	GOOD	0.43
21	Galapagos (84.77°-85.77°W)	0.78	-85.77	1.71	-84.77	151.73	66.26	±0.77	29	1.91	-0.46	+	0.75	+	GLBL	GOOD	0.89
22	North EPR (13.75°-14.82°N)	13.75	-104.15	14.82	-104.39	121.67	89.92	±1.97	14	1.15	-0.30	-	0.88	+	GLBL	MED	0.73
23	North EPR (12.91°-13.65°N)	12.91	-103.98	13.65	-104.17	84.76	93.64	±0.14	17	2.01	-0.46	-	0.93	+	GLBL	MED	0.88
24	North EPR (12.67°-12.89°N)	12.67	-103.91	12.89	-103.97	25.30	95.48	±0.40	13	5.14	-0.90	+	0.85	+	GLBL	GOOD	1.36
25	North EPR (11.69°-12.57°N)	11.69	-103.81	12.57	-103.91	98.39	97.86	±1.63	95	9.66	-0.54	+	0.70	+	GLBL	GOOD	1.23
26	North EPR (10.29°-11.87°N)	10.29	-103.58	11.87	-103.81	177.35	101.76	±2.92	206	11.62	-0.55	+	0.51	+	GLBL	GOOD	1.02
27	North EPR (9.12°-10.21°N)	9.12	-104.19	10.21	-104.34	122.23	106.99	±2.02	55	4.50	-0.52	+	0.03	-	GLBL	MED	0.61
28	North EPR (8.36°-9.12°N)	8.36	-104.14	9.12	-104.25	85.31	110.42	±1.37	30	3.52	-0.21	-	0.69	+	GLBL	MED	0.76
29	South EPR (13.08°-13.47°S)	-13.08	-110.93	-13.47	-111.10	47.08	149.60	±0.25	10	2.12	-0.09	-	0.83	+	GLBL	MED	0.81
30	South EPR (13.22°-15.92°S)	-13.22	-112.33	-15.92	-112.98	308.06	150.89	±1.36	43	1.40	-0.15	-	0.37	+	GLBL	MED	0.32
31	South EPR (16.05°-20.52°S)	-16.05	-112.98	-20.52	-113.87	505.50	153.60	±1.26	89	1.76	-0.30	+	0.21	+	GLBL	GOOD	0.35
32	South EPR (21.00°-23.02°S)	-21.00	-114.19	-23.02	-114.51	226.87	155.49	±0.43	35	1.54	-0.47	+	0.64	+	GLBL	GOOD	0.71

Plot ID refers to the plots of Figure 5.5. A and B refer to the latitude and longitude of the two extreme sample localities in the segment. The length is the distance between A and B. SR is the full spreading rate at the middle point of the segment. Range is the total variation of the spreading rate of the segment. #CG is the number of group means. SD is the sampling density: #CG per 10 km. R is the correlation coefficient on the plots of $Ca_{(8)}/Al_{(8)}$ vs $Si_{(8)}/Fe_{(8)}$ and $Na_{(8)}$ vs $Si_{(8)}/Fe_{(8)}$. "+" and "-" under 95% indicate either the correlation is significant or not at 95% confidence level. GLBL/LOCL indicate whether the chemical systematics on both plots are of global or local trend. Quality of the match shows the "goodness-of-fit" of the data to either global or local trend in terms of the slopes and correlation coefficients of the regressions on the two plots. Score is determined using "goodness-of-fit" and sample density, and is used to construct the bar chart (Figure 5.6). See appendix for score procedures.

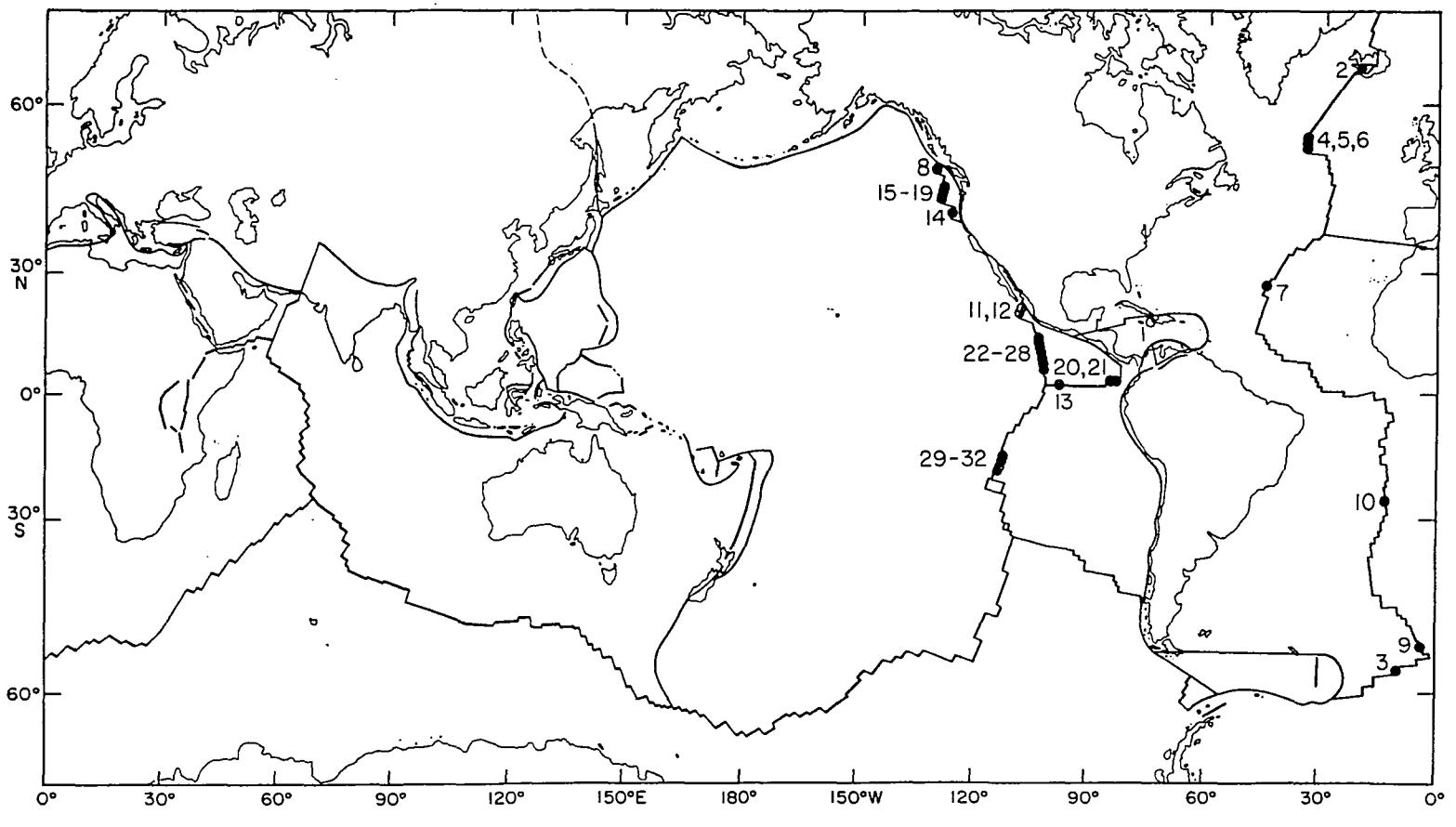

Fig. 5.4 Highly abstracted map of the mid-ocean ridge system (following *DeMets et al.*, [1990]). The thirty-two best-sampled areas selected for this study are shown with numbers keyed to Table 5.3. Note the absence of well-sampled area in the Indian Ocean and the southern Pacific south of ~ 30°S.

To do so, I select thirty-two of the best-sampled portions of the ridge system from the global data set and examine the data from each area in detail. The choice of the thirty-two ridge segments is based on the sample density only, that is, segments with sample density greater than 0.7 (chemical groups per 10 km) are considered, because the highest density below this value is 0.52 (chemical groups per 10 km) which seems too low to be reliable. These are listed in the order of increasing spreading rate in Table 5.3, which also gives the latitude and longitude endpoints of each ridge segment, its length, spreading rate, number of chemical group means and sample density. The lengths of these ridge portions vary greatly (see Table 5.3) and all have first-order discontinuities (transform faults, propagating rifts, and large over-lapping spreading centers) [*Macdonald et al.*, 1988] as endpoints. Sampling density also varies greatly, with the poorest-sampled ridge having ~ 0.7 samples per 10 km. Ideally one would choose ridge segments of comparable length and sampling density; however, the present sample distribution makes this impossible. Another consequence of incomplete sampling is that the group of thirty-two best-sampled areas does not include any portion of the Indian Ocean ridge system (Figure 5.4). Figure 5.1 shows plots of $Na_{(8)}$ and $Ca_{(8)}/Al_{(8)}$ (indices of extent of melting) against $Si_{(8)}/Fe_{(8)}$ (index of pressure of melting) for the entire data set. Figure 5.5 shows the same two plots for each of the 32 individual ridge portions of Table 5.3.

Most of the thirty-two ridge segments show clear linear trends with slopes indicative of either the global or local trend. However, some segments show less clear trends, either because of low sampling density or intrinsically no trends. In order to assess objectively how closely the data from each area approximate the global or local trend, I developed a method for assigning a numerical score to each segment. The scores are derived from: 1) the slope of the regression lines (positive or negative values of the correlation coefficient), 2) the value and significance (t-test) of the correlation coefficients, and 3) sampling density. By this method, areas with very clear trends (little scatter and many samples) receive the

Fig. 5.5 Chemical systematics of the 32 densely sampled ridges or ridge portions shown on the same two diagrams of Figure 5.1. The numerals refer to the ridge ID number listed in Table 5.3. Note the great variability in the correlation and the slopes (sign and magnitude) of the regression lines. The regression lines are obtained by simple regression of Y on X, but reduced major axis (RMA) analysis shows that the sign of the slopes, which is an important factor used to score the 32 ridge segments (see Table 5.3 and Appendix 5), remain unchanged. Table 5.3 gives correlation coefficients and values of statistical significances.

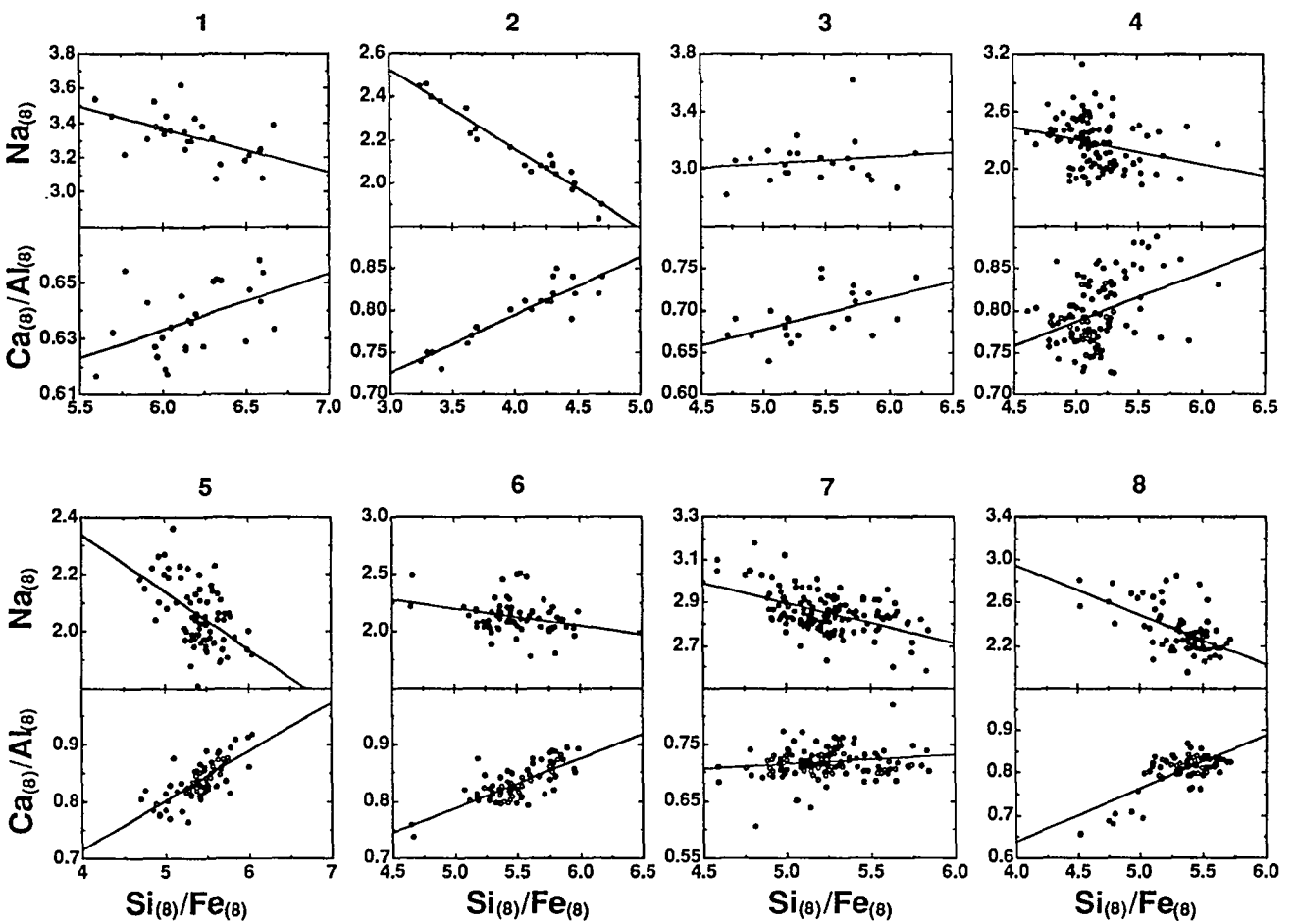
1
2
3
4
5
6
7
8
Na(8)
Ca(8)/Al(8)
Si(8)/Fe(8)

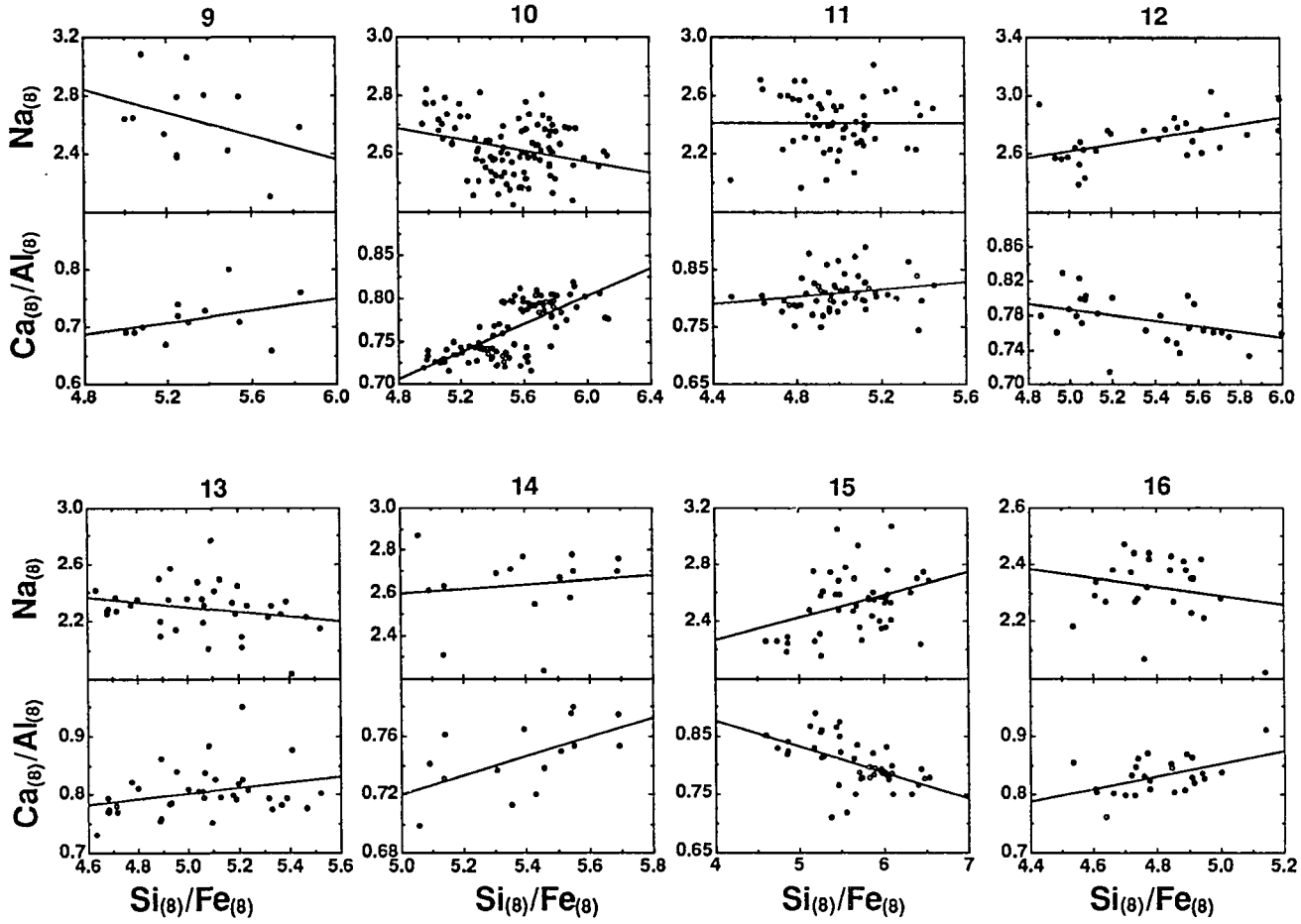
9
10
11
12
13
14
15
16
Na(8)
Ca(8)/Al(8)
Si(8)/Fe(8)

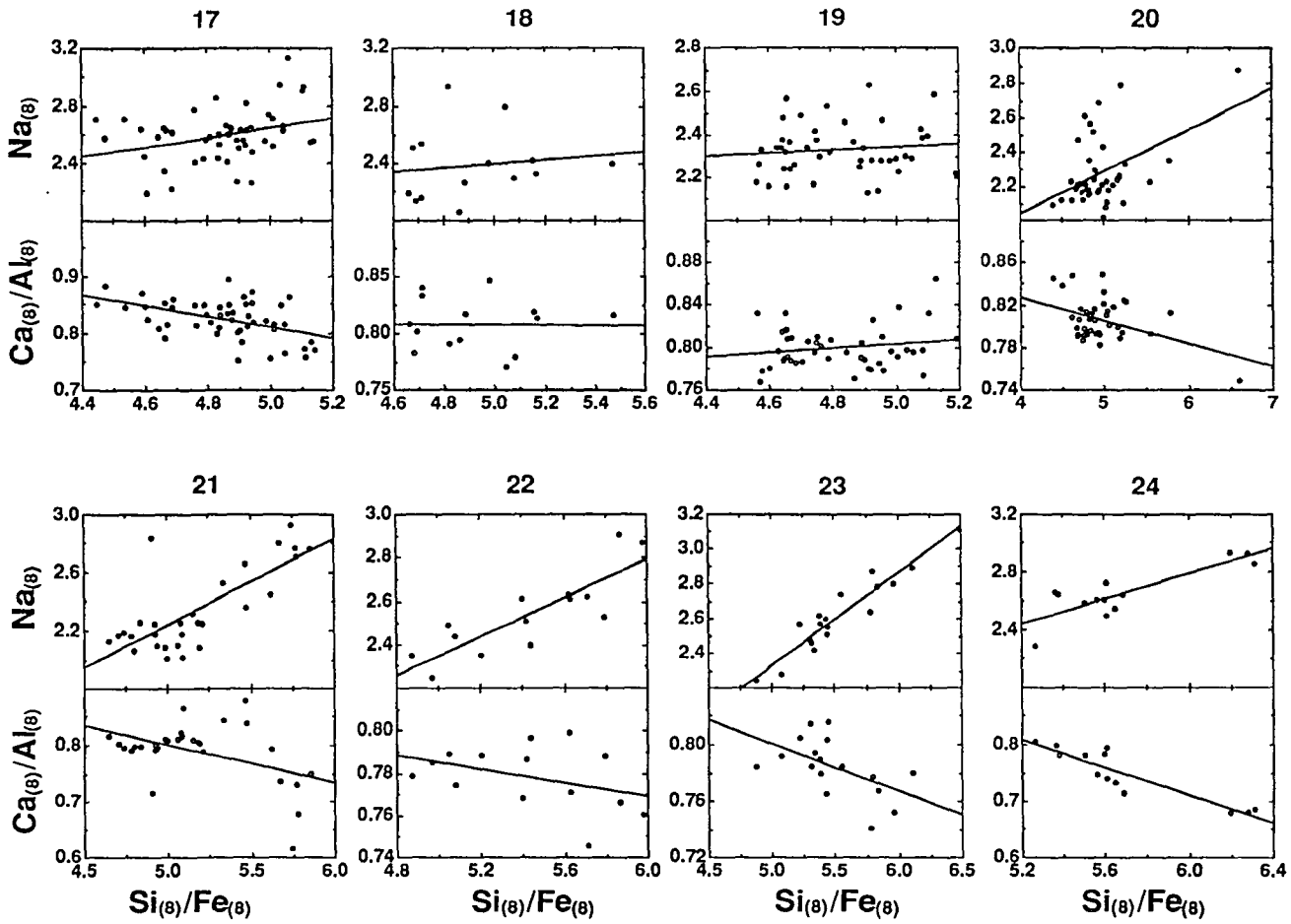
17
18
19
20
21
22
23
24
Na(8)
Ca(8)/Al(8)
Si(8)/Fe(8)

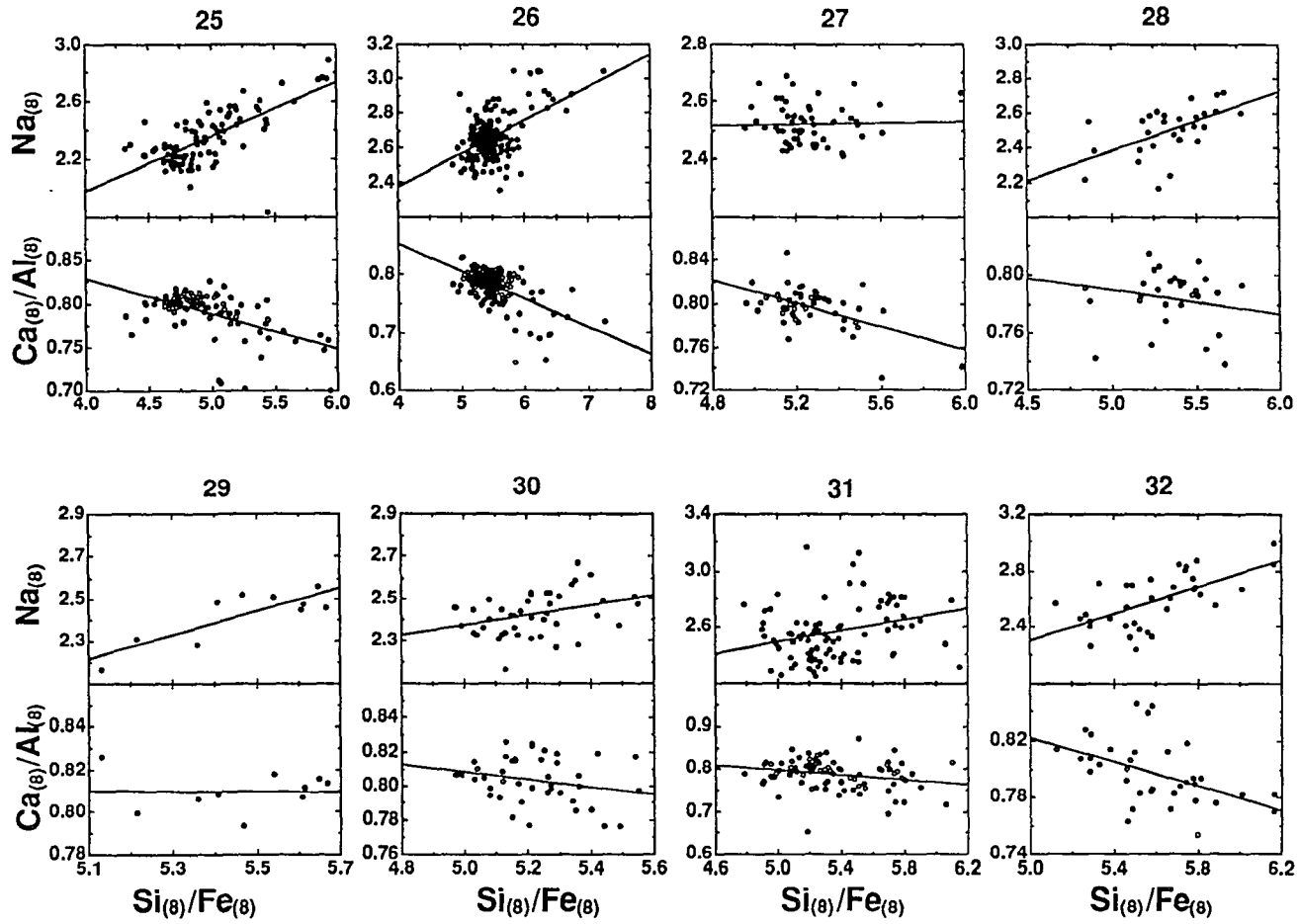
25
26
27
28
29
30
31
32
Na(8)
Ca(8)/Al(8)
Si(8)/Fe(8)

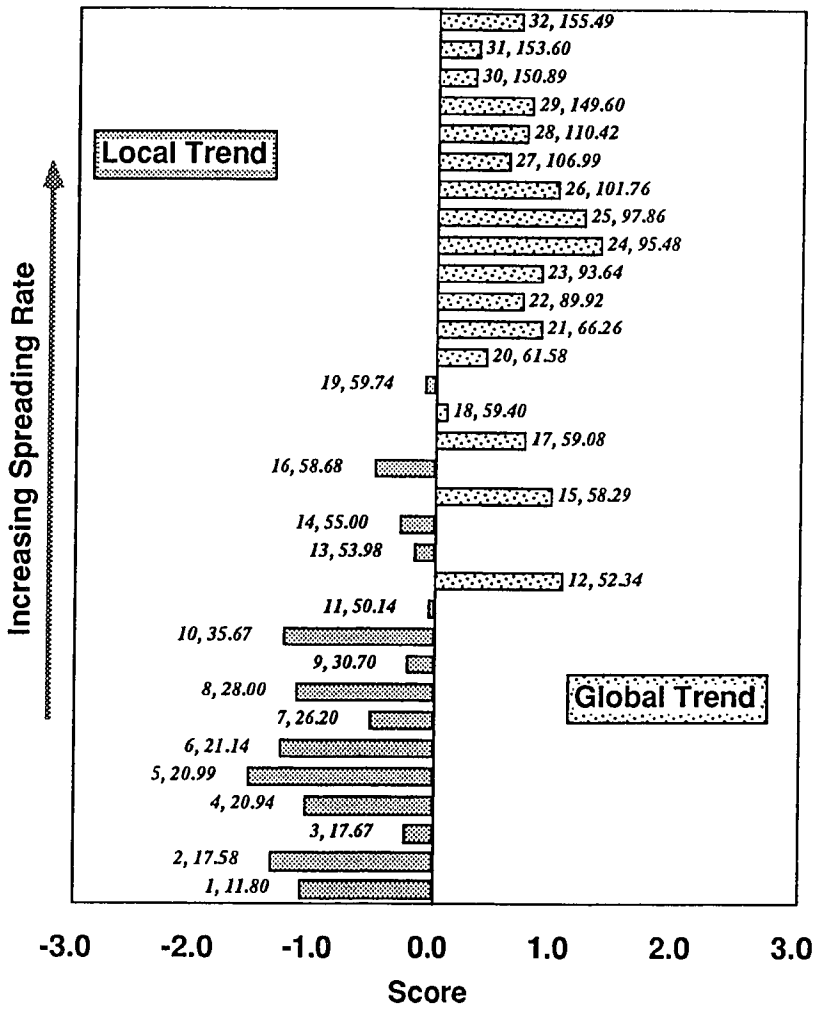

Fig. 5.6 Bar diagrams to show the relationships between chemical systematics and the full spreading rate. Each bar refers to a specific ridge segment listed in Table 5.3 and the first number gives its ID number. The value after the comma is the full spreading rate. This figure clearly shows that fast ridges follow the global trend and slow ridges the local trend. There is also a transition (50 - 60 mm/yr) where either trend is possible.

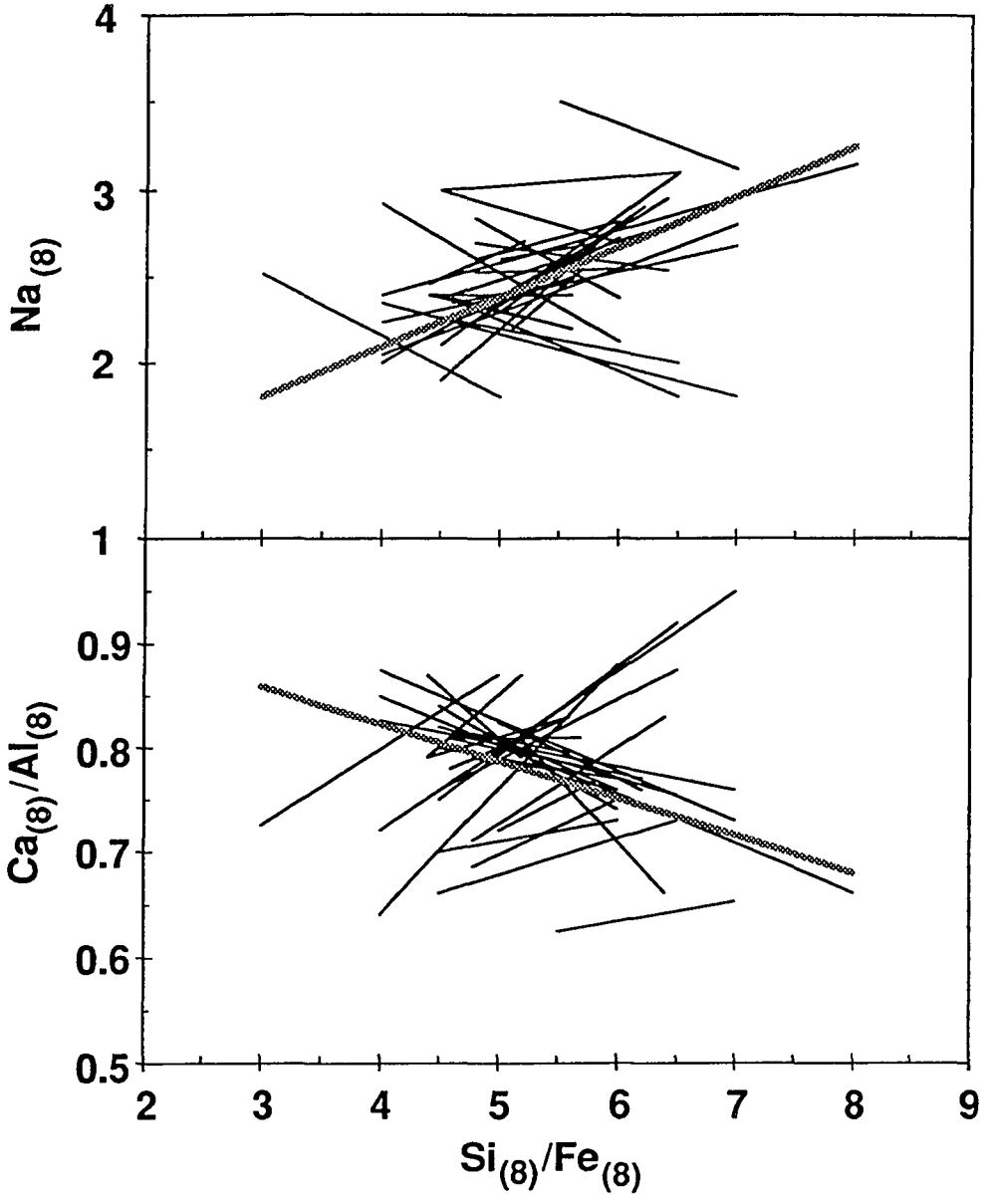

Fig. 5.7 All the regression lines of Figure 5.5 plotted together on $Na_{(8)}$ and $Ca_{(8)}/Al_{(8)}$ vs. $Si_{(8)}/Fe_{(8)}$ diagrams. The heavy line (for reference) is the global trend from Figure 5.4. Note that the slopes of both the local and global trends vary and that no simple pattern (such as a fanning pattern) exists.

highest numerical values (see Table 5.3: negative score for local trend and positive score for global trend) and areas with scattered trends and/or fewer samples receive low numerical scores. Details of the scoring procedure are given in Appendix E.

Table 5.3 and Figure 5.6 summarize the results and show clearly that MORB chemical systematics (local versus global trend) are related to spreading rate. Fast-spreading ridges (> 60 mm/yr) exhibit the global trend whereas slow-spreading ridges (< 50 mm/yr) exhibit the local trend. Further, this relationship is apparently independent of geographic length scale, as Table 5.3 has ridge segments of highly variable length. For example, at slow rates, both Narrowgate (34.2 km long) and the entire mid-Atlantic ridge south of the Kane Fracture Zone (885 km long) exhibit very clear local trends. At fast rates, both small segments and the entire northern and southern EPR follow the global trend, as shown previously in Chapter 3. Since the distribution of these chemical variation trends is apparently controlled by spreading rate and not spatial scale, as implied by the terms global and local, I will call them the fast and slow trends.

Another important result from Table 5.3 and Figure 5.5 is that the slopes of the regression lines for the fast and slow trends are not constant. Furthermore, as can be seen on Figure 5.7, the individual regression lines do not exhibit any systematic pattern (such as fanning) on the plots. One possibility is that this variability in slope is due to uncertainty in the slope of the regression lines (data scatter); however, I find no relationship between the correlation coefficients and the slope of the regression lines. Thus, it is more likely that this slope variation is real and reflects characteristics of the natural processes that result in the distinctive chemical systematics of both fast and slow-spreading ridges.

5.5 Discussion

If we assume that the mantle is approximately homogeneous for major elements, then the results of Figure 5.3 indicate that mantle temperature is independent of spreading rate.

However, chemical variation trends involving pressure and extents of melting do appear to be related to spreading rate (Table 5.3 and Figures 5.5 and 5.6). These trends, the fast ("global") and slow ("local") chemical variation trends, appear to be independent of geographic length scale along axis and the slopes of the trends are variable (Figure 5.7). These observations suggest strongly that the dynamics of mantle upwelling, thought to differ fundamentally between fast and slow ridges [e.g., *Lin and Phipps Morgan*, 1992; *Scott and Stevenson*, 1989], play a role in controlling the distribution of the fast and slow chemical trends in MORB. I hypothesize that the fast trend results from melting under conditions dominated by passive, plate-driven mantle upwelling that is broadly 2-D in character [e.g., *Phipps Morgan*, 1987]. In contrast, the slow trend would be the result of melting that occurs in rising mantle dominated by buoyant, 3-D upwelling ("plume-like") [e.g., *Sotin and Parmentier*, 1989; *Scott and Stevenson*, 1989]. Such buoyant instabilities could be embedded within a mean upward plate-driven flow [*Scott and Stevenson*, 1989]. In fact, however, because regionally-averaged data for many slow-spreading ridges as a whole also show the "global" (fast-spreading chemical trend), it seems likely that passive upwelling of mantle is also important at slow-spreading ridges.

Strong evidence exists from crustal thickness and MORB chemical data [*Klein and Langmuir*, 1987], theoretical considerations [*McKenzie*, 1984] and models of MORB melting [*Klein and Langmuir*, 1987; *McKenzie and Bickle*, 1988; also see Chapter 3] that the fast ("global") trend of MORB is due principally to differences in mantle temperature. Hot mantle rising adiabatically intersects the solidus at a deeper level than cooler mantle and continued decompression melting with matrix compaction should result in pooled melts with chemical signatures of high pressure (high $Fe_{(8)}$ and low $Si_{(8)}/Fe_{(8)}$) and high extents of melting (low $Na_{(8)}$ and high $Ca_{(8)}/Al_{(8)}$). Regional differences in mantle temperature should give rise to ensembles of data that follow the global trend. Mantle temperature differences of about 200°C are capable of producing the global array [*Klein and Langmuir*,

1987]. On a smaller geographic length scale, differences in mantle temperature can give rise to the same global-type systematics at a more local or regional level, as shown discussed in Chapter 3. Thus, this explanation of global trend is fully consistent with both petrological evidence and models of mantle flow beneath fast-spreading ridges [e.g., *Lin and Phipps Morgan*, 1992].

The fast ("global") trend is well-explained by adiabatic decompression melting of a mantle column in which polybaric melts are efficiently separated from their residues and pooled in a reservoir at low pressure [*Klein and Langmuir*, 1987; see also Chapter 3]. However, in rising diapirs at slow spreading rates, separation of melt from residue may be less efficient than at fast-spreading rates. For one thing, the melt fraction contributes buoyancy to the solid mantle, which could retard separation of melt from matrix by normal matrix compaction processes [*McKenzie*, 1984; *Ribe*, 1983; *Cawthorn*, 1975; also see Chapter 3]. Whereas rapid melt segregation in column melts of the fast trend preserves high-pressure signatures at high extents of melting [*Klein and Langmuir*, 1987], extensive melts of the slow trend have low-pressure signatures. One possible explanation is that slow melt segregation in diapirs allows matrix-melt reaction during ascent, such that high pressure signatures are only preserved in melts produced by low extents of melting shortly after initiation of a diapiric instability when dikes become efficient conduits at greater depths.

During ascent of a mantle diapir undergoing melting, inefficient melt segregation would allow melts to reequilibrate with the solid matrix. If these reequilibrated melts were tapped by dikes [*Nicolas*, 1986; *Sleep*, 1989] at various pressures, an ensemble of melts resembling the slow ("local") trend would result. Deep melts would be produced by small extents of melting soon after initiation of the diapir. With continued diapiric ascent, melting and melt-solid reequilibration, melts would have chemical signatures of successively lower pressure and more extensive melting.

Although this somewhat speculative idea is difficult to prove, there are many independent lines of evidence suggesting that diapirs are important at slow-spreading ridges. Gravity and topography data [*Lin and Phipps Morgan*, 1992; *Lin et al.*, 1990], studies of mid-ocean ridge segmentation [*Whitehead et al.*, 1984; *Schouten et al.*, 1985; *Crane*, 1985] and theoretical studies of mantle flow [*Scott and Stevenson*, 1989; *Sotin and Parmentier*, 1989] all point to the possible importance of diapirs at slow-spreading ridges. Furthermore, geologic mapping in ophiolites has revealed diapiric structure in mantle rocks [*Rabinowicz et al.*, 1987; *Nicolas*, 1986], and the observed diapiric structures small (< 10 km). These independent lines of evidence indicate that the notion of diapirs at slow-spreading ridges deserves serious consideration. Below, I develop this hypothesis further and offer two additional lines of supporting evidence. First, I discuss some illustrative mass balance calculations indicating that melts along the slow trend could be related by a melting-crystallization reaction that plausibly could occur in rising diapirs undergoing melting and melt-reequilibration. Secondly, I show that zero-age lavas of seamounts on the flanks of the East Pacific Rise exhibit both the fast and slow chemical variation trends. This is consistent with the diapir hypothesis as diapiric buoyancy instabilities may be expected to develop at the edges of the broad upwelling region below the EPR axis and flanks [*Phipps Morgan*, 1987; also see Chapter 3]. Similarly, at transitional ridges (50 - 60 mm/yr) where both the fast and slow trends may occur, diapiric and widespread passive upwelling may both occur. In this case the petrologic signature of erupted lavas may be dominated by either trend.

5.5.1 Calculations

Relatively little is known about the physico-chemical processes occurring in mantle diapirs undergoing melting [e.g., *Cawthorn*, 1975]. Diapiric instabilities could arise in the mantle below the axes or flanks of mid-ocean ridges because of thermal, compositional,

and/or melt buoyancy [e.g., *Sotin and Parmentier*, 1989; *Scott and Stevenson*, 1989; also see Chapter 2]. Once initiated, the solid or solid-plus-melt diapirs could rise and decompression-induced melting could ensue. The complex internal processes occurring within the diapir would be affected by interaction between the diapir and the surrounding mantle through which it rises. Very complex thermal, mechanical and chemical processes seem likely.

Under appropriate conditions, material in diapirs should melt just as passively upwelling mantle does. However, melt extraction by matrix compaction, a process thought to be generally important for upwelling mantle [*McKenzie*, 1984] could be inhibited by mechanical deformation within a diapir, because ascending diapirs must overcome the overload (when plate separation rate is slow) either mechanically or by thermal stoping. Furthermore, if melt buoyancy causes matrix ascent, then ordinary melt expulsion by matrix compaction may be greatly slowed. In this case, the melt and matrix would have enhanced opportunity to interact chemically, even as melting continued. I envision a process similar to that studied by *Kelemen* [1990] and *Kelemen et al.* [1990] except that the process I envision is polybaric. For this reason, the results of *Kelemen* [1990] and *Kelemen et al.* [1990] at 5 kb only cannot be rigorously applied here.

Instead, I explore possible petrologic processes in diapirs with some extremely simple but illustrative mass balance calculations. With these calculations I attempt to determine directly the minerals that might be involved in producing melts along the slow trend of chemical variation.

A fundamental difficulty of attempting to interpret the cause of the slow trend is that, by definition, this trend is comprised of samples with identical MgO = 8.0 wt %. Even though the slow trend probably is the result of dynamic physical and chemical processes which lead to variations in MgO (as well as other major element abundances), our present definition and view of the trend is an artificial, constant-MgO snapshot only. Whether

melts comprising the slow trend are related to each other directly through some petrologic process such as melting or crystallization, or related only indirectly (for example, sequential products of a petrologic process), it is most improbable that they coexist as constant-MgO melts.

In order to circumvent this problem of constant MgO, while at the same time trying to explicitly determine the major silicate phases that might be involved in the slow-spreading trend, I use simple stoichiometric least-squares modeling of the type described by *Bryan et al.* [1969] and *Bryan* [1986]. Figure 5.8 shows several well-defined trends from slow-spreading ridges which I use in my illustrative model. I implicitly assume that the magmas along the slow trend are related to one another by some petrologic processes (melting or crystallization, for example) involving major silicate phases and I attempt to determine the phases and their proportions using mole-percent least-squares mass balance calculations.

For simplicity, in Figure 5.9 I omit the data points and show only the regression lines for each of the slow trends. I essentially ask: what assemblages of silicate phases could be involved in producing the trends between **a** and **b**? To get around the problem of constant MgO, I use a two-step approach. First, in the stoichiometric modeling, I combine Fe and Mg to form one divalent cation (FM). This allows us to obtain a first order solution while, for the moment, neglecting the constant MgO problem. Using FM also allows us to temporarily disregard the complexity of Fe-Mg partitioning in natural silicate phases and the effects of pressure, temperature and composition on the partitioning behavior as I seek only a generalized solution. Once having done the initial modeling with FM, I return to consider how much MgO may actually change along the **a**-**b** or **b**-**a** paths of Figure 5.9.

With the cation FM, I make olivine (FM_2SiO_4) and pyroxene ($FM_2Si_2O_6$: both orthopyroxene and Mg-Fe components of clinopyroxene). In this simple stoichiometric modeling, I also consider end-member diopside-hedenbergite (Di-Hd), jadeite (Jd), Ca-tschermak (Ct), and albite-anorthite (Ab-An). Table 5.4 shows the liquid compositions at

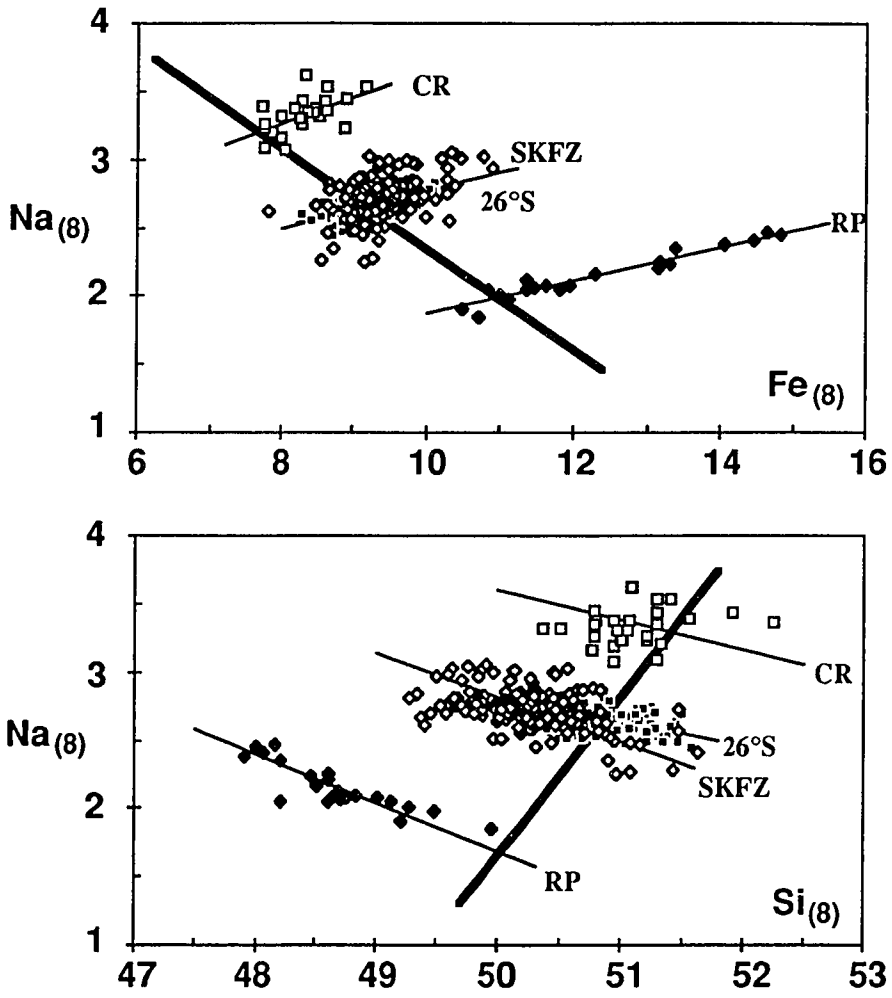

Fig. 5.8 Plots of $Na_{(8)}$ vs. $Fe_{(8)}$ and $Na_{(8)}$ vs. $Si_{(8)}$ showing the global trend of *Klein and Langmuir* [1989] (thick line) and several best-defined local trends (cross trends) recognized at slow spreading mid-ocean ridge segments [*Klein and Langmuir*, 1989; *Batiza et al.*, 1988]. CR = Cayman Rise, 26°S = MAR at 26°S, SKFZ = MAR south of the Kane Fracture Zone and RP = Reykjanes Peninsula.

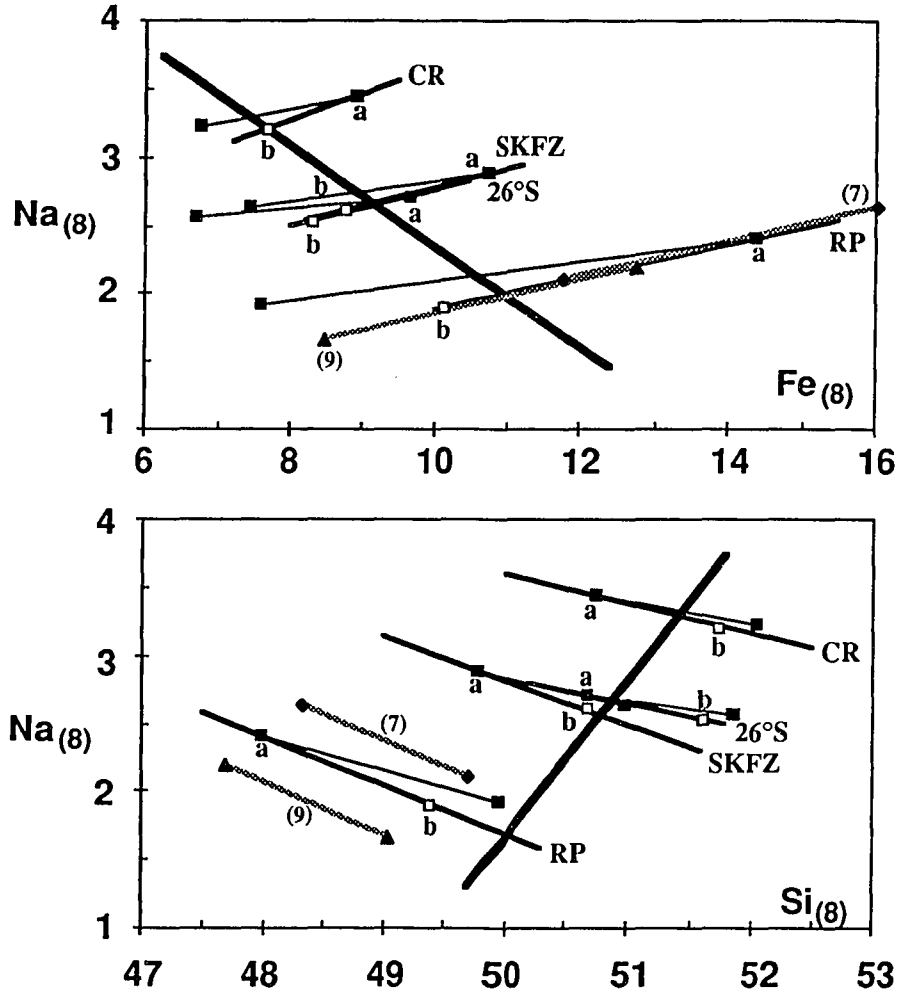

Fig. 5.9 Same as Figure 5.8 but with the data points of the local trends omitted. Regression lines are best-fit lines for all elements (not just ones shown). The points labeled **a** (filled square) and **b** (empty square) are the liquids I consider in Tables 5.4 and 5.5 which define the **a** - **b** path I attempt to model. The thin lines between solid squares are the results of my two-step modeling procedure (see Tables 5.4 and 5.5 and text for details). Note that the thin lines (model) and the thick lines (data) are generally well matched. The model I present gives a good fit to all elements, not just Na, Fe, and Si. Also shown as thick light lines for comparison are the local trend data corrected to MgO = 7.0 and 9.0 wt %, as labeled (for RP only, others are similar). Note that these have similar slopes to the MgO = 8.0 wt % local trend.

Table 5.4. Melt compositions for each local trend (Figures 8 and 9)

	RP-*a*	RP-*b*	CR-*a*	CR-*b*	SK-*a*	SK-*b*	26°S-*a*	26°S-*b*
				Wt% at MgO = 8%				
$Si_{(8)}$	48.00	49.38	50.75	51.75	49.80	50.69	50.69	51.62
$Ti_{(8)}$	2.48	1.06	1.67	1.46	1.85	1.28	1.68	1.13
$Al_{(8)}$	13.56	15.60	16.14	16.79	15.30	16.25	15.48	15.70
$Fe_{(8)}$	14.37	10.13	8.91	7.68	10.73	8.78	9.65	8.31
$Ca_{(8)}$	10.12	13.15	10.11	10.85	10.55	11.88	11.48	12.41
$Na_{(8)}$	2.41	1.89	3.45	3.20	2.89	2.61	2.70	2.52
$K_{(8)}$	0.25	0.10	0.23	0.28	0.23	0.20	0.09	0.06
$P_{(8)}$	0.24	0.07	0.18	0.18	0.19	0.13	0.16	0.11
†MgO		9.55		8.74		8.76		9.58
†FeO		8.01		6.71		7.38		6.59
				Recalculated to Cation Mole %				
Si	45.35	46.19	46.82	47.32	46.33	46.82	46.93	47.69
Ti	1.77	0.75	1.16	1.00	1.30	0.89	1.17	0.78
Al	15.10	17.19	17.55	18.10	16.77	17.70	16.90	17.09
*FM	22.63	19.08	17.88	16.78	19.44	17.80	18.52	17.44
Ca	10.25	13.18	10.00	10.63	10.52	11.76	11.39	12.29
Na	4.42	3.44	6.19	5.70	5.22	4.69	4.87	4.54
K	0.30	0.12	0.27	0.33	0.27	0.23	0.11	0.07
P	0.19	0.06	0.14	0.14	0.15	0.11	0.12	0.09

RP: Reykjanes Peninsula; CR: Cayman Rise; SK: south of the Kane Fracture Zone; and 26°S: 26°S area MAR.

* FM is the combined cation mole % of FeO and MgO (= 8.0 wt%).

† MgO and FeO compositions for b were calculated explicitly to determine their change along the a-b path. In this calculation, other elements agree with those in Table 5. I used the calculated phase proportions from Table 5.5 and peridotite modal abundances from *Dick* [1989]. I partition enstatite-ferrosilite (En-Fs) between Opx and Cpx in Table 5 in the ratio 63:37, with Opx free of diopside (Di) and hedenbergite (Hd) components. I also used $Fo_{90.3}$, Opx with $Mg^{\#}$ = 91.3 and Cpx with $Mg^{\#}$ = 94.6 from *Dick* [1989]. As explained in the text, I consider these mass balance models illustrative, not definitive.

Table 5.5. Results of the least-squares model calculations

	RP-*b*			CR-*b*			SK-*b*			26°S-*b*		
a	0.4884			0.6816			0.6667			0.5414		
Di-Hd	0.1569			0.0599			0.0841			0.1249		
Jd	0.0518			0.0597			0.0488			0.0767		
Ct	0.1704			0.0929			0.1060			0.1204		
En-Fs	0.2913			0.2220			0.2104			0.2816		
Ol	-0.1569			-0.1200			-0.1167			-0.1467		
SQ'D	0.0142			0.0654			0.0032			0.0220		
	Calc	Obser	Diff	Calc	Obser	Diff	Calc	Obser	Diff	Calc	Obser	Diff
Si	46.18	46.19	-0.01	47.32	47.32	0.00	46.82	46.82	0.00	47.68	47.69	-0.01
Ti	0.86	0.75	0.11	0.79	1.00	-0.21	0.87	0.89	-0.02	0.63	0.78	-0.15
Al	17.19	17.19	0.00	18.10	18.10	0.00	17.70	17.70	0.00	17.09	17.09	0.00
FM	19.08	19.08	0.00	16.78	16.78	0.00	17.80	17.80	0.00	17.44	17.44	0.00
Ca	13.19	13.18	0.01	10.64	10.63	0.01	11.77	11.76	0.01	12.30	12.29	0.01
Na	3.45	3.44	0.01	5.71	5.70	0.01	4.70	4.69	0.01	4.55	4.54	0.01
K	0.15	0.12	0.03	0.18	0.33	-0.15	0.18	0.23	-0.05	0.06	0.07	-0.01

points **a** and **b** of each of the local trends of Figures 5.8 and 5.9. I now use a least-squares method to determine the stoichiometric end-member phases which can, when added to liquid **a**, produce liquid **b** (or vice versa).

Although least-squares mixing models of this type, especially with few components and many phases, are notorious for giving non-unique solutions, these results appear to be robust. I have tested hundreds of models using many combinations of mineral end-members but only a few yield self-consistent results with good fits (low residuals). Representative results are shown in Table 5.5. Note that the poorest fits are for Ti and K, which is not surprising because I did not include mineral end-members containing either element (though I could add Ti to pyroxene). One interesting result is that plagioclase is apparently not needed to describe the **a** - **b** path for any locality as all solutions with plagioclase give very high residuals (> 2.0 or so), with especially poor fits for Ca and Al. This is not surprising because melting in the plagioclase stability field may be quite restricted [*Nicolas*, 1986]. Table 5.5 shows that in general, the path from **a** to **b** (Figure 5.9) seems to involve both melting and crystallization. Pyroxene components are taken into liquid **a** while olivine solidifies; together, these two effects produce liquid **b**. In all four cases, the original liquid **a** represents about half of the eventual liquid (**b**) and the ratio of pyroxene components (added to melt) to olivine component (removed from the melt) is 3.6 - 4.0. Such a trend is thus a net melting trend characterized by a mineral - melt reaction of the general form:

Liquid **a** + Pyroxene ¤ Liquid **b** + Olivine

and is similar to the reactions studied theoretically and experimentally by *Kelemen* [1990] and *Kelemen et al.* [1990] at 5 kb. Under conditions of ascent to lower pressure, this reaction would proceed to the right [e.g., *O'Hara*, 1965; *Stolper*, 1980; *Elthon and Scarfe*, 1984], obviously favoring the **a** to **b** path over the alternative **b** to **a** path.

This result seems reasonable and is consistent with processes expected in a buoyant solid-liquid diapir undergoing continued melting. Note that in Table 5.5 the combined compositions of the pyroxenes entering the melts are unlike any natural pyroxenes in that Jd, and particularly Ct are too high. This is, in fact, expected, as both orthopyroxene and clinopyroxene are residual phases during mantle melting to produce MORB [*Dick et al.*, 1984]. Continuous melting will tend to deplete Jd and Ct components in residual pyroxenes because both are incompatible during melting and less stable in pyroxenes as pressure is reduced. Thus, pyroxenes in the solid will gradually be depleted in these components, while the melt in a rising diapir will be enriched in Jd and Ct components.

I now reconsider possible changes in MgO and FeO. To calculate the MgO and FeO changes, I dispense with the use of FM. Using the phase proportions from Table 5.5, I partition FeO and MgO among the solid silicate phases (see Table 5.4 note for details) and calculate liquid **b** as a combination of liquid **a** and the phases of Table 5.5. The FeO and MgO values obtained are given in Table 5.4. MgO changes only slightly along my calculated path **a** - **b**. It is important to note that because of the MgO = 8.0 condition of the slow-spreading trend lines in Figures 5.8 and 5.9, that even though the calculations indicate a small change of MgO, the calculated **a** - **b** paths cannot be identical to the **a** - **b** paths of the slow trends. To assess the difference in the calculated vs. observed paths, I plot the calculated end points (**b**) on Figure 5.9. In addition, I plot slow trends corrected to MgO = 7.0 and MgO = 9.0, which fall close to the MgO = 8.0 positions. Thus, although the calculated **a** - **b** paths are not identical to the slow-spreading data arrays in Figure 5.9, they are close enough. Indeed, because the slopes of actual slow trends vary (Figure 5.7), there is evidently some variability in the processes leading to their formation. Given the potential complexity of physical-chemical processes in rising diapirs undergoing melting, this variability in the data is not surprising.

Note that this result is similar in some ways to the suggestion of *Kinzler and Grove* [1992] who propose polybaric fractional crystallization as a possible origin for the slow trend. I think that fractional crystallization is inevitable within rising mantle diapirs, but such fractionation may occur only during latest stages of diapirism when melting ceases due to slow ascent and higher heat loss. Mineralogic features of MORB lavas from slow-spreading ridges suggest that high-pressure fractionation may indeed play a role in their petrogenesis [*Bryan et al*, 1979, 1981; *Juster et al.*, 1989]. However, I suggest these effects are superimposed on the earlier effects of melting and solid-melt reaction.

5.5.2 Evidence from near-EPR seamounts

The near-axis flanks of the EPR have abundant seamounts composed dominantly of MORB [*Batiza et al.*, 1990]. They occur as individual seamounts and also as chains parallel to either relative or absolute plate motion. Figure 5.10 shows that the seamount MORB array is very similar to the global axial MORB array (Figure 5.1) and appears to be a combination of both the fast and slow trends. Very clear slow trends are found at individual seamounts, as shown in Figure 5.11. Thus the slow trends are not confined to slow-spreading ridges, but also are found at zero-age seamounts near fast-spreading ridges.

As shown in Chapter 3, mantle upwelling beneath the EPR appears to become less vigorous off axis such that at 40 - 50 km away from the EPR axis the upwelling is feeble. In such an off-axis mantle setting, diapiric instabilities would have adequate time to nucleate and rise, providing MORB melts for some active off-axis volcanoes. This suggestion is speculative, but the existence of diapiric instabilities below the flanks of the EPR is very plausible. If so, then the existence of the slow-spreading chemical variation trend at near-EPR seamounts is consistent with the other lines of evidence indicating that the slow trend could originate by solid-melt reaction in rising diapirs undergoing melting.

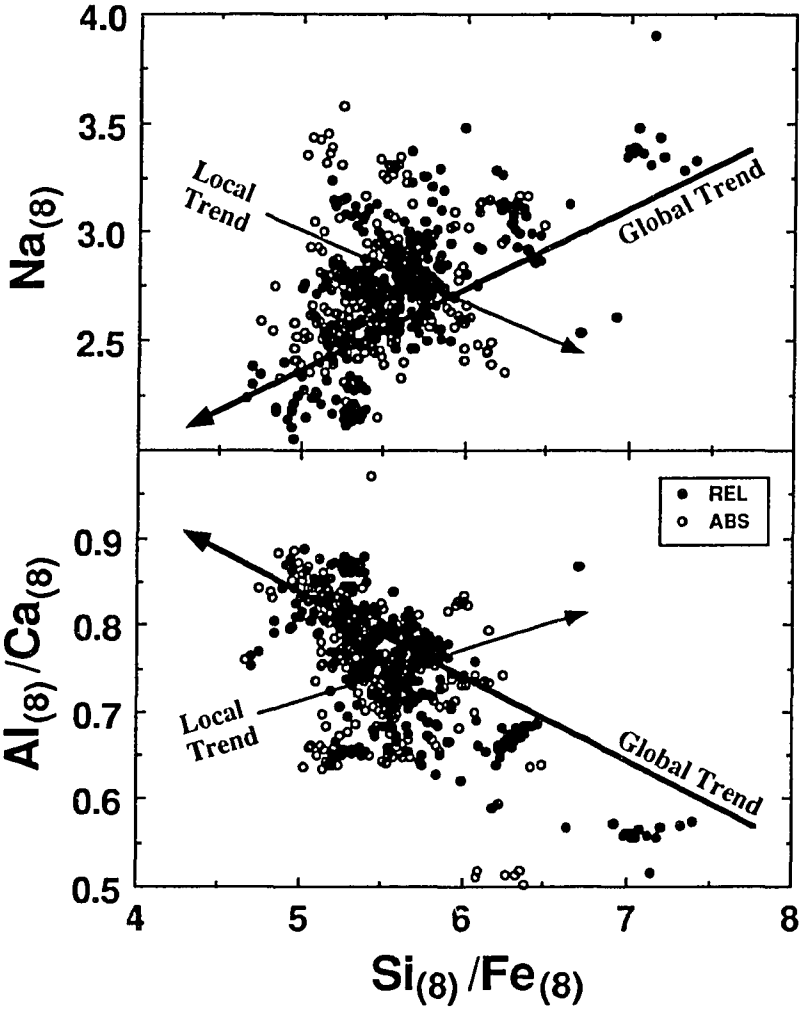

Fig. 5.10 Data for seamounts near the East Pacific Rise (8° to 15°N) from *Batiza and Vanko* [1984], *Allan et al* [1989], *Batiza et al.* [1989, 1990] and unpublished data. REL points are from members of small seamount chains parallel to relative motion; ABS for chains parallel to the absolute plate motion. For reference, I show the global trend [*Klein and Langmuir*, 1989] and a representative local trend and data for the northern EPR from Chapter 3. Note that the seamount MORB data array strongly resembles the global mid-ocean ridge MORB array (Figure 5.1).

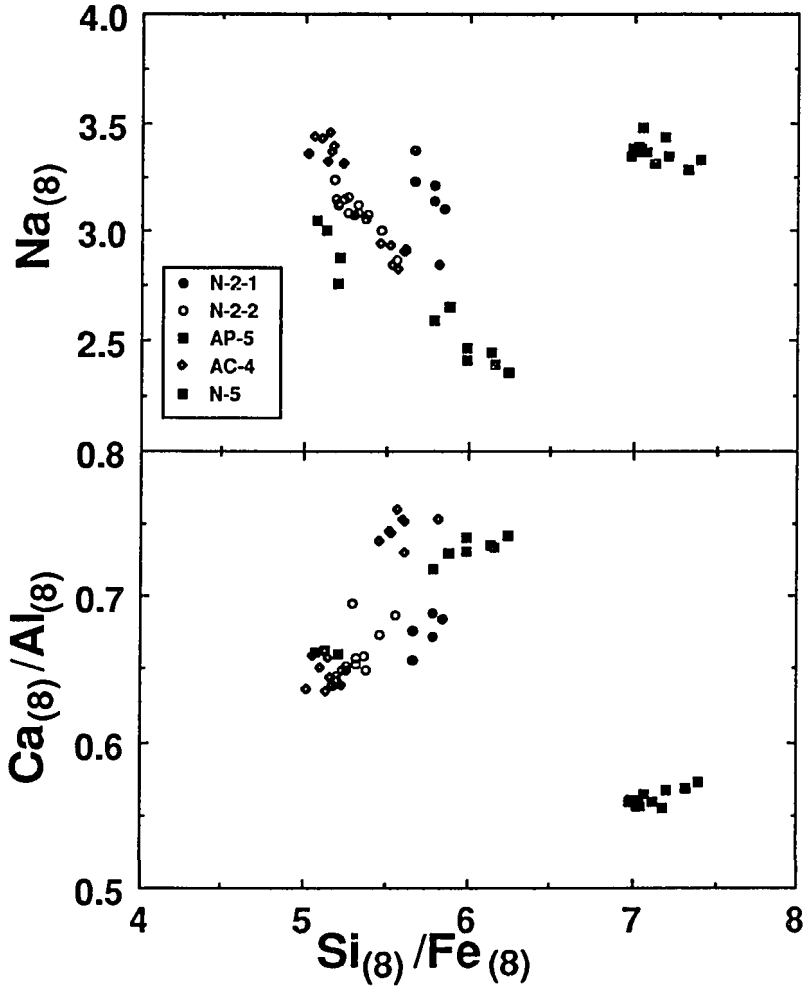

Fig. 5.11 Seamount data from *Batiza and Vanko* [1989] and *Batiza et al.* [1990] showing local trends for individual seamounts.

5.5.3 Diapirs at slow-spreading ridges

Slow-spreading ridge segments in the Atlantic [e.g., *Blackman and Forsyth*, 1992; *Grindlay et al.*, 1991; *Lin et al.*, 1990] are typically characterized by central along-axis highs and negative residual gravity anomalies. These anomalies may be due to thick crust, a thicker mantle column of low-density residual mantle, and/or higher temperature mantle. All these possibilities are consistent with focused buoyant mantle upwelling with more melting in the center of the segment. Whether such upwelling represents a single large diapir or numerous individual diapirs in the center of the segment is not known, but for the given along-axis chemical variation as well as the topography and gravity data, multiple diapirs tapped at various levels seem to be more likely. I suggest a diapir model for the origin of the slow-spreading trend of chemical variation. Such diapirs (Figure 5.12) could produce the slow trend via the diapiric melting processes I propose.

Figure 5.12 shows that for a given slow-spreading ridge segment, such as 26°S MAR, the mantle upwelling may be more focused in the center, so that there should exist an along-axis thermal profile characterized by a hotter center and cooler edges near offsets due to conductive heat loss near offsets ("cold" edge effects). In such a thermal regime, dikes could penetrate to much greater depths near offsets than in the center, so that diapirs near offsets would be tapped at a greater depth before achieving large size, whereas diapirs in the center would rise, experiencing continuous melting and solid-melt reequilibration, to much shallower levels before being tapped. The net results of this process reflected in observed chemistry are that 1) lavas near offsets are characterized by signatures of high pressure and low degree of melting; whereas 2) lavas in the center of the segment preserve signatures of high degree of melting and low pressure due to reequilibration, consistent with the observation at 26°S MAR and the chemical correlations of the slow ("local") trend. Thus, a diapiric upwelling with associated melting and melt segregation is consistent with MORB chemistry, topography, as well as gravity patterns. The terms slow and fast are

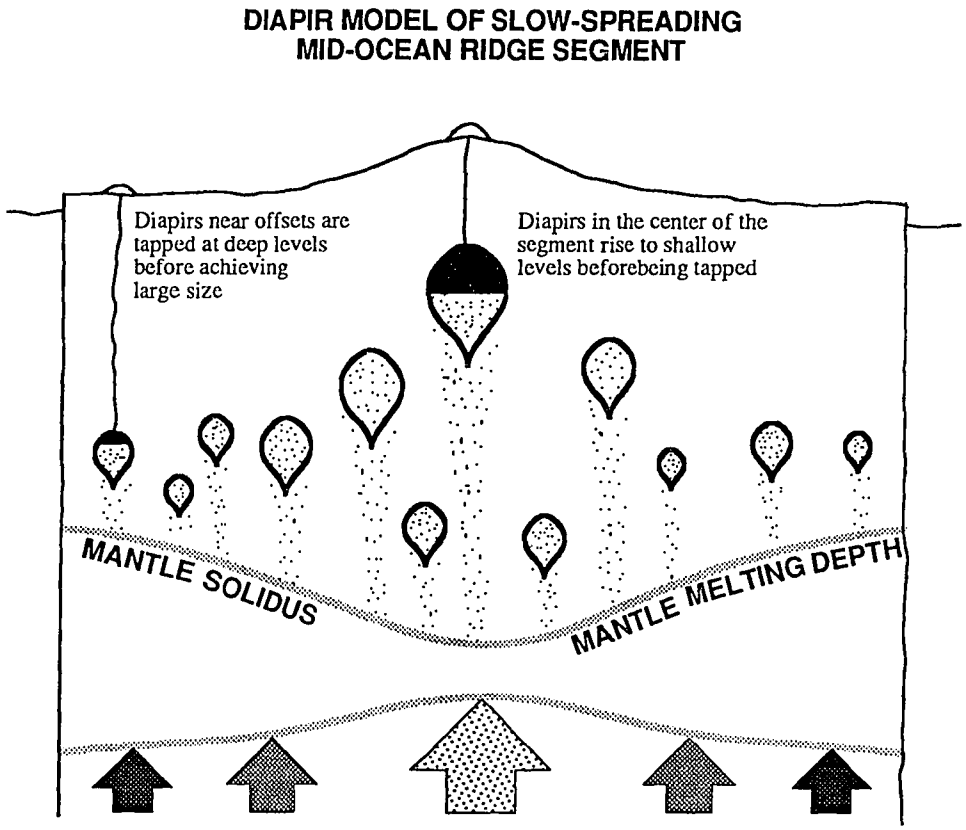

Fig. 5.12 A cartoon showing an idealized along-axis cross-section for a typical slow-spreading mid-ocean ridge segment such as the one at 26°S, MAR [*Batiza et al.*, 1988; also see Chapter 3] with two bounding offsets and a central topographic high. In this model, the mantle upwelling is more focused and hotter in the center than near offsets (as denoted by the size and pattern of the arrows) so that the solidus is depressed in the center. Black areas in diapirs are melt which forms during ascent but reequilibrates at lower pressure as the diapir rises. Dots show diapir trails. In such an environment temperature may decrease laterally toward offsets due to "cold edges", so dikes may be efficient conduits at greater depths near offsets than in the center. Thus, diapirs near offsets are tapped at deep levels before achieving large sizes (resultant MORB chemical signatures will reflect low degrees and high pressures of melting), whereas diapirs in the center of the segment rise to shallow levels before being tapped (resultant MORB chemistry will have signature of high degrees and low pressure of melting due to solid-melt reequilibration). Many independent lines of evidence favor an important role for diapirs at slow spreading ridges. I suggest that petrologic processes in rising diapirs may result in the slow-spreading trend of MORB chemical variation.

coincident with slow- and fast-spreading rates, but they pertain to slow and fast melt separation, as the slow trend also seems to occur at near-EPR seamounts.

This diapiric upwelling model makes sense because fast upwelling and rapid melt segregation at slow-spreading ridges may be restricted due to slow spreading; diapirs must circumvent the overload through buoyant forces and/or even thermal stoping as opposed to passive upwelling caused by fast plate separation. This also explains the different along-axis topography between slow- and fast-spreading ridges. Buoyant instability would be initiated in spatially discrete patterns at slow-spreading rates [e.g., *Schouten et al.*, 1985; *Crane*, 1985] which facilitate development of isolated, or centralized, upwelling as indicated by the high frequency of ridge segmentation and the dramatic topography within individual segments along the mid-Atlantic ridge [e.g., *Lin et al.*, 1990; *Lin and Phipps Morgan*, 1992].

5.6 Conclusions

1) With an expanded global data set, I confirm that slow ridges appear to generally have more primitive lavas than fast ridges.

2) There appear to be no systematic differences between slow- and fast- ridges in the depth or extent of partial melting, thus mantle temperature seems to be independent of spreading rate.

3) The so-called local and global trends of MORB systematics are a function of spreading rate. The global systematics are found at fast ridge segments and the local systematics are found at slow ridges. Either trend can be found in transitional ridges spreading at 50 - 60 mm/yr.

4) The so-called local and global trends are not apparently sensitive to length scale, so I refer to these trends as the slow and fast trends, respectively. These terms are coincident with fast- and slow-spreading rates, but they pertain to fast and slow melt segregation.

5) The slow and fast trends display a range of slopes on chemical diagrams, but no consistent or regular behavior, such as a fanning pattern.

6) Strong geophysical and field evidence (in ophiolites) points to the importance of diapirs at slow ridges. I show that the "local" trend is characteristic of slow ridges and propose that this trend could result from processes in rising diapirs undergoing melting and melt reequilibration.

7) The slow trend is not confined to slow-spreading ridges, but also occurs at near-EPR seamounts, suggesting that slow melt segregation and solid-melt reequilibration is the direct cause of the slow trend.

8) transitional ridges spreading at 50 - 60 mm/yr may display either the fast or slow trend of chemical variation. I interpret this to indicate that both 2-D, passive upwelling and buoyant, 3-D (diapiric) mantle upwelling occur and that the petrologic signatures of lavas erupted may be dominated by either process.

APPENDIX A

MICROSOFT BASIC CODE FOR DENSCAL

DENSCAL calculates densities of silicate melts and mantle minerals (olivine, orthopyroxene, clinopyroxene, garnet, spinel, and plagioclase) as a function of TEMPERATURE, PRESSURE, and COMPOSITION in magma generation environment.

First version: 11/15/1989
Second version: 02/23/1990
Final version: 04/22/1990

by Yaoling Niu
Department of Geology and Geophysics
University of Hawaii at Manoa
2525 Correa Road
Honolulu, Hawaii 96822
U.S.A.

```
WINDOW 1,,(6,28)-(506,330),2
OPTION BASE 1
DIM OXN$(10),OXW(10),OMW(10),OXMW(10),OXMF(10),PMV0(10),PMV(10)
DIM DVDT(10),BETA(10),DBETADT(10),OXBETA(10),SK(6),SDKDT(6)
DIM SDKDP(6),DST(6),DSPT(6),COM$(6),COM(6),COMW(6),COMV(6)

MAINMENU:
PRINT TAB(3)"Type one of the numbers (1 - 8) to make choice":PRINT
PRINT TAB(5)"1","DENSITY OF SILICATE MELT"
PRINT TAB(5)"2","DENSITY OF OLIVINE"
PRINT TAB(5)"3","DENSITY OF ORTHOPYROXENE "
PRINT TAB(5)"4","DENSITY OF CLINOPYROXENE "
PRINT TAB(5)"5","DENSITY OF GARNET "
PRINT TAB(5)"6","DENSITY OF SPINEL "
PRINT TAB(5)"7","DENSITY OF PLAGIOCLASE "
PRINT TAB(5)"8","QUIT":PRINT
INPUT "What is your choice";CHOICE
ON CHOICE GOTO MELT,OLIVINE,OPX,CPX,GNT,SPL,PLAG,QUIT

MELT:
CLS
CALL TEXTFONT(0):CALL TEXTSIZE(12):LOCATE 5,5
RESTORE MELT
FOR I=1 TO 10:READ OXN$(I):NEXT
DATA SiO2,TiO2,Al2O3,Fe2O3,FeO,MnO,MgO,CaO,Na2O,K2O
FOR I=1 TO 10:READ OMW(I):NEXT
DATA 60.0843,79.8988,101.9613,159.6922,71.8464,70.9374,40.32,56.08,61.98,94.2
FOR I=1 TO 10:READ PMV0(I):NEXT
DATA 26.90,23.16,37.11,42.13,13.65,14.13,11.45,16.57,28.78,45.84
FOR I=1 TO 10:READ DVDT(I):NEXT
```

```
DATA .0,.00724,.00262,.00909,.00292,.0,.00262,.00292,.00741,.01191
FOR I = 1 TO 10:READ BETA(I):NEXT
DATA 6.93,9.88,5.04,.0,4.28,.0,1.79,0.68,8.35,22.66
FOR I = 1 TO 10:READ DBETADT(I):NEXT
DATA .0,-.5,-13,.0,4,.0,14,3,11,25
NEWSAMPLE:
PRINT:INPUT "Sample Name";SN$
PRINT "Input Oxides wt % of sample"
FOR I=1 TO 10:PRINT OXN$(I);" ",:INPUT
OXW(I):OXMW(I)=OXW(I)/OMW(I):NEXT
SUMOFMOL=0:
FOR I=1 TO 10:SUMOFMOL=SUMOFMOL+OXMW(I):NEXT
FOR I=1 TO 10:OXMF(I)=OXMW(I)/SUMOFMOL:NEXT
MOLWTLIQ=0
FOR I=1 TO 10:MOLWTLIQ=MOLWTLIQ+OXMF(I)*OMW(I):NEXT
LPRINT TAB(5)" Melt Sample: ";SN$
LPRINT TAB(5)"----------"
MELTPT:
INPUT "Temperature (°C)";T:INPUT "Pressure (KB)";P
REM MELT DENSITY AT ATMOSPHERIC PRESSURE
FOR I=1 TO 10:PMV(I)=PMV0(I)+DVDT(I)*(T-1400):NEXT
PMV(6)=14.13*EXP(15.1*10^-5*(T-1400))
VLIQ=0
FOR I=1 TO 10:VLIQ=VLIQ+PMV(I)*OXMF(I):NEXT
VLIQ=VLIQ+OXMF(2)*OXMF(9)*20.28
LQDT=MOLWTLIQ/VLIQ:
FOR I=1 TO 10:OXBETA(I)=BETA(I)*10^(-3)+DBETADT(I)*10^(-6)*(T-
1400):NEXT
FOR I=1 TO 10:OXBETA(I)=OXBETA(I)*OXMF(I):NEXT
SUMBETA=0
FOR I=1 TO 10:SUMBETA=SUMBETA+OXBETA(I):NEXT
LQMUDULUS=1/SUMBETA
LQDTP=LQDT:MDD=.5
TRYLQ1:
LQDTP=LQDTP+MDD
TRYLQ2:
BM1=BM
BM=1.5*LQMUDULUS*((LQDTP/LQDT)^(7/3)-(LQDTP/LQDT)^(5/3))
IF BM<P AND BM>BM1 THEN GOTO TRYLQ1
IF BM<P AND BM<BM1 THEN MDD=MDD/2:GOTO TRYLQ1
IF BM>P AND BM>BM1 THEN MDD=MDD/2:LQDTP=LQDTP-MDD:GOTO
TRYLQ2
IF BM>P AND BM<BM1 THEN LQDTP=LQDTP-MDD: GOTO TRYLQ2
DST=LQDT:DSPT=LQDTP
GOSUB PRINTER
INPUT "Do you want a change of pressure and temperature (Y/N)";Yes$
IF Yes$="Y" OR Yes$="y" THEN GOTO MELTPT
INPUT "Do you want a change of Melt composition? (Y/N)";Yes$
IF Yes$="Y" OR Yes$="y" THEN GOTO NEWSAMPLE
GOTO MAINMENU
```

```
OLIVINE:
CLS
CALL TEXTFONT(0):CALL TEXTSIZE(12):LOCATE 5,5
PRINT:INPUT "Sample Name";SN$
INPUT "Fo%=";FO:FO=FO/100
LPRINT TAB(5)" Olivine Sample: ";SN$
LPRINT TAB(5)"----------------"
LPRINT TAB(5) "Fo = ";FO
OLPT:
N=2
INPUT "Temperature (°C)";T:INPUT "Pressure (Kbar)";P
RESTORE OLIVINE
FOR I=1 TO N:READ SK(I),SDKDT(I),SDKDP(I),COMW(I):NEXT
DATA 1271,-0.236,5.39,140.708,1368,-0.268,5.2,203.778
DST(1)=3.225-9.1526*10^(-5)*(T-25)-3.1618*10^(-8)*(T-25)^2
DST(2)=4.4-1.2124*10^(-4)*(T-25)-2.2511*10^(-8)*(T-25)^2
DST=DST(1)*FO+DST(2)*(1-FO)
GOSUB BCHMNAGAN
GOSUB PRINTER
INPUT "Do you want a change of pressure and temperature (Y/N)";Yes$
IF Yes$="Y" OR Yes$="y" THEN GOTO OLPT
INPUT "Do you want a change of Olivine composition? (Y/N)";Yes$
IF Yes$="Y" OR Yes$="y" THEN GOTO OLIVINE
GOTO MAINMENU

OPX:
CLS
CALL TEXTFONT(0):CALL TEXTSIZE(12):LOCATE 5,5
PRINT:INPUT "Sample Name";SN$
INPUT "En%=";EN:EN=EN/100
N=2
LPRINT TAB(5)" Orthopyroxene Sample: ";SN$
LPRINT TAB(5)"--------------------------"
LPRINT TAB(5) "En = ";EN
OPXPT:
INPUT "Temperature (°C)";T:INPUT "Pressure (Kbar)";P
RESTORE OPX
FOR I=1 TO N:READ SK(I),SDKDT(I),SDKDP(I),COMW(I):NEXT
DATA 1070,-.27,5,200.792,1010,-.3,5,263.862
DST(1)=3.194-9.281*10^(-5)*(T-25):DST(2)=3.998-11.62*10^(-5)*(T-25)
DST=DST(1)*EN+DST(2)*(1-EN)
GOSUB BCHMNAGAN
GOSUB PRINTER
INPUT "Do you want a change of pressure and temperature (Y/N)";Yes$
IF Yes$="Y" OR Yes$="y" THEN GOTO OPXPT
INPUT "Do you want a change of OPX composition? (Y/N)";Yes$
IF Yes$="Y" OR Yes$="y" THEN GOTO OPX
GOTO MAINMENU

CPX:
CLS
CALL TEXTFONT(0):CALL TEXTSIZE(12):LOCATE 5,5
```

```
PRINT:INPUT "Sample Name";SN$
N=6
RESTORE CPX
FOR I=1 TO N:READ COM$(I):NEXT
DATA CEn,CFs,Di,Hd,Jd,Ac
PRINT "Input % of the following CPX components:"
FOR I=1 TO N: PRINT COM$(I);:INPUT COM(I):COM(I)=COM(I)/100:NEXT
LPRINT TAB(5)" Clinopyroxene Sample: ";SN$
LPRINT TAB(5)"-------------------------"
LPRINT TAB(5)"Components: ";"CEn=";COM(1);";CFs=";COM(2);
            ";Di=";COM(3);";Hd=";COM(4);";Jd=";COM(5);";Ac=";COM(6)
CPXPT:
INPUT "Temperature (°C)";T:INPUT "Pressure (Kbar)";P
RESTORE CPXPT
FOR I=1 TO N:READ SK(I),SDKDT(I),SDKDP(I),COMW(I):NEXT
DATA 1070,-.27,5,200.792,1010,-.3,5,263.862,1130,-.2,4.5,216.56
DATA 1200,-.2,4.5,248.095,1430,-.2,4.5,202.14,1060,-.2,4.5,284.968
DST(1)=3.191-9.272*10^(-5)*(T-25):DST(2)=4.005-11.64*10^(-5)*(T-25)
DST(3)=3.277-2.108*10^(-5)*(T-25):DST(4)=3.632-2.337*10^(-5)*(T-25)
DST(5)=3.347-8.796*10^(-5)*(T-25):DST(6)=3.576-8.796*10^(-5)*(T-25)
DST=0
FOR I=1 TO N:DST=DST+DST(I)*COM(I):NEXT
GOSUB BCHMNAGAN
GOSUB PRINTER
INPUT "Do you want a change of pressure and temperature (Y/N)";Yes$
IF Yes$="Y" OR Yes$="y" THEN GOTO CPXPT
INPUT "Do you want a change of CPX composition? (Y/N)";Yes$
IF Yes$="Y" OR Yes$="y" THEN GOTO CPX
GOTO MAINMENU

GNT:
CLS
CALL TEXTFONT(0):CALL TEXTSIZE(12):LOCATE 5,5
PRINT:INPUT "Sample Name";SN$
N=6
RESTORE GNT
FOR I=1 TO N:READ COM$(I):NEXT
DATA Pyr,Alm,Gro,Spe,And,Uvr
PRINT "Input % of the following garnet components:"
FOR I=1 TO N: PRINT COM$(I);:INPUT COM(I):COM(I)=COM(I)/100:NEXT
LPRINT TAB(5)" Garnet Sample: ";SN$
LPRINT TAB(5)"--------------------"
LPRINT TAB(5)"Components: ";"Pyr=";COM(1);";Alm=";COM(2);

      ";Gro=";COM(3);";Spe=";COM(4);";And=";COM(5);";Uvr=";COM(6)
GNTPT:
INPUT "Temperature (°C)";T:INPUT "Pressure (Kbar)";P
RESTORE GNTPT
FOR I=1 TO N:READ SK(I),SDKDT(I),SDKDP(I),COMW(I):NEXT
DATA 1750,-.21,5.45,403.15,1779,-.201,5.43,497.755,1700,-.2,4.25,450.454
DATA 1742,-.2,4.59,495.028,1570,-.2,5,508.185,1620,-.2,5,500.483
DST(1)=3.557-9.332*10^(-5)*(T-25):DST(2)=4.318-11.044*10^(-5)*(T-25)
```

```
DST(3)=3.595-8.319*10^(-5)*(T-25):DST(4)=4.19-11.351*10^(-5)*(T-25)
DST(5)=3.86-9.406*10^(-5)*(T-25):DST(6)=3.848-9.378*10^(-5)*(T-25)
DST=0
FOR I=1 TO N:DST=DST+DST(I)*COM(I):NEXT
GOSUB BCHMNAGAN
GOSUB PRINTER
INPUT "Do you want a change of pressure and temperature (Y/N)";Yes$
IF Yes$="Y" OR Yes$="y" THEN GOTO GNTPT
INPUT "Do you want a change of garnet composition? (Y/N)";Yes$
IF Yes$="Y" OR Yes$="y" THEN GOTO GNT
GOTO MAINMENU

SPL:
CLS
CALL TEXTFONT(0):CALL TEXTSIZE(12):LOCATE 5,5
PRINT:INPUT "Sample Name";SN$
N=4
RESTORE SPL
FOR I=1 TO N:READ COM$(I):NEXT
DATA Spl,Her,Chr,Mgt
PRINT "Input % of the following spinel components:"
FOR I=1 TO N: PRINT COM$(I);:INPUT COM(I):COM(I)=COM(I)/100:NEXT
LPRINT TAB(5)" Spinel Sample: ";SN$
LPRINT TAB(5)"-------------------"
LPRINT TAB(5) "Components: ";"Spl=";COM(1);";Her=";COM(2);
                    ";Chr=";COM(3);";Mgt=";COM(4)
SPLPT:
INPUT "Temperature (°C)";T:INPUT "Pressure (Kbar)";P
RESTORE SPLPT
FOR I=1 TO N:READ SK(I),SDKDT(I),SDKDP(I),COMW(I):NEXT
DATA 1940,-.22,4,142.273,2103,-.2,4,173.808
DATA 1830,-.2,4,223.8366,1860,-.2,4,231.539
DST(1)=3.583-9.513*10^(-5)*(T-25):DST(2)=4.265-10.423*10^(-5)*(T-25)
DST(3)=5.086-8.907*10^(-5)*(T-25):DST(4)=5.2-21.89*10^(-5)*(T-25)
DST=0
FOR I=1 TO N:DST=DST+DST(I)*COM(I):NEXT
GOSUB BCHMNAGAN
GOSUB PRINTER
INPUT "Do you want a change of pressure and temperature (Y/N)";Yes$
IF Yes$="Y" OR Yes$="y" THEN GOTO SPLPT
INPUT "Do you want a change of spinel composition? (Y/N)";Yes$
IF Yes$="Y" OR Yes$="y" THEN GOTO SPL
GOTO MAINMENU

PLAG:
CLS
CALL TEXTFONT(0):CALL TEXTSIZE(12):LOCATE 5,5
PRINT:INPUT "Sample Name";SN$
INPUT "An%=";AN:AN=AN/100
N=2
LPRINT TAB(5)" Plagioclase Sample: ";SN$
LPRINT TAB(5)"--------------------------"
```

```
LPRINT TAB(5) "An = ";AN
PLAGPT:
INPUT "Temperature (°C)";T:INPUT "Pressure (Kbar)";P
RESTORE PLAG
FOR I=1 TO N:READ SK(I),SDKDT(I),SDKDP(I),COMW(I):NEXT
DATA  699.3,-.2,4,262.223,943.4,-.2,4,278.209
DST(1)=2.611-3.3415*10^(-5)*(T-25)-7.5322*10^(-8)*(T-25)^2
DST(2)=2.762-1.6329*10^(-5)*(T-25)
DST=DST(1)*(1-AN)+DST(2)*AN
GOSUB BCHMNAGAN
GOSUB PRINTER
INPUT "Do you want a change of pressure and temperature (Y/N)";Yes$
IF Yes$="Y" OR Yes$="y" THEN GOTO PLAGPT
INPUT "Do you want a change of PLAG composition? (Y/N)";Yes$
IF Yes$="Y" OR Yes$="y" THEN GOTO PLAG
GOTO MAINMENU
QUIT:
END

BCHMNAGAN:
FOR I=1 TO N:SK(I)=SK(I)+SDKDT(I)*(T-25):COMV(I)=COMW(I)/DST(I):NEXT
TMV=0:KV=0:KR0=0
FOR I=1 TO N:TMV=TMV+COMV(I):NEXT:
FOR I=1 TO
N:COMV(I)=COMV(I)/TMV:KV=KV+COMV(I)*SK(I):KR0=KR0+COMV(I)/SK(I):NE
XT
KR=1/KR0:KT=(KV+KR)/2
PRINT
DSPT=DST:SDD=.5
TRY1:
DSPT=DSPT+SDD
TRY2:
CP1=CP
CP=1.5*KT*((DSPT/DST)^(7/3)-(DSPT/DST)^(5/3))*(1-.75*(4-
SDKDP)*((DSPT/DST)^(2/3)-1))
IF CP<P AND CP>CP1 THEN GOTO TRY1
IF CP<P AND CP<CP1 THEN SDD=SDD/2:GOTO TRY1
IF CP>P AND CP>CP1 THEN SDD=SDD/2:DSPT=DSPT-SDD:GOTO TRY2
IF CP>P AND CP<CP1 THEN DSPT=DSPT-SDD: GOTO TRY2
RETURN

PRINTER:
LPRINT TAB(5)"Temperature:          ";T;"°C"
LPRINT TAB(5)"Pressure:             ";P;"Kbar"
LPRINT TAB(5)"Density at ";1;" bar:   ";USING "#.#### g/cc";DST
LPRINT TAB(5)"Density at";P;"Kb:    ";USING "#.#### g/cc";DSPT
PRINT
RETURN
```

APPENDIX B

MICROSOFT BASIC CODE FOR MORBCAL

MORBCAL calculates compositions of primary magma parental to MORBs as a function of melting conditions: Depth of melting and melting temperature.

First version 04/20/1990
Second version 02/20/1991
Final version 07/15/1991

by Yaoling Niu
Department of Geology and Geophysics
University of Hawaii at Manoa
2525 Correa Raod
Honolulu, Hawaii 96822
U.S.A.


```
WINDOW 1,,(6,28)-(506,330),2
CALL TEXTFONT(0):CALL TEXTSIZE(12)
PRINT TAB(1) "1) MORBCAL calculates the primary MORB major element
compositions"
PRINT TAB(3) "based on the empirical melting model detailed in Chapter three. The
default "
PRINT TAB(3) "mantle peridotite composition employed in this model is MORB-
Pyrolite-90,"
PRINT TAB(3) "the most reasonable composition of depleted oceanic upper mantle, of
Falloon"
PRINT TAB(3) "and Green (Mineral. Petrol.,1987). An option is given for you to input
your "
PRINT TAB(3) "desired mantle compositions, but the input should not be over
extrapolated out of"
PRINT TAB(3) "the available periments (see Niu and Batiza,1991). Otherwise, the
empirical"
PRINT TAB(3) "coefficients in this model may be adjusted to meet your desire if new
periments"
PRINT TAB(3) "for a variety of mantle compositions are available in future.":PRINT
PRINT TAB(1) "2) MORBCAL provides two melting models: BATCH melting and"
PRINT TAB(3) "decompression pression induced DYNAMIC melting due to plate
separation."
PRINT TAB(3) "In addition, MORBCAL also enables to calculate melting parameters
such as"
PRINT TAB(3) "F(%), Po(kb), Pf(kb), To(°C), and Tf(°C) for a ridge segment where
densely"
PRINT TAB(3) "sampled MORB compositions are available."
PRINT
GOSUB WaitKey
PRINT
DIM OXN$(8),OXMTL(8),OXLIQ(8),BOXLIQ(8),OXSOL(8),DCEF(8),DE(8)
```

```
DIM DF(8),DRF(8),DH(8),DI(8),FPT(8),FPTN$(8)
MAINMENU:
CLS
CALL TEXTFONT(0):CALL TEXTSIZE(12)
PRINT TAB(3)
"*****************************MENU*******************************"
PRINT
PRINT TAB(3)"Type a number to make choice":PRINT
PRINT TAB(5)"1", "Equilibrium BATCH Melting Model"
PRINT TAB(5)"2", "Decompression-induced DYNAMIC Melting Model"
PRINT TAB(5)"3", "Melting parameters: F(%), Po(kb), Pf(kb), To(°C), and Tf(°C)"
PRINT TAB(5)"4", "Quit":PRINT
INPUT"What is your choice"; CHOICE
ON CHOICE GOTO BATCH,DYNAMIC,FPPTT,QUIT
QUIT:
END

BATCH:
CLS
CALL TEXTFONT(0):CALL TEXTSIZE(12)
PRINT TAB(3)"******************Equilibrium BATCH Melting
model******************"
PRINT
PRINT TAB(1)"1)  BATCH model requires input of pressure (kb) & Temperature (°C)
at"
PRINT TAB(3)" which melting may occur.  IF your INPUT is a subsolidus condition,"
PRINT TAB(3)" MORBCAL will prompt you because no melting will occur.":PRINT
PRINT TAB(1)"2)  In this model, each oxide concentration is computed independently
and"
PRINT TAB(3)" no normalization is invoked":PRINT
PRINT TAB(1)"3)  Because of the limitation by available experimental data, the best"
PRINT TAB(3)" results are warranted at the conditions of P = 7 - 22 Kbars with 8 -"
PRINT TAB(3)" 30 % of melting.":PRINT
GOSUB WaitKey
RESTORE BATCH
FOR I=1 TO 8: READ OXN$(I):NEXT
DATA SiO2,TiO2,Al2O3,FeO,MgO,CaO,Na2O,K2O
FOR I=1 TO 8: READ OXMTL(I):NEXT
DATA  44.74,0.17,4.37,7.55,38.57,3.38,0.4,0.03
FOR I=1 TO 8: READ DE(I):NEXT
DATA  0.848,0.091,0.196,1.472,5.623,0.327,0.0509,0.0099
FOR I=1 TO 8: READ DF(I):NEXT
DATA  -0.0022,-0.002,-0.0065,0,-0.0451,-0.012,-0.0038,-0.0002
FOR I=1 TO 8: READ DRF(I):NEXT
DATA  0,0,-0.025,0.273,0,0.3071,0,0
FOR I=1 TO 8: READ DH(I):NEXT
DATA  0.0055,0,0.0021,-0.035,-0.081,0.0005,0,0
FOR I=1 TO 8: READ DI(I):NEXT
DATA  0,0,0,-0.013,0,0,0,0
PRINT
PRINT "This is the default MORB-Pyrolite-90:"
FOR I=1 TO 8:PRINT TAB(I*6);OXN$(I);:NEXT:PRINT
```

```
FOR I=1 TO 8:PRINT TAB(I*6);USING
"##.##";OXMTL(I);:NEXT:PRINT:PRINT
INPUT "Do you desire to input your own mantle composition? (Y/N)";MYeh$
IF MYeh$="Y" OR MYeh$="y" THEN GOSUB Mantle:PRINT
LINE INPUT "Give a name to save your results as a disk file:";Filename$
OPEN "A",1,Filename$:PRINT
IF MYeh$="Y" OR MYeh$="y" THEN MMCN$=MCN$ ELSE MMCN$="MPY-90"
PRINT#1, MMCN$;":"
FOR I=1 TO 8:PRINT#1, TAB(I*6);OXN$(I);:NEXT:PRINT
FOR I=1 TO 8:PRINT#1, TAB(I*6);USING "##.##";OXMTL(I);:NEXT
PRINT#1,
BPT:
CALL TEXTFONT(0):CALL TEXTSIZE(12)
INPUT "Pressure (Kb)";P
INPUT "Temperature(°C)";T
F=-117.149-6.028*P+(.11679+.003023*P)*T
IF F<=0,THEN BEEP ELSE GOTO BDCEF
PRINT "Subsolidus condition!!! Either P is too high or T is too low!":GOTO BPT
BDCEF:
FOR I=1 TO 8:DCEF(I)=DE(I)+DF(I)*F+DRF(I)/F+DH(I)*P+DI(I)*P/F:NEXT
FOR I=1 TO 8:OXLIQ(I)=OXMTL(I)/(F/100+DCEF(I)*(1-F/100)):NEXT
PRINT
PRINT "Equilibrium BATCH melting of";" "MMCN$;":"
CALL TEXTFONT(1):CALL TEXTSIZE(9)
PRINT "T(°C)";TAB(7);"P(kb)";TAB(14);"F(%)";:
FOR I=1 TO 8:PRINT TAB(14+I*7);OXN$(I);:NEXT:PRINT
PRINT T;TAB(7);P;TAB(14);USING"##.##";F;:
FOR I=1 TO 8:PRINT TAB(14+I*7);USING "##.###";OXLIQ(I);:NEXT:PRINT
PRINT#1,"Equilibrium BATCH melting of";" "MMCN$;":"
PRINT#1, "T(°C)";TAB(7);"P(kb)";TAB(14);"F(%)";:
FOR I=1 TO 8:PRINT#1, TAB(14+I*7);OXN$(I);:NEXT:PRINT#1,
PRINT#1, T;TAB(7);P;TAB(14);USING"##.##";F;:
FOR I=1 TO 8:PRINT#1, TAB(14+I*7);USING "##.###";OXLIQ(I);:NEXT
PRINT#1,
INPUT "Do you want a change of pressure and temperature (Y/N)";Yes$
IF Yes$="Y" OR Yes$="y" THEN GOTO BPT:PRINT
PRINT#1, "This job is done at ";TIME$;" on ";DATE$:PRINT
CLOSE 1
GOSUB WaitKey
GOTO MAINMENU

DYNAMIC:
CLS
CALL TEXTFONT(0):CALL TEXTSIZE(12)
PRINT TAB(3)"**********Decompression-induced DYNAMIC Melting
model**********"
PRINT
PRINT TAB(1)"1) DYNAMIC model requires input of Po, the depth at which melting
may"
PRINT TAB(3)" occur across the mantle solidus, and Pf, the depth at which melting"
PRINT TAB(3)" may actually stop.":PRINT
PRINT TAB(1)"2) Because of the limitation by available experiments, your input of"
```

```
PRINT TAB(3)" 5kb ≤ Po ≤ 25 with 3kb ≤ Pf ≤ Po will produce the best reliable
results":PRINT
PRINT TAB(1)"3)  In this model, each oxide concentration is computed independently"
PRINT TAB(3)" and no normalization is invoked.":PRINT
GOSUB WaitKey
RESTORE DYNAMIC
FOR I=1 TO 8: READ OXN$(I):NEXT
DATA SiO2,TiO2,Al2O3,FeO,MgO,CaO,Na2O,K2O
FOR I=1 TO 8: READ OXMTL(I):NEXT
DATA  44.74,0.17,4.34,7.55,38.57,3.38,0.4,0.03
FOR I=1 TO 8: READ DE(I):NEXT
DATA  .858,.098,.189,1.442,5.286,.318,0.111,.069
FOR I=1 TO 8: READ DF(I):NEXT
DATA  -.004,-.005,-.0051,0,-.064,-.0122,-.007,-.002
FOR I=1 TO 8: READ DRF(I):NEXT
DATA  0,0,-.025,.273,0,.272,0,0
FOR I=1 TO 8: READ DH(I):NEXT
DATA  .005,0,.0021,-.0350,-.063,.001,0,0
FOR I=1 TO 8: READ DI(I):NEXT
DATA  0,0,0,-.013,0,0,0,0
CLS
PRINT "This is the default MORB-Pyrolite-90:"
FOR I=1 TO 8:PRINT TAB(I*6);OXN$(I);:NEXT:PRINT
FOR I=1 TO 8:PRINT TAB(I*6);USING"##.##";OXMTL(I);:NEXT:PRINT
INPUT "Do you desire to input your mantle composition? (Y/N)";Yes$
IF Yes$="Y" OR Yes$="y" THEN GOSUB Mantle
LINE INPUT "Please give a name to save your results as a disk file";Filename$
OPEN "A",1,Filename$
IF MYeh$="Y" OR MYeh$="y" THEN MMCN$=MCN$ ELSE MMCN$="MPY-90"
PRINT#1, MMCN$;":"
FOR I=1 TO 8:PRINT#1, TAB(I*6);OXN$(I);:NEXT:PRINT
FOR I=1 TO 8:PRINT#1, TAB(I*6);USING "##.##";OXMTL(I);:NEXT
PRINT#1,
DPo:
INPUT "Enter Po(Kb)";Po
IF Po<5 OR Po>25 THEN BEEP ELSE GOTO DPf
PRINT "The INPUT must be: 5kb <Po <25kb !!!":GOTO DPo
DPf:
INPUT "Enter Pf(Kb)";Pf
IF Pf<3 OR Pf>=Po THEN BEEP ELSE GOTO DDCEF
PRINT "The INPUT must be: 3kb < Pf <Po":GOTO DPf
DDCEF:
F=4
FOR I=1 TO 8
DCEF(I)=DE(I)+DF(I)*F+DRF(I)/F+DH(I)*Po+DI(I)*Po/F
OXLIQ(I)=OXMTL(I)/(F/100+DCEF(I)*(1-F/100))
OXSOL(I)=(OXMTL(I)-OXLIQ(I)*F/100)/(1-F/100)
NEXT
CLS
Pff=Po
Tf=1119.7+13.098*Po-.23065*Po^2+6*Pff
PRINT "Dynamic Melting of";" ";MMCN$;" ";"from";"  Po =";Po;"Kb";" & ";"To =";:
```

```
PRINT USING"####.##";Tf;:PRINT"°C":PRINT
PRINT#1, "Dynamic Melting of";" ";MMCN$;" ";"from";"  Po =";Po;"Kb";" & ";"To
=";:
PRINT#1, USING"####.##";Tf;:PRINT#1, "°C":PRINT
CALL TEXTFONT(1):CALL TEXTSIZE(9)
PRINT "Pf";TAB(7);"Tf";TAB(16);"F%";:FOR I=1 TO 8: PRINT
TAB(I*7+16);OXN$(I);:NEXT:PRINT
PRINT#1, "Pf";TAB(7);"Tf";TAB(16);"F%";:FOR I=1 TO 8: PRINT#1,
TAB(I*7+16);OXN$(I);:NEXT
PRINT#1,
WHILE Pff>=Pf
F=F+1
Pfa=-1.2811+1.1006*Po
Pfb=.45858059322#-.04765420539#*Po+.00093799868842#*Po^2
Pfc=-.026007077679#+.0012312026894#*Po-.000038694385217#*Po^2
Pff=Pfa+Pfb*F+Pfc*F^2
Tf=1119.7+13.098*Po-.23065*Po^2+6*Pff
FOR I=1 TO 8
IF OXSOL(I)<0 OR DCEF(I) <= 0 THEN OXSOL(I)=0
DCEF(I)=DE(I)+DF(I)*F+DRF(I)/F+DH(I)*Pff+DI(I)*Pff/F
BOXLIQ(I)=OXSOL(I)/(DCEF(I)+.01*(1-DCEF(I)))
OXLIQ(I)=(OXLIQ(I)*(F-1)+BOXLIQ(I))/F
OXSOL(I)=(OXMTL(I)-OXLIQ(I)*F/100)/(1-F/100)
NEXT
PRINT USING"##.##";Pff;:
PRINT TAB(7);USING"####.##";Tf;:
PRINT TAB(16);USING"##.##";F;:
FOR I=1 TO 8: PRINT TAB(I*7+16);USING"##.###";OXLIQ(I);:NEXT
PRINT
PRINT#1, USING"##.##";Pff;:
PRINT#1, TAB(7);USING"####.##";Tf;:
PRINT#1, TAB(16);USING"##.##";F;:
FOR I=1 TO 8: PRINT#1,
TAB(I*7+16);USING"##.###";OXLIQ(I);:NEXT:PRINT#1,
WEND
CALL TEXTFONT(0):CALL TEXTSIZE(12):PRINT
PRINT#1, "This job is done at ";TIME$;" on ";DATE$:PRINT
INPUT "Do you want a change of Po and Pf (Y/N)";Yes$
IF Yes$="Y" OR Yes$="y" THEN GOTO DPo ELSE CLOSE 1
GOTO MAINMENU

FPPTT:
RESTORE FPPTT
FOR I=1 TO 5:READ FPTN$(I):NEXT
DATA Si(8),Fe(8),Al(8),Ca(8),Na(8)
FOR I=1 TO 5:PRINT FPTN$(I);" ",:INPUT FPT(I):NEXT
F=19.202-5.175*FPT(5)+15.537*FPT(4)/FPT(3)
Po=25.98+.967*F+45.277/F-5.186*FPT(1)/FPT(2)
Pf=(1.3613*Po+3.9103)+(-1.3458*Po-13.592)/F+(-.03015*Po-.2929)*F
T=1119.7+13.098*Po-.23065*Po^2+6*Po
Tf=1119.7+13.098*Po-.23065*Po^2+6*Pff
PRINT "F(%)";TAB(7);"Po";TAB(14);"Pf";TAB(21);"To";TAB(28);"Tf"
```

```
PRINT USING "##.##";F;:PRINT TAB(7);USING"##.##";Po;:
PRINT TAB(14)USING"##.##";Pf;:PRINT TAB(21);USING"####.##";T;:
PRINT TAB(28)USING"####.##";Tf
INPUT "Do you want to input another set of composition? (Y/N)";Yes$
IF Yes$="Y" OR Yes$="y" THEN GOTO FPPTT
PRINT:PRINT "This job is done at ";TIME$;" on ";DATE$:PRINT
GOSUB WaitKey
GOTO MAINMENU

WaitKey:
PRINT TAB(3) "**********Press any Key to
continue**********"
a$=INKEY$:WHILE a$="":a$=INKEY$:WEND
RETURN

Mantle:
LINE INPUT "Please give a name of your model mantle:";MCN$
FOR I = 1 TO 8:PRINT OXN$(I);" ";:INPUT OXMTL(I):NEXT:RETURN
```

APPENDIX C

A General Equation for Fractionation Correction

$$Y_2 = Y_1 + \sum_{n=1}^{M} m_n (X_2^n - X_1^n)$$

where X's are MgO wt % and Y's are any non-MgO oxides wt %; M is the order of the regression; n is the n^{th} term; and m_n is the regression coefficient of the n^{th} term. X_2 is the desired MgO level (*i.e.*, X_2 = MgO = 8.0 wt %), and X_1 is the observed MgO wt %. Y_1 is the observed non-MgO oxide wt %, and Y_2 is the wt % of the non-MgO oxide(s) that you wish to calculate at a constant MgO wt % of X_2.

Example 1, you find the regression of FeO versus MgO is a straight line,
FeO = a + m MgO, and you want to calculate $Fe_{(8)}$, then

$$Fe_{(8)} = FeO + m\ (8 - MgO)$$

Example 2, you find the 2nd order of polynomial is the best to describe the CaO versus MgO variation, $CaO = a + m_1\ MgO + m_2\ MgO^2$, and you want to calculate $Ca_{(8)}$, then

$$Ca_{(8)} = CaO + m_1\ (8 - MgO) + m_2\ (64 - MgO^2).$$

The advantages of using polynomial regression

* On MgO variation diagrams, straight line is not the best description for most of oxides, even within limited range of MgO ($5.0 \leq MgO \leq 8.5$).

* Using polynomial can overcome the non-linear variation trends (or kinks) for some oxides corresponding to joining points of mineral phases along LLD. For example, SiO_2 by pyroxene(s) and oxides, CaO and Al_2O_3 by plagioclase and cpx, Al_2O_3, FeO and TiO_2 by oxides, and P_2O_5 by apatite.

* Because of the effectiveness of polynomial in overcoming these kinks, more samples can be used. For instance, we no longer have to exclude samples with MgO > 8.5 wt % and MgO < 5.0 wt %.

APPENDIX D

FRACTIONATION COEFFICIENTS

North EPR

	a	*b*
SiO_2	2.3995	-0.1820
$Al2O_3$	0.7723	0.0066
FeO	-5.7299	0.2993
CaO	4.2838	-0.2445
Na_2O	-0.0018	-0.0152

Explorer Ridge

	a	*b*
SiO_2	-0.2561	0.0000
Al_2O_3	-1.0350	0.1170
FeO	-2.8762	0.1241
CaO	3.4471	-0.1801
Na_2O	-0.5101	0.0192

North MAR, South of 41°N

	a	*b*
SiO_2	-1.1310	0.0511
Al_2O_3	1.8410	-0.0670
FeO	-2.7260	0.1190
CaO	2.4070	-0.1471
Na_2O	-1.4180	0.0831

Africa-Antarctic

	a	*b*
SiO_2	0.5885	-0.0694
Al_2O_3	1.3506	-0.0605
FeO	-3.1522	0.1785
CaO	2.7536	-1.7330
Na_2O	-0.1261	-0.0065

South EPR

	a	*b*
SiO_2	2.5740	-0.1851
Al_2O_3	-1.0031	0.1190
FeO	-3.6282	0.1351
CaO	4.0610	-0.2210
Na_2O	-0.1260	-0.0071

Galapagos

	a	*b*
SiO_2	-0.3610	0.0000
Al_2O_3	1.3960	-0.0275
FeO	-5.9884	0.2977
CaO	3.2309	-0.1708
Na_2O	0.0910	-0.1402

Reykjanes Pininsula

	a	*b*
SiO_2	-0.3261	0.0000
Al_2O_3	0.8411	0.0000
FeO	-1.6444	0.0000
CaO	0.8623	0.0000
Na_2O	-0.2277	0.0000

Gorda Ridge

	a	*b*
SiO_2	-0.3938	0.0000
Al_2O_3	0.9015	0.0000
FeO	-1.3167	0.0000
CaO	4.0218	-0.2106
Na_2O	-0.1150	0.0000

North MAR 41°-71.3°N

	a	*b*
SiO_2	0.6141	-0.0600
Al_2O_3	1.7791	-0.0810
FeO	-4.3411	0.2011
CaO	3.1810	-0.1860
Na_2O	-0.9630	0.0580

Mid-Cayman Rise

	a	*b*
SiO_2	-0.2321	0.0000
Al_2O_3	0.6486	0.0000
FeO	-0.8820	0.0000
CaO	0.4668	0.0000
Na_2O	-0.2923	0.0000

Juan de Fuca

	a	*b*
SiO_2	3.9937	-0.3082
Al_2O_3	-0.8434	0.0000
FeO	-6.6915	0.3743
CaO	6.1176	-0.3757
Na_2O	-0.0018	-0.0152

South MAR

	a	*b*
SiO_2	-1.2950	0.0611
Al_2O_3	1.0531	-0.0100
FeO	-8.0420	0.4519
CaO	8.1173	-0.4999
Na_2O	0.5296	-0.0529

SE Indian Ridge

	a	*b*
SiO_2	0.5885	0.0694
Al_2O_3	1.3506	-0.0605
FeO	-3.1522	0.1785
CaO	2.7536	-0.1733
Na_2O	-0.0018	-0.1520

APPENDIX E

SCORE PROCEDURES

Numerical values (scores) are derived to objectively assess how well the observed trends match idealized local and/or global trend.

$R_{Ca/Al}$ and R_{Na} are the correlation coefficients of $Ca_{(8)}/Al_{(8)}$ versus $Si_{(8)}/Fe_{(8)}$ and $Na_{(8)}$ versus $Si_{(8)}/Fe_{(8)}$ respectively; $R^{95\%}$ is the critical value of the correlation coefficient at 95% confidence level (t-test); In our test, if the R's are significant at 95% confidence level, the slopes of the regression lines are also significant at that level (F-test).

Local Trend:

Good (-1.0): $R_{Ca/Al} > 0$, $R_{Na} < 0$, $R_{Ca/Al} >$ and $R_{Na} > R^{95\%}$

Med (-0.8): $R_{Ca/Al} > 0$, $R_{Na} < 0$, $R_{Ca/Al}$ or $R_{Na} > R^{95\%}$

Poor (-0.6): $R_{Ca/Al} > 0$, $R_{Na} < 0$, $R_{Ca/Al}$ and $R_{Na} \leq R^{95\%}$

Global trend:

Good (1.0): $R_{Ca/Al} < 0$, $R_{Na} > 0$, $R_{Ca/Al}$ and $R_{Na} > R^{95\%}$

Med (0.8): $R_{Ca/Al} > 0$, $R_{Na} < 0$, $R_{Ca/Al}$ or $R_{Na} > R^{95\%}$

Poor (0.6): $R_{Ca/Al} > 0$, $R_{Na} < 0$, $R_{Ca/Al}$ and $R_{Na} \leq R^{95\%}$

Transitional:

Local med (-0.4): $R_{Ca/Al} > 0$, $R_{Na} \geq 0$, Larger $R > R^{95\%}$
or $R_{Ca/Al} \leq 0$, $R_{Na} < 0$, Larger $R > R^{95\%}$

Local poor (-0.2): $R_{Ca/Al} > 0$, $R_{Na} \geq 0$, Larger $R \leq R^{95\%}$
or $R_{Ca/Al} \leq 0$, $R_{Na} < 0$, Larger $R \leq R^{95\%}$

Global med (0.4): $R_{Ca/Al} < 0$, $R_{Na} \leq 0$, Larger $R > R^{95\%}$
or $R_{Ca/Al} \geq 0$, $R_{Na} > 0$, Larger $R > R^{95\%}$

Global poor (0.2): $R_{Ca/Al} < 0$, $R_{Na} \leq 0$, Larger $R \leq R^{95\%}$
or $R_{Ca/Al} \geq 0$, $R_{Na} > 0$, Larger $R \leq R^{95\%}$

Calculated score for plotting:

To reflect the important effects of the R values and the sampling density along a ridge segment, we calculated the plotted scores by:

$$\text{Score} = \text{AGF} * \text{R} * \text{SD}^{1/4}$$

where AGF is the arbitrary "goodness-of-fit" (values in parentheses after Good, Med, and Poor); R is the larger correlation coefficient; and SD is the sample density (number of chemical group means per 10 kilometer). We arbitrarily use the radical of 4 to damp out the large range of values for sampling density while arbitrarily keeping our score numerically small.

APPENDIX F

A MACINTOSH DISKETTE

A 3.5' Macintosh floppy diskette contains the following computer programs and macros I have written for this study:

1) DENSCAL (Code and compiled application with Runtime)
2) MORBCAL (Code and compiled application with Runtime)
3) Excel macro for C.I.P.W normative mineralogy, including the following three files:
    a) C.I.P.W normative formulation
    b) C.I.P.W. macro
    c) C.I.P.W. I/O
4) ExKeys.yn: an Excel macro for petrological data manipulation
5) ProbeØ.yn: an Excel macro for calculating mineral structural formula from mineral (Olivine, Orthopyroxene, Clinopyroxene, Plagioclase, Spinel, and Garnet) analyses.
    a) ProbeØ.YN formulation
    b) ProbeØ.YN macro
    c) ProbeØ.YN I/O
6) Excel templates for making petrological Δ diagrams (compositional and phase diagrams).
    a) Tholeiitic-Calc discrimination Δ (AFM)
    b) Cpx-Ol-Qtz Δ of Walker et al (1979)
    c) Cpx-Ol-Qtz Δ of Grove et al. (1982, 1983)
    d) Cpx-Ol-Qtz and Plag-Ol-Qtz of Elthon (1983, 1984)

These have been saved on several Macintosh computers in G & G department Computer Lab for public use. I hope this will be very helpful for saving much time of the future petrologists, both students and faculty.

REFERENCES

Agee, G. B., and D. Walker, Static compression and olivine floatation in ultrasonic silicate liquid, *J. Geophys. Res.*, *93*, 3437–3449, 1988.

Ahearn, J. L., and D. L. Turcotte, Magma migration beneath an ocean ridge, *Earth Planet. Sci. Res. Lett.* , *45*, 115–122, 1979.

Allan, J. F., R. Batiza, M. R. Perfit, D. J. Fornari, and R. O. Sack, Petrology of lavas from the Lamont seamount chain and adjacent East Pacific Rise, 10°N, *J. Petrol.*, *30*, 1245–1298, 1989.

Allègre, C. J., B. Hamelin, and B. Dupré, Statistical analysis of isotopic ratios in MORB: The mantle blob cluster model and the convective regime of the mantle, *Earth Planet. Sci. Lett.*, *71*, 71–84, 1984.

Allègre, C. J., Chemical geodynamics, *Tectonophysics*, *81*, 109–132, 1982.

Anderson, D. L., and O. L. Anderson, The bulk modulus volume relationship for oxides, *J. Geophys. Res.*, *75*, 3494–3500, 1970.

Anderson, D. L., *Theory of the Earth*, Blackwell Scientific, 366pp, 1989.

Anderson, O. L., and I. Suzuki, Anharmonicity of three minerals at high temperature, forsterite, fayalite, and periclase, *J. Geophys. Res.*, *88*, 3549–3556, 1983.

Anderson, R. N., D. A. Clague, K. D. Klitgord, M. Marshall, and R. K. Nishimori, Magnetic and petrologic variations along the Galapagos spreading center and their relation to the Galapagos melting anomaly, *Geol. Soc. Am. Bull.*, *86*, 683–694, 1975.

Anderson, R. N., D. J. Sparious, J. K. Weissel, and D. E. Hayes, The interrelation between variations in magnetic anomaly amplitudes and basaltic magnetization and chemistry along the Southeast Indian ridge, *J. Geophys. Res.*, *85*, 3883–3898,1980.

Angel, R. J., R. M. Hazen, T. C. McCormick, C. T. Prewitt, and J. R. Smyth, Comparative compressibility of end-member feldspars, *Phys. Chem. Minerals, 15*, 313–318, 1988.

Babuska, V., J. Fiala, M. Kumazawa, I. Ohno, and Y. Sumino, Elastic properties of garnet solid solution series, *Phys. Earth Planet. Inter., 16*, 157–176, 1978.

Barone, A., and W. B. F. Ryan, Single plume model for asynchronous formation of the Lamont seamount chain and adjacent East Pacific Rise, 10°N, *J. Geophys. Res., 95*, 10,801–10,827, 1990.

Barr, S. M., Seamount chains formed near the crest of Juan de Fuca ridge, northeast Pacific ocean, *Mar. Geol., 17*, 1–19, 1974.

Bass, J. D., and D. J. Weidner, Elasticity of single-crystal orthopyroxene, *J. Geophys. Res., 89*, 4359–4371, 1984.

Bass, J. D., Elasticity of uvarovite and andradite garnets, *J. Geophys. Res., 91*, 7505–7516, 1986.

Batiza, R, Abundances, distribution, and sizes of volcanoes in the Pacific ocean and implications for the origin of non-hotspot volcanoes, *Earth Planet. Sci. Lett., 60*, 195–206, 1982.

Batiza, R, and D. A. Vanko, Petrology of young Pacific seamounts, *J. Geophys. Res, 89*, 11235–11260, 1984.

Batiza, R, and D. A. Vanko, Volcanic development of small oceanic central volcanoes on flanks of the East Pacific Rise inferred from narrow-beam echo-sounder surveys, *Mar. Geol., 54*, 53–90, 1983.

Batiza, R, B. R. Rosendahl, and R. L. Fisher, Evolution of ocean crust 3, Petrology and geochemistry of basalts from the East Pacific Rise and Siqueiros transform fault, *J. Geophys. Res, 82*, 265–276, 1977.

Batiza, R, Lithospheric age dependence of off-ridge volcano production in the North Pacific, *Geophys. Res. Lett.*, *8*, 853–856, 1981.

Batiza, R, W. G. Melson, and T. O'Hearn, Simple magma supply geometry inferred beneath a segment of the Mid-Atlantic Ridge, *Nature*, *335*, 428–431, 1988.

Batiza, R., and S. H. Margolis, A model for the origin of small non-overlapping offsets (SNOO's) of the East Pacific Rise, *Nature*, *320*, 439–441, 1986.

Batiza, R., and Y. Niu, Petrology of lavas from the EPR at 9°30'N: Implications for magma chamber processes, *Eos Trans. AGU, 70*, 1399–1400, 1989.

Batiza, R., Inverse relationship between Sr isotope diversity and rate of oceanic volcanism has implications for mantle heterogeneity, *Nature*, *309*, 440–441, 1984.

Batiza, R., T. L. Smith, and Y. Niu, Geologic and Petrologic evolution of seamounts near the EPR based on submersible and camera study, *Mar. Geophys. Res.*, *11*, 169–236, 1989.

Batiza, R., The Pacific Ocean Crust, In Oceanic Basalts, edited by P. A. Floyd, Blackie and sons, Glasgow, 246–288, 1991.

Batiza, R., W. G. Melson, and T. O'Hearn, Simple magma supply geometry inferred beneath a segment of the mid-Atlantic ridge, *Nature*, *335*, 428–431, 1988.

Batiza, R., Y. Niu, and W. C. Zayac, Chemistry of seamounts near the East-Pacific Rise: Implications for the geometry of sub-axial mantle flow, *Geology*, *18*, 1122–1125, 1990.

Bender, J. F., C. H. Langmuir, and G. N. Hanson, Petrogenesis of basalt glasses from the Tamayo region, East Pacific Rise, *J. Petrol.*, *25*, 213–254, 1984.

Berman, G, Internally-consistent thermodynamic data for mineral system Na_2O–K_2O–CaO-MgO-FeO-Fe_2O_3-Al_2O_3-SiO_2-TiO_2-H_2O-CO_2, *J. Petrol.*, *29*, 445–55, 1988.

Blackman, D. K., and D. W. Forsyth, Isostatic compensation of tectonic features of the mid-Atlantic ridge: 25° – 27°30'S, *J. Geophys. Res.*, *96*, 11,741–11,758, 1991.

Bonczar, L. J., E. K. Graham, and H. Wang, The pressure and temperature dependence of the elastic constants of pyrope garnet, *J. Geophys. Res.*, *82*, 2529–2534, 1977.

Botros, M., and H. P. Johnson, Tectonic evolution of the Explorer–Northern Juan de Fuca region from 8 Ma to the present, *J. Geophys. Res.*, *93*, 10421–10437, 1988.

Bottinga, Y., and C. J. Allègre, partial melting under spreading ridges, *Phil. Trans. R. Soc. Lond.*, *A*, *288*, 501–525, 1978.

Bottinga, Y., D. Weill, Richet, Density calculations for silicate liquids. I. Revised method for aluminosilicate compositions, *Geochim. Cosmochim. Acta*, *46*, 909–919, 1982.

Bougault, H., and R. Hekinian, Rift valley in the Atlantic ocean near 36°50'N: Petrology and geochemistry of basaltic rocks, *Earth Planet. Sci. Lett*, *24*, 249–261, 1974.

Bougault, H., L. Dmitriev, J.- G. Schilling, A. Sobolev, J. L. Jordan, and H. D. Needham, Mantle heterogeneity from trace elements: MAR triple junction near 14°N, *Earth Planet. Sci. Lett.*, *88*, 27–36, 1988.

Brodholt, J. P., and R. Batiza, Global systematics of unaveraged mid-ocean ridge basalt compositions: Comments on "Global correlations of ocean ridge basalt chemistry with axial depth and crustal thickness by E. M. Klein and C. H. Langmuir, " *J. Geophys. Res.*, *94*, 4231–4239, 1989.

Brodholt, J., and R. Batiza, Magma supply processes in the tomography area (~ 9°30'N) of the EPR, *Eos Trans. AGU*, *69*, 1474, 1988.

Bryan, W. B., and J. G. Moore, Compositional variations of young basalts in the mid-Atlantic ridge rift valley near lat. 36°49'N, *Geol. Soc. Am. Bull.*, *88*, 556–570, 1977.

Bryan, W. B., G. Thompson, and J. N. Ludden, Compositional variations in normal MORB from 22°–25°N: Mid-Atlantic ridge and Kane Fracture Zone, *J. Geophys. Res.*, *86*, 11,815–11,836, 1981.

Bryan, W. B., L. W. Finger, and F. Chayes, Estimating proportions in petrological mixing equations by least-squares approximation, *Science*, *163*, 926–927, 1969.

Bryan, W. B., Linked evolutionary data arrays: A logical structure for petrologic modeling of multisource, multiprocess magmatic systems, *J. Geophys. Res.*, *91*, 5891–5900, 1986.

Bryan, W. B., Regional variation and petrogenesis of basalt glasses from the FAMOUS area, Mid-Atlantic Ridge, *J. Petrol.*, *20*, 293–325, 1979.

Buck, W. R., and E. M. Parmentier, Convection beneath young oceanic lithosphere: Implication for thermal structure and gravity, *J. Geophys. Res*, *91*, 1961–1974, 1986.

Buck, W. R., and W. Su, Focused mantle upwelling below mid-ocean ridges due to feedback between viscosity and melting, *Geophys. Res. Lett.*, *16*, 641–644, 1989.

Byers, C. D., M. O. Garcia, and D. W. Muenow, Volatiles in basaltic glasses from the East Pacific Rise at 21°N: Implications for MORB sources and submarine lava flow morphology, *Earth Planet. Sci. Lett, 79*, 9–20, 1986.

Cameron, M., S. Sueno, C. T. Prewitt, and J. I. Papike, High-temperature crystal chemistry of acmite, diopside, hedenbergite, jadeite, spondumene, and ureyite, *Am. Mineral.*, *58*, 594–618, 1973.

Campsie, J., G. L. Johnson, M. H. Rasmussen, and J. Laursen, Dredged basalts from the western Nazca plate and the evolution of the East Pacific Rise, *Earth Planet. Sci. Lett.*, *68*, 271–285, 1984.

Carbotte, S., and K. C. Macdonald, East Pacific Rise 8°–10°30'N: Evolution of ridge segments and discontinuities from Sea Marc II and three-dimensional magnetic studies, *J. Geophys. Res.*, in press, 1992.

Cashman, K. V., and B. C. Marsh, Crystal size distribution (CSD) in rocks and the kinetics and dynamics of crystallization, II. Makaopuhi lava lake, *Contrib. Mineral. Petrol.*, *99*, 292–305, 1988.

Castillo, P. R., and R. Batiza, Mantle dynamics beneath the South Atlantic inferred from the Sr, Nd, and Pb isotope geochemistry of Seamounts, *Nature*, *342*, 262–265, 1989.

Castillo, P., The Dupal anomaly as a trace of the upwelling lower mantle, *Nature, 336*, 667–670, 1989.

Cawthorn, R. G., Degrees of melting in mantle diapirs and the origin of ultramafic liquids, *Earth Planet. Sci. Lett., 27*, 113–120, 1975.

Christie, D. M., and J. M. Sinton, Major element constraints on melting, differentiation and mixing of magmas from the Galapagos 95.5°W propagating rift system, *Contrib. Mineral. Petrol., 94*, 274–288, 1986.

Clague, D. A., F. A. Frey, G. Thompson, and S. Rindge, Minor and trace element geochemistry of volcanic rocks dredged from the Galapagos spreading center: Role of crystal fractionation and mantle heterogeneity, *J. Geophys. Res, 86*, 9469–9482, 1981.

Cohen, R. S., and R. K. O'Nions, The lead, Neodymium and Strontium isotopic structure of ocean ridge basalts, *J. Petrol., 23*, 299–324, 1982.

Cousens, B. L., R. L. Chase, and J.- G. Schilling, Basalt geochemistry of Explorer area, northeast Pacific Ocean, *Can. J. Earth Sci., 21*, 157–170, 1984.

Crane, K., The spacing of rift axis highs: Dependence on diapiric processes in the underlying asthenosphere?, *Earth Planet. Sci. Lett., 72*, 405–415, 1985.

Davis, A. S., and D. A. Clague, Geochemistry, mineralogy and petrogenesis of basalt from the Gorda Ridge, *J. Geophys. Res, 92*, 10467–10483, 1987.

DeMets, C, R. G. Gordon, D. F. Argus, and S. Stein, Current plate motions, *Geophys. J. Int., 101*, 425–478, 1990.

Detrick, R. S., J. C. Mutter, P. Buhl, and I. I. Kim, No evidence from multichannel reflection data for a crustal magma chamber in the MARK area of the mid-Atlantic ridge, *Nature, 347*, 61–64, 1990.

Detrick, R. S., J. P. Madsen, P. E. Buhl, J. Vera, J. Mutter, J. Orcutt, and T. Brocker, Multichannel seismic imaging of an axial magma chamber along the East Pacific Rise between 4°N and 13°N, *Nature, 326*, 35–41, 1987.

Dick, H. J. B., Abyssal peridotites, very slow spreading ridges and ocean ridge magmatism, In Magmatism in Ocean Basins edited by A. D. Saunders and M. J. Norry, *Geol. Soc. Special Pub., 42*, 71–106, 1989.

Dick, H. J. B., R. L. Fisher, and W. B. Bryan, Mineralogical variability of the uppermost mantle along mid-ocean ridges, *Earth Planet. Sci. Lett., 69*, 88–106, 1984.

Dickey, J. S., Jr., F. A. Frey, S. R. Hart, E. B. Watson, and G. Thompson, Geochemistry and petrology of dredged basalts from the Bouvet triple junction, South Atlantic, *Geochim. Cosmochim. Acta, 41,* 1105–1118, 1977.

Dosso, L., H. Bougault, P. Beuzart, J.- Y. Calvez, and J.- L. Jordan, The geochemical structure of the South-East Indian ridge, *Earth Planet. Sci. Lett., 88*, 47–59, 1988.

Duffy, T. S., and Anderson, D., Seismic velocities in mantle minerals and the mineralogy of upper mantle, *J. Geophys. Res., 94*, 1895–1912, 1989.

Duncan, R. A., and D. H. Green, The genesis of refractory melts in the formation of oceanic crust, *Contrib. Mineral. Petrol., 96*, 326–342, 1987.

Eaby, J., D. A. Clague, and J. R. Delaney, Sr isotopic variations along the Juan de Fuca ridge, *J. Geophys. Res, 89*, 7883–7890, 1984.

Elthon, D., and C. M. Scarfe, High-pressure phase equilibria of a high-magnesian basalt and the genesis of primary oceanic basalts, *Am. Mineral., 69*, 1–15, 1984.

Elthon, D., J. F. Casey, and S. Komor, Mantle chemistry of ultramafic cumulates from the North Arm Mountain Massif of the Bay of Islands ophiolite: Evidence for high-pressure crystal fractionation of oceanic basalts, *J. Geophys. Res., 87*, 8717–8734, 1982.

Elthon, D., Pressure of origin of primary mid-ocean ridge basalts, In Magmatism in Ocean Basins, edited by A. D. Saunders and M. J. Norry, *Gel. Soc. Special Pub., 42*, 25–136, 1989.

Elthon, D., The petrogenesis of primary mid-ocean ridge basalts, *Rev. Aquat. Sci., 2*, 27–53, 1990.

Engel, C. G., and R. L. Fisher, Granitic to ultramafic rock complex of the Indian Ocean ridge system, western Indian Ocean, *Geol. Soc. Am. Bull., 86*, 1553–1578, 1975.

Falloon, T. J., and D. H. Green, Anhydrous partial melting of MORB pyrolite and other peridotite compositions at 10 kbar: Implications for the origin of MORB glasses, *Mineral. Petrol., 37*, 181–219, 1987

Falloon, T. J., and D. H. Green, Anhydrous partial melting of peridotite from 8 to 35kb and the petrogenesis of MORB, *J. Petrol., 29*, 379–414, 1988.

Falloon, T. J., D. H. Green, C. J. Hatton, and K. L. Harris, Anhydrous partial melting of a fertile and depleted peridotite from 2 to 30kb and application to basalt petrogenesis, *J. Petrol., 29*, 1257–1282, 1988.

Finger, L. W., and Y. Ohashi, The thermal expansion of diopside to 800°C and a refinement of crystal structure at 700°C, *Am. Mineral., 61*, 303–310, 1976.

Finger, L. W., R. M. Hazen, and A. M. Homfeister, High-pressure crystal chemistry of spinel ($MgAl_2O_4$) and magnetite (Fe_3O_4): Comparisons with silicate spinels, *Phys. Chem. Minerals, 13*, 215–220, 1986.

Fisk, M. R., A. E. Bence, and J.- G. Schilling, Major element chemistry of Galapagos rift zone magmas and their phenocrysts, *Earth Planet. Sci. Lett., 61*, 171–189, 1982.

Flower, M. J. F., Thermal and kinematic control on ocean-ridge magma fractionation: Contrasts between Atlantic and Pacific spreading axes, *J. Geol. Soc. London, 138*, 695–712, 1980.

Fornari, D. J., M. R. Perfit, A. Malahoff, and R. Embley, Geochemical studies of abyssal lavas recovered by DSRV Alvin from eastern Galapagos rift Inca transform and Equator rift, 1. Major element variations in natural glasses and spatial distribution of lavas, *J. Geophys. Res.*, *88*, 10519–10529, 1983.

Fornari, D. J., M. R. Perfit, J. F. Allan, and R. Batiza, Small-scale heterogeneities in depleted mantle sources: Near-ridge seamount lava geochemistry and implications for mid-ocean-ridge magmatic processes, *Nature*, *331*, 511–513, 1988*a*.

Fornari, D. J., M. R. Perfit, J. F. Allan, R. Batiza, R. Haymon, A. Barone, W. B. F. Ryan, T. Smith, T. Simkin, and M. Luckman, Geochemical and structural studies of the Lamont seamounts : Seamounts as indicators of mantle processes, *Earth Planet. Sci. Lett.*, *89*, 63–83, 1988*b*.

Fornari, D. J., R. Batiza, and M. A. Luckman, Seamount abundances and distribution near the East Pacific Rise 0° – 24°N based on seabeam data, InSeamounts, Islands, and Attolls, edited by B. H. Keating et al.,*AGU Geophysical Monograph*, *43*, 13–21, 1987.

Fornari, D. J., W. B. F. Ryan, and P. J. Fox, The evolution of craters and calderas on young seamounts: Insights from Sea Marc I and Sea Beam sonar surveys of a small seamount group near the axis of the East Pacific Rise at ~ 10°N, *J. Geophys. Res*, *89*, 11069–11083, 1984.

Forsyth, D. W., D. K. Blackman, and G. A. Neumann, Segmentation of the southern mid-Atlantic ridge: Gravity signature of an unusually robust spreading segment, *Eos Trans. AGU*, *71*, 1628, 1990.

Franchteau, J., and R. D. Ballard, The East Pacific Rise near 21°N, 13°, and 20°S: inferences from along-strike variability of axial processes of the mid-ocean ridges, *Earth Planet. Sci. Lett.*, *64*, 93–116, 1983.

Francis, D., The pyroxene paradox in MORB glasses - a signature of picritic parental magmas? *Nature*, *319*, 586–588, 1986.

Frisillo, A. L., and A. L. Barsch, Measurement of single-crystal constants of bronzite as a function of pressure and temperature, *J. Geophys. Res.*, *77*, 6360–6384, 1972.

Fujii, T., and C. M. Scarfe, Composition of liquids coexisting with spinel lherzolite at 10 kbar and the genesis of MORBs, *Contrib. Mineral. Petrol.*, *90*, 18–28, 1985.

Fujii, T., and H. Bougault, Melting relations of a magnesian abyssal tholeiite and the origin of MORBs, *Earth Planet. Sci. Lett.*, *62*, 283–295, 1983.

Fujii, T., Genesis of mid-ocean ridge basalts, In Magmatism in Ocean Basins, edited by A. D. Saunders and M. J. Norry, *Geol. Soc. Special Pub.*, *42*, 137–146, 1989.

Garcia, M. O., E. W. Wolfe, Petrology of erupted lavas, In The Puu Oo eruption of Kilauea volcano, Hawaii: Episodes 1 through 20, January 3, 1983 through June 1984, edited by E. W. Wolfe,*USGS Professional paper*, *1463*, 127–148, 1988.

Garcia, M. O., F. A. Frey and D. G. Grooms, Petrology of volcanic rocks from Kaula Island, Hawaii, *Contrib. Mineral. Petrol.*, *94*, 461–471, 1986.

Gente, P., J. M. Auzende, V. Renard, Y. Fouguet, and D. Bideau, Detailed geologic mapping by submersible of the East Pacific Rise axial graben near 13°N, *Earth Planet. Sci. Lett.*, *78*, 229–236, 1986.

Ghiorso, M. S., and I. S. E. Carmichael, Chemical mass transfer in magmatic processes, II, Application in equilibrium crystallization and assimilation, *Contrib. Mineral. Petrol.*, *90*, 121–141, 1985.

Glazner, A. F., Activities of olivine and plagioclase components in silicate melts and their application to geothermometry, *Contrib. Mineral. Petrol.*, *88*, 260–268, 1984.

Graham, D. W., A. Zindler, M. D. Kurz, W. J. Jenkins, R. Batiza, H. Staudigal, He, Pb, Sr, and Nd isotope constraints on magma genesis and mantle heterogeneity beneath young Pacific seamounts, *Contrib. Mineral. Petrol.*, *99*, 446–463, 1988.

Graham, E. K., J. A. Schwab, S. M. Sopkin, and H. Takei, H., The pressure and temperature dependence of the elastic properties of single-crystal fayalite Fe_2SiO_4, *Phys. Chem. Minerals*, 16, 186–198, 1988.

Green, D. H., W. D. Hibberson, and A. L. Jaques, Petrogenesis of mid-ocean ridge basalts, In The Earth: Its origin, structure, and evolution, edited by M. W. McElhinney, Academic, San Diego, Calif., pp. 265–299, 1979.

Grindlay, N. R., P. J. Fox, and K. C. Macdonald, Second order ridge axis discontinuities in the south Atlantic: Morphology, structure, and evolution, *Mar. Geophys. Res., 13*, 21–49, 1990.

Grove, T. L., and Bryan, W. B., 1983, Fractionation of pyroxene-phyric MORB at low pressure: An experimental study, *Contrib. Mineral. Petrol., 84*, 293–309, 1983.

Grundy, H. D., and W. L. Brown, A high temperature X-ray study of low and high plagioclase feldspars, In The Feldspar, Proceedings of a Nato Advanced Study Institute, edited by W, S. MacKenzie and J. Zussman, University of Manchester Press, 162–173, 1974.

Hamelin, B., and C. J. Allègre, Large scale regional units in the depleted upper mantle: Revealed by an isotopic study of the Southwest Indian Ridge, *Nature, 315*, 196–199, 1985. et al., 1986.

Hanks, T. C., model relating heat flow values near and vertical velocities of mass transport beneath ocean rises, *J. Geophys. Res., 76*, 537–544, 1971.

Hanson, G. N., Geochemical evolution of the suboceanic mantle, *J. Geol. Soc. London, 134*, 235–253, 1977.

Harding, A. J., J. Orcutt, M. Kappus, E. Vera, J. Mutter, P. Buhl, R. Detrick and T. Brocher, The structure of young oceanic crust at 13°N on the East Pacific Rise from expanding spread profiles, *J. Geophys. Res, 94*, 12163–12196, 1989.

Harpp, K., W. M. White, and R. Batiza, Isotopic study of contrasting magmatic studies: The East Pacific Rise at 9°30'N and the MAR in the FAMOUS area, *Eos Trans. AGU*, *71*, 658, 1990.

Hart, S. R., and A. Zindler, Constraints on the nature and development of chemical heterogeneities in the mantle, In Mantle convection, edited by W. R. Peltier, Gordon and Branch Science Publishers, 261–387, 1989.

Hart, S. R., Heterogeneous mantle domains: Signatures, genesis and mixing chronologies, *Earth Planet. Sci. Lett.*, *90*, 273–296, 1988.

Haselton, H. T. Jr., B. S. Hemingway, and R. A. Robie, Low-temperature heat capacities of $CaAl_2SiO_6$ glass and pyroxene and thermal expansion of $CaAl_2SiO_6$ pyroxene, *Am. Mineral.*, *69*, 481–489, 1984.

Hawkins, J. W., and J. T. Melchior, Descriptive catalogue of basalt samples from the East Pacific Rise at 21°N, *SIO Ref. 80–4*, Scripps Inst. of Oceanogr., Univ. of Calif., San Diego, 1980.

Hayes, D. E., and A. K. Kane, The dependence of seafloor roughness on spreading rate. *Geophys. Res. Lett.*, *18*, 1425–1428, 1991.

Haymon, R, D. J. Fornari, K. Von Damm, J. Edmond, M. Lilley, M. Perfit, W. C. Shanks, J. Grebmeier, R. Lutz, S. Carbotte, D. Wright, M. Smith, E. McLaughlin, N. Beedle, J. Seewald, D. Reudelhuber, E. Olson, and F. Johnson, Eruption of the EPR crest at 9°45' – 52'N since late 1989 and its effects on hydrothermal venting: Results of the ADVENTURE Program, a ODP site survey with ALVIN, *Eos Trans. AGU, 72*, 480, 1991*a*.

Haymon, R., D. J. Fornari, M. H. Edwards, S. Carbotte, D. Wright, and K. C. Macdonald, Hydrothermal vent distribution along the East Pacific Rise crest (9°09' – 59'N) and its relationship to magmatic and tectonic processes on fast-spreading mid-ocean ridges, *Earth Planet. Sci. Lett.*, 104, 513–534, 1991*b*.

Hazen, R. M., and C. T. Prewitt, Linear compressibilities of low albite, high pressure structural implications, *Am. Mineral.*, *62*, 554–558, 1977.

Hazen, R. M., and L. W. Finger, Crystal structure and compressibilities of pyrope and grossular to 60 kbar, *Am. Mineral.*, *63*, 297–303, 1978.

Hekinian, R., and D. Walker, Diversity and spatial zonation of volcanic rocks from the East Pacific Rise near 21°N, *Contrib. Mineral. Petrol.*, *96*, 265–280, 1987.

Hekinian, R., G. Thompson, and D. Bideau, Axial and off-axial heterogeneity of basaltic rocks from the East Pacific Rise at 12°35'N – 12°51'N, *J. Geophys. Res*, *94*, 17437–17463, 1989.

Hekinian, R., J. M. Auzende, J. Francheteau, P. Gente, W. B. F. Ryan, and E. S. Kappel, Offset spreading centers near 12°53'N on the East Pacific Rise: Submersible observations and composition of the volcanics, *Mar. Geophys. Res.*, *7*, 359–377, 1985.

Henderson, P., Inorganic geochemistry, Pergamon Press, Oxford, 353pp, 1982.

Herzberg, C., Magma density at high pressure Part 1, the effect of composition on the elastic properties of silicate liquids, In Magmatic Processes, Physical Chemical Principles, edited by B. O. Mysen, *Geochem. Soc. Spec. Public.*, *1*, 25–46, 1987*a*.

Herzberg, C., Magma density at high pressure Part 2, A test of the olivine floatation hypothesis, In Magmatic Processes, Physical Chemical Principles, edited by B. O. Mysen, *Geochem. Soc. Spec. Public.*, *1*, 47–58, 1987*b*.

Hey, R. N., A new class of pseudofaults and their bearing on plate tectonics: A propagating rift model, *Earth Planet. Sci. Lett.*, *37*, 321–325, 1977.

Hey, R. N., F. K. Duennebier, and W. J. Morgan, Propagating rifts on mid-ocean ridges, *J. Geophys. Res.*, *85*, 3647–3658, 1980.

Holness, M. B., and F. M. Richter, Possible effects of spreading rate on MORB isotopic and rare earth composition arising from melting of a heterogeneous source, *j. Geol.*, *97*, 247–260, 1989.

Houseman, G., The deep structure of ocean ridges in a convecting mantle, *Earth Planet. Sci. Lett.*, *64*, 283–294, 1983.

Housh, T. B., and J. F. Luhr, Plagioclase-melt equilibria in hydrous system, *Am. Mineral.*, *76*, 477–492, 1991.

Humler, E., and H. Whitechurch, Petrology of basalts from the Central Indian ridge (lat. 25°23'S, long. 70°04'E): Estimates of frequencies and fractional volumes of magma injections in a two-layered reservoir, *Earth Planet. Sci. Lett.*, *88*, 169–181, 1988.

Humphris, S. E., G. Thompson, J.- G. Schilling, and R. H. Kingsley, Petrological and geochemical variations along the Mid-Atlantic Ridge between 46°S and 32°S: Influence of the Tristan de Cunha mantle plume, *Geochim. Cosmochim. Acta, 49*, 1445–1464, 1985.

Hunter, R. H., and D. P. McKenzie, the equilibrium geometry of carbonate melts in rocks of mantle composition, *Earth Planet. Sci. Lett.*, 92, 347–356, 1989.

Isaak, D. G., and E. K. Graham, The elastic properties of an almandine–spessartine garnet and elasticity in the garnet solid solution series, *J. Geophys. Res.*, *81*, 2483–2489, 1976.

Ito, E., W. M. White, and C. Göpel, The O, Sr, Nd, Pb isotope geochemistry of MORB, *Chem. Geol.*, *62*, 157–176, 1987.

Ito, K., Analytical approach to estimating the source rock of basaltic magmas: Major elements, *J. Geophys. Res., 78*, 412–431, 1973.

Jaeger, J. C., Cooling and solidification of igneous rocks, In Basalts, vol. 2, edited by H. H. Hess and A. Poldervaart, Intersciences Publishers, N. Y., 503–536, 1968.

Jakobsson, S. P., J. Jónsson, and F. Shido, Petrology of the western Reykjanes Peninsula, Iceland, *J. Petrol., 19*, 669–705, 1978.

Jaques, A. L., and D. H. Green, Anhydrous melting of peridotite at 0–15 kb pressure and the genesis of tholeiitic basalts, *Contrib. Mineral. Petrol., 73*, 287–310, 1980.

Johnson, K., H. B. Dick, and N. Shimizu, Melting in the oceanic upper mantle: An ion microprobe study of diopside in abyssal peridotites, *J. Geophys. Res*, 95, 2661–2678, 1990.

Jordan, T. H., Mineralogies, densities, and seismic velocities of garnet lherzolites and their geophysical implications, In Proceedings of the Second International Kimberlite Conference, vol. 2, edited by F. R. Boyd and H. O. A. Meyer, AGU, Washington, D. C, 1979.

Juster, T. C., T. L. Grove, and M. R. Perfit, Experimental constraints on the generation of FeTi basalt, andesites, and rhyodacites at the Galapagos spreading center, 85°W and 95°W, *J. Geophys. Res., 94*, 9251–9274, 1990.

Juteau, T., et al., Homogeneous basalts from the East Pacific Rise at 21°N: Steady state magma reservoirs at moderately fast spreading centers, *Oceanol. Acta, 3*, 487–503, 1980.

Kandelin, J., and D. J. Weinder, Elastic properties of Hedenbergite, *J. Geophys. Res., 93*, 1063–1072, 1988.

Karsten, J. L., J. R. Delaney, J. M. Rhodes, and R. A. Lilias, Spatial and temporal evolution of magmatic systems beneath the endeavour segment, Juan de Fuca ridge: Tectonic and petrologic constraints, *J. Geophys. Res., 95*, 19,235–19,256, 1990.

Karsten, J. L., Spatial and temporal variations in the petrology, morphology and tectonics of a migrating spreading center: The Endeavor Segment, Juan de Fuca Ridge, Ph. D. thesis, 349pp., Univ. of Wash., Seattle, 1988.

Kelemen, P. B., Reaction between ultramafic rock and fractionating basaltic magma, I. phase relations, the origin of calc-alkaline magma series, and the formation of discordant dunite, *J. Petrol., 31*, 51–98, 1990.

Kelemen, P. B., Reaction between ultramafic rock and fractionating basaltic magma, II. Experimental investigations of reaction between olivine tholeiite and harzburgite at 1150–1050°C and 5 kb, *J. Petrol., 31*, 99–134, 1990.

Kent, G. M., A. J. Harding and J. A. Orcutt, Reprocessed CDP lines between 8°50'N and 9°50'N on the East Pacific Rise: Implications for layer 2A thickness, segmentation of the axial magma chamber and decoupling of the melt source region from the neovolcanic zone, *Eos Trans. AGU,72*, 490, 1991.

Kent, G. M., A. J. Harding, and J. A. Orcutt, Evidence for a smaller magma chamber beneath the East Pacific Rise at 9°30'N, *Nature, 344*, 650–653, 1990.

Kerr, R. C., and J. R. Lister, The effects of shape on crystal settling and the rheology of magmas, *J. Geol., 99*, 457–467, 1991.

Kinzler, R. J., and T. L. Grove, Primary magmas of mid-ocean ridges basalts, *J. Geophys. Res.*, 1992, (in press).

Klein E. M. and C. H. Langmuir, Global correlations of ocean ridge basalt chemistry with axial depth and crustal thickness, *J. Geophys. Res., 92*, 8089–8115, 1987.

Klein, E. M., and C. H. Langmuir, Local versus global variation in ocean ridge basaltic composition: A reply, *J. Geophys. Res., 94*, 4241–4252, 1989.

Klein, E. M., C. H. Langmuir, H. Staudigel, Geochemistry of basalts from Southeast Indian ridge, 115°E–138°E, *J. Geophys. Res. 96*, 2089–2107, 1991.

Klein, E. M., The Clipperton Transform Team, and The CHEPR Team, Geochemistry of basalts collected during Alvin dive within and adjacent to the Clipperton transform fault (10°N, East Pacific Rise), *Eos Trans. AGU, 68*, 1540, 1987.

Krupka, K. M., R. A. Robie, and B. S. Hemingway, High-temperature heat capacities of corundum, periclase, anorthite, $CaAl_2Si_2O_8$ glass, muscovite, pyrophyllite, $KAlSi_3O_8$ glass, grossular, and $NaAlSi_3O_8$ glass, *Am. Mineral.*, *64*, 86–101, 1979.

Krupka, K. M., R. A. Robie, and B. S. Hemingway, Kerrick. D. M., and Ito, J., Low-temperature heat capacities and derived thermodynamic properties of anthophyllite, diopside, enstatite, bronzite, and wallastonite, *Am. Mineral.*, *70*, 249–260, 1985.

Kuwasawa, M., and O. L. Anderson, Elastic moduli, pressure derivatives, and temperature derivatives of single-crystal olivine and single-crystal forsterite, *J. Geophys. Res.*, *74*, 5961–5972, 1969.

Lachenbruch, A. H., Dynamics of a passive spreading centers, *J. Geophys. Res.*, *81*, 1883–1902, 1976.

Lange, R. A., and I. S. E. Carmichael, Densities of Na_2O-K_2O-CaO-MgO-FeO-Fe_2O_3-Al_2O_3-TiO_2-SiO_2 liquids, new measurements and derived partial molar properties, *Geochim. Cosmochim. Acta*, *51*, 2931–2946, 1987.

Langmuir, C. H., and G. N. Hanson, An evaluation of major element heterogeneity in the mantle sources of basalts, *Philos. Trans. R. Soc. London, Ser. A*, *297*, 383–407, 1980*a*.

Langmuir, C. H., and G. N. Hanson, Calculating mineral-melting equilibria with stoichiometry, mass balance, and single-component distribution coefficients, *Adv. Geochim.*, *1*, 247–271, 1980*b*.

Langmuir, C. H., Geochemical consequence of in-situ crystallization, *Nature*, *340*, 199–205, 1989.

Langmuir, C. H., J. F. Bender, A. B. Bence, and G. N. Hanson, Petrogenesis of basalts from the FAMOUS area: Mid-Atlantic ridge, *Earth Planet. Sci. Lett.*, *36*, 133–156, 1977.

Langmuir, C. H., J. F. Bender, and R. Batiza , Petrological and tectonic segmentation of the East Pacific Rise, 5°30'–14°30', *Nature*, *322*, 422–429, 1986.

Le Maitre, R. W., Numerical petrology, Elsevier Sci. Publ, N. Y., 281pp, 1982.

Le Roex, A. P., H. J. B. Dick, A. L. Erlank, A. M. Reid, F. A. Frey, and S. R. Hart, Geochemistry, mineralogy and petrogenesis of lavas erupted along the Southwest Indian Ridge between the Bouvet Triple Junction and 11 degrees east, *J. Petrol.*, *24*, 267–318, 1983.

Le Roex, A. P., H. J. B. Dick, A. L. Erlank, A. M. Reid, F. A. Frey, and S. R. Hart, Petrology and geochemistry of basalts from the American-Antarctic Ridge, southern ocean: Implications for the westward influence of the Bouvet mantle plume, *Contrib. Mineral. Petrol.*, *90*, 367–380, 1985.

Le Roex, A. P., H. J. B. Dick, A. M. Reid, and A. L. Erlank, Ferrobasalts from the Speiss Ridge segment of the Southwest Indian Ridge, *Earth Planet. Sci. Lett.*, *60*, 437–451, 1982.

Le Roex, A. P., H. J. B. Dick, L. Gulen, A. M. Reid, and A. J. Erlank, Local and regional heterogeneity in MORB from the Mid-Atlantic Ridge between 54.5°S and 51°S: Evidence for geochemical enrichment, *Geochim. Cosmochim. Acta, 51*, 541–555, 1987.

Leitner, B. J., D. J. Weidner, and R. C. Liebermann, Elasticity of single crystal pyrope and implications for garnet solid solution series, *Phys. Earth and Plan. Inter.*, *22*, 111–121, 1980.

Levien, L., and C. T. Prewitt, High pressure structural study of diopside, *Am. Mineral.*, *66*, 315–323, 1981.

Levien, L., D. J. Weidner, and C. Prewitt, Elasticity of diopside, *Phys. Chem. Minerals*, *4*, 105–11, 1979.

Lin, J, G. M. Purdy, H. Schouten, J.- C. Sempéré and C. Zervas, Evidence from gravity data for focused magmatic accretion along the mid-Atlantic ridge, *Nature, 344*, 627–632, 1990.

Lin, J., and J. Phipps Morgan, The spreading rate dependence of three-dimensional mid-ocean ridge gravity structure, *Geophys. Res. Lett., 19*, 13–16, 1992.

Lindstrom, D. J., and R. L. Korotev, TEABAGS: A computer program for instrumental neutron activation analysis, *J. Radioanal. Chem., 70*, 439–458, 1982.

Londsdale, P., Overlapping rift zones at 5.5°S offset of the East Pacific Rise, *J. Geophys. Res., 88*, 9393–9406, 1983.

Lonsdale, P, Non-transform offsets of the Pacific-Cocos plate boundary and their traces on the rise flanks, *Geol. Soc. Am., Bull., 96*, 313–327, 1985.

Lonsdale, P., Segmentation of the Pacific-Nazca spreading center, *J. Geophys. Res, 94*, 12197–12226, 1989.

Maaløe, S., Geochemical aspects of permeability controlled partial melting and fractional crystallization, *Geochim. Cosmochim. Acta, 46*, 43–57, 1982.

Macdonald, K. C., and P. J. Fox, Overlapping spreading centers: New accretion geometry on the East Pacific Rise, *Nature, 302*, 55–57, 1983.

Macdonald, K. C., J. C. Sempéré, P. J. Fox, and R. Tyce, Tectonic evolution of ridge axis discontinuities by the meeting, liking and self-decapitation of neighboring ridge segments, *Geology, 15*, 993–997, 1987.

Macdonald, K. C., J.- C. Sempéré, and P. J. Fox, East Pacific Rise from Siqueiros to Orozco fracture zones: Along strike continuity of axial neo-volcanic zones and structure and evolution of overlapping spreading centers, *J. Geophys. Res, 89*, 6049–6069, 1984.

Macdonald, K. C., Mid-ocean ridges: Fine scale tectonic, volcanic, and hydrothermal processes within the plate boundary zone, *Annu. Rev. Earth Planet. Sci., 10*, 155–190, 1982.

Macdonald, K. C., P. J. Fox, L. J. Perram, M. F. Eisen, R. M. Haymon, S. P. Miller, S. M. Carbotte, M.- H. Cormier, and A. N. Shor, A new view of the mid-ocean ridge from the behavior of ridge axis discontinuities, *Nature, 335*, 217–225, 1988.

Macdonald, K. C., P. J. Fox, The axial graben and cross-sectional shape of the East Pacific Rise as indicators of axial magma chambers and recent volcanic eruptions, *Earth Planet. Sci. Lett., 88*, 119–131, 1988.

Macdonald, K. C., Tectonic and magmatic processes on the East Pacific Rise, *In:* The Geology of North America, N, The Eastern Pacific Ocean and Hawaii, Geol. Soc. Am., 93–110, 1990.

Mahoney, J. J., J. H. Natland, W. M. White, R. Poreda, S. H. Bloomer, R. L. Fisher, and A. N. Baxter, Isotopic and geochemical provinces of the western Indian ocean spreading centers, *J. Geophys. Res., 94*, 4033–4052, 1989.

Malinverno, A, Inverse square-root dependence of mid-ocean ridge flank roughness on spreading rate, *Nature, 352*, 58–60, 1991.

Malinverno, A., and R. A. Pockalny, Abyssal hill topography as an indicator of episodicity in crustal accretion and deformation, *Earth Planet. Sci. Lett., 99*, 154–169, 1990.

Marsh, B. D., Crystal size distribution (CSD) in rocks and the kinetics and dynamics: I. Theory, *Contrib. Mineral. Petrol., 99*, 277–291, 1988.

Matsui, T., and M. H. Manghnani, Thermal expansion of single-crystal forsterite to 1023 K by Fizeau interferometry, *Phys. Chem. Minerals, 12*, 201–210, 1985.

McKay, G. A., Partitioning of rare earth elements between major silicate minerals and basaltic melts, *in:* Reviews in mineralogy, edited by B. R. Lipin and G. A. McKay, eds., *Mineral. Soc. Am. Public., 21*, 45–78, 1989.

McKenzie, D., $^{230}Th - ^{238}U$ disequilibrium and the melting processes beneath ridge axes, *Earth Planet. Sci. Lett.*, *72*, 137–152, 1985*a*.

McKenzie, D., and M. J. Bickle, The volume and composition of melt generated by extension of the lithosphere, *J. Petrol.*, *29*, 625–679, 1988.

McKenzie, D., The extraction of magma from the crust and mantle, *Earth Planet. Sci. Lett.*, *79*, 81–91, 1985*b*.

McKenzie, D., The generation and compaction of partially molten rock, *J. Petrol.*, *25*, 713–765, 1984.

Melson, W. G., and T. O'Hearn, "Zero" age variations in the composition of abyssal volcanic rocks along the axial zone of the Mid-Atlantic Ridge, In The Geology of North America, The Western North America region, vol. M, edited by P. R. Vogt and B. E. Tucholke, Geological Society of America, Boulder, Co., pp. 117–136, 1986.

Michael, P. J., R. L. Chase, and J. F. Allan, Petrologic and geologic variations along the southern Explorer ridge, northeast Pacific ocean, *J. Geophys. Res.*, *94*, 13895–13918, 1989.

Moore, J. G., W. R. Normark, G. R. Hess, and C. E. Meyer, Petrology of basalt from the East Pacific Rise near 21° North latitude, *U. S. Geological Survey J. Res.*, *5–6*, 753–759, 1977.

Morel, J. M., and R. Hekinian, Compositional variation of volcanics along segments of recent spreading ridges, *Contrib. Mineral. Petrol.*, *72*, 425–436, 1980.

Morel, J. M., Evolution magmatique le long des dorsales Medio-Atlantique et Est–Pacifique, Ph.D. thesis, Univ. de Bretagne Occidental, 1979.

Mutter, J. C., G. A. Barth, P. Buhl, R. S. Detrick, J. Orcutt, and A. Harding, Magma distribution across ridge-axis discontinuities on the East Pacific Rise from multichannel seismic images, *Nature*, *336*, 156–158, 1988.

Natland, J. H., Crystal morphologies in basalt dredged and drilled from the East Pacific Rise near 9°N and the Siqueiros fracture zone, In Initial Report of the Deep Sea Drilling Project, vol. 54, edited by B. R. Rosendahl and R. Hekinian, Washington (US Government Printing Office), pp.605–634, 1980*a*.

Natland, J. H., Effects of axial magma chambers beneath spreading centers on the compositions of basaltic rocks, In Initial Report of the Deep Sea Drilling Project, v. 54, edited by B. R. Rosendahl and R. Hekinian, pp.833–850, 1980*b*.

Natland, J. H., Partial melting of a lithologically heterogeneous mantle: Inferences from crystallization histories of magnesian abyssal tholeiites from the Siqueiros Fracture Zone, In Magmatism in Ocean Basins, edited by A. D. Saunders and M. J. Norry, *Geol. Soc. Special Pub., 42*, 41–70, 1989.

Neumann, E. R., and Schilling, Petrology of basalts from the Mohns-Knipovich Ridge: The Norwegian-Greenland Sea, *Contrib. Mineral. Petrol., 85*, 209–223, 1984.

Nicolas, A., A melt extraction model based on structural studies in mantle peridotites, *J. Petrol., 27*, 999–1022, 1986.

Nicolas, A., Structures of ophiolites and dynamics of oceanic lithosphere, 368pp., *Kluwer Academic*, Dordrecht, pp 368, 1989.

Nielsen, R. L., A method for the elimination of the compositional dependence of trace element distribution coefficients, *Geochim. Cosmochim. Acta, 49*, 1775–1779, 1985.

Nielsen, R. L., A method for the simulation of combined major and trace element liquid line of descent, *Geochim. Cosmochim. Acta, 52*, 27–38, 1988.

Nielsen, R. L., and M. A. Dungan, Low pressure mineral-melt equilibria in natural anhydrous mafic system, *Contrib. Mineral. Petrol., 84*, 310–326, 1983.

Niu, Y., and R. Batiza, Chemistry of near-EPR seamounts chains: Implications for magma supply process, *Eos Trans. AGU, 70*, 1400, 1989.

O'Donnell, T. H., and D. C. Presnall, Chemical variations of the glass and mineral phases in basalts dredged from 25° – 30°N along the mid-Atlantic ridge, *Am. J. Sci., 280*, 845–868, 1980.

O'Hara, M. J., and R. E. Mathews, Geochemical evolution in an advancing, periodically replenished, periodically tapped, continuously fractionated magma chamber, *J. Geol. Soc. Lond.*, 237–277, 1981.

O'Hara, M. J., Primary magma and the origin of basalts, *Scott. J. Geol., 1*, 19–40, 1965.

Oldenberg, C. M., F. J. Spear, D. A. Yuen, and G. Sewell, Dynamic mixing in magma bodies: Theory, simulations and implications, *J. Geophys. Res. 94*, 9215–9236, 1989.

Oxburgh, E. R., and D. L. Turcotte, mid-ocean-ridge and geotherm distribution during mantle convection, *J. Geophys. Res., 73*, 26–43, 1968.

Oxburgh, E. R., and E. M. Parmentier, E., Compositional and density stratification in the oceanic lithosphere - causes and consequences, *J. Geol. Soc. Lond., 133*, 343–354, 1977.

Patriat, Ph., C. Deplus, C. Rommevaux, H. Sloan, P. Hunter, and H. Brown, Evolution of the segmentation of the mid-Atlantic ridge between 28° and 29°N during the last 10 ma: Preliminary results from the SARA Cruise (R/V Jean Charcot, May 1990), *Eos Trans. AGU, 71*, 1629, 1990.

Perfit, M. R., D. J. Fornari, A. Malahoff, and R. W. Embley, Geochemical studies of abyssal lavas recovered by DSRV from Eastern Galapagos Rift, Inca Transform, and Ecuador Rift, 3. Trace element abundances and petrogenesis, *J. Geophys. Res. 88*, 10551–10572, 1983.

Perfit, M. R., D. J. Fornari, M. Smith, C. Langmuir, J. Bender and R. Haymon, Fine-scale petrologic variations along the East Pacific Rise crest 9°17'N to 9°54'N: Results

from ALVIN diving and rock coring during the ADVENTURE Program, *Eos Trans. AGU,72*, 491, 1991.

Perram, L. J., and K. C. Macdonald, A one-million-year history of the 11°45'N East Pacific Rise discontinuity, *J. Geophys. Res.*, 1992 (*in press*).

Phipps Morgan, J., and D. W. Forsyth, Three-dimensional flow and temperature perturbations due to a transform offset: Effects on oceanic crustal upper mantle structure, *J. Geophys. Res, 93*, 2955–2966, 1988.

Phipps Morgan, J., Melt migration beneath mid-ocean ridge spreading centers, *Geophys. Res. Lett., 14*, 1238–1241, 1987.

Pockalny, R. A., P. J. Fox, and R. S. Detrick, A morphological comparison of abyssal hill topography using high-resolution, multi-beam bathymetry data, *J. Geophys. Res. 88*, 10551–10572, 1983.

Presnall, D. C., and J. D. Hoover, Composition and depth of origin of primary mid-ocean ridge basalts, *Contrib. Mineral. Petrol., 87*, 170–178, 1984.

Rabinowicz, M., G. Ceuleneer, and A. Nicolas, Melt segregation and flow in mantle diapirs below spreading centers: Evidence from Oman ophiolite, *J. Geophys. Res, 92*, 3475–3486, 1987.

Renard, V., R. Hekinian, J. Franchteau, R. D. Ballard, and H. Backer, Submersible observations at the axis of the ultrafast-spreading East Pacific Rise (17°S to 21°30'S), *Earth Planet. Sci. Lett., 75*, 339–353, 1985.

Rhodes, J. M., M. A. Dungan, D. P. Blanchard, and P. E. Long, Magma mixing at mid-ocean ridges: Evidence from basalts drilled near 22°N on the mid-Atlantic ridge, *Tectonophysics, 55*, 35–61, 1979.

Ribe, N. M., Diapirism in the earth's mantle: Experiments on the motion of a hot sphere in a fluid with temperature - dependent viscosity, *J. Volc. Geotherm. Res., 16*, 221–245, 1983.

Ribe, N. M., On the dynamics of mid-ocean ridges, *J. Geophys. Res*, *93*, 429–436, 1988.

Ribe, N. M., The deformation and compaction of partially molten zones, *Geophys. J. R. Astron. Soc.*, *83*, 487–501, 1985.

Ribe, N. M., Theory of melt segregation – a review, *J. Volc. Geotherm. Res.*, *33*, 241–253, 1987.

Richter, F. M., and D. McKenzie, Dynamic models for melt segregation from a deformable matrix, *J. Geol.*, *92*, 729–740, 1984.

Riley, G. N., and D. L. Kohlstedt, An experimental study of melt migration in an olivine-melt system, In Magma Transport and Storage, edited by M. P. Ryan, John Wiley, New York, pp.77–86, 1990

Robie, R. A., M. Bethke, and K. M. Beardsley, Selected X-ray crystallographic data, molar volumes, and densities of minerals and related substances, *U. S. Geol. Survey, Bull.*, 87p., 1967.

Roeder, P. L., and R. F. Emslie, Olivine-liquid equilibrium, *Contrib. Mineral. Petrol.*, *29*, 275–289, 1970.

Rubin, K. H., and J. D. Macdougall, ^{226}Ra excesses in mid-ocean ridge basalts and mantle melting, *Nature*, *225*, 149–157., 1985.

Ryan, M. P., Neutral buoyancy and the mechanical evolution of magmatic systems, In Magmatic Processes, Physical chemical principles, edited by B. O. Mysen, *Geochem. Soc. Spec. Public.*, *1*, 259–305., 1987.

Sato, Y., M. Akaogi, and S. - I. Akimoto, Hydrostatic compression of the synthetic garnet pyrope and almandine, *J. Geophys. Res.*, *83*, 335–338, 1978.

Schilling, J.- G., H. Sigurdsson, A. N. Davis, and R. N. Hey, Easter microplate evolution, *Nature*, *317*, 325–331, 1985.

Schilling, J.- G., M. Zajac, R. Evans, T. Johnston, W. White, J. D. Devine, and R. Kingsley, Petrological and geochemical variations along the Mid-Atlantic Ridge from 29°N to 73°N, *Am. J. Sci., 283*, 510–586, 1983.

Schilling, J.- G., R. H. Kingsley, and J. D. Devine, Galapagos hot spot-spreading system, 1, Spatial, petrological and geochemical variations (83°W-101°W), *J. Geophys. Res., 87*, 5593–5610, 1982.

Schilling, J.- G., R. N. Anderson, and P. R. Vogt, Rare earth, Fe and Ti variations along the Galapagos spreading center and their relationship to the Galapagos mantle plume, *Nature, 261*, 108–112, 1976.

Schouten, H, K. D. Klitgord, and J. A. Whitehead, Segmentation of mid-ocean ridges, *Nature, 317*, 225–229, 1985.

Scott, D. R., and D. J. Stevenson, A self-consistent model of melting, magma migration and buoyancy-driven circulation beneath Mid-Ocean Ridges, *J. Geophys. Res., 94*, 2973–2988,1989.

Sempéré, J. -C., G. M. Purdy, and H. Schouten, Segmentation of the mid-Atlantic ridge between 24°N and 34°40'N, *Nature, 344*, 427–431, 1990.

Shaw, D. M., Trace element fractionation during anatexs, *Geochim. Cosmochim. Acta, 34*, 237–243, 1970.

Sigurdsson, H., First order major element variation in basalt glasses from the Mid-Atlantic Ridge: 29°N to 73°N, *J. Geophys. Res., 86*, 9483–9502, 1981.

Sinton, J. M., and R. S. Detrick, Mid-ocean ridge magma chambers, *J. Geophys. Res., 97*, 197–216, 1992.

Sinton, J. M., D. S. Wilson, D. M. Christie, R. N. Hey, and J. R. Delaney, Petrologic consequences of rift propagation on oceanic spreading ridges, *Earth Planet. Sci. Lett., 62*, 193–207, 1983.

Sinton, J. M., S. M. Smaglik, J. J. Mahoney, and K. C. Macdonald, Magmatic processes at superfast spreading ridges: Glass compositional variations along the EPR 13° – 23°S, *J. Geophys. Res.*, *96*, 6133–6155, 1991.

Skinner, B. J., Thermal expansion. Handbook of physical constants, *The Geol. Soc. Am. Memoir*, *97*, 75–96, 1966.

Sleep, N. H., segregation of magma from a mostly crystalline mush, *Geol. Soc. Am. Bull.*, *85*, 1225–1232, 1974.

Sleep, N. H., Tapping of melts by veins and dikes, *J. Geophys. Res. 93*, 10,255–10,272, 1988.

Small, C, and D. T. Sandwell, An abrupt change in ridge axis gravity with spreading rate, *J. Geophys. Res.*, *94*, 17383–17392,1989.

Smith, T., and R. Batiza, New field and laboratory evidence for the origin of hyaloclastite flows on seamounts, *Bull. Volcanol.*, *57*, 96–114, 1989.

Sotin, C., and E. M. Parmentier, Dynamic consequences of compositional and thermal density stratification beneath spreading centers, *Geophys. Res. Lett.*, *16*, , 835–838, 1989.

Sparks, D. W., and E. M. Parmentier, Melt extraction from the mantle beneath spreading centers, *Earth Planet. Sci. Lett.*, *105*, 368–377, 1991.

Spiegelman, M., and D. McKenzie, Simple 2-D models for melt extraction at mid-ocean ridges and island arcs, *Earth Planet. Sci. Lett.*, *83*, 137–152, 1987.

Stakes, D. S., J. W. Shervais, and C. A. Hopson, The volcanic-tectonic cycle of the FAMOUS and AMAR valleys, Mid-Atlantic Ridge (36°47'N): Evidence from basalt glass and phenocryst compositional variations for a steady-state magma chamber beneath valley midsections, AMAR 3, *J. Geophys. Res.*, *89*, 6995–7028, 1984.

Stolper, E., A phase diagram for mid-ocean ridge basalts: Preliminary results and implications for petrogenesis, *Contrib. Mineral. Petrol.*, *74*, 13–27, 1980.

Stolper, E., D. Walker, B. H. Hager, and J. F. Hays, Melt segregation from partially molten source region, the importance of melt density and source region size, *J. Geophys. Res.*, *86*, 6261–6271, 1981.

Suzuki, I., and O. L. Anderson, and Y. Sumino, Elastic properties of a single-crystal forsterite Mg_2SiO_4, up to 1,200 K, *Phys. Chem. Minerals*, *10*, 38–46, 1983*b*.

Suzuki, I., and O. L. Anderson, Elasticity and thermal expansion of a natural garnet up to 1,000 K, *J. Phys. Earth*, *31*, 125–138, 1983*a*.

Suzuki, I., K. Seyoshi, H. Takei, and Y. Sumino, Thermal expansion of Fayalite, Fe_2SiO_4, *Phys. Chem. Minerals*, *7*, 60–63, 1981.

Thompson, G., W. B. Bryan, and S. E. Humphris, axial volcanism on the East Pacific Rise, 10° - 12°N, In Magmatism in the Ocean Basin, edited by A. D. Saunders and M. J. Norry, *Geol. Soc. Spec. Public.*, *42*, 181–200, 1989.

Thompson, G., W. B. Bryan, and W. G. Melson, Geological and geophysical investigation of the Mid-Cayman Rise spreading center: Geochemical variation and petrogenesis of basalt glasses, *J. Geol.*, *88*, 41–55, 1980.

Tighe, S., (ed), East Pacific Rise data synthesis JOI, Inc. (publ), Washington, D. C., 1988.

Toomey, D. R., G. M. Purdy, S. C. Solomon, and W. S. D. Wilcock, the three-dimensional seismic velocity structure of the East Pacific Rise near latitude 9°30'N, *Nature*, *347*, 639–645, 1990.

Ulmer, P., The dependence of the Fe^{2+}–Mg cation-partitioning between olivine and basaltic liquid on pressure, temperature and composition, *Contrib. Mineral. Petrol.*, *101*, 261–273, 1989.

Vaughan, M. T., and J. D. Bass, Single crystal elastic properties of protoenstatite, a comparison with orthoenstatite. *Phys. Chem. Minerals*, *10*, 62–68, 1983.

Vera, E. E., J. C. Mutter, P. Buhl, J. A., A. J. Harding, M. E. Kappus, R. S. Detrick, and T. M. Brocher, The structure of 0- to 0.2-ma-old oceanic crust at 9°N on the East Pacific Rise from expanded spread profiles, *J. Geophys. Res.*, *95*, 15,529–15,556, 1990.

Vogt, P. R., Volcano spacing, fractures, and thickness of the lithosphere, *Earth Planet. Sci. Lett.*, *21*, 235–252, 1974.

Volpe, H. M., and S. J. Goldstein, Dating young MORB: ^{226}Ra-^{230}Th isotopic disequilibria measured by mass spectrometer, *Eos Trans. AGU*, *71*, 1702, 1990.

Walker, D., T. Shibata, and S. E. DeLong, Abyssal tholeiites from the Oceanographer Fracture Zone, II, Phase equilibria and mixing, *Contrib. Mineral. Petrol.*, *70*, 111–125, 1979.

Wang, H., and G. Simmons, Elasticity of some mantle crystal structures 1. Pleonaste and hercynite spinel, *J. Geophys. Res.*, *77*, 4379–4392, 1972.

Wang, H., and G. Simmons, Elasticity of some mantle crystal structures 3. Spessartine-almondine garnet, *J. Geophys. Res.*, *79*, 2607–2613, 1974.

Weaver, J. S., and C. H. Langmuir, Calculation of phase equilibrium in mineral-melt systems, *Comput. Geosci.*, *16*, 1–19, 1990.

Weaver, J. S., T. Takahashi, and J. Bass, Isothermal compression of grossular garnets to 250 Kbar and the effect of calcium on the bulk modulus, *J. Geophys. Res.*, *81*, 2474–2482, 1976.

Whitehead, J. A., H. J. B. Dick, and H. Schouten, A mechanism for magmatic accretion under spreading centers, *Nature*, *312*, 146–147, 1984.

Williams, R. W., and J. B. Gill, Effects of partial melting on the uranium decay series, *Geochim. Cosmochim. Acta*, *53*, 1607–1619, 1989.

Wilson, D. S., D. A. Clague, N. H. Sleep, and J. Morton, A model for narrow, steady state magma chambers on fast spreading ridges, *J. Geophys. Res.*, *93*, 11974–11984, 1988.

Wilson, D. S., Tectonic history of the Juan de Fuca ridge over the last 40 million years, *J. Geophys. Res.*, *93*, 11863–11876, 1988.

Winter, J. K, F. Okamura, and S. Ghose, A high-temperature structural study of high albite, monalbite, and albite-monalbite phase transition, *Am. Mineral.*, *64*, 409–423, 1979.

Yoder, H. S. Jr., *Generation of Basaltic Magma*, 265 pp., National Academy of Science Press, Washington, D. C., 1976.

Zindler, A., and S. R. Hart, Chemical geodynamics, *Ann. Rev. Earth Planet. Sci.*, *14*, 493–571, 1986.

Zindler, A., H. Staudigel, and R. Batiza, Isotope and trace element geochemistry of young Pacific seamounts: Implications for the scale of upper mantle heterogeneity, *Earth Planet. Sci. Letts.*, *70*, 175–195, 1984.

PLEASE NOTE

The disc is not included
in this material. It is available
for consultation at the author's
graduate school library.

University Microfilms International